The growth of black holes in cosmological simulations.

Yetli M Rosas Guevara

Abstract

We investigate the growth of black holes and their effects on the evolution of galaxies through cosmic time in the Λ CDM cosmology by using fully hydrodynamical simulations of structure formation.

Gas accretion onto black holes is modelled and improved via a subgrid model that takes into account the circularisation and subsequent viscous transport of infalling material. We incorporate the black hole accretion model in hydrodynamical simulations of relatively small size. The model broadly matches the observed stellar mass fractions in haloes and reproduces the expected correlation between the stellar velocity dispersion and the black hole mass. The distribution of black hole accretion rates is also compatible with observations.

Additionally, we use a state-of-the-art hydrodynamic simulation that is designed to produce a virtual Universe that closely matches the observed properties of galaxies such as the galaxy stellar mass function and the relation between the black hole mass and the stellar mass at the present day. The critical part to reproduce the galaxy stellar mass function is the subgrid models of AGN feedback and black hole growth that are based on the model investigated above. We find that the simulation reproduces the black hole mass function at the present day.

We investigate the predicted relations between the black hole mass and the stellar mass and the black hole mass and the parent halo mass and their evolution through cosmic time. We find that there is no evolution in approximately the last 10 and a half giga years ($z \lesssim 2$), while at early times the most massive galaxies were inhabited by more massive black holes. The evolution of these relations are different in large halos and small halos. This can be explained in terms of self-regulation. Black holes living in massive haloes ($\lesssim 10^{12}\mathrm{M}_{\odot}$) today self-regulate their growth via AGN feedback that quenches black hole accretion rates and star

formation, while the black holes in small haloes rapidly grow without affecting the growth of the galaxy. By looking at the relations between the gas properties and the parent halo mass, we compare the scatter of these relations to the ratio of cumulative accreted mass of black holes to halo mass. We speculate that there is a range of halos that frames the region where black holes start to grow by self-regulation.

Finally, we explore the predicted evolution of the AGN luminosity functions in X-ray bands predicted in this simulation. We find remarkable agreement with observations. In addition, we find that the observed downsizing effect of AGNs is well reproduced in the simulation as a natural consequence of reproducing the AGN luminosity functions. We also explore AGN activity in different halos. We find that the massive haloes are inhabited by AGNs with low or non activity while low mass haloes are inhabited by AGNs with high activity that contribute to the hard X ray luminosity function across time.

The evolution of black holes in cosmological simulations

Yetli M Rosas Guevara

A Thesis presented for the degree of
Doctor of Philosophy

Institute for Computational Cosmology
Department of Physics
University of Durham
United Kingdom

August 2014

Contents

List of Figures

List of Tables

Declaration

The work described in this thesis was undertaken between 2010 and 2014 while the author was a research student under the supervision of Professor Richard G. Bower and Prof. Carlos S. Frenk at the Cosmology Group and the Institute for Computational Cosmology in the Department of Physics at the University of Durham. This work has not been submitted for any other degree at the University of Durham or any other university.

Chapter 3 has been submitted in the form of a paper in Monthly Notices of the Royal Astronomical Society:

- Rosas-Guevara, Y. M.; Bower, R. G.; Schaye, J.;Furlong, M.; Frenk, C. S.; Booth, C. M.; Crain, R.; Dalla Vecchia, C.; Schaller, M.; Theuns, T., *The impact of angular momentum on black hole accretion rates in simulations of galaxy formation*, submitted to MNRAS.

All figures were produced by the author except the following:

- Figure 1.1 taken from Benson et al. (2003)
- Figure 1.2 taken from Torres (2004)
- Figure 2.1 taken from Springel et al. (2001)
- Figure 4.1 courtesy of Michelle Furlong

Most of the work in this thesis was completed by the author. Those parts not done by her are properly acknowledged in the text or in the following list:

- The GADGET code used throughout this thesis was written by Volker Springel.
- Modules of the version of the code P-Gadget3 presented in this thesis were also written by Joop Schaye, Richard Bower, Robert Crain, Michelle Furlong,

Matthieu Schaller, Tom Theuns, Claudio Dalla Vecchia, John Helly, Adrian Jenkins and Craig Booth.

- Some of the software used to analyse data from the simulations were developed by Michelle Furlong. Modifications to this software and part of the software used here was written by the author.
- The BH accretion modules were modified by the author in Chapter 3.
- Simulations used in Chapter 3 were run by the author on the COSMA-4 supercomputer, ICC, Durham University, UK.
- Simulations used in Chapter 4 and Chapter 5 were run by Robert Crain, Michelle Furlong, Matthieu Schaller on the COSMA-5 supercomputer. This supercomputer is part of the DiRAC Data Centric system at Durham University operated by the Institute for Computational Cosmology, UK.

Acknowledgements

I am deeply thankful to my supervisors Richard Bower and Carlos Frenk whose encouragement, dedication, support and incredible patience from the initial to the final level enabled me to develop myself as a researcher and acquire a better understanding of the subject. This thesis would not have been possible without their perpetual enthusiasm, useful advice and immense knowledge.

I would like to thank the Eagle team for their impartial and constructive feedback which has enormously improved my work and performance and has influenced my view of doing science. I also owe my deepest gratitude to Karen Caballero, Stan Kurtz, Sergio Mendoza and Luis Felipe Rodriguez for their useful and honest advice and guidance in my career that has allowed me to overcome any difficulties.

I am also very grateful to the Mexican Council for Science and Technology (CONACyT) for funding my research through a scholarship and Durham University for awarding me with a partial waiver of the tuition fees.

My colleagues in Durham have my gratitude for being the most efficient and problem solving people I have met so far. In particular, I would like to thank to Peter Creasey for teaching me Python, Michelle Furlong for sharing her code, Nicos Tejos for always being open to discuss any question, Nokpunyawat Tummuangpak for teaching me to be patient and empathetic with others, James Aird and Nikos Fanidakis for sharing data, my housemates and some friends Elena, Giovanni, Yajhaira, Francesca, Peter, Aranus for making my life in Durham bearable and my office mates Rob, Jack and Lilian for creating a good work environment. I also thanked to my beloved friends Karen, Orlando, Cristina, Sergio, Antonio and Luis who from the distance have always supported me.

Last but not the least, I thank those closest to me: Jens Rundegren for his love, emotional support, and understanding as well as his help with editing and carefully proofreading my thesis, my parents Jorge and Guadalupe and my sisters Cope, Dulce and Gina for their love, support and understanding.

Dedicated to

Jorge, Guadalupe, Jens, Cope, Dulce and Gina

Chapter 1 | *Introduction*

1.1 Background

1.1.1 Structure formation

Striking progress in observational cosmology has allowed us to gain a much better understanding of the evolution of the Universe, leading to the emergence of a standard model for cosmic structure formation (see recent reviews Narlikar & Padmanabhan 2001; Bertone et al. 2005). This can be summarised as follows:

- The evolution of the Universe is described by Einstein's theory of general relativity, and the mass distribution of the Universe is assumed to be homogeneous and isotropic. Direct evidence from galaxy surveys, suggests a homogeneous distribution in the Universe on scales larger than 100 Mpc. Therefore, the metric of the spacetime of the Universe can be described by the Robertson-Walker metric and its dynamical evolution by Friedman's models.

- The Universe started with a rapid expansion from a very hot and compressed state existing around 10^{10} years ago. This picture of the universe is called The Big Bang scenario. Crucial information about this early phase is found in the cosmic microwave background (CMB) radiation, that permeates the Universe and is well described by thermal black body radiation. The CMB is the most direct evidence for the Big bang scenario (e.g. Komatsu et al. 2011;Planck collaboration et al. 2013). Through a combination of several independent observations together with CMB, a consistent concordance

model of cosmology has emerged. Such observations consist of the large scale structure measured through galaxy surveys (e.g. Tegmark et al. 2004; Cole et al. 2005; Percival et al. 2007a), Type Ia supernovae (SNe) through the magnitude vs. redshift relation or Hubble diagram (e.g. Riess et al. 1998; Perlmutter et al. 1999; Kowalski et al. 2008) and abundance and properties of galaxy clusters (e.g. Koester et al. 2007; Vikhlinin et al. 2009).

In the concordance model of cosmology, the total density parameter is expressed in terms of the critical density of the Universe and it is close to unity, implying that the geometry of the space is flat (Komatsu et al., 2011; Planck collaboration et al., 2013). This is consistent with inflationary models.

The density of the baryonic matter, Ω_b, only contributes ~ 0.04 to the total energy density of the universe in agreement with Big bang nucleosynthesis predictions. However, dynamical estimates of the matter density parameter require a higher value of ~ 0.3. This discrepancy is reconciled by the existence of *non-baryonic dark matter*. The currently favoured model is the cold dark matter (CDM) model where dark matter is weakly interacting (effectively collisionless) particles that have negligible thermal velocities (non-relativistic) at the time of decoupling. Nevertheless, so far, there is no certainty about the physical identity of the dark matter particle, apart from knowing its fundamental properties, namely that it should be collisionless and heavy enough to be non-relativistic. The nature of the dark matter is one of the most important open questions in modern cosmology.

To explain the difference between the matter density parameter, Ω_m, and the flat geometry of the Universe, *a dark energy component*, Ω_λ, is required in the standard model. Dark energy is important only on large scales and has a negative pressure, leading to the accelerated expansion of the Universe. The simplest theory incorporating effects of dark energy is the Λ CDM model (Blumenthal et al., 1984), a model that includes a cosmological constant. However, the nature of the dark energy is even less clear than that of the

dark matter, which is a fundamental problem for field theories.

- Cosmic structures form via gravitational instability in the hierarchical growth paradigm. Quantum fluctuations amplified during inflation provide the seeds of the cosmic structures. In the CMB, density fluctuations of the order of 10^{-5} at redshift of $z \sim 1100$ have been detected (Komatsu et al., 2011; Planck collaboration et al., 2013). The initial growth of cosmic structures is determined by linear perturbation theory. However, cosmic structures today are highly non linear. One of the primary goals of cosmology is to understand in detail how these small seeds evolve to become the observed galaxies, massive galaxy clusters and filaments seen today. The underlying process for structure formation is gravity. However, to fully understand the evolution of growth and properties of cosmic structures, additional physical processes are required.

The points described above summarise the foundations of the standard cosmological model today and those that this thesis relies on.

1.1.2 Galaxy formation and evolution

In order to get a complete picture of the evolution of the cosmic structure, it is imperative to consider galaxies. Understanding how galaxies form and evolve have been the object of the study of galaxy formation theory.

Galaxy formation theory is closely related to Cosmology in the sense that the growth of galaxies is essentially determined by the growth of structures in the Universe. Then, galaxy formation theory is set within the cold dark matter model and therefore proceeds via a fundamentally hierarchical paradigm (see recent reviews of galaxy formation theory eg. Benson 2010) . However, galaxy evolution is more complex than only mirroring the evolution of cosmic structure in the sense that their evolution is not only influenced by gravity, but also by a rich and complex array of physical processes.

Traditionally the approach that galaxy formation theory has advanced is to

use galaxy observables that confront theorical models. These models started with a simple gas collapse model (Eggen, 1962) that included basic physics to predict some observables. Currently, confronting theory with observations is a whole industry. Through large galaxy surveys -such as the Sloan Digital Sky Survey (SDSS; York et al. 2002) which is a wide spectroscopic survey detecting the nearby Universe together with narrower surveys using photometric redshifts and often in the infrared range to observed distant galaxies in optical and near-infrared range (eg. Herschel;Pilbratt et al. 2010 and Spitzer; Werner et al. 2004)- galaxy formation theory has made huge progress in understanding the physics behind the formation and evolution of galaxies.

The way that that galaxy formation proceeds is, primarily, via two theorical tools that are widely used:

- *Semi-analytic models*. First they produce the mass assembly history (MAH) of halos via cosmological dark matter simulations and the building of halo merger trees. Then, they used physically motivated models to treat the evolution of the baryons. These models are constrained by observations. The advantage of semianalytic models is the enormous capability of exploring a large space of parameters of the models and in large cosmological volumes, allowing to make detailed comparison with observations. Their weakness is that some of the physics is assumed apart from gravity, which is determined by the N-body simulations of the dark matter component.

- *Numerical simulations* treat hydrodynamical processes along with gravity in a much more self-consistent way. They make less assumptions in the gas dynamics. However, many of the physical processes relevant for galaxy formation operate on scales smaller than the resolution of these simulations, and are implemented as sub-grid physics that are treated in a phenomenological way. In that sense, they work in the same fashion as semianalytic models. The drawback of numerical simulations is that it is not possible to explore a large space of parameters of the subgrid models because of the

high computational cost. They also have limited cosmological volumes. As a result, the agreement with observations is poor. However, in that respect, cosmological simulations have dramatically improved in recent years.

In this thesis, we will use cosmological simulations that will be reviewed in more detail in Chapter 2.

1.1.3 Initial motivation for this thesis: The Overcooling Problem

One crucial test for any galaxy formation theory is to reproduce the observed galaxy luminosity function (LF) or stellar mass function, defined as the number density of galaxies for any given luminosity or mass. The physical processes that determine the shape of the LF were first proposed by Rees & Ostriker (1977) and White & Rees (1978). These authors argued that galaxies would form as gas cools and fragments inside of dark matter halos and suggested that the break in the galaxy luminosity function arose from the long cooling times of gas in high mass halos. However, when semi-analytic models integrated the physics of this argument, they required a very low baryon density of $\Omega_b \sim 0.02$, almost half of that indicated by WMAP (Komatsu et al., 2011) to match the galaxy mass function. Assuming the WMAP cosmology, their estimates suggest that gas can cool at a sufficiently large rate that, by the present day, galaxies much more massive than any observed will have formed. This is known as the *overcooling problem* (White & Rees, 1978; White & Frenk, 1991; Katz et al. , 1996; Benson et al., 2003).

Fig 1.1 illustrates the *overcooling problem* in semianalytic models of galaxy formation (Benson et al., 2003). Fig 1.1 shows the predicted LF for different physical processes and compares it to observations from Cole et al. 2001 (circles), Kochanek et al. 2001 (squares) and Huang et al. 2002 (stars). The simplest model is model 1 (dashed line) that shows the LF obtained by assuming a fixed mass-to-light ratio to convert the dark matter halo mass function. This fixed mass-to-light ratio is chosen to match the knee of the luminosity function. However, this model

rises steeply for faint galaxies while it declines shallowly for the brightest galaxies relative to observations. By considering cooling (model 2; dotted lines), the model rises even more than model 1 for faint galaxies since cooling is too efficient in these systems while it predicts an overabundance of the brightest galaxies, but below the one predicted by model 1. Additionally, model 3 (long-dashed line) and model 4 (solid lines) include photoionization and merging, respectively. They show the persistent overabundance of both the faint and bright galaxies. This discrepancy in the low mass systems is usually overcome by postulating some form of feedback, typically from supernovae, that is controlled by star formation. However, as shown by Benson et al. (2003) ,this leads to another problem. Too much gas is kicked out the low mass halo so that, this gas is accreted into the most massive halos later on, resulting in overmassive galaxies that we observed.

The main approach to solve the overcooling problem has been heating the gas by some kind of feedback loop that reduces the efficiency of gas cooling somehow. In the case of the massive galaxies, the problem is the energy input required to balance the cooling and heating rate of the gas. An appealing physical process is the energy released from supernovae. However, it can be shown by energy arguments that there is an insufficiency of energy to heat the host halos of the massive galaxies [1].

The scenario of the feedback from active galactic nuclei (AGNs) has been the most promising solution because the energy available by AGN feedback is sufficient ($20 - 50$ higher than supernovae) to counteract the efficiency of gas cooling.

We will see in the following section that this reason together with other theoretical and observations facts, strongly support this scenario.

[1]The binding energy of the host dark matter haloes of massive galaxies scales as $M_{halo}^{5/3}$, while the energy available for supernovae, assuming the extreme case of 100% of efficient conversion of gas into stars, scales as M

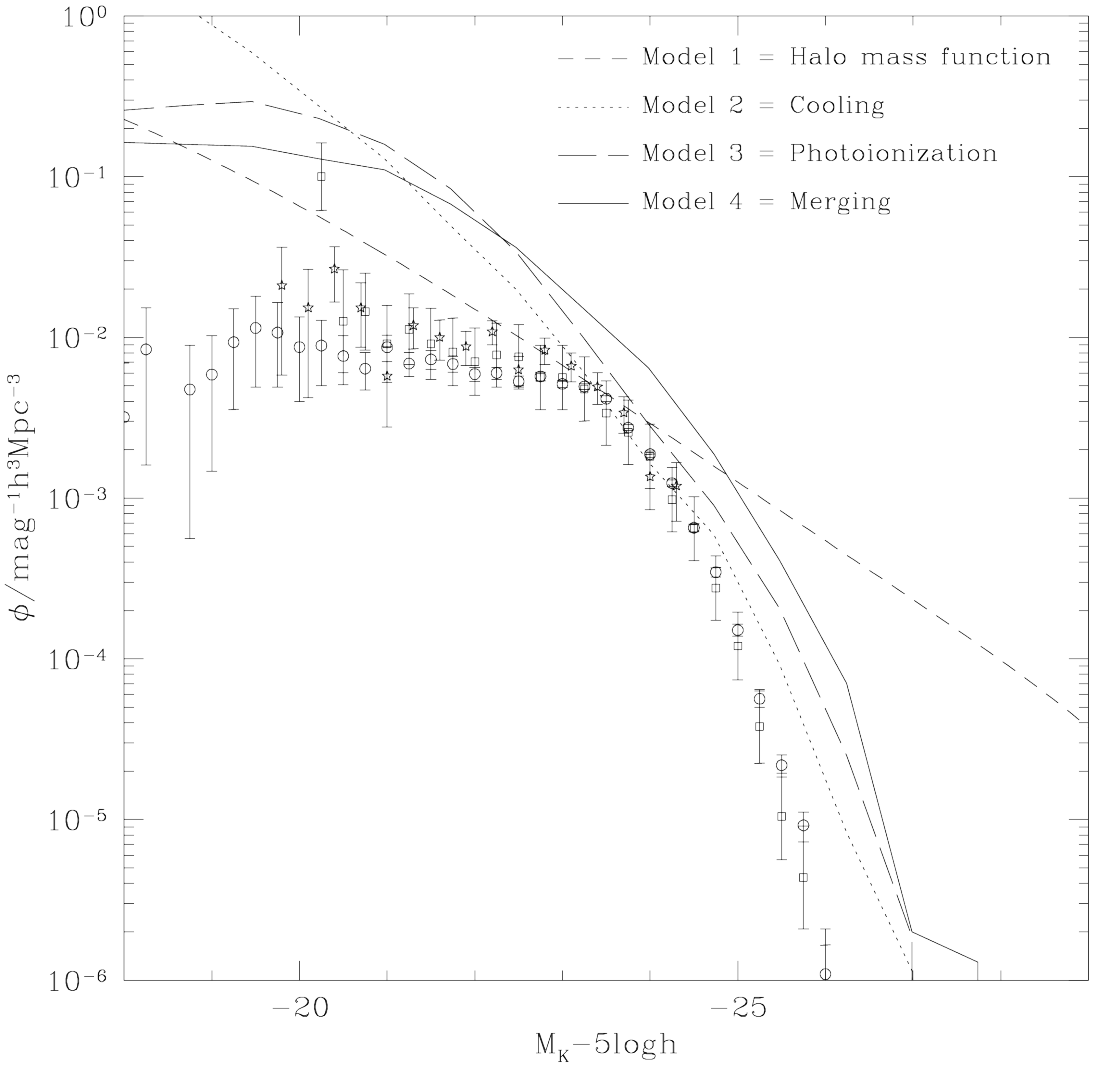

Figure 1.1: The K-Band of the luminosity function of galaxies. Observational estimates (Cole et al 2001, circles; Kochanek et al 2001, squares). Line shows different models:*Model 1* (dashed line) shows the result of converting the dark matter halo mass function into a galaxy luminosity function by assuming a fixed mass-to-light ratio. *Model 2* (dotted line) shows the result from GALFORM when no feedback, photoionization suppression, galaxy merging or conduction are included. *Models 3 and 4* (long dashed and solid lines respectively) show the effects of photoionization and galaxy merging. Illustration taken from Benson et al. (2003).

1.2 Context for this thesis

In the section above, we briefly summarised the cosmological background in which this thesis is carried out and the initial motivation for the AGN scenario in galaxy formation theory. Here, we will focus on the specific topic that this thesis explores: the source of AGN feedback, black holes (BHs), their evolution and their connection with the evolution of galaxies in a cosmological context by using cosmological simulations.

1.2.1 Nature of active galactic nuclei

Galaxies across a wide range of masses and types, show strong nuclear activity. The distinctive feature of an active galactic nucleus (AGN) is its electromagnetic spectrum over a wide range of wavelengths. An AGN differs from a normal galaxy in that a normal galaxy has a spectrum comprised primarily of the thermal emission of the sum of all its stars, while an active galaxy shows continuum emission with a non-thermal spectrum.

AGNs have been studied since Carl Seyfert (1943) systematically analysed some galaxies with extremely high surface brightness and whose central part was dominated by emission lines of very high excitation. This kind of galaxy is named *Seyfert* galaxy and belongs to a class of AGN.

Quasi-stellar radio sources (QUASARs), which belong to another class of AGN, were discovered in the 1960s and recognized as the most luminous objects in the Universe with luminosities spanning 10^{42-46}erg s^{-1}. These huge luminosities along with their rapid variability (from months to days) implied that radiation can not originate only from starlight but must come from a very compact region and gravitational nature. The idea of black holes being the engines of AGN was suggested for the first time by Salpeter (1964), Zel' Dovich (1964) and then by Lynden-Bell (1969), who ruled out the hypothesis that powerful nuclear emission was produced from a very dense star cluster. Instead, these authors suggested a model in which a massive black hole growing by gas accretion, was the central

engine of the AGNs. They also calculated the mass that these massive black holes should have ($10^6 - 10^9 \mathrm{M}_\odot$).

Accretion can be an extremely efficient way of converting gravitational energy into kinetic and thermal energy and radiation. The matter in the vicinity of the BH naturally forms a disc, namely the *accretion disc* . By redistributing the angular momentum, a high fraction of matter in the disc falls onto the BHs while the remainder carries the excess of angular momentum outward.

The best evidence for the existence of supermassive BHs is in our own Galaxy. High resolution imaging of the Galactic center has allowed to track the orbits of a number of stars in the central cluster in our Galaxy (Ghez et al., 2008). From the fitted orbits, the mass of the central object is $\approx 4 \times 10^6 \mathrm{M}_\odot$ and the size of the region in which it must be confined is ~ 120 AU. Evidence from super massive BHs residing in outside galaxies centres is more indirect by inferential methods. Such inferential methods include dynamical modelling of stars (eg. McConnell & Ma (2012)), observations of water maser's orbits (eg. Kuo et al. (2011)) and reverberation mapping (eg. Peterson et al. (2004)).

Brief overview of types of AGN

A wide range of objects are subsumed under the name AGN, all of which have in common strong non-thermal emission in the core of a galaxy. AGNs have been identified into different classes that depend on observable features such as variability, luminosity and spectra. Some of them can be explained within the *AGN Unification models* (Urry & Padovani, 1995), where the AGN features are determined by the mass of the supermassive BHs and their life stage, but primarily the viewed angle of the accreting supermassive BH.

Figure 1.2, depicts the main components of an AGN (Urry & Padovani, 1995). The central massive BH is surrounded by an accretion disc and by high-velocity gas clouds (several thousands km s^{-1}). This region is usually referred to as the *broad line region* (BLR) which is thought to be the place where broad lines that are observed in a high fraction of AGNs are produced. This component of the

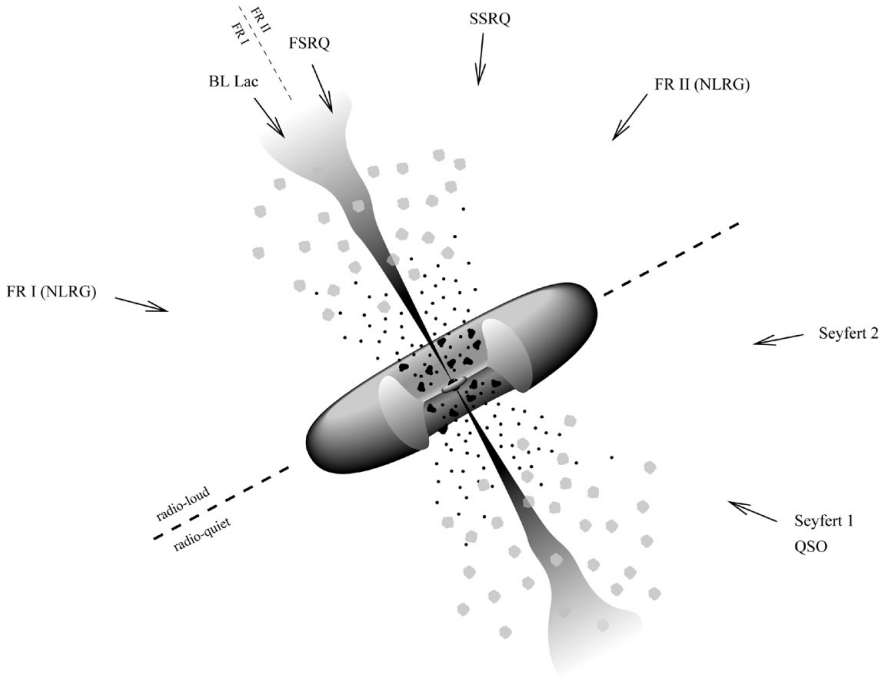

Figure 1.2: Schematic illustration of the standard unified model of AGNs. A regular quasar or a Seyfert 1 galaxy is observed for a given orientated angle , where the narrow-line and broad-line regions are visible. For large angular offsets, the broad-line region will be hidden by the torus (Seyfert 2 galaxies or type 2). The figure is adapted from Urry & Padovani (1995), Padovani (1997), Collmar et al. (2002) and Torres (2004). Illustration taken from Torres (2004).

nucleus is very important, especially for estimates of black hole masses. There is another region, named *narrow line region* (NLR) that is composed of lower velocity gas clouds, located farther away from the nucleus. Within this region narrow lines are produced. Some AGNs are optically obscured which is caused by gas and dust that hide the nuclear region and they are distributed along a torus-like axisymmetric structure. Jets are a typical phenomenon of accretion and observed in some AGNs. These jets are material accelerated from the very central region up to relativistic speeds, and these jets can extend up to a few hundreds of kpc.

A first simple AGN classification is based on the type of lines presented on the spectra. In this thesis, we will briefly summarise this simple classification:

- **Type 1** are characterized both by narrow and broad lines in their spectra, suggesting that the observer is able to look directly into the region of the

accretion disk. Type 1 AGN are, in fact, also characterized by a very bright continuum, which is the light emitted by the very central region. Approximately 10% of their light is emitted in the optical.

- **Type 2** have spectra featuring only narrow lines and a much weaker continuum. The torus is probably obscuring the central region, and only the emission lines from the lower velocity clouds (few km s^{-1}) of gas far from the center are visible. Type 2 differs from Type 1 in the percentage of their light being emitted in the optical. The fraction of type 2 is much lower than 10%.

- **Quasars**. When the nucleus outshines its host galaxy is named QUASARs. They were identified for the first time in radio surveys (1960s). The spectral energy distribution is primarily a power law. More frequently, they are found at high redshift of the Universe.

- **Seyfert Galaxies** observed by Carl Seyfert as previously mentioned. The galaxy can be observed and Seyfert galaxies have a very bright nucleus. Seyfert galaxies are usually divided into 1 and 2 according in to the classification described above.

1.2.2 AGN evolution

During the lifetime of BHs, they are assumed to undergo periods of gas accretion powering AGN. By integrating the total energy radiated by AGNs over their whole lifetime, and assuming that such energy is produced by gas accretion onto BHs, it can be proved that the total mass of the (non active) BHs today, corresponds to the integrated energy radiated from observed bright AGNs across time. This implies that most of the accretion by BHs is not obscured across time (Soltan, 1982). Therefore, the best way to understand the growth of BHs is to study the evolution of AGN activity through cosmic time.

The best way to track AGN activity through cosmic time is by determining the shape and evolution of the AGN luminosity functions. Recent progress in

detecting faint and obscured AGNs has been achieved by analysing data from X-ray surveys in the hard and soft X-ray range (XMM-Newton, Chandra, ROSAT, ASCA e.g. Miyaji et al. 2000; Cowie et al. 2003; Fiore et al. 2003; Barger et al. 2003; Ueda et al. 2003; Hasinger et al. 2005; Barger & Cowie 2005; Sazonov & Revnivtsev 2004; Nandra et al. 2005; Ebrero et al. 2009; Aird et al. 2010; Fiore et al. 2012; Kolodzig et al. 2013). Through these surveys it is possible to study a wider range of AGN luminosities with wider redshift range that enables one to study the evolution and shape of the AGN luminosity functions in detail. Some observational studies based on these surveys have revealed that AGNs are a strong evolving population with the space density of AGN undergoing a sort of luminosity dependent evolution and the density of more luminous AGN peaking at higher redshifts than the less luminous AGN populations. This observational trend is known as *downsizing*.

A large amount of theoretical work has been carried out to investigate the evolution of AGN by using semi-analytic models of galaxy formation (eg. Kauffmann & Haehnelt, 2000; Volonteri et al., 2003; Granato et al., 2004; Menci et al., 2004; Bromley et al., 2004; Monaco & Fontanot, 2005; Croton et al., 2006; Bower et al., 2006; Marulli et al., 2008; Somerville et al., 2008; Fanidakis et al., 2012; Hirschmann et al., 2012; Menci et al., 2013). In these studies, the proccess of BH formation and evolution were included. Some of these studies have reproduced the evolution of AGN luminosity functions very well and have shown that *downsizing* can be explained within a hierarchical structure formation scenario. For instance, Fanidakis et al. (2012) extend the BH model to reproduce the evolution of AGN by accounting for the spin and mass of BHs in the accretion rates. These authors successfully reproduce the evolution of AGNs using a prescription for dust obscuration and the evolution of the galaxies. The disadvantage of these semi analytic models is that many assumptions are made and these studies differ in many details that it is not possible to have a complete uniform picture of the origin of the evolution of AGN and downsizing.

In addition to this, investigation of AGN evolution in numerical simulations

have been done. Some studies using numerical simulations have been focused mainly on the evolution of AGNs but not considered the completely evolution of galaxies as semi-analytic models do. Degraf et al. (2010) have performed cosmological simulations of a $50\mathrm{Mpc}$ region. These simulations include BH formation and BH growth by mergers and gas accretion that is estimated as the Bondi accretion model. These authors were successful to reproduce the AGN luminosities for moderate AGNs ($< 10^{43}$erg s^{-1}) at $z < 2$. However,they do not consistently follow the evolution of the galaxies. Using a similar code, Khandai et al. (2014) performed a larger simulation with cosmological comoving volume of $100\mathrm{Mpc}^{-3}$ going down to $z = 0$. They underestimated luminous AGNs at $z > 0.5$ and overestimated at $z < 0.5$. In addition to this, AGN feedback was not able to quench the most massive galaxies, overestimating the high mass end of the galaxy stellar mass function at $z = 0$.

At high redshift, Di Matteo (2012) and Degraf et al. (2012) studied the evolution of the most luminous quasar using a cosmological simulation of size 0.75 Gpc^3 but only up to $z = 5$. They found that most luminous quasars had undergone a rapid growth driven by cold gas flows . Additionally, they found that the quasar luminosity function to be roughly consistent with the observational constraints.

The studies above show that so far, a numerical framework has not been completely achieved with the basic observational constraints (such as the AGN luminosity function and the galaxy mass function at $z = 0$) in cosmological simulations in order to study the evolution of the galaxies and the evolution of the AGN consistently through time. Some of the goals of this thesis are to explore the results in the evolution of AGN luminosity functions of a large cosmological simulation consistent with the evolution of galaxies.

1.2.3 BH-galaxy connection: observational facts

The notion of co-evolution between galaxies and BHs have emerged over the last decades with increasing availability of large galaxy surveys at different wavelengths. The discovery of strong and weak nuclear activity across a wide range

of masses and types of galaxies have allowed researchers to establish that AGN activity is a common process in the life of galaxies. The evolution of the galaxy population, traced by the star formation rate (SFR), has remarkable simularities to the activity of AGN across time. Both SFR and AGN activity present a steep rise by a factor of 10 from $z = 0$ to $z = 1$, a peak at $z \sim 2$ to 3 and then a strong decline at higher redshift suggesting that AGN activity and SFR are linked together somehow globally (Boyle & Terlevich, 1998; Madau et al., 1996).

In addition to the prevalence of nuclear BHs, observations indicate a link between the black hole and the properties of their host galaxy in the local universe (see review by Kormendy & Ho 2013). One such relationship was the $M_{\rm BH}$-σ_* relation Gebhardt et al. (2000); Ferrarese & Merritt (2000) which relates the mass of the black hole to the stellar velocity dispersion of the spheroidal components of the host galaxy. The mass of the supermassive BHs is also correlated with the mass of the spheroid (Magorrian et al., 1998; Tremaine et al., 2002; Haring & Rix, 2004), and the luminosity of the bulge (Marconi et al., 2003). These relations have continued to be refined as observations improve (Gultekin et al., 2009; McConnell & Ma, 2012). Moreover, Hopkins et al. (2007) suggests that black holes lie on a fundamental plane, analogous to the elliptical galaxy fundamental plane, which links together the two property correlations into a correlation in a higher dimensional space. Whatever form they take, these relationships imply a connection between the evolution of the black holes and their host galaxy.

Even more evidence is found at group and cluster scales where most of the baryons are found as a hot tenuous atmosphere between galaxies (Fabian, 1994). In the central region of the cluster where the hot atmosphere is naturally denser, cooling flows are formed. In these cooling flows, the gas cools through X-ray temperatures and is accreted onto the centre of the cluster. However, recent observations have revealed far less cooling below X-ray temperatures than expected (Peterson et al., 2003) and most of the gas must be heated and maintained at temperatures above 2 keV (Peterson et al., 2003). The promising heating mechanism across the years has been powerful jets generated by supermassive BHs

in the central galaxy of the cluster (eg. McNamara et al 2005; Birzan et al. 2004; McNamara & Nulsen 2007). This is supported by the detection of cavities and shock fronts in the cluster in X-ray images. These cavities are caused by the interaction between these powerful jets and the hot gas. Together with this, there is an observed correlation between the mechanical energy input of these powerful jets and the cooling rates of the intracluster hot gas (Birzan et al., 2004; Rafferty et al., 2006). Similarly, observations of galaxy groups have found evidence of a correlation of the energy input by radio galaxies and the cooling rates of the gas (Antognini et al., 2012; Birzan et al., 2012; Ma et al., 2013). However, how the jet energy is converted to heat is not well understood as well as if the heating mechanism is sufficient to offset the cooling rates at long timescales. Sensitive searches for the repository in optical, infrared, and radio bands (Edge et al., 2003) are required to constrain the role of the heating mechanism driven by AGN.

From the observational side, the existence of active galaxies, the similar global evolution in both AGN and galaxy populations, the ubiquity of black holes in spheroids and the observed correlation of the gas properties and the energy released by AGN in clusters suggest that there is a link between the evolution of black holes and galaxies and that is via the effect of amount of energy injected into the surroundings. However, the underlying physics behind the BH -galaxy connection is not totally understood.

1.2.4 BH-galaxy connection: theoretical results in the cosmological contexts

The observational evidence described in the previous section along with the overcooling problem has motivated numerous studies to explore the formation and evolution of BHs and AGN feedback and the possible connection to the evolution of the galaxies in the standard Λ cold dark matter (CDM) model.

A large amount of studies has been published using phenomenological or semi-analytic models (eg. Benson et al. 2003; Bower et al. 2006; Croton et al. 2006;

Fanidakis et al. 2012), where AGN feedback is assumed to be ineffective in low mass haloes, since the gas cooling time is short compared to the sound-crossing time(White & Frenk, 1991), and only to couple effectively in the quasi-hydrostatic haloes ($M \gtrsim 10^{12}\mathrm{M}_{\odot}$). This dichotomy has some observational support, since the bulk of the energy output from quasars appears to be radiated (Soltan, 1982), while the mechanical energy of radio galaxies is trapped in the overall potential. As White & Rees (1978) suggested, a characteristic mass scale is introduced where the SMF presents a break: accretion in low mass haloes is dominated by cold and rapidly cooling gas (since the cooling time is less than the free-fall or sound-crossing time), while accretion in high mass halo occurs through quasi-hydrostatic cooling gas flows (where the gas is approximately in pressure balance, and the sound crossing time is less than the cooling time). The importance of this distinction can be understood if the primary driver of the star formation rate in galaxies is the balance between outflows and inflows (i.e. the star formation rate of galaxies adjusts itself so that the inflow and outflow are in equilibrium). In the case of low mass haloes, the AGN feedback loop is (assumed to be) ineffective and the balance between gas supply and outflow is set by the supernova driven outflow rate. In higher mass haloes, AGN regulate the galaxy growth either by offsetting the cooling rate (Bower et al., 2006), or by puffing up the hot gas halo (Bower, McCarthy & Benson, 2008; McCarthy et al., 2011; Bower et al., 2012) so that the cooling rate is reduced. In either case, the result is to suppress the mass of the cold gas and reduce the star formation rate in massive haloes, creating a break in the stellar mass function.

In this scenario, the distinction between rapid cooling and hydrostatic haloes is critical. In the absence of a clear physical scale at which BH feedback becomes effective, the stellar mass function behaves as a power–law (Benson et al., 2003; Bower et al., 2012) because the impact of gas ejection builds up over a wide range of stellar mass. However, semi-analytic models make a variety of simplifying assumptions, and it is possible that AGN-driven and star-formation driven outflows might not combine as simply as is envisaged in these studies.

On the other hand, hydrodynamic simulations have the great advantage that there is no need to make an explicit distinction between hydrostatic and rapidly cooling haloes. Any dependence on the ratio of cooling and dynamical timescales should emerge from the solution of the hydrodynamic equations. There is a long history of papers that include AGN feedback in numerical simulations. The first full three dimensional simulations of mergers with feedback from AGN was by Springel et al. (2005) and Di Matteo & Springel (2005). Their simulations included a new model for star formation treating SN feedback processes (Springel & Hernquist, 2003), and a model for energy injection into the gas surrounding the black holes. Springel & Hernquist (2003) are able to not only reproduce the $M_{\rm BH}$-σ relation (Di Matteo & Springel, 2005), but also to produce remnant elliptical galaxies that have little star formation and little AGN activity (Springel, 2005), primarily because the feedback ejects much of the star forming gas to large radii, and thus low density. Hopkins et al. (2005, 2006, 2007) used the model to explore and extend the picture of quasar evolution presented in Sanders et al. (1988). During the merger, gas is torqued to the center and both powers and obscures the quasar. The feedback then blows the gas out of the center and offers a short window during which the quasar is visible before the ejection of gas shuts off activity.

Models often make a distinction between feedback modes: *quasar* where the BH is accreting efficiently and comes in the form of a hot, nuclear wind and *radio*, operates when the accretion rate is low compared to the Eddington rate and the energy is injected in the form of relativistic jets. Sijacki et al. (2007) implement different modes of feedback as two accretion modes in resimulations of clusters and in isolated galaxies and calculate the contributions of the different modes in the build up of the BH mass. Dubois et al. (2010) implement momentum-driven jets in cosmological resimulations of a galaxy cluster. In their simulations, AGN can reduce the SFR relative to a case of no AGN while Debuhr, Quataert & Ma (2011) study simulations of galaxy mergers, presenting a new model of BH accretion and AGN feedback by depositing momentum radially away from

the BH into the surrounding gas. Newton & Kay (2013) explore the role of AGN in numerical simulations of isolated Milky-Way galaxies and mergers by using different models of BH accretion. They found that in isolated galaxies, supernovae dominate the suppression of star formation while in mergers strong AGN feedback shuts off star formation.

Booth & Schaye (2009) extend the model of Springel et al. (2005) by correcting the BH accretion rates with a density dependent law. They also include a novel implementation of AGN feedback that emphasises the importance of self regulation in BHs. Booth & Schaye (2009) test their model using a suit of cosmological simulations where BHs grow until their energy output is comparable to the binding energy of the halo. As a result, they reproduce the $M_{\rm BH}$-$M_{\rm star}$ relation and found a very tight correlation between halo mass and BH mass. The slope of the correlation departs from unity because of the variation of halo concentration (Booth & Schaye, 2010). Changes in the feedback efficiency result in an offset in BH mass such that the rate by which the BH releases energy remains fixed. Their model can also reproduce some properties of the intra group medium in groups McCarthy et al. (2010). Unfortunately, their simulations can only resolve the most massive objects. Muldrew et al. (2013) further investigate the simulations of Booth & Schaye (2009) by looking at the evolution of the BH population and galaxy population. They show that the stellar mass function was driven by a power law and note the absence of a physical scale on which the BH becomes effective. This problem is also seen in other studies of the BH population and galaxy population (Puchwein & Springel 2013; Vogelsberger et al. 2013; Khandai et al. 2014).

In summary, large progress has been made in numerical simulations in order to understand the effects of AGN feedback in galaxies. Most of the studies described above support the idea that AGN feedback quenches the star formation of massive galaxies (but differ in details). These models are able to reproduce the BH scaling relations as well. However, a complete framework where the BH and galaxy populations grow together consistently is required.

As a part of this thesis, we will explore a new subgrid model of BH accretion

that accounts for angular momentum and study their effects in the evolution of a complete population of BHs. This subgrid model is suitable for cosmological simulations.

1.2.5 Evolution in the BH scaling relations

In this thesis, we will explore the evolution of the BH scaling relations. The tight correlations between the mass of the super massive BHs and the properties of the spherical component of the host galaxy (Magorrian et al., 1998; Haring & Rix, 2004; Tremaine et al., 2002; Marconi et al., 2003) suggest a coeval growth history of the central massive BHs and their host galaxies. However, the detailed physical processes that determine the coeval growth history are not completely understood.

One way to understand the BH-galaxy connection is to investigate the redshift evolution of the BH scaling relations. However, one of the major drawbacks is that dynamical measurements of the BH mass are not feasible at high redshift. While observational constraints from statistical properties of the BHs and AGNs such as evolution of the AGN luminosity functions are less complicated to determine (Hopkins et al., 2006; Marconi et al., 2004; Shankar et al., 2009), measuring BH masses of individual objects along with the property of the host galaxy is a challenge.

The approach to infer BHs has been to use broad line AGN samples. The fundamental assumption for this approach is that broad line AGN follow the same relation as inactive galaxies. The BH mass for a broad line AGN can be inferred by the *virial* method (McLure & Jarvis, 2002; Vestergaard & Peterson, 2006). This method assumes that the broad line region is virialised and the motion of the emitting clouds is dominated by the gravitational field of the central BH. The main challenge for these studies is to determine the stellar mass of the AGN host galaxies since the BH outshines the galaxy by a large factor (Merloni et al., 2010; Cisternas, 2011).

In addition, AGN surveys are biased towards more massive BHs, so that

selection effects also need to be taken into account (Lauer et al., 2007; Shen & Kelly, 2010; Schulze & Wisotzki, 2014), which can make it difficult to distinguish between evolution and no evolution of the BH scaling relations. Indeed, many observational studies have investigated the evolution of the BH mass-stellar mass relation (eg. Maiolino et al. 2007; Decarli et al. 2010; Merloni et al. 2010; Wang et al. 2010; Cisternas 2011; Targett et al. 2012) finding contradictory results. While early studies suggest a clear trend of positive evolution in the BH mass-bulge stellar mass relation, they are focused on luminous quasars and their hosts, sampling only the brightest end of the AGN luminosity function. More recent studies that use fainter AGNs, tend to find mild or no evolution (eg. Jahnke et al. 2009; Merloni et al. 2010; Cisternas 2011).

At present, no clear consensus has emerged. Recently, Schulze & Wisotzki (2014) present a common framework, based on a bivariate distribution function of the BH mass and the spheroid component to investigate and correct the possible biases of the BH scaling relations. They also demonstrate that there is no significant evidence to conclude (non) evolution of the BH scaling relations due to the selection effects of the current surveys of AGNs and their host galaxies across redshift even though bias corrections are applied.

In the theoretical side, the BH mass-stellar mass relation has been studied as well. This relation shows positive evolution in both semi-analytic models (Malbon et al., 2007; Hopkins et al., 2009) and numerical simulations (Di Matteo et al., 2008; Booth & Schaye, 2011) and the predicted magnitudes of these relations are comparable to some observational studies. These studies differ from each other in the implementation of the AGN feedback and BH growth. However, they have in common that the growth of BHs is self-regulated. This suggests that positive evolution in the BH mass-stellar mass relation is a direct consequence of self-regulated growth.

1.3 Outline of this thesis

The aim of this thesis is to better understand the evolution of the BH population as a whole and its connection with the evolution of the galaxy population in a cosmological context. For this purpose, we carry out numerical simulations that follow the evolution of dark matter and baryons in the Λ-CDM cosmology.

The outline of this thesis is as follows: In *chapter 2* we summarise the key ingredients that cosmological simulations require to simulate the evolution of the Universe. This includes the subgrid models of the galaxy formation. In *chapter 3* we introduce an improved BH accretion model as a subgrid model that accounts for angular momentum and we test its effects on the galaxy population and the BH growth by comparing to the typical models of BH accretion adopted in cosmological simulations. This BH accretion model is tested in relatively small cosmological simulations where only a sample of massive objects are simulated. In *chapter 4*, we focus on the connection between BHs and galaxies via the evolution of the BH scaling relations. Our strategy is to use a larger-scale cosmological simulation which has advanced subgrid physics of galaxy formation that were calibrated to reproduce some local properties of galaxies. The BH accretion model and AGN feedback are similar in spirit to the subgrid used in *chapter 3* and they are a critical part of reproducing the break of the galaxy stellar mass function. We also discuss the connection between BHs and their host halos. In *chapter 5*, we focus on the AGN evolution using the cosmological simulation used in the previous chapter. We focus on the predictions of the AGN luminosity function in X-ray bands and compare them to observations. We discuss the trend of downsizing in AGN activity as well as the possible connection with the host haloes. Finally, in *chapter 7*, we summarise and discuss the findings of this thesis and present ideas for future work.

Chapter 2

Simulating the Universe

In this chapter, we will describe the main elements of the simulation used here, emphasizing the subgrid modelling of galaxy formation that have been implemented in the computational code utilized in Chapters 3, 4 and 5.

For the purposes of this thesis, we begin by motivating why cosmological simulations are required to study the evolution of galaxies.

The starting point for structure formation theory (and then numerical simulations) is the initial state of the Universe. This is determined by inflation where the Universe started with a rapid expansion from a very hot and compressed state. This is supported and constrained by observations from CMB radiation and the large-scale distributions of galaxies (see Chapter 1). The seeds of the cosmic structures originates from quantum fluctuations amplified during inflation. These density fluctuations are of the order of 10^{-5} in the CMB.

As a first approximation, the linear perturbation theory explains accurately the initial growth of these fluctuations by gravitational instability in an expanding UniversePeebles (1980). Linear theory perturbation provides an accurate description of the early evolution of these fluctuations while these fluctuations are much less than unity.

Once the fluctuations become nonlinear, their evolution is more complicated, and linear theory perturbation is not valid anymore. Structure formation theory endeavour to understand the evolution of the initial fluctuations in an expanding Universe governed by gravity. Simple arguments provides some insight into the basic behaviour. For example, the spherical top hat collapse, where a spherical top-hat perturbation evolves in time until eventually collapses. This perturbation reaches dynamical equilibrium via virialisation. However, to fully capture the complex dynamical evolution of these fluctuations to become the highly non linear

structures seen today, it is imperative the requirement of numerical schemes. For that reason, cosmological simulations is one of the most powerful tools to study the evolution of galaxies in the context of modern galaxy theory.

One vital ingredient in numerical simulations is gas dynamics. To capture a full picture of the evolution of cosmic structure, we have to consider how gas evolves. Its evolution is more complicated since it is not only governed by gravity but also a set of complex and diverse physical processes. In numerical simulations, these physical processes are implemented as galaxy formation subgrid modules. These modules include physical processes by which gas can be heated, cool and converted into stars and black holes (BHs). However, some of these processes that are important to shape the properties of the galaxies, fall below the scales resolved in numerical simulation so that they are implemented as *subgrid models*. These galaxy formation subgrid models are essential to confront observations with theory and to reproduce many of the fundamental observables of the galaxies, intragalactic medium and BHs.

A massive growth in the size of cosmological simulations has been seen in the last decades since the first numerical simulations were performed with 100 particles that simulate the evolution of a galaxy cluster (Aarseth et al., 1963), while in this thesis the largest simulation utilized contains less than 7 billion particles following the gravitational and hydrodynamic evolution of dark matter and baryons from $z = 127$ to $z = 0$.

In this chapter, we will summarise all the key ingredients that cosmological simulations require in order to produce a simulated Universe, in particular those that have been implemented in the cosmological simulation used here.

2.1 Gravity calculations

Since the dominant matter component in the Λ CDM paradigm is the collisionless cold dark matter (CDM) that only interact gravitationally, gravity calculations are indispensable in the cosmic evolution of structure formation. CDM can be

described as a collisionless, non relativistic fluid of particles of mass m, comoving momentum $\mathbf{p}$ and comoving position $\mathbf{x}$. As a collisionless fluid, DM can be described by the Boltzmann equation in an expanding Universe (usually set as the Friedmann-Lemaitre model)

$$\frac{\partial f}{\partial t} + \frac{\mathbf{p}}{ma^2}\nabla f - m\nabla\Phi\frac{\partial f}{\partial \mathbf{p}} = 0, \tag{2.1}$$

where $f(\mathbf{x}, \mathbf{p}, t)$ is the phase-space distribution function and a is the expansion factor. This equation is coupled with the Poisson equation

$$\nabla^2\Phi = 4\pi G a^2 \overline{\rho}\delta \tag{2.2}$$

where $\delta = 1 - \overline{\rho}/\rho$ represents the density fluctuations and could be obtained by the integration of the phase-space density function over the momenta and Φ is the peculiar potential after subtracting expansion. This is a very complex set of equations to be solved. Usually the method for solving them is by sampling the phase-space density by a number of N tracer particles. Therefore, the problem is reduced to solving the motion equations of those tracers.

The straightforward method to obtain the acceleration is to sum directly the contribution of the individual tracer particles to the gravitational potential:

$$\phi(\mathbf{r}) = -G\Sigma_j \frac{m_j}{(|\mathbf{r} - \mathbf{r_j}|^2 + \epsilon^2)^{\frac{1}{2}}} \tag{2.3}$$

where m_j is the particle mass and ϵ is the gravitational softening length that smooths the gravitational force between two particles.

The sum should generate the particle's acceleration at high precision. The drawback, however, is that the number of calculation required scales as $N(N-1) \sim N^2$ which becomes quite expensive even for moderate number of particles. By compromising precision in a reasonable way, there are different methods to obtain the acceleration. We will focus specifically on the methods used in the simulations presented in the following chapters. These simulations were run in

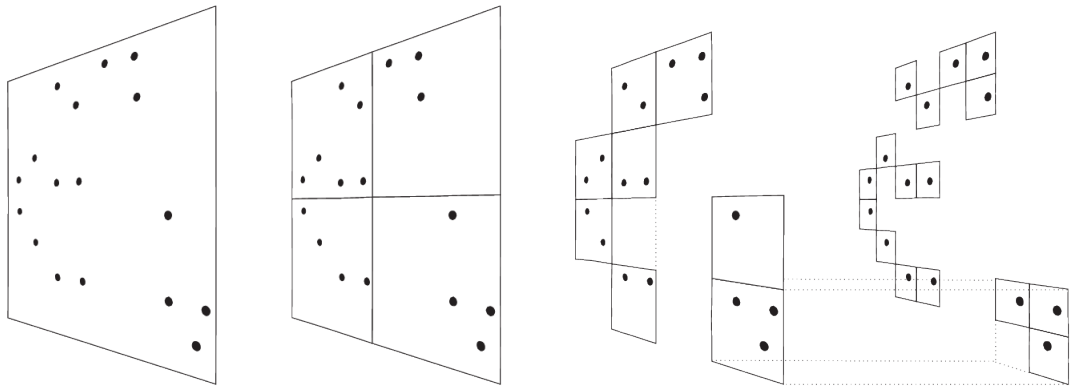

Figure 2.1: Sketchy picture of the oct-tree method from Barnes & Hut (1986) in two dimensions. The particles are enclosed in a *parent* root node. Such node is divided recursively into eight *daughter* nodes up to reach the finest level of calculations or *leaf* nodes where one particle is contained. Illustration taken from Springel et al. (2001)

P-Gadget-3 which is an updated version of Gadget-2 (Springel, 2005). The gravity calculation in P-Gadget-3 consists of two separate methods that maximise the efficiency of the gravity calculation. These methods are *the tree method* and *the particle mesh methods*.

2.1.1 Tree method

This is the main algorithm that Gadget uses to gain space adaptability and it is based on the hierarchical multipole expansion (Barnes & Hut, 1986). The hierarchical grouping is obtained recursively by subdivision of the space as shown in Fig 2.1. A cubic root node represents the total volume which is subdivided into eight *daughter nodes* of half the side length, until one ends up with *leaf* nodes which contain single particles. Therefore, force is calculated by 'walking' the tree. It begins in the root node and then a decision is made whether the force at this level of the multipole expansion is sufficiently accurate or not. If the answer is 'yes', the force calculation is terminated, if the answer is "no", the force calculation continues to the next daughter nodes until the force calculation is sufficiently accurate or the leaf nodes are reached. The desired accuracy in the force calculation is controlled via an opening criterion. In the case of Gadget2, a

node enclosing mass, M, and side length, l, at distance, r, is accurate enough if

$$\frac{GM}{r^2}\left(\frac{l}{r}\right)^2 \geq \alpha|a|, \tag{2.4}$$

where α is a tolerance parameter and $|a|$ is the magnitude of the acceleration at the previous timestep. For the first timestep $|a| = 0$ and then an geometric opening criterion is applied.

In particular, the tree method used in Gadget 2 is the oct-tree which is more shallow in comparison with the binary tree since fewer internal nodes are needed for a given number of particles. This is particularly advantageous in terms of memory consumption.

Gadget 2 also adopts the simplicity of monopole moments rather than higher-order multipole moments in the gravitational calculation in order to optimise memory usage. As Springel (2005) has discussed, including higher order multipole moments in the calculations can be offset by additional processing and memory overhead. By computing the monopole about the centre-of-mass of each cell, the dipole term vanishes and so do the error scales as the quadrupole moment.

2.1.2 Particle mesh methods

The Particle Mesh (PM) method (eg. Klypin & Shandarin 1983) differs to the tree method in treating the force as a field quantity by computing it on a mesh. Differential operators, such as the Laplacian, are replaced by finite difference approximations. Typically, such method is performed in three steps. First, the density field on the mesh points is mapped by assigning densities to the mesh via some kernel-based mass assignment scheme. Second, the density field is transformed to Fourier space, where the Poisson equation is solved, and then the potential is calculated by using Green's method. Finally, the forces for the individual particles are obtained by interpolating the derivatives of the potentials to the particle positions. There are many schemes to assign the mass density to

the mesh such as the 'Nearest-Grid-Point' (NGP) and Triangular-Shaped-Cloud (TSC). In Gadget, the scheme used is Cloud-in-Cell scheme (CIC) which is a better approximation to the force. CIC scheme distributes every particle over the nearest 8 grid cells, and then weighs them by the overlapping volume. This is obtained by assuming the particles to have a cubic shape of the volume corresponding to the mesh cells.

The advantage of the PM methods is the speed, because the number of operations scales as $N\log(N_m)$, where N is the number of particles and N_m the number of mesh points. However, the drawback is that the dynamical range becomes limited by N_m , which is usually limited by the available memory. Therefore, particularly for cosmological simulations, adaptive methods are needed to increase the dynamical range and follow the formation of individual objects.

2.2 Hydrodynamics

The treatment of baryons in cosmological simulations is described as an ideal fluid. To follow the evolution of this fluid is required to solve the set of hydrodynamic equations in addition to gravitational calculation:

$$\frac{\mathrm{d}\mathbf{v}}{\mathrm{d}t} = -\frac{\nabla P}{\rho} - \nabla\Phi, \tag{2.5}$$

$$\frac{\mathrm{d}\rho}{\mathrm{d}t} + \rho\nabla\mathbf{v} = 0 \tag{2.6}$$

and

$$\frac{\mathrm{d}u}{\mathrm{d}t} = -\frac{P}{\rho}\nabla \bullet \mathbf{v} - \frac{\Lambda(u,\rho)}{\rho}. \tag{2.7}$$

where $\mathbf{v}$, P, ρ and u are the velocity, pressure, density and u the the internal energy per unit mass. $\Lambda(u,\rho)$ is the cooling function and describes the radiative losses of the fluid. These expressions, altogether, are the Euler equations, continuity equation and the first law of the thermodynamics, respectively. They form a closed set of equations along with the equation of state ($P = (\gamma - 1)\rho u$). In the case of

cosmological hydrodynamic flows, the treatment of baryons is more complex and challenging due to the high non linearity in the gravitational clustering of the Universe. One of these challenges is the supersonic motion of the density peaks due to gravitational instability leading to strong shocks and discontinuities developed within smooth but complex structures.

Another challenge is the large dynamic range required in space and time as well as the wide range associated with the properties of the gas. In order to overcome such challenges, two primary approaches to hydrodynamics have emerged. One is particle methods which discretise mass in a Lagrangian flow and the other is grid-based methods that discretise space in an Eulerian flow. Both approaches are widely used in cosmological simulations. Smoothed particle hydrodynamics (SPH, Gingold & Monaghan 1977;Lucy 1977) has become the most popular Lagrangian code (e.g. Evrard 1988;Katz et al. 1996; Wadsley 2004; Springel 2005), whereas Eulerian codes have featured both fixed meshes (e.g. Cen & Ostriker 1992; Pen 1998) and adaptively refined meshes (Bryan & Norman, 1997; Norman & Bryan, 1999; Fryxell et al., 2000; Quilis, 2004; Teyssier, 2007).

Both methods present their advantages and disadvantages. Here, we mention some differences between them. While Eulerian codes suffer from limited spatial resolution, they work extremely well in both low- and high-density regions, as well as dynamical instabilities such as Kelvin-Helmholtz or Rayleigh-Taylor. On the other hand, Lagrangian codes can achieve good spatial resolutions in high-density regions but they work poorly in low-density regions; they also suffer from limited resolution in shock regions.

However, a key advantage of Lagrangian methods is that they manage large adaptability to cope with a large dynamical range in similar fashion to gravitational calculations. Additionally, they are intrinsically Galilean invariant and they do not have a fixed reference frame. Altogether, it makes such methods appealing for numerical simulations. For the sake of this thesis, we will focus on Lagrangian codes in particular SPH which is used in P-Gadget-3 and Gadget 2.

2.2.1 SPH

The basic idea of SPH relies on two concepts. Firstly, the phase space distribution of a gas can be represented by a distribution of discretise particles. Secondly, the properties of the gas can be estimated by interpolation by using a kernel function $W(|\mathbf{r}-\mathbf{r}_i|, h)$ of smoothing length, h. The smoothing kernel is normalised to unity:

$$\int W(\mathbf{r}-\mathbf{r}_i, h)\mathrm{d}\mathbf{r}' = 1 \tag{2.8}$$

with the condition that the kernel collapses to a delta function if h approaches to zero, namely $W(\mathbf{r}-\mathbf{r}_i, h) \to \delta(\mathbf{r}-\mathbf{r}_i)$ if $h \to 0$. Originally, Gingold & Monaghan (1977) chose a Gaussian as a kernel, however, it has the disadvantage that it does not approach zero at a higher distance. Then, the most commonly used is a spline kernel:

$$W(r,h) = \frac{8}{\pi h^3}\begin{cases} 1-6\left(\frac{r}{h}\right)^2+6\left(\frac{r}{h}\right)^3, & 0 \le \frac{r}{h} \le \frac{1}{2}, \\ 2\left(1-\frac{r}{h}\right)^3, & \frac{1}{2} < \frac{r}{h} \le 1, \\ 0, & \frac{r}{h} > 1. \end{cases} \tag{2.9}$$

where $r = |\mathbf{r}-\mathbf{r}_i|$. The fundamental equation of SPH is the estimate of the density for each particle,

$$\rho_i = \sum_{j=1}^{n} m_j W(r, h_i). \tag{2.10}$$

In the case of Gadget2 (Springel, 2005), the adaptive smoothing lengths, h_i of each particle are defined so that the mass enclosed in their kernel volumes remains constant, this can be expressed as

$$\frac{4\pi}{3}h_i^3\rho_i = N_{\mathrm{sph}}\overline{m}, \tag{2.11}$$

where N_{sph} is the typical number of smoothing neighbours, and $\overline{m}$ is an average particle mass. Note that Gadget-2 differs from other implementations in that the kernel drops to zero at h rather than $2h$ to keep consistency with Springel et al. (2001) and Springel et al. (2005).

Following the conserved-entropy formulation of Springel & Hernquist (2002), one can obtain the equations of motion for SPH particles as

$$\frac{\mathrm{d}\vec{v}_i}{\mathrm{d}t} = -\sum_{j=1}^{N} m_j \left[f_i \frac{P_i}{\rho_i^2} \nabla_i W_{ij}(h_i) + f_j \frac{P_j}{\rho_j^2} \nabla_i W_{ij}(h_j) \right], \tag{2.12}$$

where the coefficients f_i are defined by

$$f_i = \left[1 + \frac{h_i}{3\rho_i} \frac{\partial \rho_i}{\partial h_i} \right]^{-1}, \tag{2.13}$$

where $W_{ij}(h_i) = W(|\mathbf{r}_i - \mathbf{r}_j|, h_i)$ and $P_i = A_i \rho_i^{\gamma}$ as the pressure of the SPH particle. The equations above define the reversible fluid dynamics in SPH if there are no shocks nor external sources of heat. As a result, the entropy A_i for each particle remains constant.

The drawback of this approach is that it is inviscid. To alleviate this problem, shocks are captured by an artificial viscosity in SPH. In the case of Gadget 2, is expressed as

$$\left.\frac{\mathrm{d}\vec{v}_i}{\mathrm{d}t}\right|_{\mathrm{visc}} = -\sum_{j=1}^{N} m_j \Pi_{ij} \nabla_i \overline{W}_{ij}\,, \tag{2.14}$$

where $\Pi_{ij} \geq 0$ is non-zero only when particles approach each other in physical space. The viscosity generates entropy as

$$\frac{\mathrm{d}A_i}{\mathrm{d}t} = \frac{1}{2} \frac{\gamma - 1}{\rho_i^{\gamma - 1}} \sum_{j=1}^{N} m_j \Pi_{ij} \vec{v}_{ij} \cdot \nabla_i \overline{W}_{ij}\,, \tag{2.15}$$

transforming kinetic energy of gas motion irreversibly into heat. The symbol $\overline{W}_{ij}$ is the arithmetic average of the two kernels $W_{ij}(h_i)$ and $W_{ij}(h_j)$.

2.2.2 Improvement in the simulations used here

The previous section shows the basis of SPH approach that is incorporated in Gadget 2. Further details can be found in Monaghan (1984) and Balsara (1995). In the simulations presented in this thesis, SPH modifications have been done that

improve the performance on some standard hydrodynamical tests compared to the standard implementation in Gadget 2 and P-Gadget 3.

In the simulations used in Chapters 3, 4 and 5, we add enhancements to reduce the simulation viscosity when the time derivative of the flow divergence is small (Cullen & Dehnen, 2010) and to ensure that timesteps of particles receiving feedback energy are limited (Durier & Dalla Vecchia, 2012).

Additionally, the simulations presented in Chapters 4 and 5, we made use of an artificial conduction switch similar to Price et al. (2008). We adopted a pressure-entropy formulation (Hopkins et al., 2013) of SPH, that removes the spurious 'surface tension' force substantially improving the treatment of fluid mixing and contact discontinuities. We used the high order C^2 Wendland SPH kernel with 58 neighbours. More details of these modifications can be found in Dalla-Vecchia (2014 in preparation).

In the next section, we will discuss further treatment in baryons that goes beyond the description of gravitational interactions and hydrodynamical fluids.

2.3 Subgrid Physics of galaxy formation

In this section we will give a brief review of additional physical processes included in numerical simulations of structure formation and that are important in Galaxy formation; because their complexity and the scales in which they operate, such physical processes are implemented as subgrid physics. In particular, we will review the subgrid physics implemented in our simulations which is based on the suite of simulations performed by Schaye et al. (2010) and Schaye et al. (2014). Extended explanation of BH subgrid physics is included in Chapter 3.

2.3.1 Radiative Processes

One of the complex ways that baryons differs from DM, is that gas can radiatively cool and form BHs and molecular clouds, where stars will eventually be born and form galaxies. Therefore, a detailed treatment of gas cooling is one of the essential

elements of galaxy formation. Gas cooling is considered in the $\Lambda(u, \rho)$ term of the gas in the equation 2.7 (first law of the thermodynamics) and it is the rate of radiative losses. We will refer to $\Lambda(u, \rho)$ as a cooling function.

Standard implementations of the cooling function usually assume that gas is optically thin, in ionization equilibrium and neglecting three-body cooling process. The most popular implementations are similar to the first proposed by Katz et al. (1996), in which the ionization balance of hydrogen and helium is computed in the presence of a cosmological ultraviolet background radiation field which affects the cooling process in the low density regions. In addition to this, the presence of metals can dramatically increase the number of processes by which gas can cool, and therefore, to change the evolution of metal enriched systems (Aguirre et al., 2005). On the other hand, including metals in the cooling functions could be computationally very demanding, that usually tabulated, pre-computed cooling functions is opt for. Most models have adopted the metallicity-dependent cooling rates calculated by Sutherland & Dopita (1993) for a plasma slab.

In the version of P-Gadget-3 used in the simulations presented in this thesis, radiative cooling is quite sophisticated and extensively based on Wiersma et al. (2009a). The effects of photo-ionization of heavy elements by the meta-galactic UV/X-ray background (Haardt & Madau., 2001) are included as well as those of variations in relative abundances on the cooling rates of optically thin gas in ionization equilibrium. The radiative cooling and heating rates were computed by running large grids of photo-ionization models using the software CLOUDY (Ferland et al., 2013). These calculations account for line emission/absorption and thermal Bremsstrahlung, for primordial gas and nine separate metals (C, N, O, Ne, Mg, Si, S, Ca, Fe). Prior to reionization, no ionizing background is presented and gas is assumed to conserve collisional ionization equilibrium. After that, cooling rates for gas accounts for the CMB and the photo-dissociating background obtained by cutting the z= 9 Haardt & Madau (2001). The computation of cooling rates is by element-to-element-basis, implying that the cooling rates deviates from that at solar abundance, in contrast to the cooling tables of Sutherland & Dopita

(1993).

The tables also include the contribution to cooling from the inverse Compton scattering of CMB photons by energetic electrons in the IGM. This mechanism is particularly effective at high redshift, due to its strong dependency on the density of both CMB photons and free electrons.

2.3.2 Reionization

Hydrogen reionization, is implemented by turning on the ionization background from Haardt & Madau. (2001) at $z = 11.5$ that is consistent with the optical depth meausured by Planck collaboration et al. (2013). This ionization background has a dependency in time and it is spatially uniform. Toward high redshifts, we use net cooling rates that accounts for the CMB and the photo-dissociating background obtained by cutting the z= 9 Haardt & Madau. (2001).

To account for the boost in the photoheating rates during reionization since we are assuming optically thin rates, we inject 2 eV per atom. This ensures that the photoionised gas is quickly heated to 10^4K. In the case of for HeII, the extra heat is distributed in redshift with a Gaussian centred on $z = 3.5$ of width $\sigma(z) = 0.5$.

2.3.3 Star Formation

Although, star formation is the fundamental ingredient in the evolution of the galaxies, it is a poorly understood process. The spatial and time scales that star formation operates in are too small ($10 - 50$ pc for a giant molecular cloud) and too short (30 Myr for a solar mass protostar), which makes it impossible to implement it consistently in cosmological simulations. Usually, it is assumed that an interpolation of the properties of ISM can be done at the minimum reliable scale to the scales at which star formation operates. In that respect, cosmological simulations treat star formation in a very similar way to semi-analytic models but at the minimum scale that the simulation can resolve.

One prescription which has been widely adopted in cosmological simulation

is that proposed by Springel & Hernquist (2003) model . This scheme proposed that each SPH gas particle consists in two media : cold dense clouds and hot ambient gas in pressure equilibrium. The cold dense clouds are considered in star formation and gravitational calculation whereas the hot ambient gas is only considered to the hydrodynamical and gravitational calculation. The mass and energy exchange processes between both media are computed in a particle-particle basis and incorporate the main characteristics of ISM from the theoretical model by McKee & Ostriker (1977).

The model used in the simulations that we present, is the one proposed by Schaye & Dalla Vecchia (2008) including metallicity-dependent density threshold (Schaye et al., 2010). In this model, to set the efficiency of star formation at the resolved scales of the simulation (a few kpc), the model uses the empirical Schmidt-Kennicut law (Schmidt, 1959; Kennicutt, 1983, 1998) which specifies the surface density of star formation as function of surface density of gas:

$$\dot{\Sigma}_* \propto \Sigma_g^{n_K}, \tag{2.16}$$

where $n_K \approx 1-2$, specifically Kennicutt (1998) found $n_K = 1.4 \pm 0.15$. This relation is based on observational data (Bigiel, 2008). Schaye & Dalla Vecchia (2008) show that this can be expressed in terms of a pressure-law because the surface density in a self-gravitating system is directly related to pressure. Observational data from Bigiel (2008) along with the theorical model from Schaye & Dalla Vecchia (2008) show that there is a threshold in the surface density in which SF does not occur. Above this threshold, there is a trigger of thermo-gravitational instabilities that allows two gas phases to coexist: cold ($T \sim 100$K) and warm ($T \sim 10^4$K). Originally this threshold was set to $10 \mathrm{M}_\odot \, \mathrm{pc}^{-2}$, but in the version used here, the threshold density depends on the gas metallicity as proposed for Schaye (2004); Schaye et al. (2010). The metallicity dependence accounts for the fact that the transition from a warm, neutral to a cold, molecular phase occurs at lower densities and pressures if the metallicity is higher, and hence also the dust-to-gas

ratio, is higher since dust shields dense clouds from UV radiation.

This can not be modelled. Schaye & Dalla Vecchia (2008) propose one equation of state (EOS) that is imposed for densities higher than a threshold ($n_H > n_{H*}$), where the pressure is such that

$$P \propto \rho_{eff}^{\gamma}, \tag{2.17}$$

where γ_{eff} is assumed to be $4/3$. For which both the Jeans mass and the ratio of the Jeans length to the SPH kernel are independent of the density [1], preventing spurious fragmentation due to a lack of numerical resolution.

The advantage of this model is under the assumption that the gas is self-gravitating we can rewrite the observed Kennicutt-Schmidt star formation law as a pressure law (Schaye & Dalla Vecchia, 2008):

$$\dot{m}_* = m_g A (1\mathrm{M}_\odot \mathrm{pc}^{-2})^{-n_K} (\frac{\gamma}{G} f_g P)^{(n-1)/2}, \tag{2.18}$$

where m_g is the mass of the gas particle, $\gamma = 5/3$ (not confused with γ_{eff}) is the ratio of specific heats, f_g is the mass fraction in gas (assumed to be unity) and P is the pressure. Hence, the free parameters A and n_K are observables and not tuned parameters. Another advantage is that if we impose an equation of state, then the observed surface density law will still be reproduced without any further tuning in the star formation parameters.

Finally, the star formation model is implemented stochastically which means that each gas particle has a star formation rate associated and it is converted into a particle star in a time step with a given probability $P = \max(\dot{m}_* \delta t / m_g, 1)$.

2.3.4 Stellar and chemical evolution

Star particles in cosmological simulations are more massive than a single star, so they are treated as simple star population (SSP) of galaxy described by initial mass function of Chabrier (2003) in a range between $0.1 - 100\mathrm{M}_\odot$. The Chabrier

[1] The Jeans length is the radius of a pressurised, self-gravitating cloud for which the pressure and gravitational forces are balanced.

mass function is based on a Gaussian for stars with mass less than 1 solar mass and a power law for stars with mass above as follows:

$$\xi(\log_{10} m) = \begin{cases} A\exp(-(\log_{10}(m/m_c))^2/2\sigma^2) & \text{if } m \leq \mathrm{M}_\odot \\ Bm^{-x} & \text{if } m > \mathrm{M}_\odot \end{cases} \tag{2.19}$$

where $x = 1.35$, $m_c = \log_{10} 0.08$ and $\sigma = 0.69$. The evolution of this simple stellar population represented by a star particle determines the effects on the ISM.

Stars lose mass during their lifetime and a considerable fraction of this is released at the end of their life as AGB or SNe. During these phases, there are two main effects on the ISM : the synthesis of heavy elements and the injection of feedback energy. To calculate these effects, the lifetime of the stars is required that is based mainly on their initial mass and initial metal abundances. In the case of the simulation, the lifetime is calculated from the evolutionary tracks of Portinari et al. (1998). In particular, we consider three phases in the stars where the synthesis of heavy elements and the injection of feedback energy are important: AGB, SNIa and SNII.

AGB stars are intermediate mass stars ($< 8\mathrm{M}_\odot$) on the asymptotic giant branch. Their cores have already exhausted hydrogen, causing the external layers to expand and cool. Eventually, the core starts to burn helium. In terms of chemical evolution, AGBs produce carbon which eventually it dredged up from the core and injected into the ISM.

SNIa is more likely to occur in binary star systems in which one of the companions is a white dwarf star ($\leq 1.4\mathrm{M}_\odot$). White dwarfs are not burning any material and their support against gravity is by the electron degeneracy pressure. Accretion onto white dwarf could approach the Chandrasekhar limit which is the maximum mass of a star that can be supported by electron degeneracy pressure and not collapse. This triggers a supernovae explosion which releases metals into the ISM. The time of the release is $\approx 10^9$ yrs and the main production is Iron.

SNII is the end of the most massive stars ($> 8\mathrm{M}_\odot$) that have the shortest lifetimes (10^7 yrs). This explosion is the most powerful and violent of those

from AGB and SNIa. It is triggered by the collapse of the massive core, once their core has exhausted all the elements possible to burn by nuclear fusion. The main elements that are produced and eventually released into the ISM are alpha-elements - oxygen, magnesium, neon, silicon - in addition to iron. We deal with the energy injection in subsection 2.3.5.

The implementation in the simulations used here is based on Wiersma et al. (2009b). For each star particle at each time step, the fraction of the star population that has reached the SNe or AGB phase is determined. Then, the metal mass loss is determined through winds by such phases from the nucleosynthesis models of Portinari et al. (1998) and Marigo (2001). The elements H, He, C, N, O, Ne, Mg, Si, and Fe are tracked individually, while the mass ratios of Ca and S are assumed relative to Si of 0.094 and 0.605, respectively.

2.3.5 Energy feedback from star formation

Together with expulsion of mass and metals into the ISM, SNII, AGBs and SNIa also inject energy into the ISM and generate turbulence through stellar winds. These effects are the key for the regulation of star formation of small and intermediate galaxies. If star formation is sufficiently intense, then the generation of large-scale galactic winds is driven by SN feedback.

In the context of cosmological simulations, large efforts have been done to model feedback sufficiently efficient to regulate the star formation in galaxies. One of the issues that contributes to inefficient stellar feedback is the lack of resolution in cosmological simulations. The structures of the simulated winds are smoothed and their expansion velocity and cooling rates are overestimated, leading to short cooling times. If the feedback is injected thermally, it tends to be radiated away (Katz et al. , 1996).

Another factor which causes the feedback energy to be inefficient has been discussed by Dalla Vecchia & Schaye (2012); Creasey et al. (2012). They discuss that the mass of the gas in which the energy injected into the ISM is too large in simulations in comparison to the mass of a simple stellar population. Because too

much mass is heated, the temperature is too low and the cooling time too short.

Several types of subgrid models have been adopted to alleviate these problems in one way or another. One of them is by injecting energy into kinetic form (Springel & Hernquist, 2003; Dalla Vecchia & Schaye, 2008; Dubois & Teyssier, 2008) along with temporary decoupling of wind particles from hydrodynamic forces in order to contribute their escape from dense disc of ISM (Springel & Hernquist, 2003; Oppenheimer & Dave, 2008). , temporary turning off radiative cooling (Gerritsen et al., 1997; Stinson et al., 2006) and explicitly decoupling thermal phases (Marri & White, 2003; Scannapieco, 2006; Murante et al., 2010). In the case of the simulations used here, stochastic thermal feedback is considered. This model is based on Dalla Vecchia & Schaye (2012) (see also Kay et al. 2003).

The stochastic thermal feedback makes it possible to control the amount of energy for feedback event. The model is characterized by two parameters. One parameter is, f_{th}, the fraction of available SN energy for a star particle that is actually used to perform the feedback and sets its efficiency; the second is the temperature jump ΔT of the heated gas particles. Both parameters are used to calculate the fraction of the energy from core collapse supernovae per stellar mass unit that is injected on average.

When the stellar particle has reached the age $3 \times 10^7 yr$, which corresponds to the maximum lifetime of stars that explode as core collapse supernovae, the total available energy per unit stellar mass provided by SNII, $\epsilon_{\rm SNII} = n_{\rm SNII} E_{\rm SNII}$, is given by

$$\epsilon_{\rm SNII} = 8.73 \times 10^{15}\ {\rm erg} \left(\frac{n_{\rm SNII}}{1.736 \times 10^{-2}\ {\rm M}_\odot^{-1}} \right) E_{51}, \tag{2.20}$$

where $E_{\rm SNII} \equiv E_{51} \times 10^{51}\ {\rm erg}$ is the available energy from a single SNII event and we assume $E_{51} = 1$, and $n_{\rm SNII}$ is the number of stars per stellar mass unit ending their life as SNII. Then, the amount of energy available in a SSP particle is $m_* \epsilon_{\rm SNII}$, where m_* is the initial mass of the star particle.

The temperature jump if an amount of gas mass, $m_{\rm g,heat}$, is heated is

$$\begin{aligned}\Delta T &= (\gamma-1)\frac{\mu m_{\rm H}}{k_{\rm B}}\epsilon_{\rm SNII}\frac{m_*}{m_{\rm g,heat}} \\ &= 4.23\times10^7\,{\rm K}\left(\frac{n_{\rm SNII}}{1.736\times10^{-2}\,{\rm M}_\odot^{-1}}\right)\left(\frac{\mu}{0.6}\right)\times \\ &\quad E_{51}\frac{m_*}{m_{\rm g,heat}},\end{aligned} \tag{2.21}$$

where $\gamma = 5/3$ is the ratio of specific heats for an ideal monoatomic gas, $k_{\rm B}$ is the Boltzmann constant, $m_{\rm H}$ is the mass of the proton, and $\mu m_{\rm H}$ is the mean particle mass.

Then, the energy released by a single star particle is shared among a fraction of the N_{ngb} neighbouring resolution elements. The calculation of the number of N_{ngb} heated is given by

$$\begin{aligned}\langle N_{\rm heat}\rangle &= 1.34\,E_{51}f_{th}\left(\frac{n_{\rm SNII}}{1.736\times10^{-2}\,{\rm M}_\odot^{-1}}\right)\left(\frac{\mu}{0.6}\right)\times \\ &\quad \left(\frac{\Delta T}{10^{7.5}\,{\rm K}}\right)^{-1}.\end{aligned} \tag{2.22}$$

Ideally, the energy should on average be shared with at least one gas neighbour to make the feedback local to the star particle and to ensure that the metals released by massive stars can be driven outwards. Note that making $\Delta T >> 10^{7.5}$K or $f_{th} << 1$ would imply that only few star particles inject energy to the surroundings. Dalla Vecchia & Schaye (2012) found via analytic arguments that a minimum heating temperature is required for the injection of thermal energy to be efficiently converted into kinetic energy. In fact, they found that by considering the ratio of cooling time to the sound time across a resolution element, there is a maximum density, $n_{\rm H,t_c}$, where energy feedback would be efficient

$$n_{\rm H,t_c} \propto 10\,{\rm cm}^{-3}\left(\frac{T}{10^{7.5}{\rm K}}\right)^{3/2}\left(\frac{m_g}{10^6{\rm M}_\odot}\right)^{-1/2} \tag{2.23}$$

where m_g is the gas particle mass, T is the temperature after the energy injections

and ΔT is the increase of temperature to the heated gas.In the simulation actually ΔT is set to $10^{7.5}$K and $T > \Delta T$ to ensure efficiency.

As we mentioned in section 2.3.3, metallicity has a high impact in the star formation efficiency. If the ISM is sufficiently metal-enriched, cooling for metal lines can be important. Wiersma et al. (2009b) found that for temperatures $10^5\text{K} < T < 10^7\text{K}$, this occurs when $Z \gtrsim Z_\odot$. In the simulation, these effects are captured by setting f_{th} as a function of metallicity and density varying between 0.3 and 3.

2.3.6 BH subgrid physics

AGN feedback and BH evolution have been incorporated in numerical simulations. Because the gravitational scale of the BH ($\sim$ pc) is below the usual space resolution of cosmological simulations ($\sim$ kpc), this is implemented as subgrid models.

The BH subgrid physics presented in this thesis is based on the Booth & Schaye (2009) model, which is an extension of the model of Springel et al. (2005). We explore and improve this model in Chapter 3. Here, we summarise the main features in three steps: BH seeding, BH growth and AGN feedback.

- **BH seeding**. There are two possible scenarios of formation of the supermassive BHs in the center of the galaxies. BHs could be formed by direct collapse of massive stars or star clusters or from initial small seeds growing slowly by gas accretion. Neither processes can be resolved by the simulation. Thus, to capture this, BH seeds are injected into halos at the position of the minimum potential well of the halos with total mass greater than $10^{10}h^{-1}\text{M}_\odot$ and no BH has been placed. To identify these haloes, an FOF algorithm (see 2.5) is used every period of time equivalent to the condition of $\Delta a = 0.005a$ where a is the expansion factor. The most bound gas particle is then converted into a BH. This BH particle has two associated masses: the *subgrid mass* which is used to calculate the accretion rates and the amount of energy liberated into the ISM, typically set to $10^5\text{M}_\odot$ and the *particle mass*

which is the mass of the gas particle before it is converted into a BH and it is used in the gravitational calculations.

- **BH growth**. BHs can grow by two processes: *BH mergers* and *gas accretion*.

  A *BH merger* occurs when BHs are separated by a distance that is smaller than several times gravitational softening length, and their relative velocity is smaller than the circular velocity at the distance h_{BH} , $v_{rel} < \sqrt{GM_{\rm BH}/h_{BH}}$, where h_{BH} and $M_{\rm BH}$ are the smoothing length and subgrid mass of the most massive BH respectively in the merger. The limit of the allowed relative velocity prevents BHs from merging during the initial stages of galaxy mergers.

  To calculate BH growth via *gas accretion*, simulations typically implement the Bondi accretion model in which accretion rates depend on density and sound speed of the neighbouring SPH gas and $M_{\rm BH}$. Usually to compensate the lack of resolution in the simulations, a boost parameter is added. Springel et al. (2005) adopted a constant parameter and Booth & Schaye (2009) adopted a power law of the ratio of local density to the star formation density threshold. In this thesis, we used a novel BH accretion model that accounts for the angular momentum of the neighbouring gas and it is suitable for cosmological simulations. The full description will be given in Chapter 3.

  Once the *subgrid mass* exceeds the *particle mass*, it is allowed to accrete neighbouring SPH gas particles stochastically, then both masses grow across time.

- **AGN feedback** It is modelled in a similar fashion to stellar feedback described in 2.3.5 which is thermal and stochastic. The energy rate $\dot{E}_{AGN}$ is injected into the ISM by gas accretion as

$$\dot{E}_{AGN} = \epsilon_{\rm f}\epsilon_{\rm r}\dot{m}_{\rm BH}c^2, \tag{2.24}$$

where $\epsilon_{\rm r}$ is the fraction of energy which is radiated and $\epsilon_{\rm f}$ is fraction of the radiated energy coupled with the ISM. Booth & Schaye (2009) show that $\epsilon_{\rm f}$ sets the final BH mass and then affect the normalization of the BH scaling relations.

BHs only inject energy into the ISM where they have sufficient energy to heat at least one of the gas SPH neighbours. Otherwise, BHs store their energy. In each time step, BHs increase their energy storage as $\dot{E}_{AGN}\Delta t$. Note that this implies a condition of the energy per unit mass that BHs can inject:

$$\Delta\epsilon_{AGN} = \frac{n_{heat} m_g k_B \Delta T_{AGN}}{\gamma - 1 \mu m_{\rm H}}, \tag{2.25}$$

where ΔT_{AGN} is the minimal increase in temperature of n_{heat} neighbours. Then the heating probability is given by

$$P = \frac{E_{AGN}}{\Delta\epsilon_{AGN} N_{ngb} < m_g >} \tag{2.26}$$

where N_{ngb} is the number of gas neighbours and $< m_g >$ is the average mass. The critical parameter that shapes the power of AGNs is ΔT_{AGN}. Larger values of ΔT_{AGN} lead to more energetic heating events; the values of ΔT_{AGN} are higher that that from SN II because the neighbouring gas of the BH is denser.

2.4 Initial Conditions

The starting point of a cosmological simulation is the initial conditions which are determined by observations of the large-scale distribution of galaxies and of the Cosmic Microwave Background (CMB). Both observations agree in good precision with the theoretical expectations. The growth of the structures starts from a Gaussian random field of initial density fluctuations. The Gaussian field is thus completely described by the power spectrum $P(|k|)$. The shape of this Gaussian field is theoretically well motivated and determined by the cosmological

parameters and the nature of Dark Matter. The displacements and velocities of the particles are usually calculated by the Z'eldovich approximation.

In the case of the simulations presented here, this gaussian field is generated by choosing a set of random phases that are taken from the public code Panphasia (Jenkins, 2013; Jenkins & Booth, 2013). The method to create the initial conditions is described in Jenkins (2010). The advantage of this method is that it can be applied to multimass particle distributions making it suitable for creating resimulation, or 'zoom' initial conditions. This method creates second order Lagrangian perturbation theory (2LPT) resimulation initial conditions. The displacement and velocities are calculated by Z'eldovich approximation, adding second-order Lagrangian growing modes.

2.5 Subfind algorithm

The method that is employed to find gravitationally bound structures, subhalos, is the Subfind algorithm of Dolag et al. (2009). This is an extension of the first version of Springel et al. (2001) that only accounts for dark matter simulations. The Subfind algorithmic takes into account the gas and stars particles in the calculations. The method primarily consists of three steps. Firstly, dark matter (DM) halos are identified by the Friends-of-Friends (FOF) algorithm with linking length 0.2. The FOF algorithm selects haloes that are bounded at approximately the same DM overdensity contour, independent of the presence or absence of baryons. After that, each gas and star particle is then associated with its nearest DM particle in the case that this DM particle belongs to a FOF halo. In the second step, candidates of subfind haloes are identified in the overdensity contour of the FOF halo where candidates are defined as bounded regions that pass through a saddle point of the density field in the FOF halo. Finally, these subhalos candidates are subjected to a gravitational unbinding procedure where only the self-bound part is retained. Then, the candidates of subfind haloes are registered as genuine *subhalos* if the number of bound particles is larger than the number of particles

left. These subhaloes are identified as galaxies. We consider central galaxies as the most massive subfind haloes in each FOF halo and satellite galaxies as the remaining Subfind haloes.

2.6 Summary

Cosmological simulations are currently one of the most powerful tool to study the evolution of galaxies since it is possible to create a simulated universe to confront observations. In this chapter, we summarise the main ingredients that cosmological simulations are required to follow the evolution of the galaxies. The start point is the initial condition of the primordial structures set in the current cosmological Λ CDM model.

In particular, we focus on reviewing the main features of P-Gadget-3 such as the techniques to perform efficiently gravitational calculations of the particles. We also review the techniques adopted to perform hydrodynamics calculations, in particular SPH which is the formulation that P-Gadget -3 is based on. Additionally, we review the advanced galaxy formation subgrid physics that has been developed to follow the evolution of gas, stars and BHs and are essential to study the evolution of galaxies. In particular, radiative cooling, star formation, chemical evolution, feedback energy from SN and from AGNs and growth of BHs.

In the following chapters, we will use two sets of numerical simulations that differ in cosmology, size and in some subgrid models. In each chapter, we will specify the diffences between simulations. However, both sets of simulations are based on similar codes. We refer to the reader to the original papers to complete detail in Springel et al. (2005) for the hydrodynamic and gravitational calculations, and for Schaye et al. (2010), Wiersma et al. (2009a,b) and Schaye et al. (2014), Crain et al. (2014 in preparation) and Furlong et al (2014 in preparation) for the subgrid models, to find complete details.

In the next chapter, we will focus on the modifications of the subgrid BH accretion model described here. This model accounts for angular momentum and

it is suitable for cosmological simulations.

Chapter 3

Modelling BH accretion in cosmological simulations

3.1 Introduction

In this chapter, we will take another look at the BH accretion models used in numerical simulations. The BH accretion models typically adopted in numerical simulations, are based on the Bondi estimate. This assumes that material falling through the Bondi radius free-falls into the BH. As recently discussed by several authors (eg. Krumholz et al. 2005; Power et al. 2010; Debuhr, Quataert & Ma 2011; Angles-Alcazar et al. 2013), neglecting the angular momentum of the flow may lead to significant errors. Power et al. (2010) propose a new model in which a BH particle represents a self-regulating torus. Orbits are used to estimate whether particles are captured within a given accretion region of the BH. Then, gas particles are accreted onto the BH after a viscous time. Both the accretion region and viscous time are given by free parameters in their model. Their method is suitable for ultra high resolution calculations (with particle mass $1.1 \times 10^2 \mathrm{M}_{\odot}$) where the accretion region is ~ 3 pc, but it is not suitable for the multi-megaparsec scale simulations that are required to study the galaxy population (Muldrew et al., 2013). Debuhr, Quataert & Ma (2011) also propose a BH accretion model that depends on the angular momentum. Specifically, the accretion rate is proportional to the mean gas surface density, the local sound speed squared and the inverse of the rotational angular frequency. They apply their model in isolated major

mergers, finding self-regulation of the resulting BH but no clear evidence of suppression of the star formation in the resulting galaxy.

We will present a model that is similar in spirit to that Debuhr, Quataert & Ma (2011). We propose a simple scheme that takes into account the angular momentum of the gas flow, but does not require such high resolution so that it can be used in simulations of the cosmological population. The sub-grid model that we propose is suitable for inclusion in simulations of galaxy formation, and thus allows us to revisit the interaction of BH feedback and galaxy formation. We show that including angular momentum has a profound impact on the behaviour of BH accretion, reproducing the behaviour postulated in semi-analytic models. In contrast to the common interpretation, however, the BH accretion shapes the mass function not because the efficiency of BH *feedback* varies with halo mass, but because BH accretion is strongly suppressed in cold star forming discs (relative to the rate estimated when angular momentum is not accounted for). We show that the new model not only matches the observed galaxy stellar mass fractions, but also generates accretion patterns that strongly resemble quasars in lower mass haloes and radio galaxies in the highest mass haloes that we probe.

The chapter is organised as follows. In section 3.2, we describe the main features of the Bondi-like accretion implemented in many of the current cosmological models. The model originates from the seminal work of Springel et al. (2005), but we focus on the developments described by Booth & Schaye (2009) (BS09). We briefly discuss the critical radius and critical timescales in Bondi accretion and discuss the impact of angular momentum. We discuss how this can be included in the sub-grid prescription of BH accretion in section 3.2.2. In section 3.2.2, we present its implementation as a sub-grid physics module suitable for 100 Mpc scale simulations. In section 3.3, we describe the simulation code, the initial conditions and the simulations used in this chapter. To illustrate the impact of including angular momentum in the calculation, we perform a suite of cosmological simulations showing the effects of two models: the new accretion model dependent on angular momentum and the Bondi-like accretion model.

This is presented in section 3.4. Finally, we summarise our results and discuss the fundamental implications of the BH accretion model in section 3.8.

3.2 BH accretion modelling in cosmological simulations

Most cosmological simulations include accretion onto central BHs via a subgrid model based on the Bondi-Hoyle-lyttleton accretion (Bondi & Hoyle, 1944), possibly adding an accretion coefficient to account for the multiphase nature of the local gas and the finite resolution of the simulation (eg. Springel et al. 2005; Di Matteo & Springel 2005; BS09) . The Bondi accretion rate estimate assumes that the gas in the neighbourhood of the BH is spherically symmetric. When the gas is not spherically distributed the angular momentum should determine the BH accretion rate. In this section we will present a physical motivated extension of the BH accretion model of Springel et al. (2005) and BS09 dependent on angular momentum which we described in detail below.

3.2.1 The OWLS BH accretion model

Following Springel et al. (2005), a BH seed with a mass $m_{\rm seed}$ is injected into each new friends-of-friends halo that exceeds the mass threshold, $m_{halo,min}$. In order to prevent the BH from being ejected by two-body encounters, the BH seed is assumed to track the position of the minimum potential in the halo. Subsequently, BHs grow by two processes: mergers with other BHs or accretion of nearby gas particles. The gas accretion obeys a modified version of the Bondi-Hoyle-Lyttleton (Bondi & Hoyle, 1944) formula:

$$\dot{m}_{\rm BS09} = \alpha \frac{4\pi g^2 M_{\rm BH}^2 \rho}{(c_{\rm s}^2 + v^2)^{3/2}}, \tag{3.1}$$

where $M_{\rm BH}$ is the mass of the BH, $c_{\rm s}$ is the sound speed, ρ density of the local medium, v is the velocity of the BH relative to the ambient medium and α is a dimensionless efficiency parameter that is introduced to account for the multiphase nature of the gas that surrounds the BH. In the original Springel et al. (2005) model, α is a fixed number that accounts for the limited resolution of the simulations and ensures that the BHs grow enough to follow the observed scaling relations. Springel et al. (2005) set $\alpha = 100$. BS09 extend the model, so that α becomes a function of local density,

$$\alpha = \begin{cases} 1 & \text{if } n_{\rm h} < n_{\rm h}^{*} \\ \left(\frac{n_{\rm h}}{n_{\rm h}^{*}}\right)^{\beta} & \text{otherwise,} \end{cases} \tag{3.2}$$

where $n_{\rm h}$ is the local gas density and $n_{\rm h}^{*}$ is the threshold density of the gas that obeys the multiphase equation of state (see Schaye & Dalla Vecchia 2008), the parameter α is thus a power law of the ratio between density threshold and the density of gas, if $n_{\rm h} > n_{\rm h}^{*}$, but in lower density regions, where no cold phase is expected (Schaye, 2004) and the Jeans scales can be resolved, the Bondi-like accretion rate is applied without modification. BS09 show that the parameter β does not play a crucial role since the accretion rate of BHs is usually limited by the AGN feedback. We will refer to equation 3.1 and 3.2 as the Bondi-like model in what follows.

The model also assumes that the actual accretion rate cannot exceed the Eddington accretion rate limit,

$$\dot{m}_{\rm edd} = \frac{4\pi g m_{\rm p} M_{\rm BH}}{\sigma_{\rm t}\, c\, \epsilon_{\rm r}}, \tag{3.3}$$

where $m_{\rm p}$ is the proton mass, $\sigma_{\rm t}$ is the Thomson cross section for the scattering of free electrons and $\epsilon_{\rm f}$ is the fraction of the energy liberated per accreted rest mass energy and is set at 0.1. The final accretion rate is

$$\dot{m}_{\rm bh} = \max(\dot{m}_{\rm BS09}, \dot{m}_{\rm edd}). \tag{3.4}$$

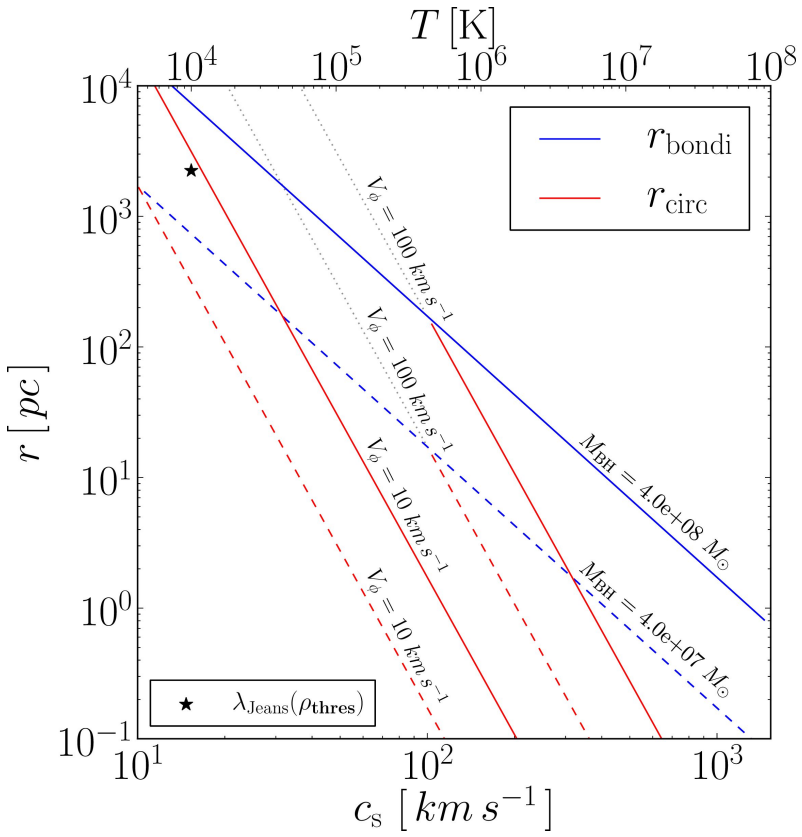

Figure 3.1: the Bondi (blue lines) and viscous (red lines) radii as a function of the sound speed for $M_{\rm BH} = 4 \times 10^7 {\rm M}_\odot$ (dashed lines) and $M_{\rm BH} = 4 \times 10^8 {\rm M}_\odot$ (solid lines) and for $V_\phi = 10 km\, s^{-1}$ and $100 kms^{-1}$. The grey dotted lines show the unstable regime in which our assumption that $(V_\phi / c_{\rm s}) \leq 1$ breaks down. Although both radii decrease with the sound speed and increase with $M_{\rm BH}$, the circularisation radius is a stronger function of the sound speed. The star marker represents $\lambda_{\rm Jeans}$ in a gas at $T = 10^4$K and at the SF threshold density ($n_{\rm H}^* = 0.1\, cm^{-3}$) . The simulations are designed so that this is well resolved.

3.2.2 An accretion model that accounts for angular momentum

In this section, we describe and physically motivate a simple extension of the BS09 model that accounts for the angular momentum (AM) of the surrounding gas. In the absence of angular momentum, the accretion rate is determined by the gas density and effective sound speed at the Bondi radius $r_{\rm Bondi}$, defined as the radius at which the BH gravity dominates over the thermal and turbulent

pressure of the surrounding gas. The Bondi radius is given by

$$r_{\rm Bondi} = \frac{GM_{\rm BH}}{c_{\rm s}^2} \approx 430\big(\frac{M_{\rm BH}}{10^7{\rm M}_\odot}\big)\big(\frac{c_{\rm s}}{10\,km\,s^{-1}}\big)^{-2} pc. \tag{3.5}$$

in the Bondi estimate gas within this region must inevitably fall into the BH. However, when net angular momentum is accounted for, the infall is eventually halted at the circularisation radius, $r_{\rm circ}$ which is defined as

$$r_{\rm circ} = \frac{j^2(r_{\rm circ})}{GM_{\rm BH}} \tag{3.6}$$

where j is the specific angular momentum. at the circularisation radius, gas will be accreted if it transfers its angular momentum outwards.

We assume that the accretion can be treated in two parts, firstly an almost radial infall from the Bondi radius to the circularisation radius and then a slower flow of material through the disc to the last stable orbit. Assuming angular momentum is conserved in the initial phase, the circularisation radius depends on the specific angular momentum of material crossing the Bondi radius, which we express in terms of the Bondi radius and the circular speed at the Bondi radius, $V_\phi(r_{\rm Bondi})$. Then, the specific angular momentum is given by $\mathbf{j} = \mathbf{r}_{\rm Bondi} \times \mathbf{V}_\phi$. The circularisation radius can be expressed as

$$\begin{aligned} r_{\rm circ} &= \frac{r_{\rm Bondi}^2 V_\phi^2}{GM_{\rm BH}} = GM_{\rm BH}\frac{V_\phi^2}{c_{\rm s}^4} \\ &\approx 430\big(\frac{M_{\rm BH}}{10^7{\rm M}_\odot}\big)\big(\frac{V_\phi}{10\,km\,s^{-1}}\big)^2\big(\frac{c_{\rm s}}{10\,km\,s^{-1}}\big)^{-4} pc. \end{aligned} \tag{3.7}$$

Note that our assumption implies that $(r_{\rm circ}/r_{\rm Bondi}) \leq 1$, therefore $(V_\phi/c_{\rm s}) \leq 1$ independently of the BH mass. As discussed by BS09, if the simulations resolve the Jeans scale, they will be able to resolved the Bondi radius for a BH with mass larger than the gas particle mass, including angular momentum in the BH

accretion estimate inevitably brings into play the circularisation radius. To get a sense of the values of the Bondi and circularisation radii relative to the Jeans scale in the simulation, we include Fig. 3.1. The figure illustrates the variation of $r_{\rm circ}$ (red lines) and $r_{\rm Bondi}$ (blue lines) with the circular speed and the effective sound speed (or equivalently, the *effective temperature*) of the surrounding gas [1]. We limit coloured lines to the region $(V_\phi/c_{\rm s}) \leq 1$ where circularisation radius is smaller than the Bondi radius as required for our assumption. Fig. 3.1 also shows $r_{\rm Bondi}$ and $r_{\rm circ}$ for two values of the BH mass $M_{\rm BH}$ at 4×10^8 (solid lines) and $4 \times 10^7 {\rm M}_\odot$ (dotted lines) and two values for the circular speed V_ϕ, 10 and 100 $km\,s^{-1}$. Both the Bondi and circularisation radii vary from thousands of parsecs when the sound speed is $10\,km\,s^{-1}$ (gas temperature $\sim 4 \times 10^3$K) to less than 1 parsec when the sound speed is $10^3\ km\,s^{-1}$ (gas temperature $\sim 4 \times 10^7$K). However, the circularisation radius shows an even more dramatic variation as a result of the dependency on $r^2_{\rm Bondi}$. In comparison with the Jeans length $\lambda_{\rm Jeans}$ ($\sim 2.2\,kpc$, black star) for the gas at the star formation density threshold ($n^*_{\rm h} = 0.1\,cm^{-3}$) with an effective temperature 10^4K [2], the Bondi radius ($r_{\rm Bondi} = 7.3\,kpc$) becomes larger and the circularisation radius comparable only if $V_\phi \sim 10\,km\,s^{-1}$ for a BH with mass $\geq 4 \times 10^8 {\rm M}_\odot$. In the case when the BH mass is comparable to the Jeans mass ($2 \times 10^7 {\rm M}_\odot$), the Bondi radius is similar to the Jeans length (the difference is due to definition); the circularisation radius falls below the Jeans length or in the region outside of our assumptions. This indicates that in our simulation where the resolution has been set to resolve the Jeans length in gas at the star formation threshold, we will be able to resolve the Bondi radius in the most massive BHs. This is not the case for the circularisation radius. Inevitably, we must rely on the sub-grid model to determine both radii when the gas is hot or the BH mass

[1] The effective sound speed $c_{\rm s} \equiv \left(\frac{\gamma k_b t}{\mu m_h}\frac{1}{f_{\rm th}}\right)^{1/2}$ where $f_{\rm th}$ is the fraction of pressure which is thermal.we assume $f_{\rm th} = 1$ since the gas temperature is given by the effective equation of state, and set $\mu = 0.59$.

[2] There is no unique definition of the Jeans length. This usually differs by a factor which depends on the geometry of the object. We define $\lambda_{\rm Jeans} \equiv \left(\frac{c_{\rm s}^2}{g\rho}\right)^{1/2} = c_{\rm s} n_{\rm h}^{*-1/2}\left(\frac{x f_{gas}}{g\mu m_h}\right)^{1/2}$ where $f_{gas} = 0.3$ is the gas mass fraction and $x = 0.752$ is the hydrogen mass fraction. giving $c_{\rm s} \sim 15.3\,km\,s^{-1}$, $\lambda_{\rm Jeans} \sim 2.2$ kpc. We define the corresponding Jeans mass as $m_{\rm Jeans} = 4/3\pi\rho\left(\frac{\lambda_{\rm Jeans}}{2}\right)^3$ that takes the value $2 \times 10^7 {\rm M}_\odot$.

is significantly smaller than the particle mass. In cosmological simulations, this extrapolation is unavoidable.

The Bondi timescale and the viscous timescale

As we discussed in the last section, the presence of angular momentum introduces an additional spatial scale into the accretion model. This creates an additional timescale that is dependent on the angular momentum of the infalling material. In the extreme case of zero angular momentum, the time for the gas to be accreted will be the timescale corresponding to the Bondi accretion which is the Bondi time

$$\begin{aligned} t_{\rm Bondi} &= \frac{r_{\rm Bondi}}{c_{\rm s}} = \frac{GM_{\rm BH}}{c_{\rm s}^3} \\ &\approx 42\big(\frac{M_{\rm BH}}{10^7 {\rm M}_\odot}\big)\big(\frac{c_{\rm s}}{10\,km\,s^{-1}}\big)^{-3}{\rm Myr}. \end{aligned} \tag{3.8}$$

If the gas has angular momentum, a disc will be formed once the gas crosses the circularisation radius and it will spiral inwards to the last stable orbit where it will finally be accreted. To estimate this timescale, we assume that the disc formed is thin (i.e., that the gas cools efficiently) and that the radial motions are small in comparison to the rotation. In this case, gas follows roughly keplerian orbits and the disc scale height h is given by

$$\frac{H}{R} \sim \frac{c_{\rm s}'(r_{\rm circ})}{v_{\rm circ}'(r_{\rm circ})} = \frac{V_\phi}{c_{\rm s}}\frac{c_{\rm s}'}{c_{\rm s}} \ll 1, \tag{3.9}$$

where $v_{\rm circ}'$ is the circular velocity within the disc, and $c_{\rm s}'$ is its sound speed. The second equality comes from our assumptions that ($r_{\rm circ}/r_{\rm Bondi} \leq 1$) and conservation of specific angular momentum between the circularisation radius and the Bondi radius ($r_{\rm circ}v_{\rm circ}'(r_{\rm circ}) = r_{\rm Bondi}V_\phi(r_{\rm Bondi})$) using equations 3.5 and 3.7. To be consistent with these assumptions and that of a thin disc, $c_{\rm s}' \ll c_{\rm s}^2/V_\phi$, which follows if there is strong turbulence in the ISM. The transport through the disc can be described by a diffusion equation where the kinematic viscosity ν is usually

parameterized as

$$\nu = \alpha_{\rm visc}\, c_{\rm s} H, \tag{3.10}$$

with $\alpha_{\rm visc}$ as a dimensionless number (Shakura & Syunyaev, 1973). The viscous time can then be expressed as

$$t_{\rm visc} = [\alpha_{\rm visc}(H/R)^2]^{-1} t_{\rm dyn} \sim \frac{r_{\rm circ}^2}{\nu}, \tag{3.11}$$

where $t_{\rm dyn}$ is the dynamical timescale of the disc. The values for H/R lie in the range $0.1 - 0.001$ for a thin accretion disc in the α-disc parameterization (Shakura & Syunyaev, 1973) and values of $\alpha_{\rm visc}$ lie in the range $\sim 0.1 - 0.3$ from the observational evidence (King et al., 2007; Schreiber et al., 2004; Buat et al., 2001; Cannizzo, 2001a,b). Using eq. 3.10, 3.11, 3.6 and 3.7, the viscous time becomes

$$\begin{aligned} t_{\rm visc} &= C_{\rm visc} \frac{r_{\rm circ}}{V_{\rm circ}} = C_{\rm visc} \frac{j^3}{G^2 M_{\rm BH}^2} \\ &= C_{\rm visc} \frac{r_{\rm Bondi}^3 V_\phi^3}{G^2 M_{\rm BH}^2} = C_{\rm visc} G M_{\rm BH} \frac{V_\phi^3}{c_{\rm s}^6} \\ &\approx 42\, C_{\rm visc} \left(\tfrac{M_{\rm BH}}{10^7 {\rm M}_\odot}\right) \left(\tfrac{V_\phi}{10\, km\, s^{-1}}\right)^3 \left(\tfrac{c_{\rm s}}{10 km\, s^{-1}}\right)^{-6} {\rm Myr}, \end{aligned} \tag{3.12}$$

where $C_{\rm visc} = 2\pi[\alpha_{visc}(H/R)^2]^{-1}$ only depends on the properties of the thin disc.

Fig. 3.2 shows $t_{\rm Bondi}$ (blue lines) and $t_{\rm visc}$ (red lines) as a function of the effective sound speed (or equivalent gas temperature) for BH masses $M_{\rm BH} = 4 \times 10^7 {\rm M}_\odot$ and $M_{\rm BH} = 4 \times 10^8 {\rm M}_\odot$ and $C_{\rm visc} = 2.1 \times 10^6$ under the same region of our assumptions. The Bondi time and viscous time are both decreasing functions of the sound speed, but the viscous time is stronger dependent on the sound speed. For instance, for a BH with $M_{\rm BH} = 4 \times 10^8\, {\rm M}_\odot$, the Bondi timescale is $\sim$ 1Gyr if $c_{\rm s} \sim 15.3 {\rm km\, s^{-1}}$, but shorter by six orders of magnitude ($\sim 10^3$ yrs.) when $c_{\rm s} \sim 10^3 {\rm km\, s^{-1}}$ ($T \sim 4 \times 10^7$K)[3]. For $t_{\rm visc}$, the sound speed dependency is even stronger: the viscous time ~ 10 Gyr ($\sim$ the age of the Universe) at $c_{\rm s} \sim 90 {\rm km\, s^{-1}}$, and $\sim 10^3$ yrs at $c_{\rm s} \sim 10^4 {\rm km\, s^{-1}}$ in the case of low circular speed of $10 {\rm km\, s^{-1}}$. In

[3]Although the accretion timescale is much shorter when c_s is large, the overall accretion rate depends on the local density. At fixed pressure, the accretion rate declines with increasing c_s.

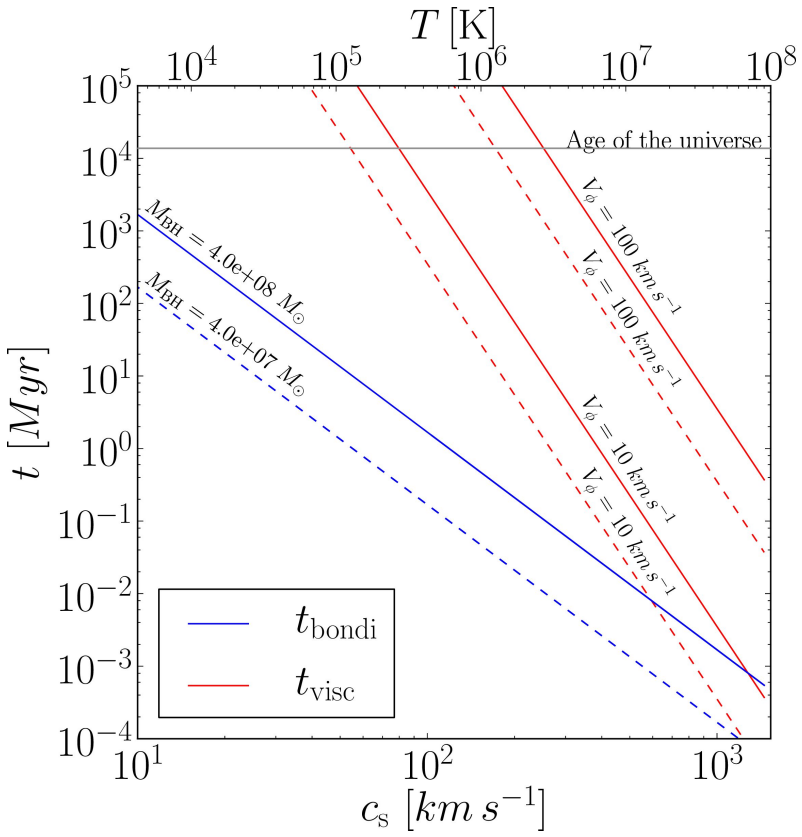

Figure 3.2: The Bondi time (blue lines) and viscous time (red lines) for our fiducial model with $C_{\rm visc} = 2 \times 10^6$ (eq. 3.12). At low values of $c_{\rm s}$, the viscous time can be as long as the age of the Universe, but it reaches much shorter values when the sound speed is high. The Bondi time also decreases with high sound speed but the effect is weaker: even for low circular speed ($10\,{\rm km\,s^{-1}}$), the accretion rate is limited by the viscous timescale unless the sound speed is as high as $c_{\rm s} \sim 10^3 {\rm km\,s^{-1}}$.

contrast, both timescales are relatively weak functions of the BH mass. The main feature of the figure is that because of the stronger dependency of $t_{\rm visc}$ on local sound speed, the mass accretion rate will be almost always limited by the viscous time for the typical angular momentum measured in the simulations.

BH accretion rate accounting for angular momentum

In the scenario of our sub-grid model, material with sufficiently low specific angular momentum falls through the Bondi radius forming an angular momentum supported disc. The long viscous timescale of this disc creates a bottle neck for accretion onto the BH. We will assume that mass is ejected from the disc (by super-

nova driven feedback within the disc, for example) at a rate that is proportional to the disc mass. In this case, the disc mass, M_{disc}, builds up until an approximate equilibrium is reached ($M_{disc}(t) \sim$ constant). At this point, the rate of the accretion onto the BH is given by

$$\dot{m}_{\rm BH} \sim \frac{M_{disc}}{t_{\rm visc}} \sim \frac{\dot{m}_{\rm Bondi} t_{\rm Bondi}}{t_{\rm visc}}. \tag{3.13}$$

The details of mass loss from the disc are not important to the accretion rate and are degenerate with the proportionality constant $C_{\rm visc}$. Following this argument, the critical factor is, then, the ratio of Bondi and viscous times:

$$\begin{aligned} \frac{t_{\rm Bondi}}{t_{\rm visc}} &= \frac{r_{\rm Bondi} c_{\rm s}^{-1}}{C_{\rm visc}[r_{\rm Bondi} V_\phi]^3 [G M_{\rm BH}]^{-2}} \\ &= \frac{1}{C_{\rm visc}} \frac{c_{\rm s}^3}{V_\phi^3}. \end{aligned} \tag{3.14}$$

Thus $t_{\rm Bondi}/t_{\rm visc}$ depends only on $[c_{\rm s}/V_\phi]^3$. Note that if $t_{\rm visc}$ is larger than $t_{\rm Bondi}$ (ie., $C_{\rm visc}^{1/3} V_\phi > c_{\rm s}$) the accretion rate is limited by the Bondi rate and we can ignore the time spend in the accretion disc phase. We therefore write the BH accretion rate as

$$\dot{m}_{\rm BH} = \begin{cases} \dot{m}_{\rm BS09} \left[\frac{1}{C_{\rm visc}} \left(\frac{c_{\rm s}}{V_\phi} \right)^3 \right] & \text{if } C_{\rm visc}^{1/3} V_\phi > c_{\rm s}, \\ \dot{m}_{\rm BS09} & \text{Otherwise} \end{cases} \tag{3.15}$$

where $\dot{m}_{\rm BS09}$ is the mass accretion rate given in the eqs. 3.1 and 3.2, corresponding to the Bondi-like accretion model and $C_{\rm visc}$ is a free parameter which parameterizes the efficiency of angular momentum transport and also the mass loss from the disc. We take $C_{\rm visc} = 2.1 \times 10^6$ as our fiducial value (see section 3.6 for the effects of changing $C_{\rm visc}$, which is weakly sensitive in moderate variations). We see that the circular speed of material at the Bondi radius needs to exceed a critical value before the accretion timescale is suppressed. V_ϕ takes a critical value above which the BH accretion is hindered. In the case of our fiducial value, $C_{\rm visc} = 2.1 \times 10^6$, this critical value is given by $V_\phi \approx c_{\rm s}/128$. For sound speeds of $10^3\,{\rm km\,s^{-1}}$, the

critical value is $10\,\mathrm{km\,s^{-1}}$, and it is $0.1\,\mathrm{km\,s^{-1}}$ for low sound speeds of $10\,\mathrm{km\,s^{-1}}$. Below this critical value, even though a disc forms, transport through the disc is more rapid than the rate at which material is accreted. In the opposite case, the viscous time is long compared to the rate at which material is accreted through the Bondi radius and the material will be expelled from the disc by supernova feedback before being accreted into the BH.

The model also assumes that the overall accretion rate cannot exceed the Eddington.

Implementation of angular momentum (AM) dependent accretion as a sub-grid model

In order to implement the AM dependent accretion rate as a sub-grid model, we estimate the circular velocity of the gas surrounding a BH using the SPH smoothing kernel to determine the weighted AM of the surrounding gas and then dividing by the smoothing length h:

$$V_\phi = \Big| \sum_{i=0}^{N_{\rm SPH}} \mathbf{r_i} \times \mathbf{v_i}\, m_i W(\mathbf{r_i}, h) \frac{1}{\rho h} \Big| \tag{3.16}$$

where $W(r, h)$ is the SPH smoothing kernel used in Gadget, h is the SPH smoothing length of the BH and ρ is the smoothed density given by $\rho = \sum_{i=0}^{N_{\rm SPH}} m_i W(r_i, h)$. We extrapolate the circular speed from the SPH smoothing length to the Bondi radius assuming a flat rotation curve in this region (ie., $V_\phi \sim$ constant). This way of calculating the circular velocity gives stable values even though the smoothing length and thus the AM may fluctuate wildly. We also find that the estimated value of the circular speed is largely independent of the number of neighbours used in the smoothing kernel. Note that our approach is very different from Debuhr, Quataert & Ma (2011), who estimate the circular speed using the gravitational mass only. This difference is important: as we will show later, variations in the circular speed (driven by local gas conditions) result in a distinctive accretion patterns for stable discs and merger induced outbursts. The circular speed is then

used to compute the viscous timescale using Eq. 3.12, and thus the modified accretion rate using Eq. 3.15. The accretion rate is also constrained to be smaller than the Eddington accretion rate. Other aspects of the implementation are identical to Booth & Schaye (2009) which we will describe briefly in section 3.3.

3.3 The Numerical Code and Hydrodynamic Simulations

The simulations we present are based on the GADGET-3 SPH code (Springel, 2005), adding enhancements to reduce the simulation viscosity when the time derivative of the flow divergence is small (Cullen & Dehnen, 2010) and to ensure that timesteps of particles receiving feedback energy are limited (Durier & Dalla Vecchia, 2012). These enhancements will be described in more detail in Dalla Vecchia (in prep). The code uses an extensive network of sub-grid modules to account for the turbulent pressure of the ISM, and implement star formation following the empirical Kennicutt-Schmidt law (Schaye & Dalla Vecchia, 2008), chemical enrichment (Wiersma et al., 2009b) and cooling tracking 11 elements (Wiersma et al., 2009a). These modules were originally developed for the OWLS (Schaye et al., 2010) and GIMIC (Crain et al., 2009) simulation projects. Here we use a metallicity dependent gas density threshold of Schaye (2004) (as in OWLS model SFTHRESZ) and a revised treatment of the equation of state (Dalla Vecchia & Schaye, 2012). Feedback from supernovae is implemented as stochastic thermal energy injection events, using a fixed heating temperature of $10^{7.5}$K, in order to avoid spurious radiative losses (Dalla Vecchia & Schaye 2012, see also Creasey et al. 2011). We moderate the supernova feedback efficiency, f_E (the fraction of SN energy available to perform feedback) as a function of the local dark matter velocity dispersion (Okamoto et al., 2008) in order to obtain a good match to the faint end slope of the galaxy stellar mass function. A similar variation is commonly used in semi-analytic models (eg., Guo et al. 2011; Bower et al. 2012) and is supported by small-scale simulations of galaxy winds such as Creasey et al.

(2012). The feedback efficiency f_E is set as a function of the equivalent halo virial temperature, varying between 1.0 (in low temperature haloes) and 0.1 (in high temperature systems), following the equation:

$$f_E = 1.0 - 0.9 \left(\frac{1}{1 + \exp\left[-2(\log T - \log T_0)\right]} \right), \tag{3.17}$$

where $\log T$ is the logarithmic virial temperature calculated from the local dark matter velocity dispersion, $\sigma_{\rm DM}$, with the following condition:

$$\frac{3Tk_{\rm B}}{2} = \frac{1}{2}\mu m_{\rm p}\sigma_{\rm DM}. \tag{3.18}$$

After some experimentation, we set the transition temperature to $T_0 = 10^{5.5}$K.

In this paper, our focus is the interaction between feedback from BH accretion and the formation of galaxies. We fix the supernova feedback efficiency and its scaling and vary the parameters of BH feedback. Throughout the paper, we use the stochastic heating model of BS09 with a heating temperature of 10^8K, and a density power $\beta = 2$ in eq.3.2. By default we assume that the energy liberated per accreted rest mass energy is $\epsilon_{\rm r} = 0.1$, and that the heating efficiency (this is the fraction of liberated energy coupled to the surrounding gas medium) is $\epsilon_{\rm f} = 0.15$; we show the effect of reducing the heating efficiency below. Accretion is always limited to be less than the Eddington accretion rate. BH seeds are inserted into haloes that exceed a Friends-Of-Friends halo mass of $10^{10}h^{-1}{\rm M}_\odot$, corresponding to ~ 1500 dark matter particles. Such haloes are well defined and there is no danger of injecting BHs into spurious systems (BS09). BH are injected with an initial mass of $10^4h^{-1}{\rm M}_\odot$. They are allowed to merge within their SPH smoothing kernel and have relative velocity less than 0.5 of the sound speed of the surrounding gas. In section 3.2.2, we enhance the standard accretion model to account for the circular speed of gas within the smoothing kernel of the BH.

The simulations used in this chapter are summarised in Table 3.1. All the simulations use the same sub-grid parameters to describe star formation and stellar feedback, and only differ in the BH sub-grid physics. There are in total 4

Table 3.1: A list of the simulations used in this paper. Each simulation has the same supernova feedback parameters, and a co-moving volume of $(25\ Mpc)^3$. The simulation use 2×360^3 particles, with initial baryonic particle mass $1.4 \times 10^6 h^{-1}\mathrm{M}_\odot$ and dark matter mass particle $6.3 \times 10^6 h^{-1}\mathrm{M}_\odot$; the mass of seed BHs is set $m_{\rm seed} = 10^4 h^{-1}\mathrm{M}_\odot$ and the minimum halo mass in which BH seeds are injected is $10^{10} h^{-1}\mathrm{M}_\odot$. The columns show: 1) Name of the simulation; 2) Efficiency with which energy emitted by a BH is coupled into the ambient gas; 3) Radiative efficiency of BH accretion discs

Name (1)	$\epsilon_{\rm f}$ (2)	$\epsilon_{\rm r}$ (3)	Accretion model (4)
NO-AGN	–	–	–
BS09	0.15	0.1	Bondi-like accretion model eqs. 3.1 and 3.2.
BS09-LE	0.015	0.1	Bondi-like accretion model eqs. 3.1 and 3.2.
AM	0.15	0.1	AM accretion model eq.3.15, $C_{\rm visc} = 2 \times 10^6$.
Section 3.6	0.15	0.1	AM accretion model $C_{\rm visc} = 6 \times 10^6$ – 6×10^4 .

simulations :

- *NO-AGN*: This simulation does not include BH physics.
- *BS09* : We use BS09's model with the feedback efficiency set to $\epsilon_{\rm f} = 0.15$ in the Bondi-like accretion eqs. 3.1 and 3.2. Accretion is also limited by the Eddington rate.
- *BS09-LE* : We set this simulation as the above except that the feedback efficiency is set to $\epsilon_{\rm f} = 0.015$.
- *AM*: This simulation uses the AM dependent accretion model eq.3.15, with $C_{\rm visc} = 2.1 \times 10^6$.

The results are not particularly sensitive to the moderate choice of $C_{\rm visc}$ (by 2 orders of magnitude), and we show some example variations in sec 3.6. All of the models assume that the accretion rate cannot exceed the Eddington limit (eq. 3.3).

Initial conditions were generated using second-order lagrangian perturbations (Jenkins, 2010) at a starting redshift of 127. We use initial gas and dark matter particle masses of $1.4 \times 10^6 h^{-1}\mathrm{M}_\odot$ and $6.3 \times 10^6 h^{-1}\mathrm{M}_\odot$ respectively; the *co-moving* gravitational softening lengths are set to $2\,h^{-1}$ kpc with a maximum physical softening of $0.5\,h^{-1}$ kpc. The simulations are carried out in periodic boxes of $25\,\mathrm{Mpc}$ on each side. The largest structure that forms in the simulation has a mass of $1.65 \times 10^{13}\mathrm{M}_\odot$ at $z = 0$. Comparing to large simulation volumes we find that a box of this size does not noticeably bias galaxy properties as a function of virialised halo mass (Haas et al., 2012), allowing us to efficiently test the impact of different sub-grid models. Because of the limited box size, we compare galaxy properties to the stellar fractions ($f_{\mathrm{star}} = M_*/M_{200}$) inferred from observations as a function of halo mass, rather than to galaxy stellar mass function itself.

We adopt the Λ-CDM cosmology with $h = 0.704$, $\Omega_\Lambda = 0.728$, $\Omega_\mathrm{m} = 0.272$, $\Omega_b = 0.0455$, $\sigma_8 = 0.810$, and $n_\mathrm{s} = 0.967$. These values were derived from the Wilkinson Microwave Anisotropy Probe 7 year (WMAP7) data (Komatsu et al., 2011).

3.4 The global impact of BH accretion on galaxies

In this section we examine the impact of BH feedback on the galaxies in the simulations described above. We focus on the stellar mass fraction–M_{200} (halo mass) relation and the M_{BH}–M_{200} relation, in particular. We first present results based on the Bondi–like models (*BS09* and *BS09-LE*), and then contrast them with the AM dependent model.

3.4.1 Simulations with BS09 Bondi–like accretion models

Firstly, we look at the simulations based on the Bondi-like accretion model: *BS09* and *BS09-LE* and compare these with the *NO-AGN* simulation. The left-hand panel of Fig. 3.3 shows the stellar mass fraction, $M_{\mathrm{star}}/M_{200}$ (where the stellar mass is measured within 30 kpc radius) for central galaxies as a function of M_{200}. Given

the small box size, this provides a convenient way to compare with observational data. The solid lines represent the median relation in bins of halo mass, with the 10–90% range of the data indicated as coloured regions. Grey lines show observational estimates based on abundance matching from Moster (2009) and Guo et al. (2010).

The simulation *NO-AGN* (yellow colour) is consistent with the abundance matching results up to a halo mass of $10^{12}\mathrm{M}_{\odot}$, indicating that the feedback from AGNs have little or no effect in the low-mass haloes whereas the lack of AGN feedback leads to an overproduction of stellar mass in high-mass haloes in disagreement with the abundance matching results. The figure 3.3 also shows the simulations *BS09* (blue line) and *BS09-LE* (red line). In both simulations, the impact of BH feedback has a strong effect on a wide range of halo mass, causing a reduction of the stellar mass fraction by a factor of 2 in $10^{11}\mathrm{M}_{\odot}$ haloes and an order of magnitude in the high mass haloes at $10^{12}\mathrm{M}_{\odot}$. The models are incompatible with the observational data.

We note that the effects of AGN feedback become significant at lower masses and are more severe than in the low redshift OWLS simulations, which agree well with observations (McCarthy et al., 2010), because our particle masses are lower by nearly two orders of magnitude (allowing us to convincingly resolve galaxies with stellar masses greater than $10^{9}\mathrm{M}_{\odot}$ with 500 particles) and we have not adjusted any parameters to compensate for the large increase in resolution.

Comparing the simulations *BS09* and *BS09-LE* , where the efficiency of feedback differs by an order magnitude ($\epsilon_{\mathrm{r}} = 0.15$ and 0.015 respectively), it is clear that the AGN feedback produces similar suppression of star formation and low stellar mass fractions in both runs, which is consistent with the findings of BS09 and Booth & Schaye (2010).

The tendency for the BHs to self-regulate, and thus to correlate strongly with the binding energy of the (inner) halo has been emphasised by Booth & Schaye (2010). As a result, a strong correlation is expected between the BH mass and M_{200}. The right panel of the Fig. 3.3 shows the BH mass as a function of M_{200} for the

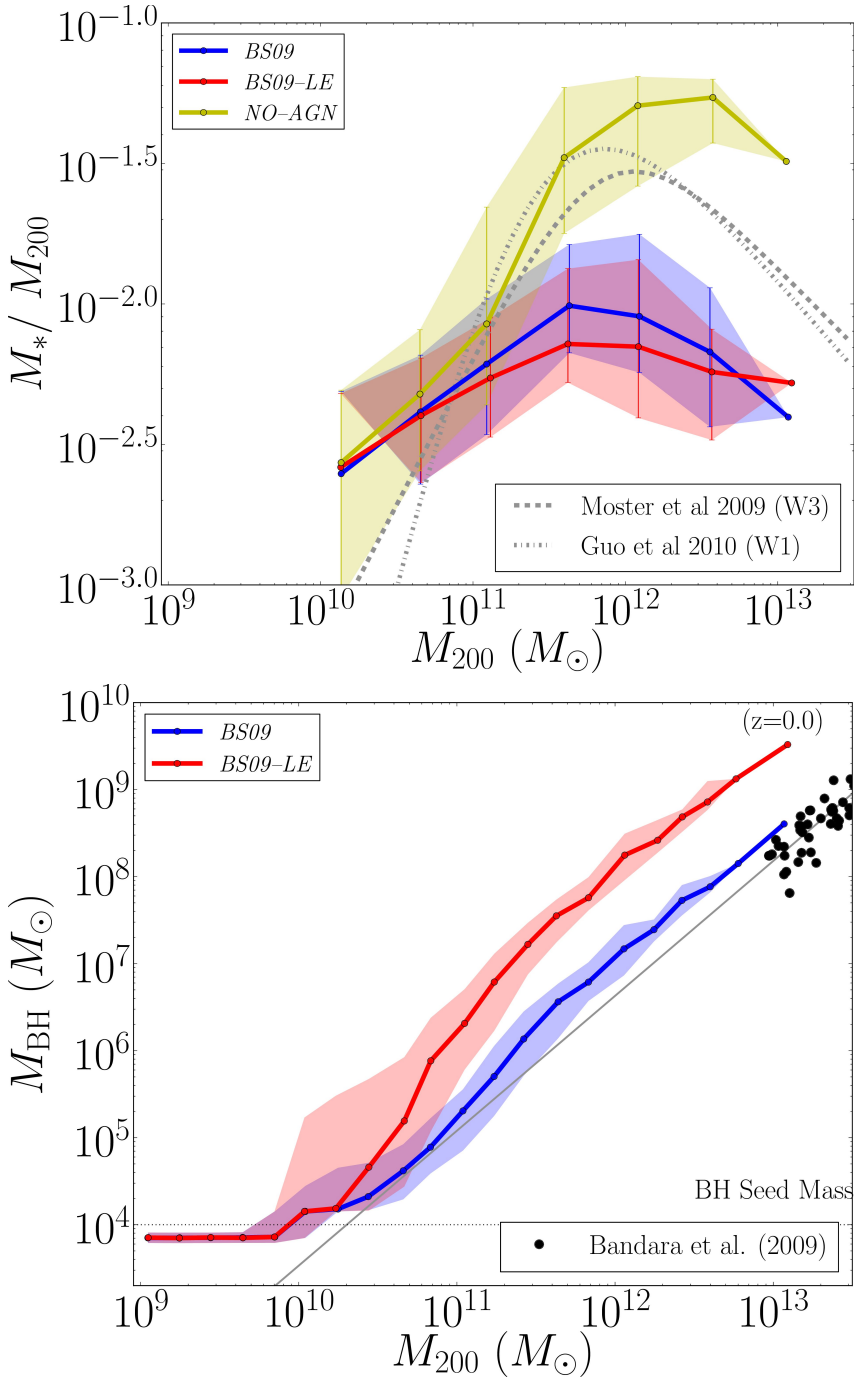

Figure 3.3: The top panel shows the stellar mass fraction as a function of M_{200}, while the bottom panel shows the $M_{\rm BH}$–M_{200} relation. The solid lines show the medians of M_*/M_{200} (or $M_{\rm BH}$) for the simulations *NO-AGN* (yellow), *BS09* (blue) and *BS09-LE* (red) (see table 3.1). The shaded region shows the 10-90% range of the data. The grey dashed and dashed–dotted lines in the left panel represent abundance matching results derived from Moster (2009) and Guo et al. (2010) respectively and the grey line in the right panel indicates the observational $M_{\rm BH}$–M_{200} relation derived by Bandara et al. (2009). The figure shows that efficient BH self-regulation creates a strong correlation between BH mass and halo mass, but strongly suppresses the formation of stars across a wide range of halo mass. Although changing the efficiency of BH feedback alters the normalisation of the $M_{\rm BH}$-M_{200} relation, it has little effect on the host galaxy properties.

simulations *BS09* and *BS09-LE*. In order to provide an observational baseline, black stars show estimates of the BH mass in 48 galaxy-scale strong gravitational lenses from the Sloan lens ACS and grey lines represent the fit of data from Bandara et al. (2009) based on the $M_{\rm BH}$–σ_* relation of Gultekin et al. (2009). The simulation *BS09* gives a correlation between the BH mass and halo mass in good agreement with observations as found by Booth & Schaye (2010). As expected, reducing the feedback efficiency, by a factor of 10 produces more massive BHs at fixed halo mass, leading to a $M_{\rm BH}$–M_{200} relation that is offset from the observational data. As has already been shown by Booth & Schaye (2010), the total feedback energy remains the same in both models, consistent with the idea that the BHs grow until they begin to unbind the gas halo of the system. At this point they become self-regulating growing in lock-step with the halo mass.

The results from the two panels suggest that the self-regulated growth of the black hole overwhelms the stellar mass growth of the central galaxy if BH accretion is efficient. The gas, which would have been able to form stars in the absence of AGN feedback, is expelled from the system or prevented from accreting, starving the central galaxy of fuel for further star formation. A comparison of the red and blue curves shows that the issue cannot be resolved by altering the efficiency with which energy is deposited. However, following the scenario discussed in section 3.2.2, we have already noted that a vital component of the accretion model is missing: gas that is supported by angular momentum cannot accrete as rapidly as the Bondi-like BS09 formula would suggest.

One heuristic solution is to only inject BHs into higher mass haloes. For example, injecting BHs at a halo mass of $10^{11.5}h^{-1}\,{\rm M}_\odot$, provides a good description of galaxy properties. However, this is clearly unsatisfactory: at the resolution we consider, the haloes of $10^{10}h^{-1}\,{\rm M}_\odot$ contain more than 1500 particles and are well defined and with persistent features. There is no physical justification for not attempting to model BHs in these haloes. Another simple solution is to adopt a much lower accretion rate. Decreasing β in eq. 3.2 where the multiphase nature of the ISM is ignored, achieves the required goal of suppressing BH growth

within galaxies. However, this strongly suppresses the accretion rates of early BHs making it difficult to form a BH population at high-redshift as required by observations of massive BHs at redshifts ~ 7 (Mortlock et al., 2011).

3.4.2 Simulation with the AM accretion model

In this section, we explore the effect of accounting for angular momentum in the accretion model. Fig. 3.4 is similar to Fig. 3.3, except that we show the *AM* simulation where the accretion rates account for angular momentum as in eq.3.15, in purple. The top panel shows that the *AM* simulation leads to stellar mass fractions that are in much better agreement with the abundance matching relation (grey lines) and still able to reproduce the turnover of the relation in high mass haloes. Note that the stellar mass fraction found in halos less massive than $10^{12}\mathrm{M}_{\odot}$ is similar to those in the simulation *NO AGN*, supporting the idea that AGN feedback plays a minor role in regulating star formation in these galaxies. Looking at the M_{BH}–M_{200} relation in the right panel, we see that the BHs residing in halos with mass lower than $10^{12}\mathrm{M}_{\odot}$ in the *AM* simulation, grow more slowly than expected for self-regulation. However, above this halo mass, both models lock onto the same self-regulated relation, in good agreement with observations.

The model we have shown adopts $C_{\mathrm{visc}} = 2.1 \times 10^{6}$. The dependence on the value of this parameter is surprisingly weak — as illustrated in section 3.6. We will argue below that the mass scale at which BH accretion becomes self-regulating is set by the properties of the halo rather than by the details of the AM accretion model.

Although the BHs in lower mass haloes fall below the (extrapolated) observational relation, the correlation between BH mass and halo mass is a very indirect observational test of the models. A better approach is to compare the BH mass to the stellar velocity dispersion of the model. This is shown in Fig. 3.5. Since the models have significantly different stellar mass and dynamics, we would expect the models to differ in this plot, and this is indeed seen. Observational data is shown from Gultekin et al. (2009) and McConnell & Ma (2012) with the

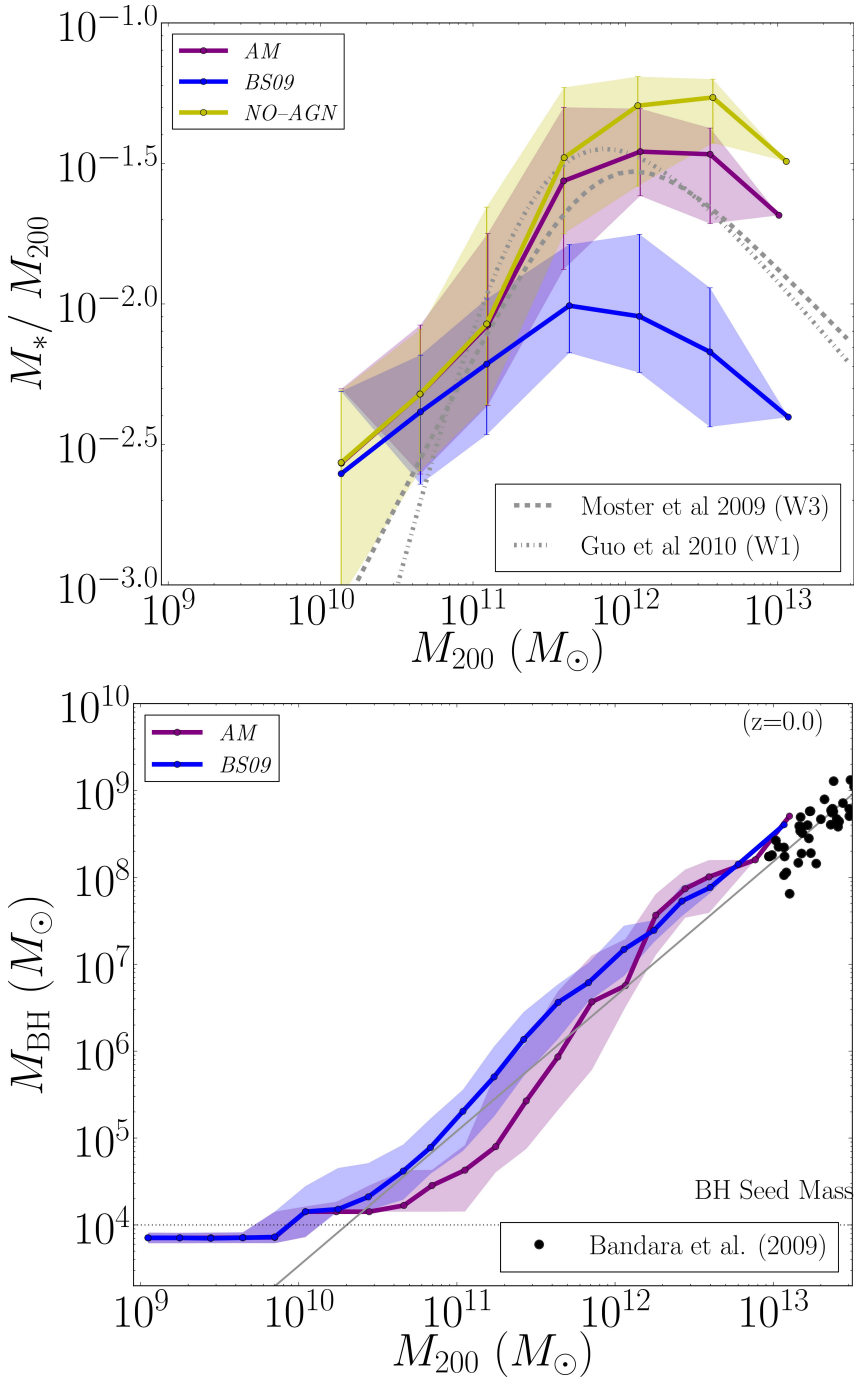

Figure 3.4: The top panel shows the correlation of stellar mass fraction with M_{200} for the angular momentum dependent accretion model, contrasted with two of models considered in section 3.4.1. The bottom panel shows the $M_{\rm BH}$–M_{200} relation for the same models. The yellow and blue coloured lines correspond to those in figure 3.3. The *AM* simulation is shown in purple. The AM model results in resemble agreement with both the abundance matching relationship of the stellar mass fraction (grey lines) and with the observational $M_{\rm BH}$-M_{200} relation. The key to achieving this match is that BHs residing in halos with mass below $\sim 10^{12}{\rm M}_\odot$ grow less than required for self-regulation.

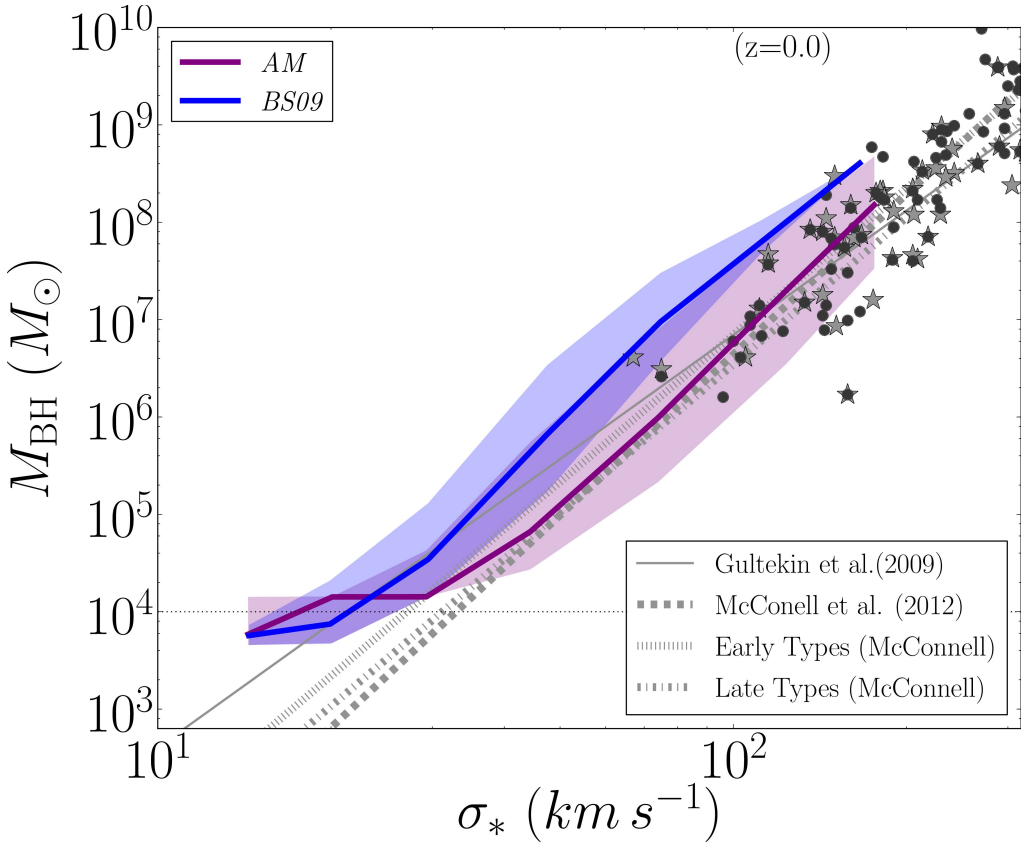

Figure 3.5: $M_{\rm BH}$–σ_* relation for the models presented in Fig. 3.4. Line colours are reproduced from that figure. Observational data are shown in grey, taken from Gultekin et al. (2009) (stars) and McConnell & Ma (2012) (circles) with the grey solid and dashed lines the authors' respective observational fits. The grey dotted and dashed-dotted lines are fits only considering early type galaxies and late type galaxies respectively. The median relation from the *AM* simulation (purple line) is in good agreement with the fit expected for the early type galaxies of McConnell & Ma (2012) at the high σ_* end while it encompasses the observational data for late type galaxies at the lower σ_* values.

grey solid and dotted lines respectively showing the expected median relations for early-type galaxies (dotted line) and late-type galaxies (dotted-dashed line). The difference between observational relations arises because McConnell & Ma includes data for BGCs resulting in a steeper fit. The model is clearly able to pass the test offered by the $M_{\rm BH}$-σ_* relation.

3.5 Tests for convergence of the subgrid extended BH Model

Because of the small relative scales of the BH and its accretion disc relative to the scale of the simulation, the most challenging part of the calculation is the difficulty of adequately describing the properties of the multi-phase gas in the region around the BH. Because of this, it would not be surprising if the parameters of the model were functions of scale. Nevertheless, we present a comparison of two versions of simulation *AM* carried out at different resolutions in the standard 25 Mpc volume. Specifically, we run the simulation *AM LOWRES* with a lower mass resolution by a factor of 8 with 2×180^3 particles and with mass $5.88 \times 10^7\ h^{-1}\mathrm{M}_\odot$ and $1.18 \times 10^7\ h^{-1}\mathrm{M}_\odot$ for dark matter and gas particles respectively, while the mass resolution of the *AM* simulation is $1.4 \times 10^6 h^{-1}\mathrm{M}_\odot$ for gas and $6.3 \times 10^6 h^{-1}\mathrm{M}_\odot$ for dark matter particles. The co-moving gravitational softening length was set to $4h^{-1}$ kpc for the simulation *AM LOWRES* and $2h^{-1}$ kpc for the simulation *AM* with a maximum physical softening of $1h^{-1}$ kpc and $0.5h^{-1}$ kpc respectively.

Figure 3.6 shows the stellar mass fraction–M_{200} relation and the $M_{\rm BH}$–M_{200} relation for these simulations in purple and cyan colours for well resolved halos in each simulation. The stellar mass fractions have similar values of the medians and scatter. From this measure, the convergence seems good. In the case of the $M_{\rm BH}$–M_{200} relation, the medians take somewhat smaller values for the low-mass BHs in the simulation *AM LOWRES*, but the two resolutions show a large overlap in terms of the scatter and appear to converge at high and low masses. The convergence is nevertheless better than for the accretion disc particle scheme (Power et al., 2010) when it is applied at this resolution (Muldrew et al., 2013).

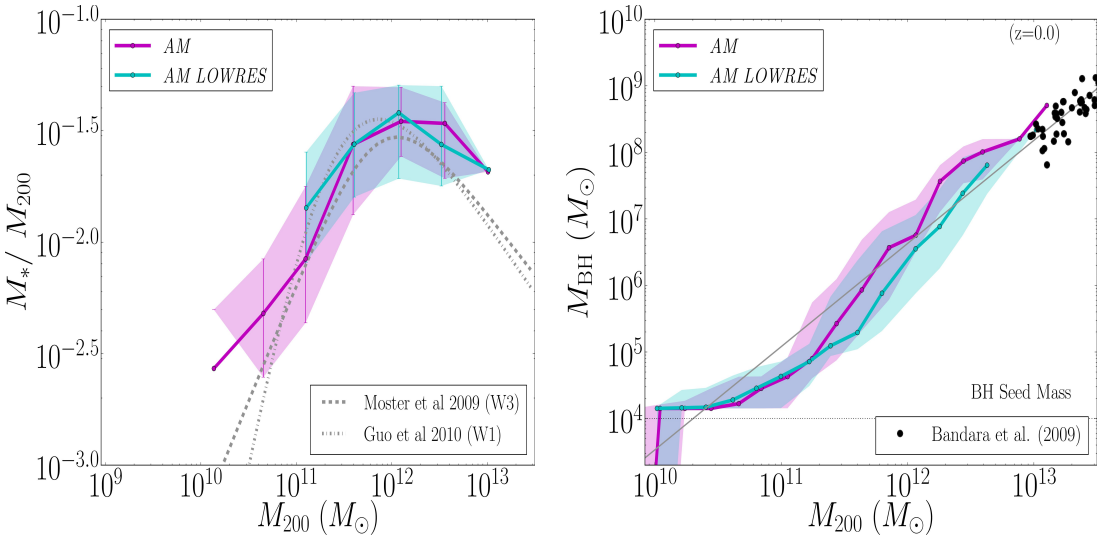

Figure 3.6: The right panel shows the correlation of stellar mass fraction with M_{200}, while the left panel shows the $M_{\rm BH}$–M_{200} relation. The simulation *AM* is shown in purple colour while the simulation *AM LOWRES*, with lower resolution in mass, is included in cyan colour. Although there is some residual offset in BH masses in the right hand panel, the stellar mass fractions (left hand panel) shows good convergence in halos well resolved.

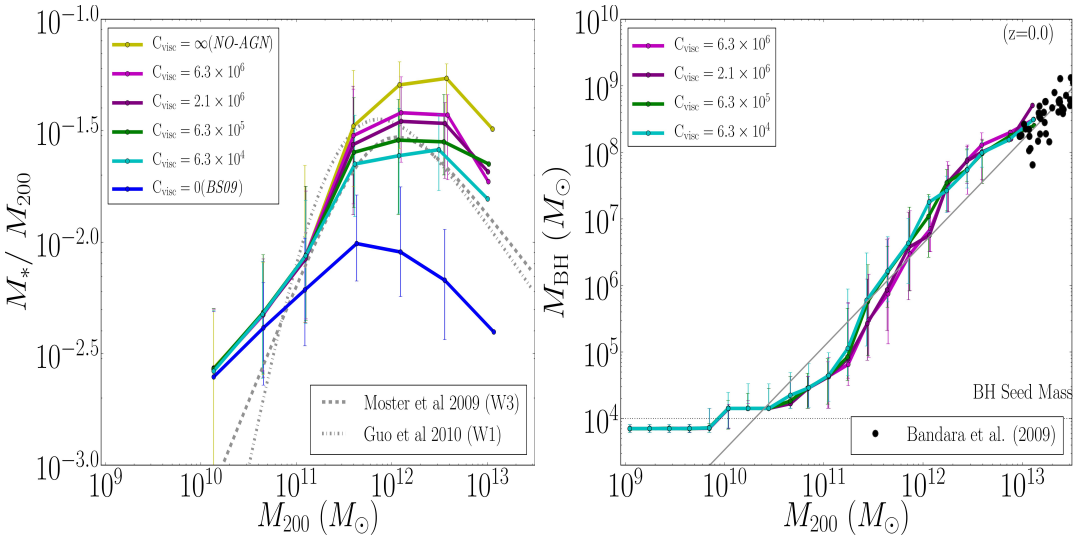

Figure 3.7: The left panel shows the stellar mass fraction-M_{200} relation and the right panel shows the $M_{\rm BH}$–M_{200} relation for simulations similar to *AM* ($C_{\rm visc} = 2.1 \times 10^6$), but with varying $C_{\rm visc}$ as is indicated in the legends. The simulations *NO-AGN* ($C_{\rm visc} = \infty$, yellow colour) and *BS09* ($C_{\rm visc} = 0$, blue colour) show extreme cases of the effects of $C_{\rm visc}$. The smaller $C_{\rm visc}$,the higher the suppression in the stellar mass fraction is above a critical mass halo. The critical halo mass decreases slightly as $C_{\rm visc}$ decreases. The $M_{\rm BH}$–M_{200} relation is not affected above this critical mass, but as $C_{\rm visc}$ decreases slightly less massive BHs are hosted by halos below this critical mass.

3.6 The effect of changing effective viscosity parameter $C_{\rm visc}$

In this section, we show the effect of changing the value of the effective viscosity parameter on the stellar mass fraction in the simulated galaxy population and on the $M_{\rm BH}$–M_{200} relation. We increase $C_{\rm visc}$ by two orders of magnitude from 6.3×10^4 to 6.3×10^6 (our fiducial value is 2.1×10^6, purple line). The figure 3.7 shows the stellar mass fraction and the $M_{\rm BH}$–M_{200} relation when $C_{\rm visc}$ takes these values. We have included the simulations *NO-AGN* ($C_{\rm visc} = \infty$, yellow colour) and *BS09* ($C_{\rm visc} = 0$, blue colour) as extreme cases of $C_{\rm visc}$.

Decreasing $C_{\rm visc}$ (corresponding to a higher disc viscosity or thicker disc) results in the haloes being regulated by BH accretion at slightly lower stellar masses and as a result the stellar mass fraction (left panel) breaks at a critical halo mass, however, how sharp the turnover in the stellar mass fraction depends on $Cvisc$. The extreme case of this effect is shown in the simulation *BS09* ($C_{\rm visc} = 0$) where the stellar mass fraction lies below the abundance matching results. For less extreme values, the dependence on $C_{\rm visc}$ is weak, re-enforcing the idea that the break in the mass fraction is set by the impact of periods of AGN heating (and hence on the halo's cooling and dynamical time scales) rather than on the details of the BH accretion model.

Looking at the $M_{\rm BH}$–M_{200} relation (right panel), for haloes above mass $10^{12}{\rm M}_\odot$ variations in $C_{\rm visc}$ have little effect: in this regime, BHs are able to self-regulate their growth regardless of the details of the accretion model. Halos below this critical mass tend to host less massive BHs, although the dependence on value of $C_{\rm visc}$ is again weak.

Hence, the main results are relatively insensitive to variations of $C_{\rm visc}$ regarding to the critical halo mass in which the break of stellar mass fraction occurs, reproducing a turnover for halos with mass larger than the critical mass. The sharpness of the turnover depends on the choice of $C_{\rm visc}$. Huge changes in $C_{\rm visc}$ are required to have significant impact because the suppression by angular momen-

tum is only effective when $(C_{\rm visc})^{1/3} V_\phi > c_{\rm s}$ (see. eq.3.15). Although the changes in $C_{\rm visc}$ affect the sharpness of the turnover in the mass fraction, this allows to adjust the location of the break in the stellar mass fraction seen in cosmological volume simulations.

3.7 The accretion history of one BH

In order to understand the transition between the low- and high-mass halo behaviour better, we plot the "timeline" of a typical massive BH in the simulation in fig. 3.8. The curves in the upper panel illustrate the mass of the most massive progenitor (red line, left-hand axis), its accretion rate (coloured dots and right hand axis) and the Eddington accretion rate (red line, right-hand axis) as a function of redshift. The points plotted below the horizontal line represent BH accretion rates $\dot{m}_{\rm BH} < 10^{-4} {\rm M}_\odot yr^{-1}$. The colour code corresponds to $\log_{10}(C_{\rm visc}) + 3 \times (\log_{10} V_\phi / c_{\rm s})$ (where $\log_{10}(C_{\rm visc}) = 6.3$). This quantity is the factor by which the mass accretion rate has been suppressed by taking AM into account. For comparison, the FoF mass and the total stellar mass of the host halo are shown in the lower panel as black and green lines respectively (left-hand axis), along with the total star formation rate as the blue line (right-hand axis).

The BH is injected with a seed mass of $1.4 \times 10^4 \, {\rm M}_\odot$. Initially BH growth is limited by the Eddington accretion rate, but the BH growth soon settles down. Although the BH undergoes episodes of accretion close to the Eddington limit, the absolute mass growth is small. Over time, the suppression factor increases in importance. Eventually, promoted by a merger event that begins at $z \sim 5$, the BH undergoes a more sustained period of Eddington limited accretion. At the end of this event, the accretion rate drops probably due to the suppression by the angular momentum. There is marginal further BH growth until $z \sim 3.0$ when another period of Eddington limited accretion begins. The BH undergoes two further periods of Eddington limited accretion until its host halo reaches a mass of $2 \times 10^{12} {\rm M}_\odot$. During these high accretion rate periods, the suppression

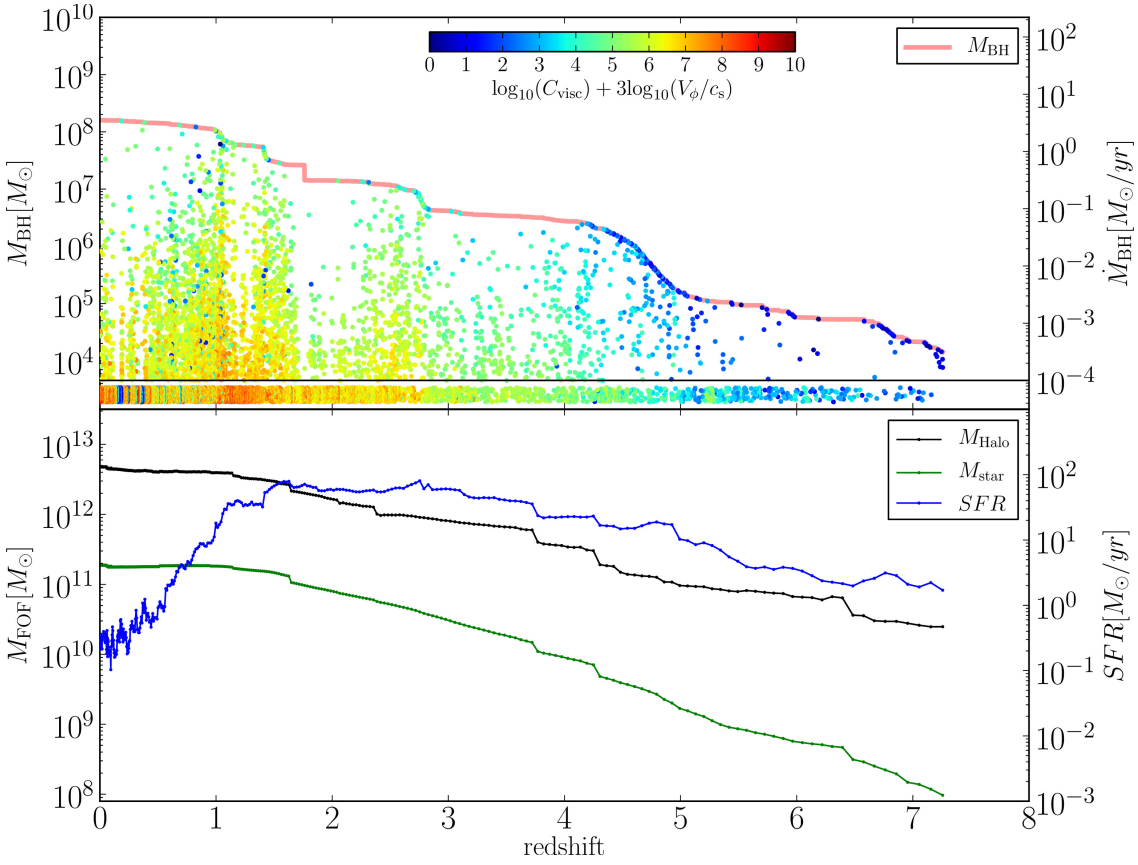

Figure 3.8: History of a massive BH and its host galaxy in the *AM* simulation. The top panel shows the growth of the second most massive BH at $z = 0$ as a function of redshift (red line and left-hand y-axis) as well as its instantaneous mass accretion rate (coloured points and right-hand axis). The colour code indicates the log suppression factor by which the mass accretion rate is reduced, $\log_{10} C_{\rm visc} + 3 \times \log_{10} V_\phi/c_{\rm s}$ where $\log_{10} C_{\rm visc}^{=} 6.3$ for the simulation. High accretion rates shows small suppression factor. The red line represents simultaneously BH mass and Eddington accretion. Above $z = 6$, the BH frequently accretes at Eddington limit, but its mass and consequently its energy output are small. At intermediate redshift, the BH undergoes phases of high mass accretion rate ($z \sim 4.7$, 2.75 and 1.1), interspersed with periods of quiescence. Below $z = 1$, the BH shows frequent outbursts reaching 1–10% of the Eddington rate. The bottom panel shows the FoF mass (black line) and total stellar mass (green line) of the host halo (on the left y-axis) as a function of the redshift. The blue line represents the total star formation rate (right-hand y-axis).

factor is much lower than during the quiescent periods in between. It would seem reasonable to associate these high accretion rate events with QSO activity. Below $z = 1$, the nature of accretion onto the BH appears to change again. Although the accretion rate fluctuates, it rarely reaches the Eddington limit, typically peaking at 1% to 10% of it. The outbursts are more frequent, but not sustained. The correspondence between colour and accretion rate suggests that the accretion is limited by the angular momentum. There is also an apparent increase in the suppression factor as a function of redshift.

The lower panel of Fig. 3.8 allows us to contrast the growth of the halo with that of the host galaxy of the BH. Since the plot shows the total halo mass in each case, it does not identify galaxy mergers well. However, it does emphasise the steady growth of the halo and its constituent galaxies, that is quite at odds with the episodic growth of the BH. Despite the periods of strong BH activity, the star formation rate of the halo seems little affected until the halo reaches a mass of $2 \times 10^{12} \mathrm{M}_{\odot}$ at $z \sim 2$. In the following outburst, the star formation rate is clearly set-back, with the outburst at $z \sim 1.1$ initiating a sustained decay.

The simplest way to understand what drives the sustained accretion events seen in Fig. 3.8, is to examine a movie of the evolution (available from the website shown in footnote 4 [4]. Six frames from the movie are shown in Fig. 3.9, illustrating some of the important features. Examining the sequence in detail, however, shows that the outburst typically lags behind the obvious morphological disturbance. The first three outbursts follow a clear pattern. Immediately after the outburst, the accretion leads to the expulsion of gas surrounding the BH. Although a strong wind is generated, the void which this leaves around the BH is quickly refilled by cool filaments that efficiently carry cool gas to the centre of the halo. The final outburst is qualitatively different, however: once the central gas is ejected, the surrounding matter does not flow in to replace it. Although there continues to be some cool material at the centre of the halo, this does not settle quickly around the BH. We can understand the change in behaviour from the nature of accretion

[4] http://star-www.dur.ac.uk/~rgb/Eagle/images_2nd_bh/movie_width5.0/phase_movie.avi

in haloes of different mass. As Van de Voort et al. (2010) have demonstrated in the OWLS simulations (see also White & Frenk 1991; Dekel & Birnboim 2006; Kereš et al. 2009), the fuelling of high mass haloes is qualitatively different from their low mass counterparts; high mass haloes are dominated by slow accretion from the hot halo, while lower mass haloes are supplied through rapid inflow along cold streams.

3.8 Discussion

3.8.1 The importance of angular momentum

The simulations that we have discussed in the previous sections show the importance of accounting for the angular momentum of accreting gas. In particular, angular momentum appears to establish a scale above which BH feedback regulates the cooling of the halo and below which star formation and supernova feedback are the dominant mechanisms. The key to understanding the nature of this transition is to examine the balance of gas accretion versus star formation and outflows. Since the mass locked up in stars is relatively small, the most important consideration is the outflow of gas. This may be driven by the growth of the BH, or by the formation of stars. Recent papers have emphasised that this leads to self-regulation, both for feedback from star formation and for feedback from BHs (White & Frenk 1991; Bower et al. 2006; Bower, McCarthy & Benson 2008 also Schaye et al. 2010; Booth & Schaye 2010; Dubois et al. 2013 and Puchwein & Springel 2013). The observed shape of the galaxy mass function (and thus the stellar mass fraction) requires that star formation dominates the regulation at low halo masses, while it is dominated by BHs at high stellar masses. The challenge is to understand why this switchover occurs.

In these simulations we use a lower particle mass than BS09, in order to better sample star formation in lower mass galaxies, but the same ISM equation of state (so that the minimum ISM Jeans mass is the same in both calculations). In the

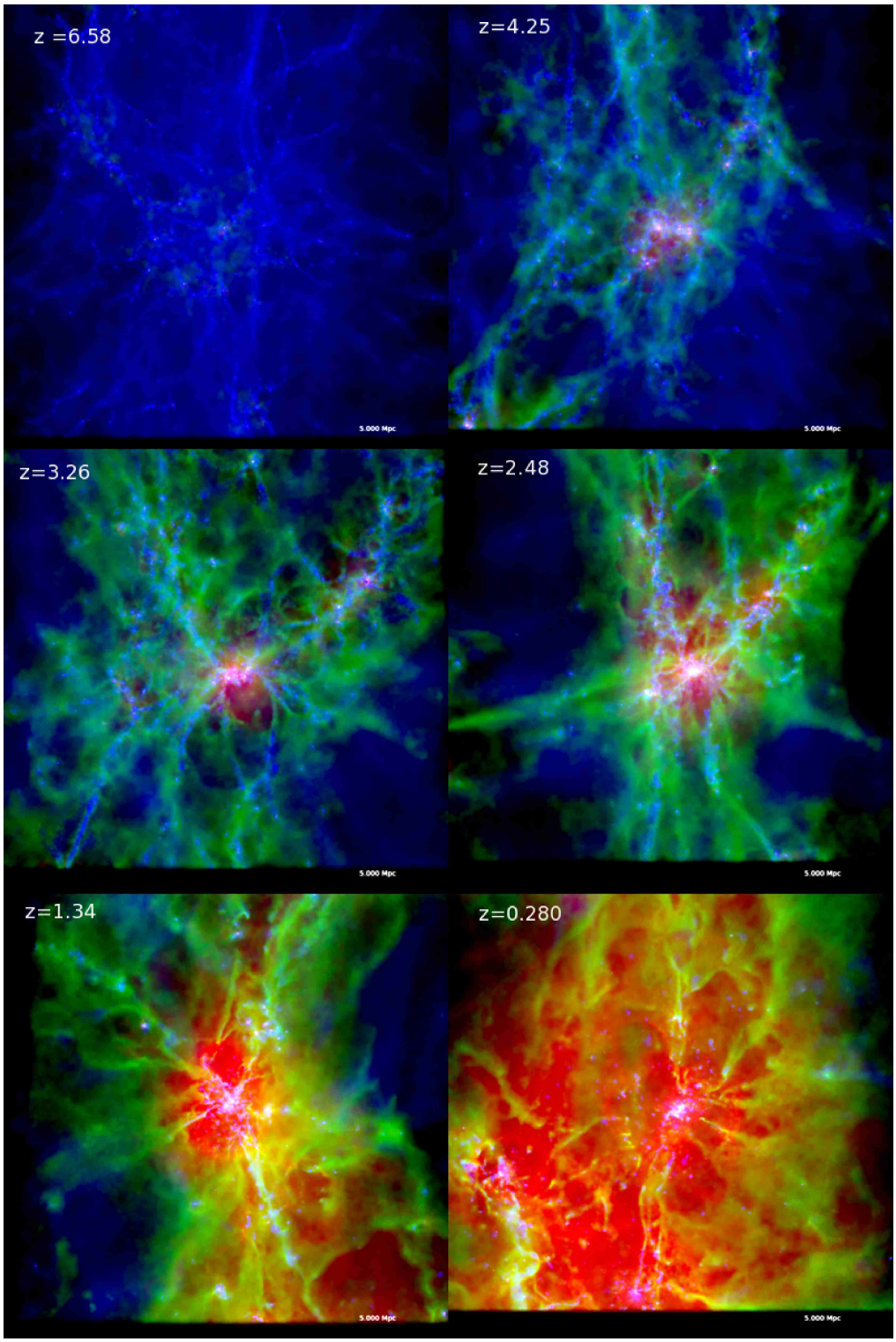

Figure 3.9: This sequence of images illustrates the evolution of the galaxy and halo of the BH shown in Fig.3.8. The colour channels show the projected gas density of gas with temperature $T < 10^{4.5}$K (blue), $10^{4.5} < T < 10^{5.5}$K (green) and $T > 10^{5.5}$K (red). The projected star density is shown in pink. The box above shows 5 Mpc on each side, representing $1/125$ of the total simulation volume. The redshifts have been chosen to illustrate the change in the behaviour of AGN feedback. The complete movie can be downloaded from the website shown in footnote 4).

case where we determine accretion rates using the BS09 formula, BH feedback regulates cooling of gas over the full range of halo mass. As a result, BHs grow in mass, tracking the growth of the halo from the halo mass at which they are injected to the largest halo masses formed in the simulation. Across this full range of masses, BHs dominate the self-regulation. The growth of the BH and the resulting outflow of gas from the halo leaves little room for star formation: the growth of the halo is accompanied by only a small increase in the stellar fraction, and the model does not match the observational data. The flat stellar fraction drives the stellar mass function to a power-law shape that is in complete contrast to the observed Schechter function (see Benson et al. 2003).

In semi-analytic models, it is typically assumed that the break in the stellar mass function occurs because of the changes in the efficiency of BH feedback. Such variations are entirely plausible. For example, the feedback efficiency may be a strong function of the accretion rate because of the disc scale height dependence on jet energy. In order to explore this possibility, we considered the case of Bondi-like accretion in which the feedback efficiency was lowered by a factor of 10, compared to our fiducial value. However, this modification does not change the dominance of BH feedback at lower stellar masses. We find that the self-regulation of BHs and their haloes is so strong that reducing the efficiency of the feedback results in an increase in BH mass at given halo mass, but does not reduce the energy output (see also Booth & Schaye 2009, 2010). As a result, the effects on the galaxy population are similar as in the model with higher efficiency: the stellar mass fraction is almost flat as a function of halo mass. This has an important implication: a modification to the model which changes the efficiency of heating as a function of halo mass, but still uses a Bondi-like accretion rate, cannot reproduce the observed shape of the galaxy mass function.

In Fig. 3.4 we showed the $M_{\rm BH}$–M_{200} relations for the AM model. The effect of the angular momentum has been to suppress accretion onto BHs in low-mass haloes, but to allow efficient accretion in higher-mass haloes. Since BHs grow slowly in the low-mass haloes, the balance of outflow and inflow is established

through star formation. As the low-mass halo grows, the stellar mass increases rapidly. This growth results in masses that are compatible with the abundance matching results, although the precise growth rate has been set by adopting an appropriate dependence of supernova feedback on stellar mass. Above a halo mass of $\sim 10^{12}\mathrm{M}_{\odot}$, AGN accretion becomes effective, and dominates the self regulation of the halo at the expense of star formation, leading to a turn-over in the stellar mass fraction of haloes. We therefore need to explain why BHs do not grow in low mass haloes as quickly as Bondi-like accretion predicts, and yet become efficient sources of energy in haloes more massive than $\sim 10^{12}\mathrm{M}_{\odot}$.

3.8.2 BH accretion and its dependence on local gas properties

In order to better understand the interplay between the pressure and angular momentum of gas around the BH, and to generalise from examining one object to the population as a whole, we show mass accretion rates of the central BHs residing in the 9 most massive halos ($M_{200} > 10^{12}\mathrm{M}_{\odot}$) at $z = 0$ in Fig. 3.10. We show 9 counterparts drawn from halos with mass just below $M_{200} = 1.5 \times 10^{11}\mathrm{M}_{\odot}$ in the bottom panel. Each panel divides the plot into different redshift bins showing BH accretion rate as a function of the local gas pressure, with points coloured by the $\log$ suppression factor as indicated in Fig.3.8. We find that the trends are clearer if we use the effective fluid pressure as the x-axis. For star forming particles, we impose an equation of state to account for unresolved structure and turbulence, and the ISM pressure is a function of the sound speed ($P/k \approx 109\,(c_{\mathrm{s}}/10\,km\,s^{-1})^{8} cm^{-3}\mathrm{K}$ for the equation of state with $\gamma_{eff} = 4/3$ as is assumed here). The points plotted below the horizontal line represent BH accretion rates $\dot{m}_{\mathrm{BH}} < 10^{-4}\mathrm{M}_{\odot} yr^{-1}$ ($\dot{m}_{\mathrm{BH}} < 10^{-8}\mathrm{M}_{\odot} yr^{-1}$ for the lower mass halos shown in Fig 3.11). Points which are coloured blue have a relatively low circular speed and low suppression factor. Red through yellow and green points, with higher circular speeds relative to local sound speed, are offset to much lower accretion rates. The diagram is somewhat complicated by points for which the accretion rate is Eddington limited. These are highlighted by black dots, but the

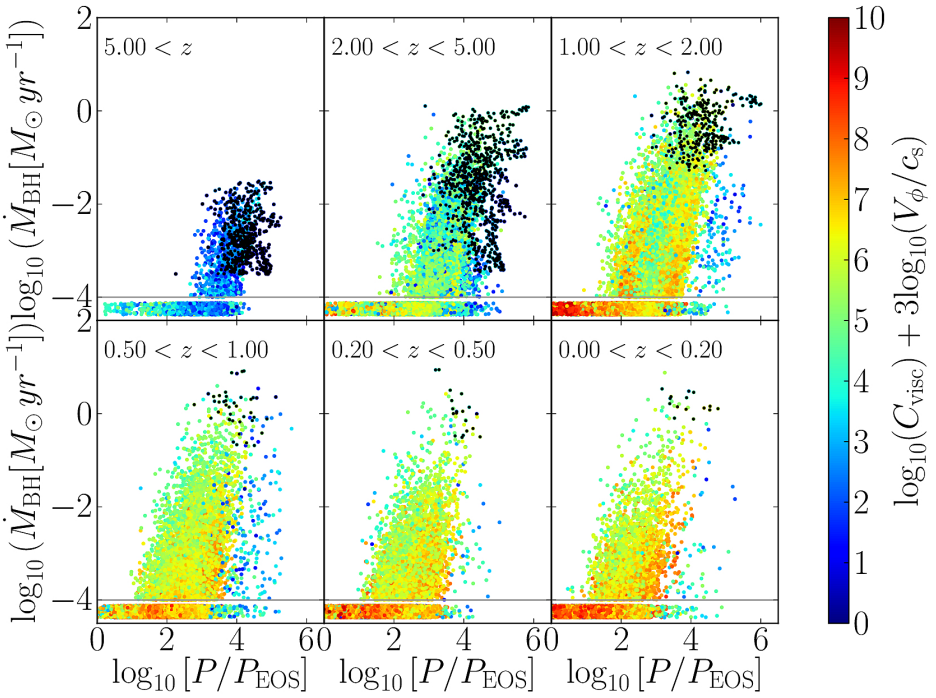

Figure 3.10: BH accretion rates versus the surrounding gas pressure (in units of $P_{\rm EOS}/k = 2.3 \times 10^3 cm^{-3}$K) for the most massive progenitor of the central BHs residing in the 9 halos with $M_{200} > 10^{12.5}$M$_\odot$ at z=0. Each small panel represents a different redshift bin as indicated in all panels. The colour scale indicates the $\log_{10}$ suppression factor as in Fig.3.8. In each small panel, the black points (upper panel) and crosses (lower panel) show Eddington limited accretion events. Significant accretion rates take place when the suppression factor is small for high-mass haloes. BHs in high mass haloes are surrounded by local ISM with higher pressure promoting significant accretion.

Eddington limit only significantly distorts the diagram in the highest redshift panel.

The figure confirms the behaviour seen for a single BH in §5.2. The accretion rates tend to increase strongly with the pressure of the surrounding gas. Most gas particles close to the BH lie on the ISM equation of state so that the pressure and the sound speed are closely correlated. In part, the trends in pressure arise because of the strong modulation of the accretion rate by the BS09 α parameter in equations 3.2 and 3.1. As the gas pressure increases in the simulation, the sub-grid model assumes that the density distribution of the ISM becomes increasingly clumpy and cold. This trend is modulated by the viscous suppression factor

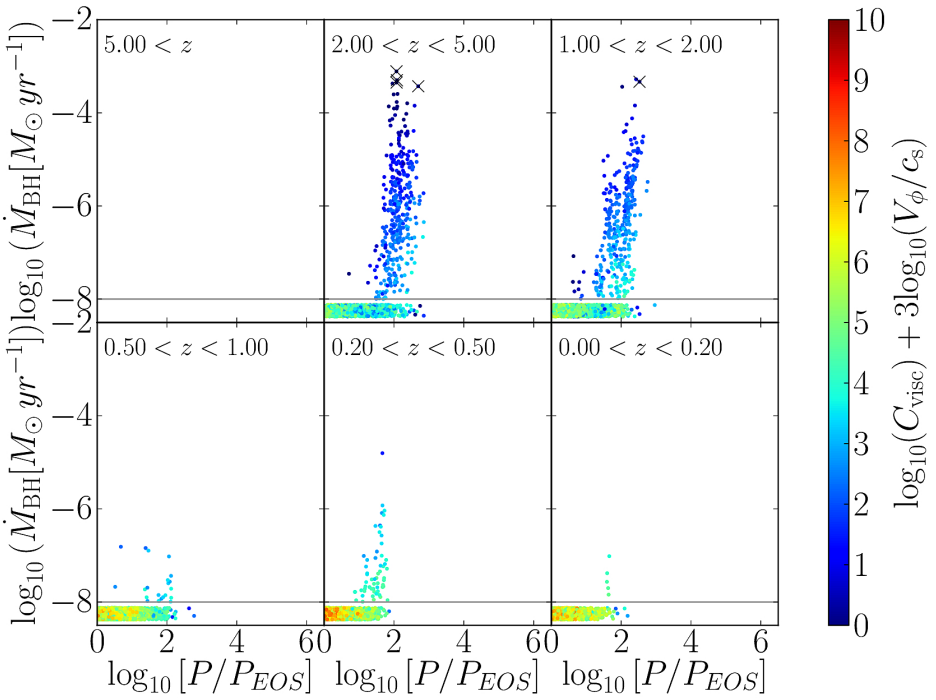

Figure 3.11: BH accretion rates versus the surrounding gas pressure (in units of $P_{\rm EOS}/k = 2.3 \times 10^3 cm^{-3}$K) for the most massive progenitor of the central BHs residing in 9 halos with $M_{200} < 1.5 \times 10^{11}$ at z=0. Each small panel represents a different redshift bin as indicated in all panels. The colour scale indicates the $\log_{10}$ suppression factor as in Fig.3.8. In each small panel, the black points crosses show Eddington limited accretion events. BHs in low-mass haloes are surrounded by local ISM with low pressure at any redshift.

(shown by the colouring of the points) since increasing pressures reduce the importance of the circulation speed (the increasing gas pressure reduces the Bondi radius with the result that the circulation radius and the viscous timescale are also reduced). In addition to the main trend, a few points have high pressure but low suppression factor and relatively low accretion rates. These are episodes when the BH accretes from the hot (but low density) intra-group medium, rather than from a central pool of ISM.

Focusing on the differences between the redshift panels, we see firstly that the typical accretion rate increases across the 3 first panels, but then gradually decreases. This confirms the trend seen for an individual BH in Fig. 3.8. In the highest redshift panels, BHs accrete close to their Eddington limits. In subsequent

panels, the accretion rates remain similar (and decline slightly) while the BHs grow significantly in mass. Examination of the figures shows that two factors contribute. Firstly, the pressure in the surrounding medium reaches a maximum in the intermediate redshift panels and then slowly declines to lower redshift. This possibly arises from the features of the BH's host galaxies : galaxies are less concentrated at lower redshifts as well as the galaxy gas fractions decline below $z = 1$. As a result, gas presses around the BH less tightly and tends not to accrete as strongly, despite the growth of BH mass. Secondly, the suppression factor increases to lower redshift. This trend is driven by decreasing ISM pressure rather than by increasing V_ϕ.

In the Fig 3.11, we show the equivalent plot to quantify the accretion history of smaller BHs, in the M_{200} range $6 \times 10^{10}\mathrm{M}_\odot$ to $1.5 \times 10^{11}\mathrm{M}_\odot$. This allows us to distinguish the trend due to redshift from those due to BH mass. These BHs have much lower masses at the final time and have not reached the self-regulation regime in the right panel of Fig 3.4. The accretion rate axis has been rescaled so that the Eddington accretion rate of the BHs can be distinguished. Comparing the high and low mass panels, the main difference is that the surrounding ISM of the galaxy does not reach high pressures, and that the maximum accretion rates fall off sharply with decreasing redshift. As in Fig 3.10, the colouring of the points illustrates the important role of the circulation speed, strongly suppressing the accretion rates, particularly in the lower redshift panels. Because of the low baseline accretion rate, significant accretion occurs only when the suppression factor is extremely low, so that it is difficult for these lower mass BHs to grow efficiently. As a result, the inflow-outflow balance of the halo is set by supernova feedback rather than AGN activity in haloes of this mass.

3.8.3 Implications for observable AGNs

We will present an in-depth comparison of a similar model in a simulation with a significant volume with observational data in the next chapter. Here, we limit ourselves to a brief look at the Eddington ratio distribution of accreting sources

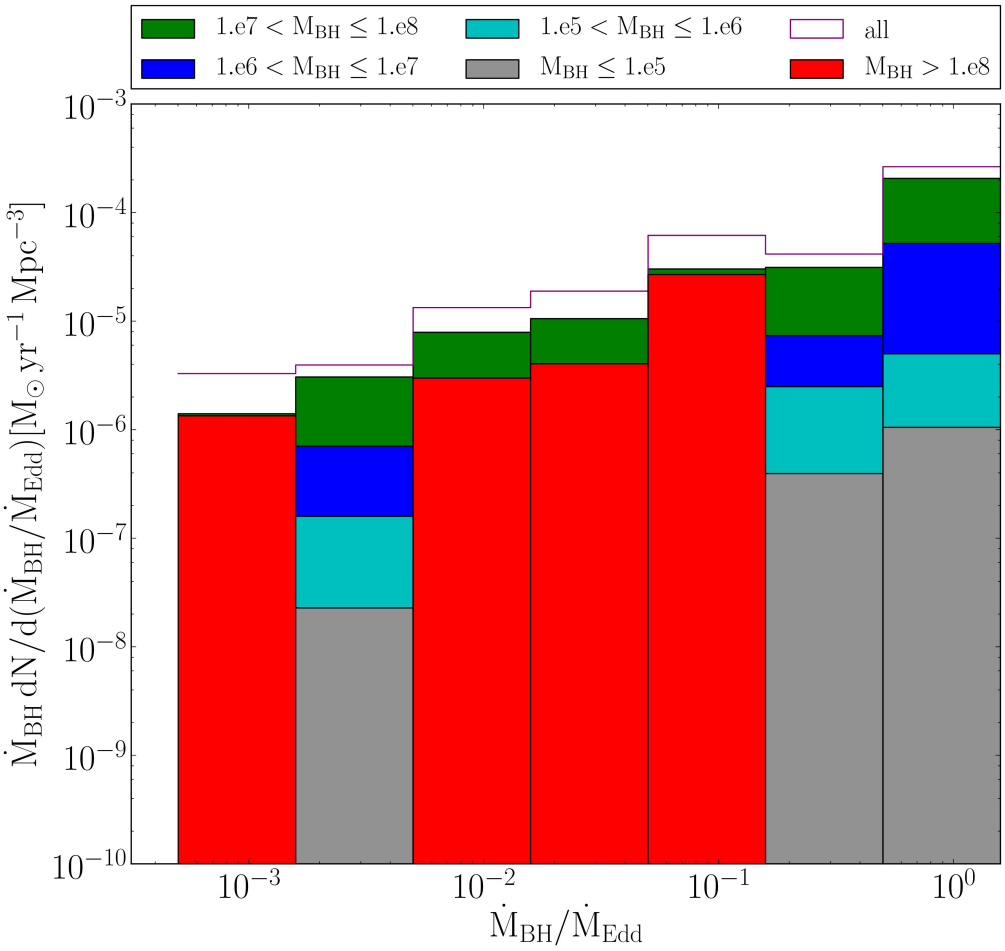

Figure 3.12: The distribution of Eddington ratio weighted by the mass accretion rate of each accretion source (i.e., the accretion luminosity). This plot shows the distribution at $z = 1$. The total distribution is shown as a purple line; The contributions of BHs in different mass ranges are illustrated by different colours. For BHs less massive than $10^8 M_\odot$, the distributions are similar, with larger BHs making a greater contribution to the BH mass budget. Above $10^8 M_\odot$, however, high Eddington ratio sources become rare.

for the *AM* model. In Fig. 3.12, we plot a histogram of the Eddington ratio distribution (defined as $\dot{M}_{\rm BH}/\dot{M}_{Edd}$). We weight each source by its accretion luminosity so that the histogram shows the contribution to the growth of the BH mass density as a function of both BH mass and Eddington ratio. We have chosen to plot the distribution at $z = 1$ (combining outputs in the range $z = 0.78$ to 1.12); similar plots can be constructed at other redshifts, but the features of the distribution functions remain similar.

The purple solid line shows the Eddington ratio distribution of all BHs: the integral under this plot gives the total mass growth rate of BHs at this epoch. Because, we have weighted the source contribution by their accretion luminosity, the highest Eddington ratio sources dominate the BH mass growth budget. If we had simply counted sources, the histogram would show that low Eddington ratio sources are far more numerous. It is instructive, however, to examine how this distribution is built up for BHs of different masses. Different colour lines distinguish the contributions from BHs of different masses, starting from the lowest mass BHs, below $10^5{\rm M}_\odot$ (grey region), and building up to show the contribution of the most massive BHs, above $10^8{\rm M}_\odot$ (red region). Because of the weighting by accretion rate (or luminosity), the smallest BHs contribute little to the total. The shape of the Eddington ratio distribution is similar for BH masses up to $10^8{\rm M}_\odot$. The relative similarity of the distributions has previously been noted in observational data (Aird et al., 2012).

Above a BH mass of $10^8{\rm M}_\odot$, however, high Eddington ratio sources become rare, and the growth of these BHs is dominated by accretion events that are $\sim 10^{-1}$ of Eddington. Although there are only a handful of such high mass BHs in the simulation, they make a significant contribution to the energy budget because of their high mass. Studies of quasar clustering suggest that quasars do not tend to occupy the most massive haloes at lower redshift, and that the most massive haloes are occupied by radio galaxies (Romano–Diaz et al., 2010; Angulo et al., 2012; Fanidakis et al., 2013), whose power output tends to be in the form of a kinetic jet, but not in the form of highly visible luminosity. It is quite plausible that

this dichotomy arises from a change in the Eddington rate distribution with BH mass (Meier, 2001; Nemmen et al., 2006). We will test this aspect of the simulation against observation in more detail in the next chapter.

3.8.4 How do BHs shape the galaxy mass function?

We began this chapter by stressing the role that AGN feedback plays in shaping the properties of galaxies. In semi-analytic models, the key to reproducing the observed dependence of the stellar mass fraction on halo mass is the link between effective AGN feedback and the halo cooling time. This results in the full impact of AGN accretion only being felt in haloes more massive than $\sim 10^{12}\mathrm{M}_{\odot}$. We have shown that the angular momentum dependent BH accretion model used in this chapter has a similar overall impact, limiting BH self regulation to the most massive haloes in the simulation.

In the simulations, the break in the stellar mass fraction – halo mass relation (Fig. 3.4) is created as BH accretion becomes the dominant regulation mechanism in the halo. At a halo mass of $\sim 10^{12}\mathrm{M}_{\odot}$, the mass of the BH quickly increases to fall onto the self-regulation regime and the injection of accretion energy into the halo suppresses the cooling of further material onto the central galaxy. But what determines the change in the behaviour of BHs at this mass? Comparing the BH accretion versus local ISM pressure diagram (Fig. 3.10) suggests that the decline in pressure of material around a lower redshift BH plays an important role in causing the decline of AGN accretion at low redshift. A plausible interpretation is that the BHs which fail to grow large enough during the high pressure era (around $z \sim 2$) are unable to catch on to the self-regulated regime at lower redshifts. But such a microscopic explanation does not provide an easy explanation for the halo mass scale of the mass function break.

Indeed, this scenario would suggest that BH self-regulation would play an important role in lower mass galaxies at higher redshift, an effect that it is not seen in the simulation. Moreover, we still have to explain the halo mass scale at which AGN start to self regulate. It is notable that the transition in BH behaviour

occurs at a halo mass that corresponds to the transition from the rapid cooling of inflowing gas, generating cold streams to more diffuse, longer timescale of accretion due to cooling instabilities in the surrounding gas (White & Frenk, 1991; Kereš et al., 2005; Dekel & Birnboim, 2006; Van de Voort et al., 2010).

As can be seen from the section 3.6, the mass at which self-regulation occurs is weakly sensitive to variations in the accretion disc structure parameter, $C_{\rm visc}$, strongly suggesting that the halo mass, its cooling time, or the structure of the surrounding inflow play a key role in creating the transition. However, the precise nature of the interaction is much harder to tease out of the simulation. Several possibilities spring to mind:

1. a transition in the angular momentum of the material falling onto the central object could create greater angular momentum in the discs formed in lower mass haloes. Such a transition could be driven by the change from rapid cooling (with accretion occurring through misaligned streams) to more spherical accretion through the surrounding hot gas halo. In the spherical case, the angular momentum of the inflow would be shared with the full mass of the halo, while in the first case, the densest material would accrete directly without sharing its angular momentum (and thus without smoothing it over the accretion history of the halo). Examining the variation of V_ϕ with halo mass and redshift does not reveal a clear trend, however.

2. a transition in the merger rate. Efficient accretion is likely to be driven by mergers of stellar clumps that disrupt the angular momentum of the gas disc. While it is not immediately evident why this should be dependent on the halo mass (since the halo merger rate is not strongly dependent on halo mass), the strongly non-linear dependence of the stellar mass fraction on halo mass provides a possible explanation. This has the result that mergers between comparable mass galaxies are much more common in haloes above the critical mass than below it. While this may be part of the story, it is still surprising that the transition to the self regulated regime is so sharp and

ubiquitous. Detailed examination of the BH accretion events below $z = 1$ in Fig. 3.8, does not show a strong correspondence between major mergers and the frequent outbursts that seem to distinguish the self-regulated regime from the widely separated outbursts that occur earlier in the BH's history.

3. a transition in the impact of the gas heated by the BH feedback. In low mass haloes does the material simply leave the system without redistributing its energy effectively, while the energy is trapped within higher mass haloes? In Fig. 3.9, we can clearly identify expanding shells of material in the massive haloes; however, when we trace the final location of particles as a function of halo mass (relative to the halo virial radius), no clear trend is evident. It is hard to push the analysis further because of the very different geometries and cooling times of these haloes.

4. the ability of the halo to recover after an AGN feedback event. In lower mass haloes, the cooling time of inflowing material is short, and its finger-like geometry tends to limit the effect of a feedback outburst. Examination of individual events suggests that, in lower mass haloes, the outburst only affects the material in the galaxy briefly, and that the system is quickly refuelled by accretion from the surrounding cold streams. Accretion in larger haloes is more fragile, since the cooling time is long and the cool streams evaporate before reaching the central object: once the streams are disrupted by an AGN outburst, they struggle to re-establish themselves. While some cool material continues to accumulate at the centre of the halo, this appears to primarily accumulate from cold gas stripped from satellite galaxies.

We speculate that the last mechanism appears to provide the best explanation. Qualitatively, the connection with halo mass appears evident in the images shown in Fig 3.9, and in the linked animation (see footnote 4). During the early universe, the haloes are able to recover quickly due to the strong filamentary nature of their accretion. This effect does not appear sufficient on its own, because if this

was the case, then BS09's accretion model would be able to reproduce the stellar mass fraction in haloes. The angular momentum model plays an important role in the determining the frequency of energy input. In the angular momentum model, accretion events are interspersed with quiescent periods during which the stellar component of the galaxy grows strongly as shown in Fig 3.8. The balance of these periods depends on the gas density needed around the BH in order to trigger efficient accretion, and hence on the parameterisation of the sub-grid accretion model. The history of each individual BH is, however, complex and all of the mechanisms may contribute at some level. The net effect is similar, but not identical, to the mechanisms invoked by semi-analytic models (Bower et al., 2006; Croton et al., 2006), but significantly more work is required to explore the similarities and differences in more detail.

Finally, we note that the halo mass scale at which AGN feedback becomes effective is insensitive to variations in $C_{\rm visc}$ (see section 3.6). The sharpness of the turnover of the stellar mass fraction shows a much stronger variation with $C_{\rm visc}$ however. As a result, it is difficult understand this dependency from first principles, the effect allows us to adjust the location of the break in the stellar mass function by varying $C_{\rm visc}$. However, since $C_{\rm visc}$ enters in the equations to the power of $1/3$, relatively large variations in $C_{\rm visc}$ have quite modest effect on the stellar mass function.

Acknowledgements

The author would like to thank to James Mullaney, Nicolas Tejos, James Aird and Rob Thacker for a careful reading of the paper that this chapter is based on, useful comments and discussions. This work would have not be possible without Lydia Heck's technical support.

Chapter 4

Evolution of the BH scaling relations

4.1 Introduction

The relation between mass of the supermassive black holes and the properties of the host galaxies is now well established in the local Universe for massive galaxies. Such relations have been interpreted as a consequence of the coeval growth history of the central massive BHs and their host galaxies. However, the details of the underlying physical processes that lead to such relations is still an open question.

A wide variety of theorical studies have explained that the growth of BHs is likely to be self-regulated. Such self-regulated BH growth is given via AGN feedback that quenches star formation and gas accretion onto the BH. A key prediction of this scenario is the relation between central black hole mass and bulge stellar mass (Silk & Rees, 1998; Sijacki et al., 2007; Booth & Schaye, 2010). Alternatively, recent studies have emphasized that it may be possible to reproduce the BH scaling relations without the need of self-regulation via AGN feedback, either as a natural consequence of common merger history or in a BH growth scenario (Angles-Alcazar et al., 2013) via gravitational torques (Debuhr, Quataert & Ma, 2011).

The studies above show that the origin of the BH scaling relations is still in debate. The evolution of the relations between the mass of the BH and the properties of its host halo are essential to constrain or provide clues concerning the physical processes that drive the BH scaling relations. Nevertheless, dynamical

measurements of the BH mass are not feasible at high redshift, the promising alternative is through widths of low ionization lines that are associated with the broad line region close to the BHs by assuming virial equilibrium. Another challenge is to determine the galaxy masses for these objects as the BH outshines the galaxy by a large factor. Since AGNs are biased towards most massive BHs, selection effects also need to be taken into account.

The BH scaling relations have also been studied using numerical simulations and semi-analytics models. In particular the Booth & Schaye (2010) model presents self-consistent hydrodynamical simulations. They find evolution of the ratio of BH mass to bulge mass which depends on redshift as $(z+1)^{0.5}$. Di Matteo et al. (2008) also performed numerical simulations up to $z = 1$ and they find a similar evolution. In this chapter, we will investigate the evolution of the BH scaling relation relation by using cosmological simulations

An improved BH accretion model that accounts for AM and implemented as subgrid model in cosmological simulations was discussed in Chapter 3. This BH accretion model is able to reproduce the peak in the stellar mass fraction as a function of halo mass. The resulting BH accretion rates were generally low in low mass halos ($\lesssim 10^{12}\mathrm{M}_{\odot}$) while the BH accretion rates occur continuously in massive haloes. Driven by mergers, massive BHs present outbursts (episodes of mass accretion rates limited by Eddington), resembling quasars.

Although the improved BH accretion model shows compelling results in the growth of BHs, the BH population in the numerical simulations used in Chapter 3 are limited by the box size of the simulation. To study the complete BH and galaxy population, numerical simulations of a larger cosmological region are required.

In this chapter, a variant of the BH accretion model is applied as a subgrid model in a larger cosmological simulation (boxsize $= 100\mathrm{Mpc}$) that provides a more representative BH and galaxy population. This simulation is part of a suite of cosmological simulations that were run using a state-of-the-art galaxy formation subgrid model for radiative cooling, and mass loss, energy feedback from star formation, star formation and stellar evolution. Additionally, AGN feedback and

BH growth are included that are similar in spirit to those described in Chapter 3. The galaxy formation subgrid models were calibrated to match the galaxy stellar mass function at $z = 0$ along with the constraint that galaxy sizes should be reasonable. In particular, the BH accretion model and AGN feedback were calibrated to match the break in the galaxy stellar mass function and the efficiency of AGN was calibrated to match the normalization of the BH mass-stellar relation at $z = 0$.

This chapter is organised as follows. We will describe the simulation used and emphasize the difference to the simulations used in the previous chapter in section 4.2. In section 4.3, we show the resulting galaxy stellar mass function that the galaxy formation models were calibrated. In section 4.4, we show the prediction of the BH mass function and its evolution. Next, we show the results of the BH scaling relations at $z = 0$ such as BH mass- stellar mass relation, the BH mass-Halo mass relation and BH mass and stellar velocity dispersion relation at $z = 0$ in sections 4.5, 4.6 and 4.7, respectively. In sections 4.8 and 4.10 we present predictions in the evolution of the BH mass-stellar mass and BH mass -halo mass from $z = 0$ to $z = 6$. In section 4.11, we will investigate the connection between the BH growth and the binding energy of the halo by looking at the properties of the gas in the inner region of the halo. Finally, in the last section we will summarize our results.

4.2 Simulation Details

In this chapter, we will mainly analyse a large size cosmological simulation $(100Mpc)^3$, with an initial particle number 2×1504^3. Table 4.1 gives an overview of the simulations here and the next chapter. We have adopted a Λ CDM model with parameters chosen according to the Planck collaboration data (Planck collaboration et al., 2013) with $\Omega_{\rm m} = 0.307$, $\Omega_{\rm b} = 0.04825$, $\Omega_\Lambda = 0.693$ and $h = 0.6777$. The initial power spectrum follows $n_s = 0.9611$ and is normalised $\sigma_8 = 0.8288$ and the primordial abundance of helium is $Y = 0.248$.

Table 4.1: A list of the simulations used in this chapter. The columns show: 1) Name of the simulation; 2) Boxsize in units of comoving length; 3) Initial number of particles, 4) Initial mass of dark matter particles ($m_{\rm DM}$); 5) initial mass of gas particles (m_g); (6) Comoving softening length ($\epsilon_{\rm com}$) and 7) maximum proper softerning length ($\epsilon_{\rm prop}$).

Name	size Mpc	Initial number	$m_{\rm DM}$ $\rm M_\odot$	m_g $\rm M_\odot$	$\epsilon_{\rm com}$ co kpc	$\epsilon_{\rm prop}$ kpc
L100N1504	100	1504^3	9.70×10^6	1.81×10^6	2.66	0.70
L050N0752	50	752^3	9.70×10^6	1.81×10^6	2.66	0.70

Our simulations are based on the parallel cosmological TreePM-SPH code P-GADGET3 (Springel, 2005) whose main features have been summarised in Chapter 2. Some improvements have been done in the SPH calculations such as pressure-entropy formulation derived by Hopkins et al. (2013), artificial viscosity switch by Cullen & Dehnen (2010) and artificial conduction switch similar to Price et al. (2008). We are using a C2 kernel with 58 neighbours. Initial conditions were generated using second-order lagrangian perturbations (Jenkins, 2010) at a starting redshift of 127 to $z = 0$.

The simulations used here and next chapter differ from those used in Chapter 3 in the calibration and the use of different subgrid models and Cosmology model (switch to Planck as we described above). In this chapter, the efficiency of the SN feedback model (Crain et al. 2014 in preparation) depends on the metallicity and density of the gas as

$$f_{\rm th} = f_{\rm th,min} + \frac{f_{\rm th,max} - f_{\rm th,min}}{1 + (\frac{Z}{Z_\odot})^{n_Z} (\frac{n_{\rm H,birth}}{n_{\rm H,0}})^{-n_n}}. \tag{4.1}$$

where $n_{\rm H,birth}$ is the density of its parent gas particle at the time it was converted into a stellar particle and n_Z, n_n and $n_{\rm H,0}$ are parameters which were calibrated in the simulation to obtain the best match of the galaxy formation model.

The main keys of the subgrid physics in the simulations used here, have been reviewed in Chapter 2 and we refer the reader to Schaye et al. (2014), Crain et al.(2014) and Furlong et al. (2014) in preparation for further details. In particular, the BH accretion model and AGN feedback are similar to the BH model described

in Chapter 3. They differ from that model in the recalibration of some parameters and modifications of the AGN feedback implementation in order to be consistent with the pressure-entropy formulation of SPH. The BH seed mass is set to $10^5\,h^{-1}\mathrm{M}_\odot$, and the viscous parameter $C_{\rm visc}$ (see 3.15) takes the value of 2π and $2\pi \times 10^2$ respectively for the $100\mathrm{Mpc}$ and $50\mathrm{Mpc}$ simulations. The boost factor α in eq. 3.1, which compensates the inability of resolving the Bondi accretion ,is set to 1 and is equivalent to set $\beta = 0$ in eq. 3.2, turning down the dependency on the density ratio. In the AGN feedback model, the recalibrated parameter is the fixed temperature increase to $\Delta T_{\rm AGN} = 10^{8.5}\mathrm{K}$.

The first BH that appears in the 100-Mpc simulation is at $z = 14.5$, the most massive BH has a mass of $4.1 \times 10^9\mathrm{M}_\odot$ and the most massive halo has a mass of $6.4 \times 10^{14}\mathrm{M}_\odot$ at $z = 0$. The total number of BHs at $z = 0$ is 241310 which 18 have masses $> 10^9\mathrm{M}_\odot$, 525 have masses $> 10^8\mathrm{M}_\odot$ and 2006 have masses $> 10^7\mathrm{M}_\odot$. A large fraction of the BHs have masses slightly above the seed mass (the initial mass of the BH when they are injected into halos). These BHs have probably grown by small mergers or sporadic accretion events, but they have not accreted more mass than the seed mass.

4.3 The galaxy stellar mass function

Fig 4.1 shows the galaxy stellar mass function (GSMF) at $z = 0$ for the simulation L100N1504. The galaxy mass considered here is the mass within a 30-kpc-aperture in each subfind halo. The vertical line corresponds to the mass of 100 baryonic particles. Below this mass, the GSMF is affected by resolution. Simulation results (blue solid line) are compared with observational data from Li & White (2009) (SDSS; black stars) and Baldry et al. (2012) (GAMA survey; black circles). The GSMF is in excellent agreement with observations over the complete stellar mass range that the simulation can resolved, with small discrepancies that are not larger than ~ 0.3 dex. The break of the simulated GSMF ($M_{\rm star} \sim 10^{10.8}\mathrm{M}_\odot$) is slightly underestimated by up to 0.2 dex whereas the faint end of the GSMF

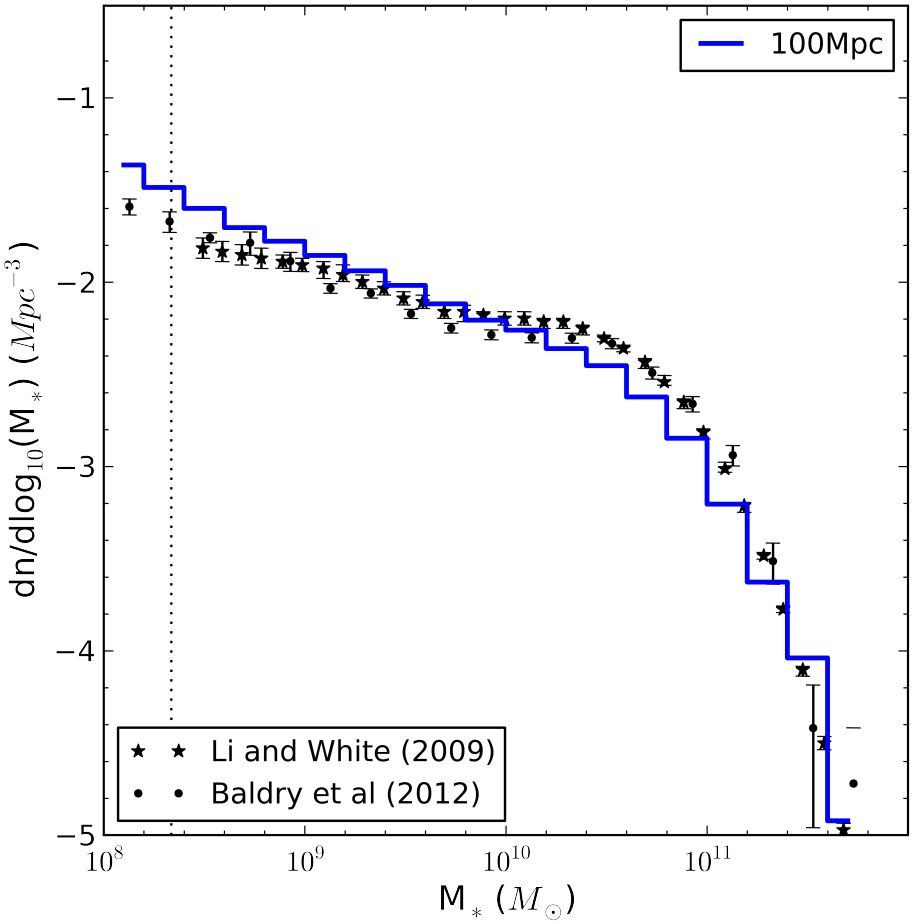

Figure 4.1: The predicted galaxy stellar mass function (GSMF) in the simulation $L100N1504$(blue solid line) compared to the observational GSMF by Li & White (2009) (black stars) and Baldry et al. (2012) (black circles). The vertical line corresponds to galaxies with mass equivalent to 100 m_g and below this mass, the GSMF is affected by resolution. The galaxy mass is the mass contained in 30kpc-aperture of each subfind halo. The predicted GSMF is in excellent agreement with observational data. Small discrepancies are shown at the break of the GSMF, becoming up to 0.2dex. The galaxy formation modules were calibrated to obtain this remarkable agreement, in particular the SN and AGN feedback are responsable to regulate the star formation in halos. Courtesy of Michelle Furlong.

($M_{\rm star} \sim 10^{8.5}{\rm M}_{\odot}$) is overproduced by 0.2 dex.

Note that the good agreement seen in the GSMF was obtained by calibrating the galaxy formation subgrid models; then it can not be considered as a prediction of the simulation. However, so far it is the first cosmological simulation to reach this level of agreement in the GSMF. The critical subgrid models that were calibrated to reproduce the GSMF were the SN and AGN feedback. Both processes are responsible for the regulation of the star formation by injecting energy into the ISM. In particular, BH accretion and AGN feedback are critical in reproducing the break in the stellar mass function. In our subgrid model, the viscous parameter $C_{\rm visc}$ (see 3.15) is calibrated .

4.4 BH Mass Function

The BH mass function, which is defined as the space density distribution of BH masses for a given time, is a useful tool to study the connection between BHs and galaxies. Attempting to measure the BH mass function observationally is not a straightforward process because of the large uncertainty in the determination of reliable estimates in mass and the inability to have BH mass over a wide range of masses (Kelly & Shen, 2013). As a result, many studies have inferred the BH mass function by employing the correlations between BHs and the properties of their host galaxy bulge and luminosity. The observational estimate of the BH mass function implicitly assumes a connection in the growth of BHs and galaxies.

In the case of cosmological simulations, in some way, there is an underlying physical connection between BHs and galaxies. In the sense that AGN feedback (and BH growth) is effective to quench star formation in the most massive galaxies, and then reproduce the knee in the galaxy stellar mass function at $z = 0$ (see Fig. 4.1; blue line). We will see below that $M_{\rm BH}$-$M_{\rm star}$ relation at $z = 0$ is in reasonable agreement with observations (see Fig 4.4). Therefore, we expect that both observational and predicted BH mass function have some level of agreement. However, we stress that the AGN feedback and BH accretion models were not

calibrated to match the BH mass function.

Fig 4.2 shows the predicted BH mass function at $z = 0$. The vertical dashed line indicates the initial mass of a gas particle in the simulation before it is converted into a BH. Below this mass, the BH mass function is affected by the value of the seed mass. The predicted BH mass function (blue solid line) is compared to the estimates found by Marconi et al. (2004) (grey circles) and Shankar et al. (2004) (grey squares). The predicted BH mass function is in excellent agreement with observational estimates over a wide mass range, particularly for BHs with masses $> 10^6 \mathrm{M}_\odot$ and discrepancies are not larger than 0.4 dex. The predicted BH mass function is slightly underestimated in the mass range $10^{6.5-7.4}\mathrm{M}_\odot$ in comparison with observations. However, observations show discrepancies between them by a factor 0.2 dex. So, this is the level of agreement we can obtain. The BH mass function continues to rise to the BH seed mass ($10^5\mathrm{M}_\odot$), but observations below $10^6\mathrm{M}_\odot$ are not available and the simulated BH mass function is affected by the resolution of the simulation.

Interestingly, the shape of the BH mass function resembles the shape of the galaxy mass function in the simulation as shown in Fig 4.1. The break in the BH mass function occurs at a critical BH mass ($M_{\mathrm{BH}} \sim 10^8\mathrm{M}_\odot$). The median of BHs near to the break are hosted by galaxies with $M_{\mathrm{star}} \sim 10^{10.5-11}\mathrm{M}_\odot$ as shown in Fig. 4.4, suggesting the existence of a BH mass scale where AGN feedback has effects on the host galaxy. The reason that this BH mass exists is partly because of the fact that the efficiency of AGN feedback sets the BH mass as a result of self-regulated growth (Booth & Schaye, 2010) for the most massive objects (see also Chapter 3) and partly, because it appears from the hydrodynamics of our model.

Turning towards higher redshifts, Fig 4.3 shows the predicted BH mass function for redshifts up to $z = 6$. Colour represents redshifts as indicated in the legend. The BH mass function rapidly evolves over the complete mass ranges that the simulation can resolve ($> 10^6\mathrm{M}_\odot$) up to $z = 3$ (green color). After that, the BH mass function continues to evolve less rapidly in normalization by 0.4 dex up to $z = 1$. At $z < 1$, the intermediate BH masses have been formed

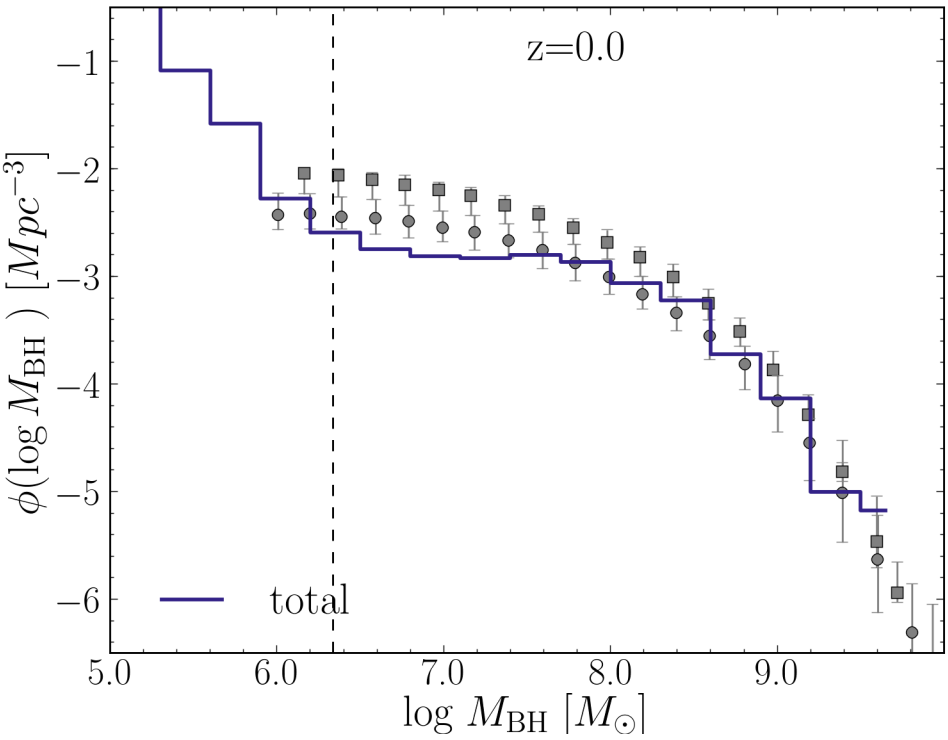

Figure 4.2: The predicted BHMF in the simulation (blue solid line) at $z = 0$ is compared to the observational estimates by Marconi et al. (2004) (grey-circles) and Shankar et al. (2004)(grey squares). The vertical dashed line corresponds to the initial mass of the gas particle before a gas particle is converted into a BH. The errors bars correspond to 1σ uncertainties. The predicted BHMF agrees very well with the observational estimates. Small discrepancies appear in the low mass end ($< 10^{7.4}\mathrm{M}_\odot$) where there are discrepancies between observations as well, becoming up to 0.2 dex. The good match in the BHMF is a direct consequence of the good agreement of the GSMF and the BH mass-stellar mass relation with observations.

($M_{\rm BH} \sim 10^{7.2-8.2}\mathrm{M}_\odot$). The faint end of the BH mass function ($M_{\rm BH} < 10^{7.2}\mathrm{M}_\odot$) shows a small increase of 0.4 dex while the high mass end evolves, presenting a shallower slope and higher normalization by up to ~ 1.0 dex at $z = 0$.

This is consistent with the evolution seen in Figs 4.7 and 4.10 in the following sections where the $M_{\rm star}$-$M_{\rm BH}$ and M_{200}-$M_{\rm BH}$ relations hardly show evolution at $z < 2$ and are consistent with the peak in both the global star formation rate and the global activity of the density of quasars that observational studies have shown Madau et al. (1996); Boyle & Terlevich (1998).

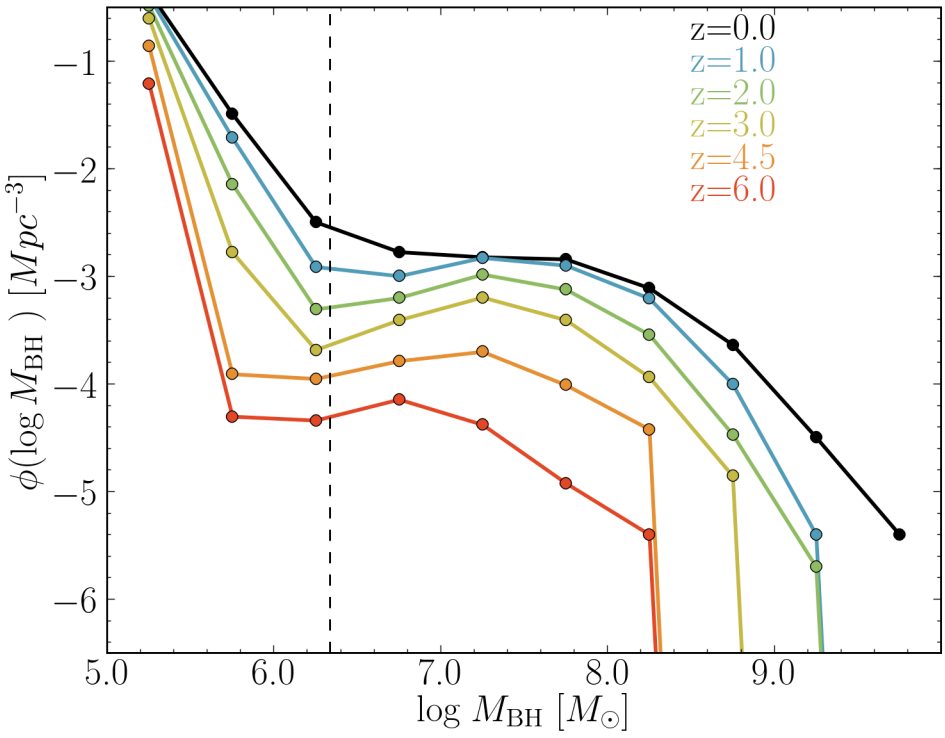

Figure 4.3: Evolution of the BH mass function from $z = 0$ to $z = 6$ as solid lines. Colours represent different redshifts as shown in the plot. The BH mass function shows a rapid evolution in normalization over the whole mass range from $z = 6$ to $z = 3$. After that, the BH mass function steadily grows in normalization up to $z = 1$ where the evolution is not significant apart from the evolution in the slope of high mass end which is shallower at $z = 0$.

The predicted BH mass density at $z = 0$ in the simulation is $2.8 \times 10^5 \mathrm{M}_\odot Mpc^{-3}$ and lies marginally below the range of estimates of the local mass density of SMBHs obtained by Marconi et al. (2004) and Shankar et al. (2009) ($\rho_{BH} = 4.3^{+1.8}_{-1.3} - 3.9 \pm 1.0 \times 10^5 \mathrm{M}_\odot Mpc^{-3}$ assuming h=0.6777). These authors estimate the density by integrating the BH mass function and assuming the correlations between BH mass to bulge, luminosity or stellar velocity dispersion to galaxy luminosity and velocity functions. Similarly, a high value of $\rho_{BH} = 4.5^{+1.17}_{-0.92} \times 10^5 \mathrm{M}_\odot \mathrm{Mpc}^{-3}$ (h=0.6777) is found by Hopkins et al. (2007) who determined the local BH mass density by applying the Soltan argument to the Bolometric luminosity functions. Soltan (1982) showed that the total mass density built up by gas accretion onto BHs can

be deduced by integrating the bolometric luminosities of QSOs through time and converted into mass via a mass to radiation conversion efficiency. Interestingly, the density obtained will be independent of H_0 and the quasar lifetime. Using Soltan argument, Aird et al. (2010) obtained a closer value of the predicted density ($\rho = 2.2 \times 10^5 \mathrm{M}_\odot Mpc^{-3}$) but using only the hard X-ray luminosity function. Yu & Tremaine (2002) also found a similar value to our simulation ($2.5 \times 10^5 \mathrm{M}_\odot Mpc^{-3}$) by estimating the local BH density based on velocity dispersion of early-types galaxies in the Sloan Digital Survey (SDSS). In summary, the simulation predicts a density similar to the values found in observations.

4.5 The BH mass-stellar mass relation

Fig 4.4 shows the central BH mass-stellar mass relation at $z = 0$ for the simulation L100N1504. In Fig 4.4, M_{star} corresponds to the stellar mass contained in a 30-kpc-aperture and M_{BH} to the central massive BH in such aperture for each subfind halo. We choose a 30-kpc-aperture in order to be consistent with the stellar masses plotted in the GSMF and from the aperture obtained in observations for a galaxy. The simulated M_{BH}-M_{star} relation is compared to the set of observations compiled by McConnell & Ma (2012) which includes improved observations of the Haring & Rix (2004) set. In these observations, the central BH mass is inferred by the dynamical motions of the nuclear gas, stars or massers from nearby galaxies and the stellar mass corresponds to that of the bulge in contrast to the simulation in which the stellar mass corresponds to that in 30-kpc-aperture. The simulated M_{BH}-M_{star} relation fits very well with observational data for galaxies with $M_{\mathrm{star}} > 10^{10.8}\mathrm{M}_\odot$ except in some points. This is partly because we plot M_{star} in 30 kpc aperture and partly because, most of the galaxies in observations are classified as early-type galaxies whose dominant component is the bulge apart from few points. Therefore, for the most massive galaxies where B/T becomes $> 50\%$ our comparison could become fair at 50% or more (ie. 0.3 dex). This good match in the M_{star}-M_{BH} relation for massive galaxies is a result of the self-

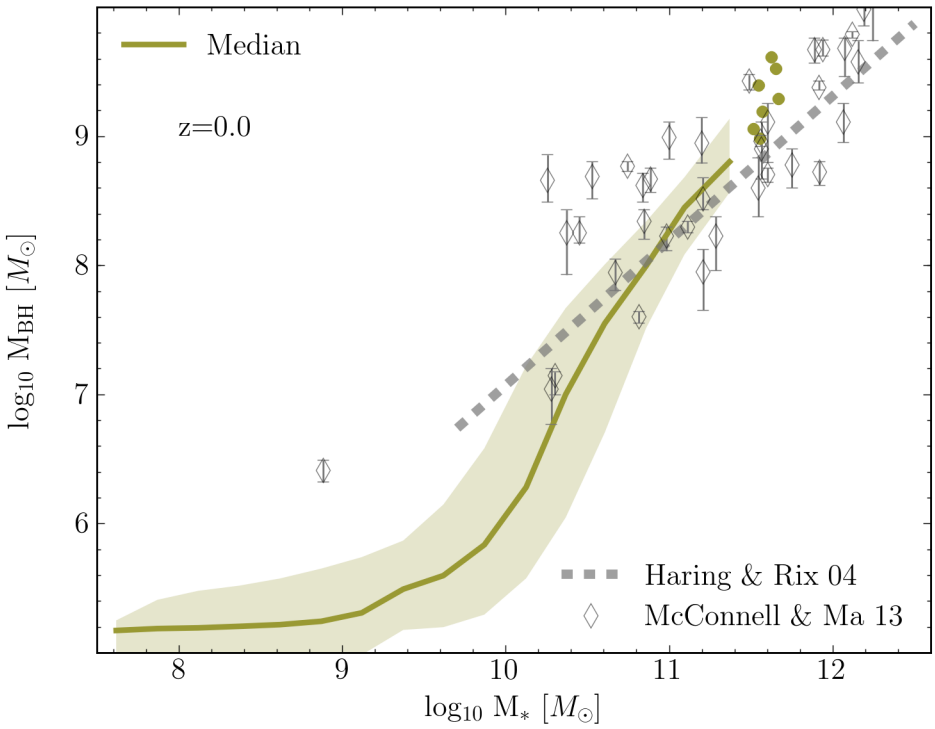

Figure 4.4: $M_{\rm star}$-$M_{\rm BH}$ relation at $z = 0$ for the simulation L100N1504, where $M_{\rm star}$ corresponds to the stellar mass contained in 30-kpc-aperture and $M_{\rm BH}$ corresponds to the central BH mass within this aperture. Solid lines represent the median of the relation and the shaded region represents the 10^{th} and 90^{th} percentiles of the distribution. Each bin contains more than 10 objects and filled circles represent the actual objects in bins with less than 10 objects. Diamonds correspond to observations of the bulge mass and BH mass from McConnell & Ma (2012) and the error bars indicate $1-\sigma$ errors. The dashed line corresponds to the fit obtained by Haring & Rix (2004). The simulated relation is in reasonable agreement with observational points for galaxies with $M_{\rm star} > 10^{10.2}{\rm M}_{\odot}$, where a large fraction of the mass corresponds to the bulge component. Below this $M_{\rm star}$, the simulation predicts a steep decline as decreases stellar mass.

regulated growth of BHs. As Booth & Schaye (2010) have found, the efficiency of AGN feedback sets the final BH mass.

For $M_{\rm star} < 10^{10.8}{\rm M}_{\odot}$, the simulated $M_{\rm BH}$-$M_{\rm star}$ relation increases steeply as the stellar mass increases, which presents a break in the slope in the $M_{\rm BH}$-$M_{\rm star}$ relation. However this part of the $M_{\rm star}$-$M_{\rm BH}$ relation is affected by the BH seed mass injected into halos. The break in the slope would be sharper with smaller BH seeds mass ($10^4{\rm M}_{\odot}$) since a galaxy with a given stellar mass $< 10^8{\rm M}_{\odot}$ would inhabit a less massive BH while the relation would remain constant for the most massive galaxies.

4.6 The BH mass-halo mass relation

Fig 4.5 shows the median M_{200}-$M_{\rm BH}$ relation at $z = 0$ where M_{200} corresponds to the total mass enclosed within r_{200} which is the radius at which the density of the halo is 200 times the critical density of the Universe. $M_{\rm BH}$ is the central massive BH. The simulated M_{200}-$M_{\rm BH}$ relation is compared to the inferred relation from Bandara et al. (2009) (diamonds) which by parameterizing a lens model, determined the gravitational mass of a set of galaxy-scale strong gravitational lenses from the Sloan Lens ACS Surveys (SLACS) and by inferring $M_{\rm BH}$ with the σ_*-$M_{\rm BH}$ relation from Haring & Rix (2004).

The simulated M_{200}-$M_{\rm BH}$ relation is apparently lower than the estimates from Bandara et al. (2009). The discrepancy is not as large as 0.3 dex. However, observation should be interpreted with caution since M_{200} and $M_{\rm BH}$ are inferred quantities and are not direct observable. Additionally, observations lie in a narrow range of M_{200} ($\sim 10^{12.9-13.5}{\rm M}_{\odot}$) while the halo mass range in the simulation spans by 4 orders of magnitude.

Similar to the $M_{\rm BH}$-$M_{\rm star}$ relation, the $M_{\rm BH}$-M_{200} is shaped by the self-regulated growth of the BHs and therefore, the normalization of the relation is set by the efficiency of AGN. The $M_{\rm BH}$-M_{200} relation is tight for the most massive haloes with a scatter of ~ 0.6 dex. This is consistent with results found by Booth & Schaye

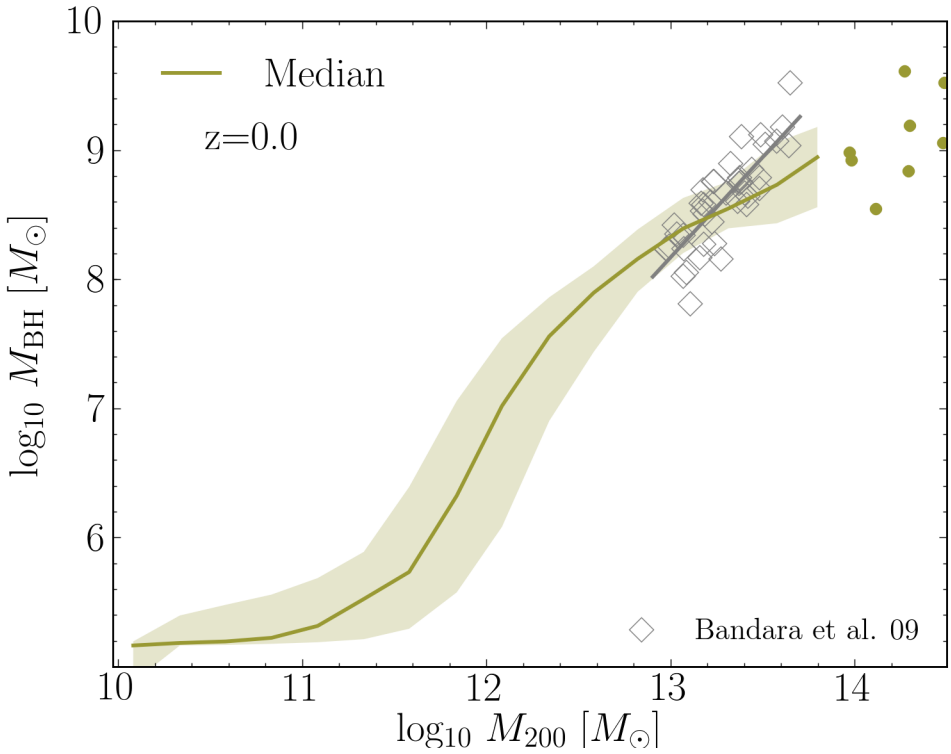

Figure 4.5: The median $M_{\rm BH}$-M_{200} relation at $z = 0$ for the simulation L100N1540 where $M_{\rm BH}$ is the central BH mass and M_{200} is the enclosed mass within r_{200}. The simulated $M_{\rm BH}$-M_{200} relation is compared to observational estimates from Bandara et al. (2009) that based on a biased sample of strong gravitational lenses infer M_{200} ($10^{12.9-13.7}{\rm M}_\odot$) while $M_{\rm BH}$ is inferred by $M_{\rm BH}$-σ relation (Haring & Rix, 2004). The simulated $M_{\rm BH}$-M_{200} relation is tight and shallower than observational data . Because of the self regulated growth of the BHs, the $M_{\rm BH}$-M_{200} relation is tight for halos above $10^{12}{\rm M}_\odot$ where its normalization is set by the efficiency of AGN feedback. For haloes below $M_{200} < 10^{12.3}{\rm M}_\odot$, $M_{\rm BH}$-M_{200}-relation presents a break indicating that self-regulated BH growth does not apply for such haloes.

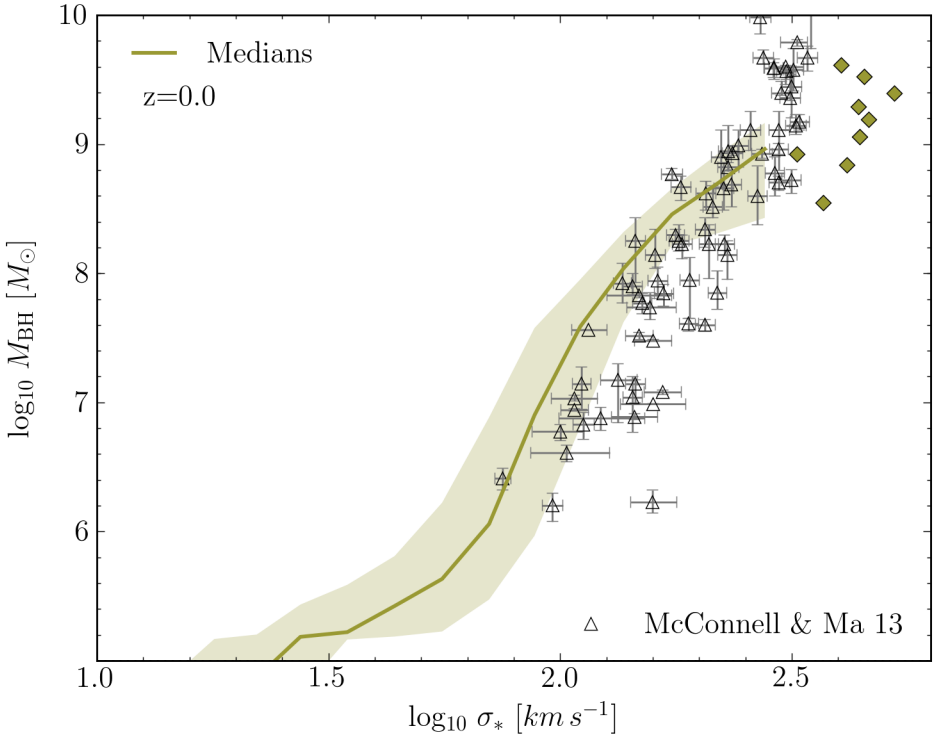

Figure 4.6: $M_{\rm BH}$-σ_* relation $z = 0$ where σ_* is the stellar velocity dispersion in each subhalo. Triangles correspond to observations compiled from McConnell & Ma (2012). The σ_* in observations correspond to bulge and in simulations within the subhalo.

(2010) for massive galaxies. However, the scatter increases as M_{200} decreases, showing that the correlation in low mass haloes is not as tight as the one found in the most massive halos ($M_{200} > 10^{12}{\rm M}_\odot$). This implies that BHs do not self-regulate their growth after a critical halo mass (or stellar mass).

4.7 The BH mass-stellar velocity dispersion relation

Fig 4.6 shows the $M_{\rm BH}$-σ_* relation where σ_* corresponds to the stellar velocity dispersion of the stars within each subfind subhalo and $M_{\rm BH}$ to the central massive BH. For comparison, we include observational data from McConnell & Ma (2012) as grey triangles and $1-\sigma$ errors as error bars. The observational stellar velocity dispersion corresponds to that in the bulge. Note that we compare the total stellar

velocity dispersion in the simulation to the stellar velocity dispersion of the bulge in observations.

The predicted $M_{\rm BH}$-σ_* lies on the region with observations in galaxies with $< 10^{2.0} < \sigma_* < 10^{2.6} kms^{-1}$. In galaxies with larger stellar velocity dispersion ($\sigma_* > 10^{2.6} km\, s^{-1}$), the σ_*-$M_{\rm BH}$ relation present a 'bend' in the simulation while the observational data saturates at 350 km s^{-1}. This discrepancy is caused by the definition of σ_* along observations and the simulation. For instance, the observational stellar velocity dispersion depends on the spatial extent of the kinematic data. To remove the dependency on the spatial extent, usually data within r_{inf} are excluded where r_{inf} corresponds to the influence radius $r_{inf} \equiv GM_{\rm BH}/\sigma_*$. By doing so, σ_* substantially decreases by up to 10-15% (McConnell & Ma, 2012) in the most massive galaxies. This discrepancy reflects that a fairer comparison is required.

To summarise, the three BH-scaling relations at $z = 0$ show reasonable agreements with the observational constraints available throughout the literature. A complete comparison, however, is not possible because a representative BH population is required over the whole range of stellar mass, stellar velocity dispersion and halo mass. We stress that the galaxy formation subgrid models were calibrated to reproduce the GSMF, and not the BH-scaling relations. This good agreement for the massive galaxies is attributed to the fact that BHs regulate their growth in our BH accretion model and AGN feedback that was inherited from the model of Booth & Schaye (2009). As a result, by setting the efficiency of AGN feedback, the BH masses are determined and then the normalization of the BH-scaling relations at $z = 0$ are determined as well.

The immediate question to address is how these BH scaling relations evolve across time and we will describe that in the following section.

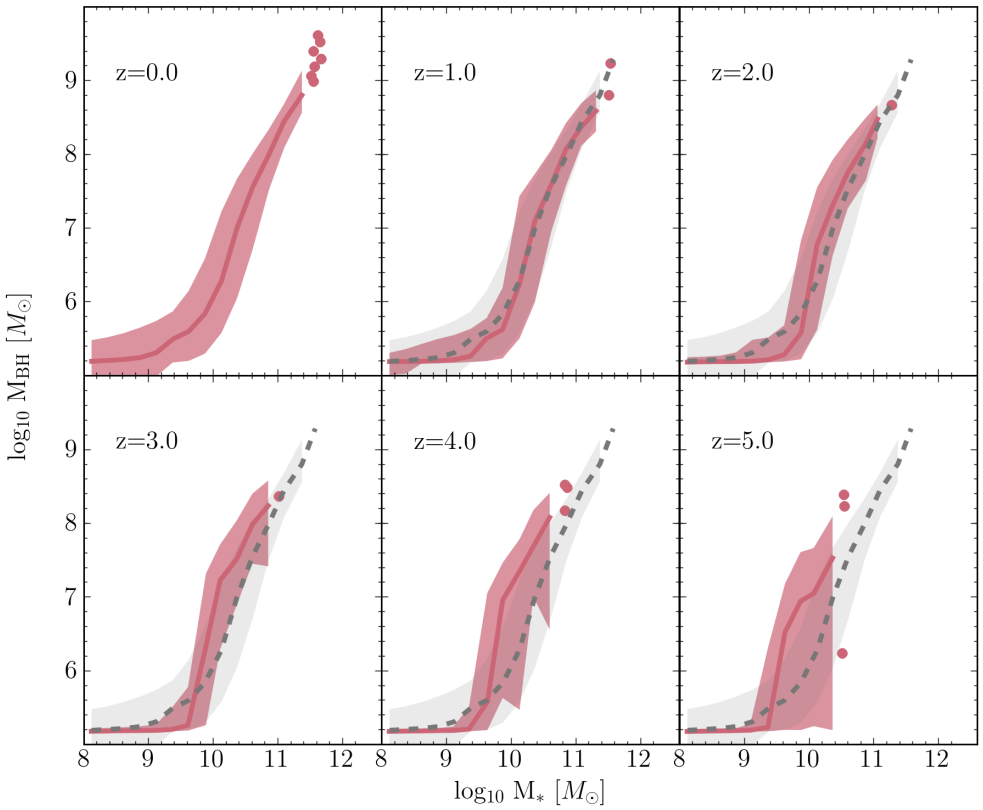

Figure 4.7: $M_{\rm BH}$-$M_{\rm star}$ relation for various redshifts from $z = 0$ to $z = 5$. The pink solid lines represent the median $M_{\rm BH}$-$M_{\rm star}$ relation where $M_{\rm BH}$ is the central BH and the shaded region represents the 10^{th} and 90^{th} percentiles of the distribution. Each $M_{\rm star}$ bin has at least 10 objects. Points represent the actual objects in bins with less than 10. The grey colour represents the $M_{\rm BH}$-$M_{\rm star}$ relation at $z = 0$. The relation does not show significant evolution up to $z < 2$. At high redshift ($3 < z < 5$), a break in the $M_{\rm BH}$-$M_{\rm star}$ relation is more prominent and shifts to lower mass, the normalization of the median relation becomes slightly higher by up to 0.5 dex in galaxies with $M_{\rm star} = 10^{9.6-10.6}{\rm M}_{\odot}$.

4.8 Evolution of the BH mass-stellar mass relation

In this section, we turn our attention to the evolution of the relation of $M_{\rm BH}$-$M_{\rm star}$. Fig 4.7 shows the median $M_{\rm BH}$-$M_{\rm star}$ relation (pink solid lines) for different redshifts from $z = 0$ to 5 and the shaded region represents the 10^{th}-90^{th} percentiles of the distribution. By comparison, the grey dashed line represents the median z=0 $M_{\rm BH}$-$M_{\rm star}$ relation discussed above.

The $M_{\rm BH}$-$M_{\rm star}$ relation does not show evolution over the complete mass range up to $z < 2$. After that redshift, the $M_{\rm BH}$-$M_{\rm star}$ relation becomes steeper compared to the $z = 0$ $M_{\rm BH}$-$M_{\rm star}$ relation, indicating that galaxies for a given mass host more massive BHs than galaxies with the same mass at $z = 0$. Something interesting is the break of the relation at $M_{\rm star} > 10^{10}{\rm M}_{\odot}$ at $z = 3$ which becomes more prominent as redshift increases and it moves to lower stellar masses. In terms of the scatter, the $M_{\rm BH}$-$M_{\rm star}$ relation is tight up to $z = 3$ and then it becomes more robust at $z = 5$.

This predicted evolution has some implications about the growth of BHs. As we discussed above, BHs self-regulate their growth. By this, we mean that BHs inject an amount of energy into the ISM which remains the same, even though the efficiency of AGN feedback could change over various orders of magnitude. As a result, BHs adjust their masses and therefore the normalization of the BH scaling relations are changed. The simulation predicts that there is no evolution up to $z < 2$ in the $M_{\rm BH}$-$M_{\rm star}$ relation which implies that BHs are in the self-regulation regime since $z = 2$. If we look at the evolution of the BH mass function at $z = 2$, the shape of the BH population seems to be almost built up (apart from the high mass end of the BH mass function, see Fig 4.3). Both results suggest that BHs are able to self regulate once they have sufficiently grown to affect the gas properties of their host galaxy. This apparently occurs at $z \sim 2$ when both the global SFR and AGN activity peak.

The scenario is different at higher redshift ($z > 2$), the $M_{\rm BH}$-$M_{\rm star}$ relation becomes steeper and presents a break at $M_{\rm star} < 10^{10}{\rm M}_{\odot}$ at $z = 3$, indicating that

BHs undergo a rapid growth (and it is consistent with the strong evolution of BH mass function at higher redshift), and more rapid than the growth of their host galaxies.

In terms of observational evidence of the evolution of the $M_{\rm BH}$-$M_{\rm star}$ relation, there is no clear consensus throughout observational studies. As we discussed in Chapter 1, dynamical measurements of the BH mass are not available at high redshift, the only route for observational studies is to infer BH mass via broad line AGN samples where the BH mass is inferred via the *virial* method. The main problem is to identify the properties of the host galaxy such as the stellar mass. While early studies show a clear trend of positive evolution of $M_{\rm BH}$-$M_{\rm star}$ relation, they preferentially focused on luminous quasars and their hosts, sampling a narrow range of luminosity and stellar mass. More recent studies that use fainter AGN, tend to find mild or no evolution (Jahnke et al., 2009; Merloni et al., 2010; Cisternas, 2011).

More recently, Schulze & Wisotzki (2014) demonstrate that there is no significant statistical evidence for positive evolution in the BH mass-stellar mass relation via a fitting method that account for effects of the sample selection. They apply this method to four observational studies (Merloni et al., 2010; Decarli et al., 2010; Wang et al., 2010; Cisternas, 2011) and they find that with the current data is not possible to differentiate between an evolutionary scenario from that with no evolution of the ratio of $M_{\rm BH}$ to $M_{\rm star}$.

To further explore the (non) evolution of the $M_{\rm BH}$-$M_{\rm star}$ relation, we include Fig 4.8. The figure shows the $M_{\rm BH}$-to-$M_{\rm star}$ ratio as a function of redshift for various galaxy populations. Different colours indicate different $M_{\rm star}$ bins. Fig 4.8 shows that the median of $M_{\rm BH}$-to-$M_{\rm star}$ ratio does not significantly evolve as a function of redshift, on average. For comparison with the scenario of evolution and non evolution, the dotted line represents the evolution predicted by previous numerical simulations for massive galaxies (Booth & Schaye, 2009; Di Matteo et al., 2008). These numerical studies predict that $M_{\rm BH}/M_{\rm star}$ evolves as $(z+1)^{\gamma}$ where $\gamma = 0.5$ and it is in agreement with some observational studies that show

positive evolution in the $M_{\rm BH}$-to$M_{\rm star}$ ratio (Merloni et al., 2010; Decarli et al., 2010) and the typical stellar mass in the samples lies in $10^{10.5-11.5}\mathrm{M}_{\odot}$. The solid horizontal dark line represents the $M_{\rm BH}$-to-$M_{\rm star}$ ratio from Haring & Rix (2004) for the local $M_{\rm BH}$-$M_{\rm star}$ relation as representation of a non evolution scenario. We chose this relation as a conservative constraint for evolution and to be consistent with the previous numerical and observational studies.

The most massive galaxies ($10^{10.9}$ - $10^{11.7}\mathrm{M}_{\odot}$; orange colour) have been formed at $z = 3$. The $M_{\rm BH}$-to-$M_{\rm star}$ ratio decreases by less than 0.1 dex from $z = 3$ to $z = 1$. After that redshift, the deviation from evolution or non evolution scenario is up to 0.3 dex. Massive galaxies present a narrow scatter (~ 0.5 dex at $z = 0$) relative to those in the other galaxy populations as we expected.

For intermediate galaxies ($10^{10.1-10.9}\mathrm{M}_{\odot}$; green colour), the median $M_{\rm BH}$-to-$M_{\rm star}$ ratio presents a decreasing trend with decreasing redshift from -2.6 to -3.4. However, the associated scatter is too large. Contrary, the galaxy population with $10^{9.3-10.1}\mathrm{M}_{\odot}$ (light blue colour) presents a steep decline from -3.6 at $z = 5$ to -4.0 at $z = 4$ and then it remains more or less constant. Note that both galaxy populations (light blue and green colours) are populations below and above the break in the $M_{\rm BH}$-$M_{\rm star}$ relation at high redshift (see bottom panels of Fig 4.7). This corresponds to the redshifts where the $M_{\rm BH}$-$M_{\rm star}$ relation evolves and it is reflected also in the large scatter associated with them. As a result, the relation $M_{\rm BH}$-$M_{\rm star}$ in low mass galaxies is not as tight as that for the massive galaxies. This is expected since the SFR in low massive galaxies is regulated by feedback from star formation and not AGN.

Finally, the small galaxies ($M_{\rm star} = 10^{9.5-10.5}$,dark blue) show no evolution since they only have BHs with mass slightly above the seed mass.

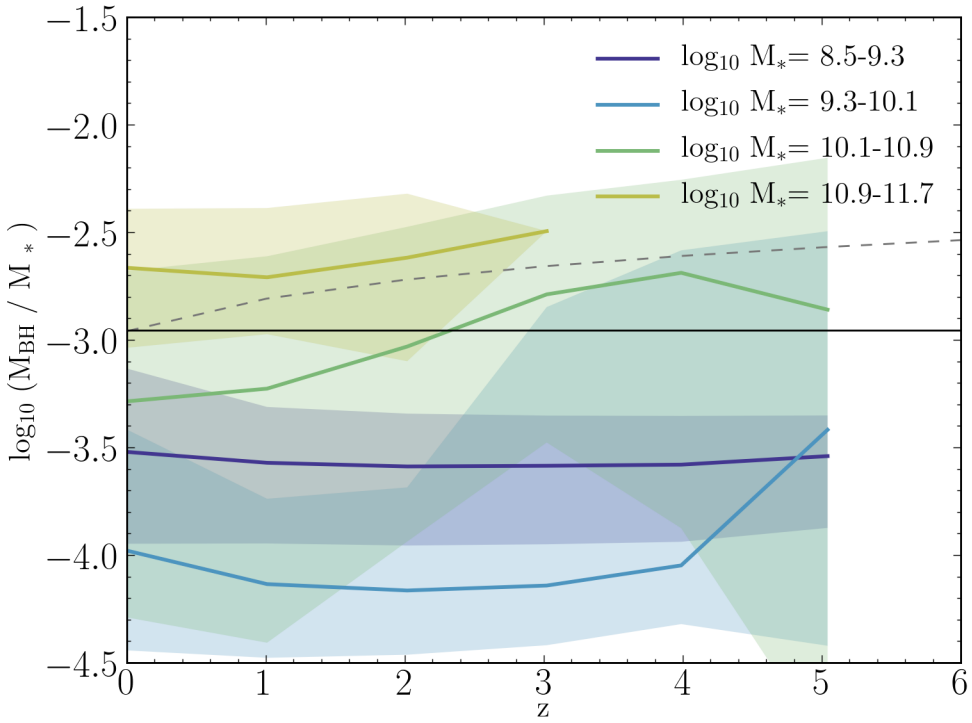

Figure 4.8: $M_{\rm BH}$-to-$M_{\rm star}$ ratio as a function of redshift for various galaxy populations where $M_{\rm BH}$ is the central massive BH and $M_{\rm star}$ corresponds to the stellar mass in a 30-kpc aperture. The coloured solid lines represent the medians and the shaded regions correspond to the 10-90th percentiles. The black solid line represents the $M_{\rm BH}$-to-$M_{\rm star}$ ratio inferred from Haring & Rix (2004) fit at $z = 0$ and the dashed line the evolution of $M_{\rm BH}$-to-$M_{\rm star}$ ($\propto (z+1)^{0.5}$) inferred by Booth & Schaye (2010) and Di Matteo et al. (2008). Both results are consistent with the current observational constraints according to the fit method outlined in Schulze & Wisotzki (2014). The most massive galaxies (yellow lines) in the simulation are in robust agreement with the evolution inferred from previous numerical simulations up to $z = 1$, after that redshift, it slightly increases. The $M_{\rm BH}$-to-$M_{\rm star}$ ratio lies below observational constraints for galaxies below $10^{10.9}{\rm M}_{\odot}$. Apart from the galaxy population in $10^{10.1-10.9}{\rm M}_{\odot}$, there is no significant evolution. For this population ($10^{10.1-10.9}{\rm M}_{\odot}$), a decrease in the $M_{\rm BH}$-to-$M_{\rm star}$ ratio as decreasing redshift is shown.

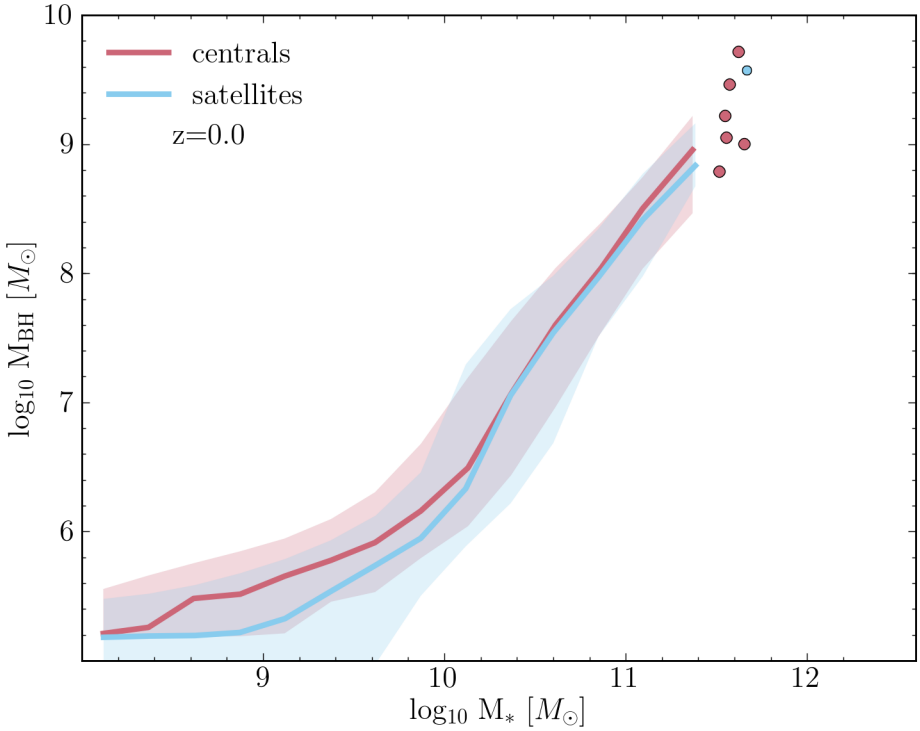

Figure 4.9: The median $M_{\rm BH}$-$M_{\rm star}$ relation for central (pink lines) and satellites galaxies (light blue lines) at $z = 0$. The shaded regions correspond to the 10^{th}-90^{th} percentiles of the distribution. The $M_{\rm BH}$-$M_{\rm star}$ relation is similar for central galaxies and satellites for galaxies with $M_{\rm star} > 10^{10}{\rm M}_{\odot}$ with a discrepancy by less than 0.2 dex. For lower $M_{\rm star}$, satellites tend to host smaller BHs that central galaxies with the same $M_{\rm star}$. BHs become larger in central galaxies by 0.4 dex where satellites galaxies host a BHs close to the seed mass while central galaxies which have grown at least twice their mass.

4.9 The BH mass-stellar mass relation in centrals and satellites

Having discussed the evolution of $M_{\rm star}$-to-$M_{\rm BH}$ ratio, this section shows the evolution of the $M_{\rm BH}$-$M_{\rm star}$ relation when we divided the galaxy population into central galaxies and satellite galaxies at $z = 0$. This allows us to investigate the effect of the environment in the $M_{\rm star}$-$M_{\rm BH}$ ratio as well as gain some insight into the effects of mergers.

Fig 4.9 shows the median of the $M_{\rm BH}$-$M_{\rm star}$ relation at $z = 0$ where $M_{\rm star}$ corresponds to the stellar mass at 30 kpc in aperture and $M_{\rm BH}$ the central massive

BH. Blue line represents the median for satellite galaxies and the red line for central galaxies. The shaded regions represent the 10^{th}-90^{th} percentiles of each distribution.

From the figure, we can see that the median of the $M_{\rm BH}$-$M_{\rm star}$ relation presents similar evolution in both centrals and satellites at $M_{\rm star}$ larger than $10^{10}{\rm M}_{\odot}$. The scatter of the relation does not show any difference between them. Below such stellar mass, the media $M_{\rm BH}$-$M_{\rm star}$ relation declines more rapidly for satellites than centrals indicating that centrals host more massive BHs than satellites with the same mass.

These results are in broad agreement with previous results from dark-matter only simulations. For instance Angulo et al. (2009) find that satellite-central mergers are more likely to occur than satellite-satellite mergers in massive host haloes, leading to a shallower or similar $M_{\rm BH}$-$M_{\rm star}$ relation for centrals in comparison to the relation for satellites.

Our findings differ from those found by McGee (2013) who studied variations in the $M_{\rm BH}$-$M_{\rm star}$ relations due to environment. McGee (2013) investigated the $M_{\rm BH}$-$M_{\rm star}$ relation using several environmental indicators such as number density, group mass and if the galaxy is satellite or central. McGee (2013) found that the $M_{\rm BH}$-$M_{\rm star}$ relation in centrals had a steeper relation than that from satellites for galaxies with $M_{\rm star} > 10^{10}{\rm M}_{\odot}$ in the local universe. McGee (2013) based his study on the early type galaxies from the set of data from McConnell & Ma (2012), However it is possible that a representative population of satellites is not included in the data from McConnell & Ma (2012).

4.10 Evolution of the BH mass-halo mass relation

We turn our attention to the evolution of the relation between the mass of BHs and the mass of the halo.

Fig 4.10 shows the evolution in the $M_{\rm BH}$-M_{200} relation in the simulation for different redshifts from $z = 5$ to $z = 0$. The medians of the $M_{\rm BH}$-M_{200} relation

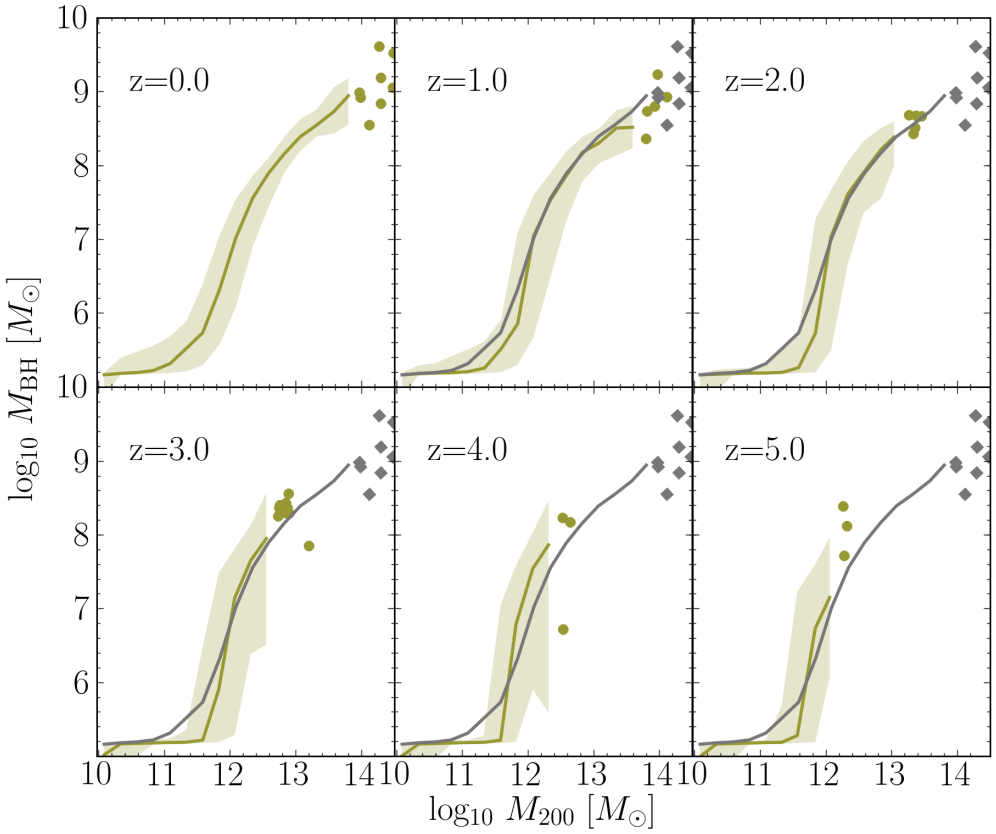

Figure 4.10: M_{200}-$M_{\rm BH}$ relation for various redshifts from $z = 0$ to $z = 5$. The green solid lines represent the median M_{200}-$M_{\rm BH}$ relation. The grey colour represents the M_{200}-$M_{\rm BH}$ relation at $z = 0$. The relation does not show significant evolution at $z < 2$ for halos above $10^{12}{\rm M}_{\odot}$ while it shows a steep rise for halos with $M_{200} \sim 10^{11.5-12}{\rm M}_{\odot}$. Toward high redshifts, the relation shows higher normalisation in halos $> 10^{11.5}$ than at $z = 0$ whereas for halos below this mass, the normalisation is lower than the expected one from $z = 0$. In other words, for a given halo with mass $> 10^{11.5}$ hosts typically, more massive BHs at high redshift than those in halos with similar mass at $z = 0$. In contrast, halos below $10^{11.5}$ host less massive BHs that those halos at $z = 0$.

are shown as green lines and the 10^{th}-90^{th} percentiles as coloured regions. Points represent the actual halos for bins with fewer than ten objects. For comparison, we include the $M_{\rm BH}$-M_{200} relation at $z = 0$ as grey colour in each panel and the objects as diamonds. The $M_{\rm BH}$-M_{200} relation, similar to the $M_{\rm BH}$-$M_{\rm star}$ relation, does not show significant evolution up to $z = 2$ for halos with $M_{200} > 10^{12}{\rm M}_{\odot}$, while for small halos ($M_{200} < 10^{12}{\rm M}_{\odot}$), the $M_{\rm BH}$-M_{200} relation becomes steeper as redshift increases. Interestingly, the scatter is relatively narrow in comparison to that found in the evolution of the $M_{\rm BH}$-$M_{\rm star}$ relation. Toward high redshifts ($z = 3$ to $z = 5$), the $M_{\rm BH}$-M_{200} relation presents a sharp increase for halos with $M_{200} \lesssim 10^{11.4}{\rm M}_{\odot}$ and it becomes steeper than the $z = 0$ $M_{\rm BH}$-M_{200} relation for massive halos ($\gtrsim 10^{11.6}$) by up to 0.4 dex. This suggests that the BHs and halos undergo a strong evolution such that halos with a given mass larger than $10^{11.6}{\rm M}_{\odot}$ are inhabited by more massive BHs than those living in halos with the same mass at $z = 0$. In contrast, haloes with mass below $M_{200} \lesssim 10^{11.4}{\rm M}_{\odot}$ tend to have less massive BHs, however, the scatter is larger at high redshift.

This evolution in the $M_{\rm BH}$-M_{200} relations is consistent with the BH model from Booth & Schaye (2010) for the most massive halos. Booth & Schaye (2010) propose that the binding energy of the host halos of the massive galaxies that are inhabited by BHs is the fundamental property that determines the BH mass. Booth & Schaye (2010) argue that the $M_{\rm BH}$-M_{200} relation should evolve since the binding energy depends on redshift, halo mass and concentration c (which also depends on halo mass and redshift). Because the concentration of the halo evolves with redshift and halo mass, halos for a given mass at $z = 0$ will be more concentrated than those with the same mass at higher redshift. As a result, halos with the same mass host more massive BHs at higher redshift ($z > 2$) than those at $z = 0$. They speculate that the BH growth is due to dry mergers. We observe in the simulation that a tight relation is found for the most massive halos ($M_{200} \gtrsim 10^{12.0}{\rm M}_{\odot}$) and we find a similar evolution that their model predicts for the such halos. Nevertheless, the evolution of the halos below such mass is different, which presents a steep rise and large scatter in the $M_{\rm BH}$-M_{200} relation, suggesting that the BHs inhabited halos

below this mass do not grow in a complete self regulation regime. In particular, we see strong evolution in halos with $M_{200} \sim 10^{11.5} - 10^{12}\mathrm{M}_{\odot}$ at all redshifts and we will see in the next section that there is a transition region between self-regulation and not in the mass range of the halos with $M_{200} \sim 10^{11.5-12}\mathrm{M}_{\odot}$.

4.11 Connection between the BH mass and the binding energy of the host halo

To gain more insight into the relation between the BH mass and the properties of the halo, we look at the relations between some properties of the gas such as star formation rate and the gas which are not star forming and M_{500} where M_{500} is the total mass within the radius that encloses a mean density of 500 times the present-day critical density of the Universe, r_{500}. Specifically, we look at gas falling into the centre that is not star-forming and the star formation rate within r_{500} and compare those to M_{500} at $z = 1$. We choose $z = 1$ because it allows us to enlarge the number of halos of a given halo mass with different BH masses.

Fig 4.11 shows the relation of non star-forming gas M_{notSF} as a function of M_{500}. The black solid line is the best linear fit found by linear regression and the colour points represent the ratio of $M_{CumlAccr}$ to M_{500} where $M_{CumlAccr}$ is the cumulative accreted mass that a BH has built up by gas accretion up to $z = 1$. Therefore, it is proportional to the energy that a BH or its predecessors have injected into the ISM since they were born and M_{500} is related to the binding energy of the host halo. Therefore, the ratio of $M_{CumlAccr}$-to-M_{500} is closely related to the comparison of the energy injected into the ISM by the BH and the binding energy of the host halo.

As shown in Fig 4.11, the non star-forming gas that is falling into the centre of the potential well of the halo increases as increasing M_{500}; something expected only because the total mass merely increases with the size of the halos. A colour trend that reflects that the ratio of $M_{CumlAccr}$ to M_{500} increases as increasing halo mass is also shown. This relation is due to the increasing M_{200}-M_{BH} relation

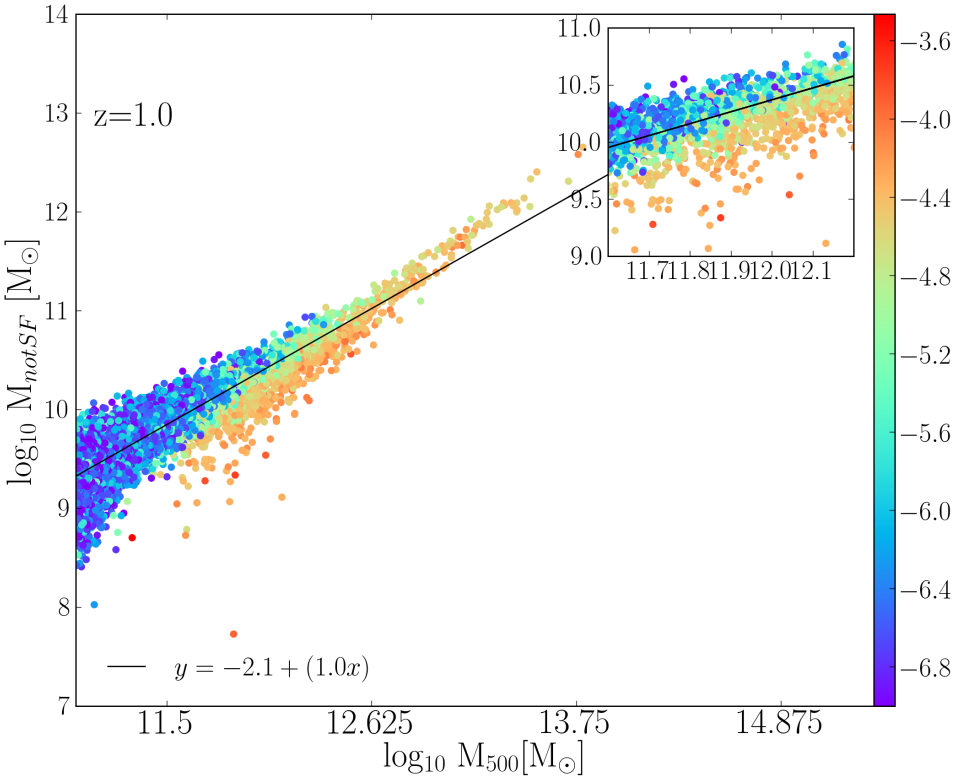

Figure 4.11: M_{500}-$M_{notSF}(< r_{500})$ relation at $z = 1$. The figure shows the gas that is not star forming M_{notSF} within r_{500} as a function of M_{500}. Colour points represent the ratio of the cumulative accreted mass $M_{Cuml,Accr}$ (the BH mass that was built up by gas accretion) to M_{500}. This ratio is closely related to the ratio of the energy injected into the ISM by the BH to the binding energy of the host halo. The ratio of $M_{Cuml,Accr}$ to M_{500} rises with M_{200} because of the relation between the central BH mass and the halo mass. The scatter of the relation for a given mass shows a colour trend in halos with $M_{500} \sim 10^{11.7-12.5}\mathrm{M}_\odot$, indicating that the scatter of the M_{500}-M_{notSF} relation is related somehow to the ratio of $M_{Cuml,Accr}$ to M_{500} for such halos.

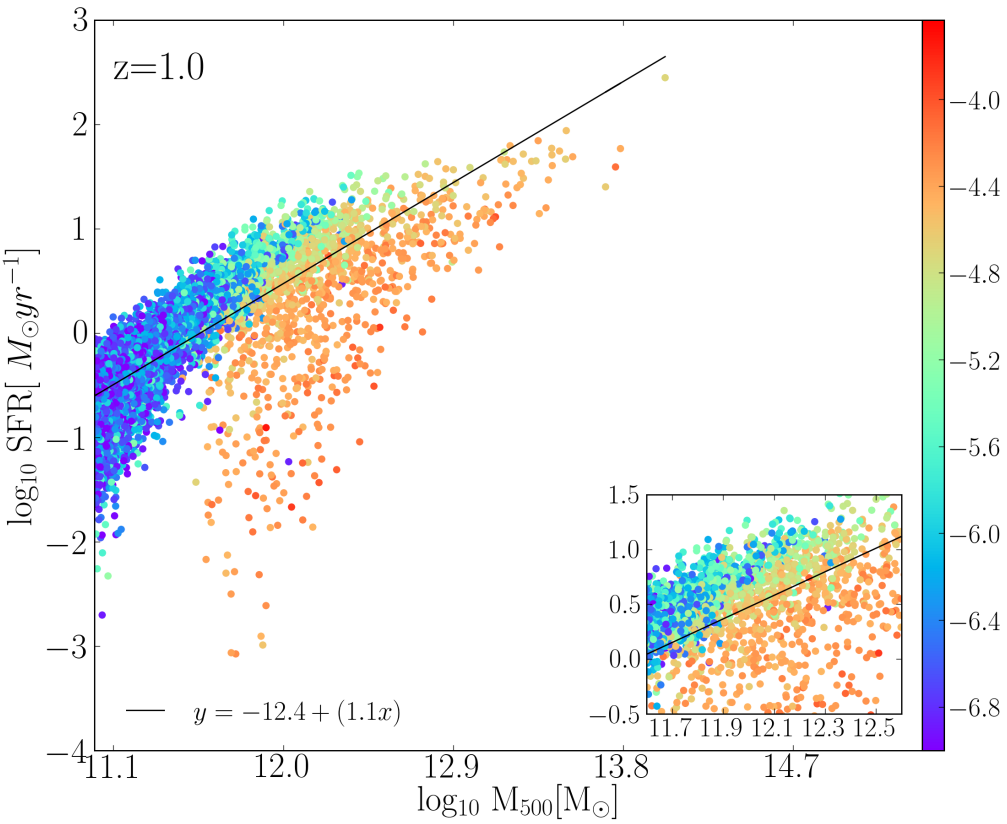

Figure 4.12: M_{500}-SFR($< r_{500}$) relation $z = 1$ where SFR is the star formation rate within r_{500}. Coloured points represent the ratio of $M_{CumlAccr}$-to-M_{500} described in Fig 4.11. The small panel is a close-up of the M_{500}-SFR($< r_{500}$) in halos with $M_{500} = 10^{11.7-12.5}\mathrm{M}_\odot$. The scatter in M_{500}-SFR($r < r_{500}$) relation shows similar trends seen as for the not-star forming gas in Fig 4.11. Here also in halos with $M_{500} = 10^{11.7-12.5}\mathrm{M}_\odot$, the scatter in the relation seems to be related to the ratio of $M_{CumlAccr}$-to-M_{500}.

shown in the previous section.

What it is interesting from the plot is the scatter of the non-star forming gas relation in comparison to the ratio of $M_{CumlAccr}$ to M_{500} for a given halo mass. We can divide the plot into 3 regions for small halos ($M_{500} < 10^{11.7}\mathrm{M}_\odot$) and massive halos ($M_{500} > 10^{12.5}$) and Milky way-like halos ($10^{11.7} < M_{500}/\mathrm{M}_\odot < 10^{12.5}$). For instance, for halos with mass $10^{11.1}\mathrm{M}_\odot$ that is in the small halos region, the scatter in the M_{500}-M_{nonSF} relation does not show any particular relation to the logarithmic ratio of $M_{CumlAccr}$ to M_{500} that spans from -5.6 to -6.8. Similarly, for halos with mass $10^{13}\mathrm{M}_\odot$ that is in the region of massive haloes , the scatter in

the M_{500}-M_{nonSF} relation does not show any particular relation to the logarithmic ratio of $M_{CumlAccr}$ to M_{500} (-4.6 to -3.6) either. For the low mass halos, combined effects take place: the cooling time of the halos is so short that the halo has the ability to recover from any energy that is injected into the gas quickly. In addition, the BH is too small to affect the gas properties of the halo in a dynamical time of the host halo. For the most massive halos, the BHs are large enough to inject energy into the ISM that affect the gas properties of the host halos such as heating the gas or expelled gas from the inner part of the halos. This is attributed to the fact that BHs self-regulate their growth. In the cases of halos with mass $10^{11.5-12.5}\mathrm{M}_{\odot}$, the scatter in the M_{500}-M_{nonSF} relation is apparently related to the log ratio of $M_{CumlAccr}$-to-M_{500} (-6.8 to -3.8), showing a transition in colour: for a given halo mass, halos with higher M_{nonSF} tend to have lower $M_{CumlAccr}$-toM_{500} ratio while halos with lower M_{nonSF} tend to have higher $M_{CumlAccr}$-to-M_{500}. Because those halos have a similar mass, it implies that $M_{CumlAccr}$ drives the scatter in the M_{500}-M_{nonSF} relation for a given M_{500}. The scatter in $M_{CumlAccr}$ is related to the difference between the evolution of host halos, so the gas channel that falls onto the BH varies between halos for a given M_{500}.

Similar results are shown, looking at the SFR as a function of M_{500}. Fig 4.12 shows the SFR as a function of M_{500} and colours represent the ratio of $M_{CumlAccr}$ to M_{500}. The SFR increases as a function of halo mass up to $M_{500} < 10^{11.5}\mathrm{M}_{\odot}$ where there is a break in the relation and the most massive galaxies present a large scatter in the SFRs. For instance, halos with $M_{500} \sim 10^{12}\mathrm{M}_{\odot}$ show SFRs between $10^{1.5}$ and $10^{-3}\mathrm{M}_{\odot}\mathrm{yr}^{-1}$, this effect is known as the quenching of SFR in massive galaxies. Similar to Fig 4.11, the ratio of $M_{CumlAccr}$-to-M_{500} increases as a function of halo mass. For low mass halos ($M_{500} < 10^{11.5}\mathrm{M}_{\odot}$), we know that SN feedback regulates the SFR in such halos, then it is expected that there is no relation between the scatter and the ratio of $M_{CumlAccr}$-to-M_{500}. For high halos mass ($M_{500} > 12.5\mathrm{M}_{\odot}$), the SFR is regulated by AGN feedback which directly shuts off SFR, then the scatter in the M_{500}-SFR relation is apparently independent of the ratio of $M_{CumlAccr}$-to-M_{500}. Again, the plot shows a region of transition

that frames to regimes of BH growth and it is shown as a trend in colour in the plot. The scatter of the relation is related to the ratio of $M_{CumlAccr}$-to-M_{500} in halo masses between $10^{11.5} - 10^{12.5}\mathrm{M}_{\odot}$ but it is more subtle than that found in the M_{nonSF}-M_{500} relation. Overall, the SFR-halo mass plots shows similar results found in the M_{nonSF}-M_{500} relation.

4.12 Summary and Conclusions

In this chapter, we have analysed a hydrodynamical, fully cosmological simulation of 100 comoving Mpc region from $z = 127$ to $z = 0$. The simulation accounts for less than 7 billions of particles with an initial baryonic particle mass of $1 \times 10^{8}\mathrm{M}_{\odot}$ and force resolution of 0.7 proper kpc. The simulation includes a state-of-the-art galaxy formation subgrid models that include radiative cooling, star formation, reionization, chemical evolution, stellar evolution and mass loss, feedback from star formation and BH growth and AGN feedback that were calibrated to reproduce the observational stellar mass function at $z = 0$ and the efficiency of AGN feedback was set to reproduce the break of the galaxy stellar mass function and the normalization of the BH mass-stellar mass relation at $z = 0$.

In this chapter, we show the results of the observables that took part of the calibration of the galaxy formation subgrid models such as the galaxy stellar mass function at $z = 0$ and the BH mass-stellar mass relation at $z = 0$. We also show the other BH scaling relations at $z = 0$: the relations between the central BH mass and the mass of the host halo and the stellar velocity dispersion. Additionally, we focus on the predicted evolution of the BH mass-stellar mass relation and BH mass-Halo mass from $z = 0$ to $z = 6$. Finally we discuss the connection between the build-up of the BH mass via gas accretion and the binding energy of the host halo by looking at the scatter of the relation between some gas properties and the host halo mass. We came to the following conclusions:

- The simulated galaxy stellar mass function is in excellent agreement with observations over a wide stellar mass range. The galaxies in this range

are well resolved ($10^{8.4} < M_{\rm star}/{\rm M}_{\odot} < 10^{11.6}$) and the discrepancies with observations are smaller than 0.2 dex. This is the highest level of agreement achieved for a cosmological simulation so far. The critical subgrid models to calibrate the stellar mass function is SN and AGN feedback and BH growth. In particular, AGN feedback and BH growth models were calibrated to reproduce the break in the stellar mass function.

- As a consequence of the good agreement between the galaxy stellar mass function $z = 0$ and the BH mass-stellar mass function compared with observations, the BH stellar mass function at $z = 0$ is in good agreement with observations over a wide mass range. In particular, we find that the discrepancies with observations are not larger than 0.4 dex for BH masses larger than $10^6{\rm M}_{\odot}$. Below this mass the BH mass function is affected by the seed mass.

- We show the predicted evolution of the BH mass function from $z = 0$ to $z = 6$. We find that the BH mass function rapidly evolves up to $z = 3$ following a less rapid evolution up to $z = 1$ where the shape of the BH mass function have been placed. After this redshift, only the high mass end of the BH mass function evolves.

- The central BH mass-stellar mass relation agrees with observations but the scatter in the model is smaller than that observed. The simulation predicts that BHs residing in galaxies below 10^9 and $10^{10}{\rm M}_{\odot}$, typically host BHs with masses below that of the extrapolation of the observational fit from Haring & Rix (2004).

- The central BH mass-total velocity dispersion relation falls in the region where the observations lie. However, the shape is different to a power-law fit. This discrepancy appears because we are not comparing the total velocity dispersion in the simulation with the bulge stellar velocity dispersion in observations. Even in observations, the values of the bulge stellar ve-

locity dispersion are sensitive to the definition of the bulge stellar velocity dispersion, varying by $\sim 10\%$ (McConnell & Ma, 2012).

- We show the central BH mass-halo mass relation at $z = 0$ and compare to inferred observational data. We find that the relation is a tight relation for halos above $10^{12.3}\mathrm{M}_{\odot}$. Below this halo mass, the relation presents a break following a steep decline for halos in $10^{12.3} - 10^{11.6}\mathrm{M}_{\odot}$. For smaller halos, the relation is shallower. The median of the relation is shallower than the inferred relation from observations by up to 0.3 dex. However, only observations from a narrow range of halo masses of $10^{12.9} - 10^{13.7}\mathrm{M}_{\odot}$ are considered.

- The simulation predicts that the BH mass-stellar mass relation does not significantly evolve up to $z = 2$. At higher redshifts, halos that lie on $10^{9.6} - 10^{10.6}\mathrm{M}_{\odot}$, typically host BHs more massive than the halos at $z = 0$. The relation also present a break in these halos and the break shifts to lower mass as redshift increases. The scatter increases as redshift increases. We also investigate the predicted evolution M_{BH}-to-M_{star} ratio that many observational studies have explored. Direct comparison with observations is not possible because observations are biased toward the masses of the most luminous quasars. Different studies find evolution while other studies not. However Schulze & Wisotzki (2014) show that with the data available so far it is not possible to determine the evolution or non evolution of the ratio of BH mass-to-stellar mass. Nevertheless, we compare the evolution of the most massive galaxies $10^{10.9-11.7}\mathrm{M}_{\odot}$ with the evolution predicted by previous numerical simulations (Booth & Schaye, 2010; Di Matteo et al., 2008) that is in agreement with some observational studies. These numerical studies show positive evolution with redshift. We find that the predicted evolution of the most massive galaxies in the simulation is in robust agreement with previous studies. No considerable evolution is seen in the rest of the galaxy population.

- The predicted evolution of the BH mass-halo mass mirrors the evolution of the BH mass-stellar mass relation, overall. In haloes above ($10^{12}\mathrm{M}_{\odot}$) , the relation is tight and it does not present any evolution up to $z = 2$ while halos below this mass, are typically inhabited by less massive BHs as redshift increases. At higher redshift, the normalization of the relation is higher than that at $z = 0$ while a steep rise is presented in haloes between $10^{11.5-12.0}\mathrm{M}_{\odot}$. The evolution of high mass end of the relation can be explained in terms of self-regulation growth of the BHs with the halo binding energy as the fundamental property that sets the final BH mass (Booth & Schaye, 2010). For the low mass end, it is likely that self-regulation is not applied.

Finally, we look at the scatter of the relations between the not star forming gas falling into the halo and halo mass and the SFR in the inner part of the halo and halos mass with the purpose to investigate the relation between the BH mass and the binding energy of the host halo. In general, we find a large scatter in the relation for halos below $10^{11.5}\mathrm{M}_{\odot}$ and a small scatter for halos above $10^{12.5}\mathrm{M}_{\odot}$. We compare the scatter of the relation with the ratio of the cumulative accreted BH mass to halo mass that is linked to the ratio of energy injected into the ISM to binding energy of the host halo. We note that the ratio does not apparently have a link with the scatter of the relation in both groups of halos. The large scatter in small haloes ($10^{11.5}\mathrm{M}_{\odot}$) is due to the combined effect that BHs are small to affect the gas falling into the center in a long timescale together with the fact that SN feedback regulates the SFR in low mass haloes. In the massive haloes, the scatter is small because the BHs self regulate their growth via AGN feedback, then the SFR and gas falling into the center are tightly related to the halo mass. Additionally, there is a transitional region between halos with $10^{11.5} - 10^{12.5}\mathrm{M}_{\odot}$, where the scatter of the relations is likely to be connected to the ratio of the cumulative accreted BH mass to halo mass. This region may frame the transition between halos where the self-regulated BH growth takes place and halos where the self-regulated growth is not strong. This result suggests that the host halo plays an important role in determining the growth of BHs. Further investigation

is required to understand the physical process taking place in such range of halos.

Chapter 5

Evolution of AGNs in cosmological simulations

5.1 Introduction

Active galactic nuclei (AGNs) are an essential ingredient of the Universe, playing an important role in the evolution of the structure of the Universe. In particular, the evolution of AGNs are vital in models to constrain the accretion history of BHs, the BH growth and BH formation over cosmic time. Additionally, the evolution of AGNs constrains the models of galaxy formation where AGN feedback is important for reproducing the properties of the most massive galaxies. The evolution of AGNs can be traced by determining the evolution of AGN luminosity functions. To study that, a representative AGN population is required across time.

However, one of the main observational challenges is to provide a complete survey of AGNs. Recent progress in detecting faint and obscured AGNs has been achieved by analysing data from X-rays in hard and soft X-ray. Such studies have revealed that AGNs are a strong evolving population with the space density of AGNs undergoing a sort of luminosity dependent evolution and the density of more luminous AGNs peaking at higher redshifts than the less luminous AGN populations.

In this chapter, we will focus on the evolution of AGNs using cosmological simulations and the growth history of the super massive BHs. In particular, we use a simulation of a 100-comoving-Mpc region that is part of a suite of cosmological simulations that were run using a state-of-the-art galaxy formation subgrid model. These galaxy formation subgrid models include radiative cooling, mass

loss, energy feedback from star formation, star formation and stellar evolution. Additionally, AGN feedback and BH growth are included that are similar in spirit to those described in Chapter 3. The galaxy formation subgrid models were calibrated to match the galaxy stellar mass function at $z = 0$ along with the constraint that galaxy sizes should be reasonable. In particular, the BH accretion model and AGN feedback were calibrated to match the break in the galaxy stellar mass function and the efficiency of AGN was calibrated to match the normalization of the BH mass-stellar relation at $z = 0$. In Chapter 4, we described the galaxy stellar mass function along with the BH mass-stellar mass relation at $z = 0$, the simulation is able to produce a BH mass function at $z = 0$ which is in remarkable agreement with observations. We investigate the connection between the growth of BHs and the evolution of galaxies. We study the evolution of the BH scaling relations, and find that BHs self-regulate their growth in the most massive galaxies(haloes), while BHs that inhabited galaxies below a critical mass (halo mass), are likely to grow outside of the self regulation regime.

In summary, this numerical simulation has been successful to produce three fundamental observables in connection to the galaxy and BH populations at $z = 0$. Such observables are the galaxy stellar mass function, the BH mass function and the BH mass and stellar mass function, two of them are observationally well constrained whereas the BH mass function is a direct consequence of the other two observables. Here, we will study the evolution of the AGNs across time as well as the evolution of the different population of AGNs.

This chapter is organized as follows.In section 5.2, we will outline some details of the simulations used here. More details and more extensive description are found in Chapters 2 and 4. In section 5.3, different accretion regimes are defined for the BH populations. In section 5.4, we discuss the evolution of different accreting BH populations and their contribution in the BH mass function. In section 5.5, we outline the method to determine the AGN luminosity functions in hard and soft X rays. We study the evolution of the hard and soft X ray luminosity functions of AGNs from $z = 0$ to $z = 5$ and compare them to observations and

the bolometric luminosity function. In section 5.6 we show the evolution of the space density of AGNs for different AGN populations. In section 5.8, we show the evolution of the Eddington ratio distribution from $z = 0$ to $z = 6$. In section 5.9 we show the global growth of the BH population across time as well as the contributions of BHs with different mass. We also show the evolution of the global accretion rates per unit volume. We discuss the connection between AGNs and the host halo by looking at the BH mass- halo mass relation as well as the Eddington ratio distribution in different ranges of halo masses in section 5.10. Finally, in the last section we summarise our results and conclusions.

5.2 Details of the simulation

A summary of the key ingredients of the simulations is found in Chap 2 and specifications are found in section 4.2. Complete details of the simulation are found in Schaye et al. (2010) and Schaye et al. (2014).

The first BH that appears in the 100-Mpc simulation is at $z = 14.5$, the most massive BH has a mass of $4.1 \times 10^9 \mathrm{M}_\odot$ and the most massive halo has a mass of $6.4 \times 10^{14} \mathrm{M}_\odot$ at $z = 0$. The total number of BHs at $z = 0$ is 241310, of which 18 have masses $> 10^9 \mathrm{M}_\odot$, 525 have masses $> 10^8 \mathrm{M}_\odot$ and 2006 have masses $> 10^7 \mathrm{M}_\odot$. A large fraction of the BHs have masses few times the seed mass. These BHs probably have grown by small mergers or sporadic accretion events, but they have not accreted more mass than the seed mass.

5.3 Definition of accretion regimes

As we described previously, the BH accretion model a priori does not make any distinction between different modes of feedback or accretion since the accretion rates are only estimated by the properties of the local gas. However, for this study it is essential to make a distinction between BHs which are *active* from those that are not. Therefore, we define two regimes of accretion and *inactive* BHs in terms

of the Eddington ratio, $\lambda_{\rm Edd}$, which is defined as

$$\lambda_{\rm Edd} = \dot{m}_{\rm BH}/\dot{m}_{\rm Edd}, \tag{5.1}$$

where $\dot{m}_{\rm BH}$ and $\dot{m}_{\rm Edd}$ are the BH mass accretion rate and the Eddington limit, respectively. We identify *inactive* BHs as BHs with $\lambda_{\rm Edd} < 10^{-4}$. The two regimes of accretion that we define are : *Shakura-Sunyaev disc* (SSD) where the disc around the BH is assumed to be thin and radiative cooling is efficient; we assume that the physics of the disc is described by the standard Shakura-Sunyaev disc model and *Advection Dominated Accretion Flows* (ADAFs) where the disc is thick and radiatively inefficient since cooling is via advection. We consider as an ADAF, accreting BHs whose Eddington ratios span $10^{-4} \leq \lambda_{\rm Edd} < 0.01$ and a SSD for Eddington ratios $\lambda_{\rm Edd} \geq 0.01$. These limits are motivated with the typical values found in the literature for ADAFs (Rees et al., 1982; Narayan & Yi, 1994; Abramowicz et al., 1995) and for SSD (Shakura & Syunyaev, 1973).

5.4 BH Mass Function

In Chapter 4, we discussed the BH mass function for the complete BH population and its evolution. We find that the BH mass function is in good agreement with observations as a direct consequence of the calibration of the galaxy formation subgrid model to match the stellar mass function of galaxies at $z = 0$. In this section, we present the contributions of BHs in the different accretion regimes as well as BHs that are defined as inactive BHs to the BH mass function.

Fig 5.1 shows a modified version of BH mass function at $z = 0$ shown in Chap. 4 (see Fig. 4.2), but including the contributions of ADAFs, SSDs and inactive BHs at $z = 0$. From Fig 5.1, it is apparent that inactive BHs (light blue lines) are the most abundant BHs and dominate the BH mass function with a fraction of 0.63 of the total BHs with $M_{\rm BH} > 10^6 {\rm M}_\odot$, following BHs powering ADAFs (green line) that contributes with a fraction of 0.32 for ($M_{\rm BH} > 10^6 {\rm M}_\odot$). They only become

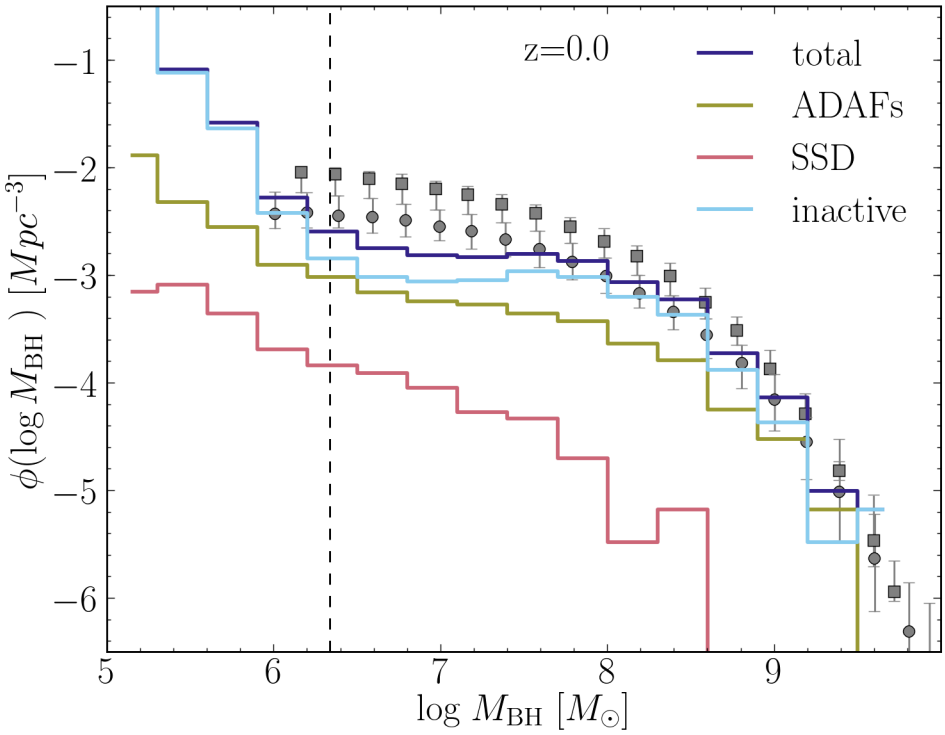

Figure 5.1: The contribution of BHs in different accretion regimes to the predicted BH mass function in the simulation L0100N1504 (blue solid line) and observational estimates by Marconi et al. (2004) (grey-circles) and Shankar et al. (2004)(grey squares). The light-blue line corresponds to inactive BHs ($\lambda_{\rm Edd} < 10^{-4}$), green line to BHs accreting as ADAFs ($10^{-4} \leq \lambda_{\rm Edd} < 0.01$) and the red line to SSDs ($\lambda_{\rm Edd} \geq 0.01$). The errors bars in observations correspond to 1σ uncertainties. The inactive BHs are the major contributor to the BH mass function over a wide mass range apart from BHs with $M_{\rm BH} > 10^{9.0}{\rm M}_\odot$, following ADAFs that dominate in $10^{9.0} < M_{\rm BH} < 10^{9.3}{\rm M}_\odot$ and the SSDs contribute less than 1% to the total BH mass function. The most massive BHs are not accreting as SSDs ($> 10^{8.6}{\rm M}_\odot$). By comparing the contribution of different accreting BHs to the BH mass function, it is possible to determine the average duty cycle of BHs. The predicted duty cycle for SSDs results to be ~ 0.01.

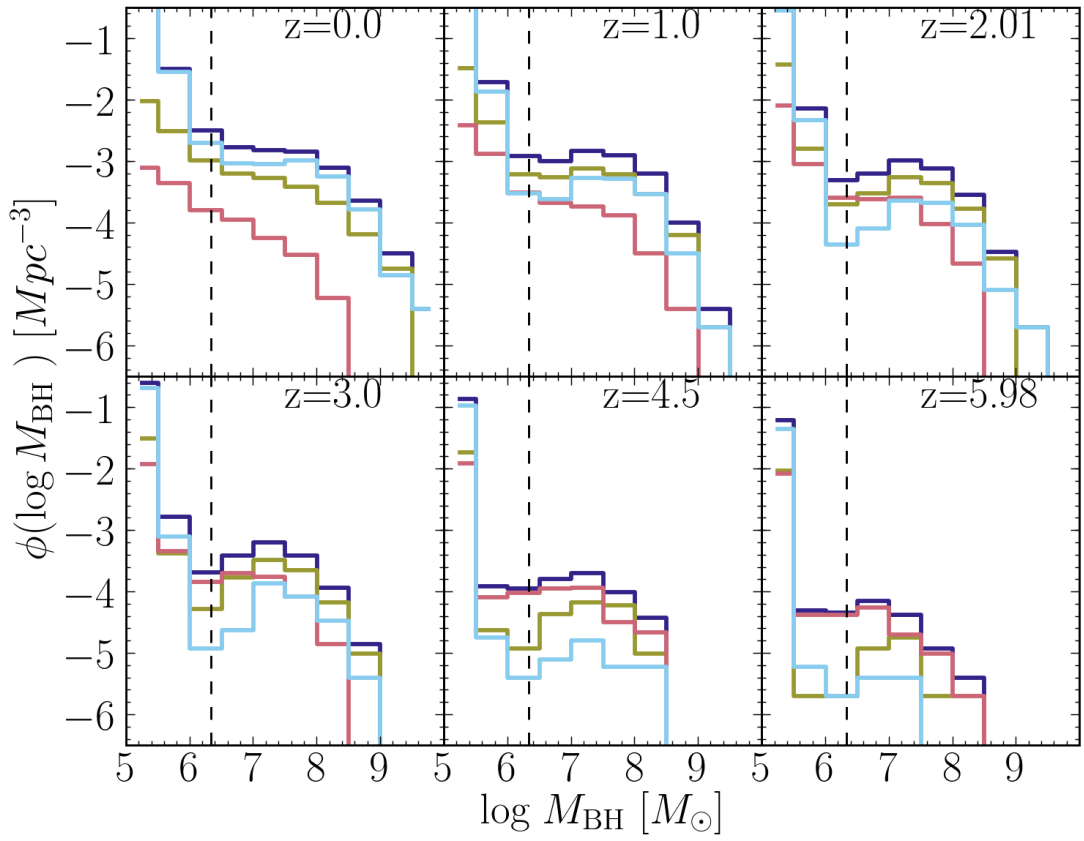

Figure 5.2: The contribution of accreting BHs to the predicted BH mass function at various redshift from $z = 0$ to $z = 6$. The contribution of different accreting BH populations strongly varies across time. The BH mass function is mainly shaped and dominated by ADAFs across time, except at $z > 3$ where the SSDs are as comparable as ADAFs, dominating the BH mass function. Inactive BHs become to be significant at $z \leq 1$ where most of the BH population has placed and they become less abundant with increasing redshift. The most massive BHs ($> 10^{8.5}\mathrm{M}_\odot$) are accreting as ADAFs or inactive.

more abundant than inactive BHs in the most massive bins ($M_{\rm BH} > 10^{9}{\rm M}_{\odot}$). A tiny fraction of BHs are accreting as SSDs (red line) with a fraction of less than 0.04 of the total population of BH with mass $> 10^{6}{\rm M}_{\odot}$. Note that the most massive BHs ($> 10^{8.6}{\rm M}_{\odot}$) are found accreting as ADAFs or inactive.

Another important feature is the discrepancy in the shape and the normalization of the BH mass function from BHs accreting as ADAFs to those accreting as SSDs. While the BH mass function of ADAFs and inactive BHs show a similar shape of the total population, BHs powering SSDs show a power law function decreasing with increasing $M_{\rm BH}$. This indicates that ADAFs are driven by different physical processes than those which drives SSDs. From the BH scaling relations (see Chapter 4, Fig 4.4), we know that the most massive BHs inhabit the most massive galaxies. Such galaxies contain hot gas (see Chapter 3, Fig 3.10) and old stellar populations (see Chapter 3 3.4) since their star formation efficiency is low. This is consistent with the scenario proposed by Kauffmann et al. (2008) based on the Eddington ratios in local galaxies. They found different modes of BH growth in galaxies when they are divided into galaxies that contain old population of stars and those with supplies of cold gas.

Regarding normalization, the BH mass function also varies by considering different accretion regimes. The normalization is dominated by inactive BHs, following BHs powering ADAFs and then SSDs. Through these differences in normalization, it is possible to infer an average *duty cycle* for BHs accreting as SSDs. Such an average *duty cycle* refers to the probability of finding a BH being active for a given time. We obtain that for the most massive BHs accreting as SSDs ($M_{\rm BH} > 10^{8.3}{\rm M}_{\odot}$), the duty cycle is $\sim 1 \times 10^{-2}$ whereas the duty cycle of AGNs powered by BHs with mass below $10^{8.3}{\rm M}_{\odot}$ varies between $\sim 10^{-3}$ to 10^{-2}. These values are roughly consistent with those estimated from recent observational studies of nearby AGNs identified in Hard-X rays and infrared wavelengths (Goulding et al., 2010).

The contribution of different accreting BHs populations varies through time too. Fig 5.2 shows the contributions of ADAFs and SSDs to the global BH mass

function across time. From the figure, it can be seen that the contributions of ADAFs, SSDs and active BHs evolve in shape and normalization at all redshifts. At $z < 2$, the shape and normalization of the BH mass function is dominated by ADAFs and inactive BHs. Both BH mass functions preserve a similar shape to the global BH mass function. In contrast, the BH mass function of SSDs presents strong variation in shape from $z = 0$ to $z = 2$, showing a similar shape to those of inactive and ADAFs at $z \geq 1$ but differing in normalization. Similar to the BH mass function at $z = 0$, the most massive BHs ($> 10^{8.5}\mathrm{M}_{\odot}$) continue to accrete as ADAFs or being inactive up to $z = 2$, after that redshift there are no BHs with mass larger than that mass. In addition, inactive BH are less abundant with increasing redshift. For instance, at $z = 2$, small BHs ($M_{\mathrm{BH}} < 10^{7}\mathrm{M}_{\odot}$) are more likely to be accreting as ADAFs or SSDs than inactive BHs since their contribution are lower by ~ 0.5 dex than those from accreting BHs.

Toward high redshifts, inactive BHs continue decreasing while BHs accreting as SSDs become more abundant and continue to be comparable to BHs accreting as ADAFs at $z = 4.5$. At higher redshift, the BH mass function is shaped by BHs accreting as SSDs, following ADAFs and only a small fraction of BHs are inactive BHs which are BHs with mass $< 10^{7.5}\mathrm{M}_{\odot}$.

The results described above imply that , the BH mass function at lower redshift is dominated by inactive BHs or ADAFs and only a tiny fraction of the BH population is undergoing strong accretion. In contrast, accreting BHs become dominant in shaping the BH mass function at high redshift ($z > 2$) which is consistent with the rapid evolution seen on the BH mass function. BHs accreting as SSDs become more common and have a large contribution to the BH mass function for $M_{\mathrm{BH}} < 10^{8.4}\mathrm{M}_{\odot}$, while ADAFs mirror the evolution of the total BH population over the whole BH mass range at all redshifts. Inactive BHs become significant at $z < 2$, where the BH population have placed ($z = 2$) while they are more rare as increasing redshift.

We will see that the evolution of the BH mass function for different BH populations is consistent with the evolution of AGNs by looking at the luminosity

functions in the next section.

5.5 AGN Luminosity Function

In this section we will focus on the evolution of AGN luminosity functions, primarily X-ray luminosity functions which are ideal to compare with the simulation due to the dynamical range of AGN densities that can be resolved. In addition, X-ray luminosity functions are some of the most powerful statistical properties to study the AGN population due to the existing unbiased surveys. Hard-X-ray luminosity accounts for a considerable fraction of bolometric luminosity originated in the accretion disc that is relatively unaffected by absorption, showing that the Hard X-rays are a direct indicator of accretion activity.

We start by describing the method by which we determine the AGN luminosity functions in the X-ray bands. The calculations of the bolometric corrections as well as the obscuration effect in the soft-X ray band are similar to those adopted by Fanidakis et al. (2012), who extend the semi-analytic model GALFORM (Bower et al., 2006) to obtain the evolution of AGN luminosities functions in different bands. In their study, they find good agreement of the model with observations.

5.5.1 AGN luminosity functions

The AGN LF is calculated in the redshift ranges that are determined by observations in any given band or bolometrically. To follow the activity of AGNs, we account for 406 outputs with basic information of the properties of BHs, gas, DM, and stars and we refer to these outputs as snipshots. We also account for 28 outputs across time which have more specific properties of BHs, stars, DM and gas and properties of the haloes. We refer to them as snapshots. To determine AGN LF, we use the snipshots. The lapsed time between each snipshot spans 10 to 60 Myrs. Initially, this allows us to follow AGN activity in timescales of Myrs that we use to improve the probability of finding an active BH in each luminosity bin. For each redshift range, there are between 17 and 45 snipshots to determine

the AGN luminosity functions that are weighted by the inverse of the number of snipshots. By doing so, both shape and normalisation remain unaffected apart from improving the statistics associated in each lumninosity bin.

While the size of the simulation ($100\mathrm{Mpc}$) is relatively small for reproducing the entire dynamic range of observed space densities of AGNs which spans 10^{-3} to $10^{-10}\mathrm{Mpc}^{-3}$, it is sufficiently large to provide a representative sample of moderate luminous AGNs ($L_{bol} \sim 10^{40-46}$erg s^{-1}) across time. The space density of moderate luminous AGNs varies between $10^{-2.5}$ to $10^{-7}\mathrm{Mpc}^{-3}$. If we assume that each well resolved halo with $M_{200} > 10^{10}\mathrm{M}_{\odot}$ has an accreting BH sitting at the centre of the potential, the corresponding AGN density will lie in the density range of haloes with $M_{200} > 10^{10}\mathrm{M}_{\odot}$. This density range in our simulation spans 10^{-1} to $10^{-6}\mathrm{Mpc}^{-3}$ which corresponds to those found in Deep X-ray surveys for moderate luminous AGNs. Therefore, we compare the simulation with observations in the soft (0.5-2 keV) and hard X-ray (2-10 keV) bands. We also add the evolution of the bolometric AGN luminosity function for consistency but not with the purpose of comparing to observations because our simulation is not sufficiently large to identify the most luminous quasars.

This method could be useful in some regards. If we assume that in every snipshot there is a random population of active BHs, it would allow us to explore the density range resolved by the simulation a bit further. As we will see in the next section, we find that this method does not make much difference in lower luminosities bins while it could help for the lower densities of AGNs if such AGNs do not correspond to the same BHs in consecutive snipshots. We found that this is true most of the time.

To determine the AGN luminosity function, we consider only AGNs whose radiative component is dominant. This is expected in AGNs powered by SSDs ($\lambda_{\mathrm{Edd}} > 0.01$) Therefore, we consider the bolometric luminosity of this radiative-efficient component as

$$L_{\mathrm{bol}} = \frac{\epsilon_{\mathrm{r}}}{1-\epsilon_{\mathrm{r}}}\dot{m}_{\mathrm{BH}}c^2, \tag{5.2}$$

where ϵ_{r} is the radiative efficiency and is set to 0.1 as suggested by Shakura &

Syunyaev (1973) for thin discs. In the rest of this chapter, we will refer to this radiative-efficient component as bolometric luminosity.

To convert the predicted bolometric luminosity into hard and soft X-rays, we calculate the bolometric corrections according to Marconi et al. (2004). These bolometric corrections are expressed as third degree polynomial relations (Marconi et al., 2004) for each X-ray band as follows:

$$\begin{aligned} \log\left(\frac{L_{HX}}{L_{bol}}\right) &= -1.54 - 0.24L - 0.012L^2 + 0.0015L^3 \\ \log\left(\frac{L_{SX}}{L_{bol}}\right) &= -1.64 - 0.22L - 0.012L^2 + 0.0015L^3, \end{aligned} \tag{5.3}$$

where $L = \log(L_{bol}/L_{\odot}) - 12$. These corrections are calculated with a template spectrum which is truncated at $\lambda > 1\mu m$ in order to remove the IR bump (Marconi et al., 2004). These relations are assumed to be independent of redshift.

Additionally, we consider a correction of obscuration to the predicted luminosities as suggested by several observational studies (Ueda et al., 2003; Hasinger et al., 2005; La Franca et al., 2005). In such studies, it has been shown that the obscured fraction of AGNs is a decreasing function of luminosity. If gas and dust in galaxies are responsible of obscuring AGNs and if their abundance depends on SFR, then it is expected that the obscured AGN fraction would be a redshift-dependent function. While old studies (eg. Ueda et al. 2003;Steffen et al. 2003) do not find any clear evidence of redshift dependency on obscuration, recent studies (eg. Ballantyne 2006,Gilli et al. 2007,Hasinger 2008) suggest a strong evolution of AGNs with a redshift dependency in the obscured AGN fraction.

Since the simulation predicts the energy output from AGNs and not the observed output, we opt to use an empirical law to account for obscuration. Specifically, we use the empirical prescription of Hasinger (2008), which is based on the comparison of selected AGNs in soft and hard X-ray bands. Hasinger found that the fraction of obscured AGNs increases strongly with decreasing luminosity with a dependency on redshift. The obscured fraction of AGNs f_{obs}

can be written in terms of $L_{\rm HX}$ and redshift as

$$f_{obs}(L_{\rm HX}, z) = -0.28 \log_{10}\Big(\frac{L_{\rm HX}}{10^{43.75} ergs^{-1}}\Big) + A(z), \tag{5.4}$$

where $L_{\rm HX} = 10^{42} - 10^{46} ergs^{-1}$. From several studies, $A(z)$ can be described as a power-law with a slope $\sim (1+z)^{0.62\pm0.11}$, saturating at redshift of $z \sim 2$ or a simple power-law fit $\sim (1+z)^{0.48\pm0.08}$ in the redshift range (eg. Hasinger 2008). We consider $A(z) = (1+z)^{0.48}$ in order to consistently compare with previous studies (eg.La Franca et al. 2005; Fanidakis et al. 2012; Ueda et al. 2003). Note that the obscured fraction could be negative or larger than 1 when $L_{\rm HX} < 10^{42}$erg s^{-1} or $z > 5$. In these situations, we imposed two conditions: For $z > 5$, $f_{obs} = 0$ and for $L_{\rm HX} < 10^{42}$erg s^{-1}, $f_{obs}(L_{\rm HX} < 10^{42}, z) = f_{obs}(10^{42}, z)$.

In summary, our methodology is as follows: Firstly, we obtain the intrinsic hard and soft X-ray luminosities associated with the bolometric correction eq 5.3. By calculating the obscured fraction of AGNs in the soft X ray band eq 5.4, the visible fraction of AGNs is given by $f_{vis} = 1 - f_{obs}$. Thus, the soft X-ray LF could be expressed as

$$\begin{aligned} \phi(\log L_{\rm SX})_{vis} &\equiv \Big(\frac{{\rm d}N}{{\rm d}\log_{10} L_{SX}}\Big)_{vis} \\ &= f_{vis}(L_{\rm HX}, z)\phi(\log L_{\rm SX}). \end{aligned} \tag{5.5}$$

In the case of the Hard X-ray LF, we did not account for any obscuration. Finally, we stress that in our method, we did not adjust any value to get a good agreement with observations.

5.5.2 Hard X-ray Luminosity Functions

Figure 5.3 shows the predicted hard X-ray luminosity function (HXRLF) obtained from the method described above. We only account for BHs that are powered by SSDs for various redshifts ranges from 0 to 3.5 (solid pink lines). To compare with

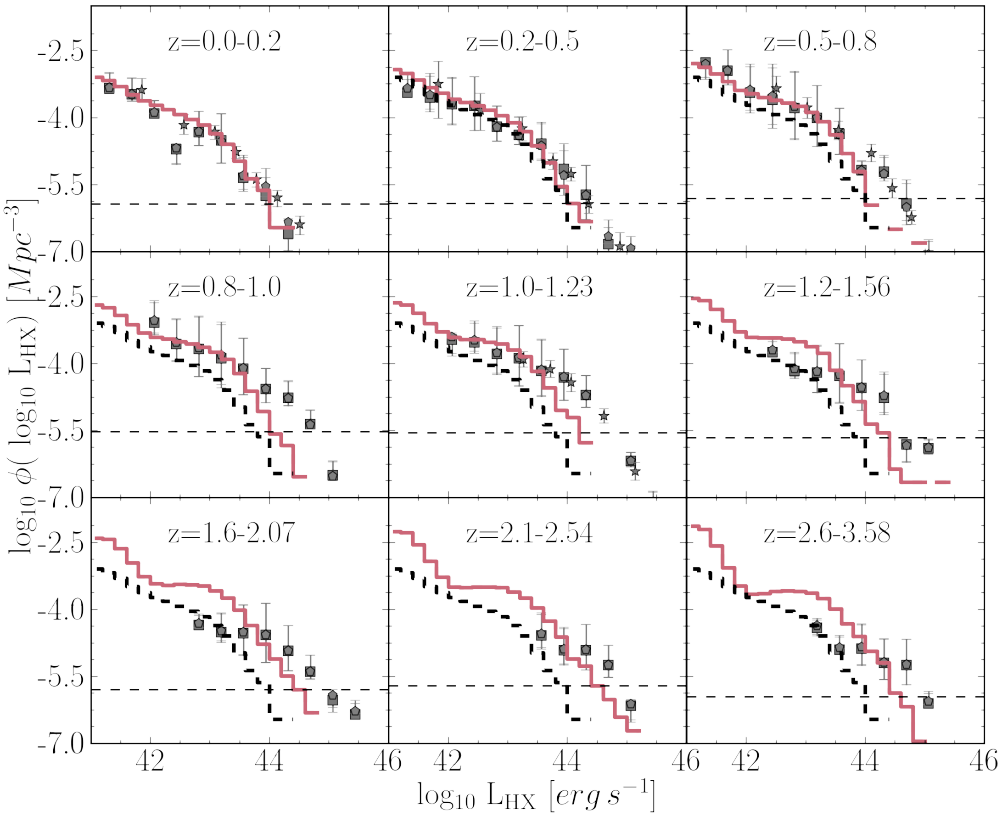

Figure 5.3: Hard X-ray luminosity function. Each panel represents the HXRLF (pink solid lines) at different redshifts. Black dashed lines represent the HXRLF at $z = 0$. Grey squares, hexagones and stars correspond to observational estimates of HXRLF from Aird et al. (2010) and Ueda et al. (2003) respectively. The horizontal dashed line represents the density at which there are 10 AGNs in the comoving volume divided to the number of snipshot used in each redshift range. Luminosity bins below the line account for less than ten AGNs.

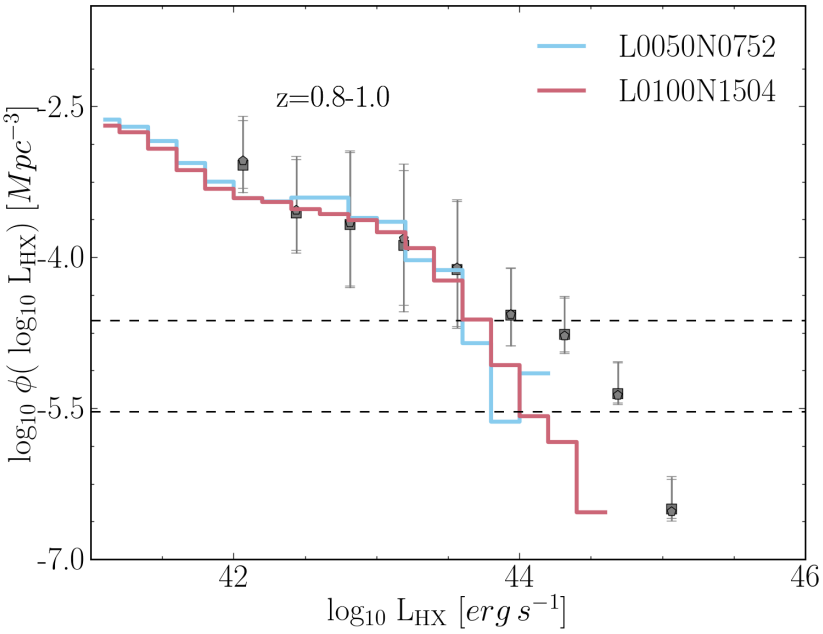

Figure 5.4: The Hard X-ray luminosity function for the two simulations described in section5.2 in the redshift range $z = 0.8 - 1.0$. Solid lines represent different simulations: pink colour for 100 Mpc and blue colour for 50 Mpc regions. Horizontal dashed lines represent the corresponding density of 10 objects in the comoving volume weighted by the number of snipshots in each simulation. Good agreement is found in both simulations above the horizontal dashed line at~ -4.75 which corresponds to the density of 10 objects in the 50-Mpc run. Below this, discrepancies between simulations become up to ~ 0.5 dex at $L_{\rm HX} > 10^{43.8-44.2}$erg s^{-1}. Both simulations also present similar underprediction in comparison to the observational data. This indicates that the underprediction of the bright end of the HXRLF does not originate from the limited size of the simulation.

observations, the redshifts ranges used in the predicted HXRLF corresponds to those from observations. We compare the predicted HXRLF to observed estimates from Aird et al. (2010) (grey squares and hexagons) and Ueda et al. (2003) (grey stars). To illustrate how many objects are in each luminosity bin, the horizontal black dashed line corresponds to the density of 10 objects in the co-moving volume divided by the number of snipshots used in each redshift bin. Below this density, luminosity bins contained less than 10 objects and indicates that the size of the simulation is too small to provide a representative sample even if we combine snipshots. This horizontal line varies in each panel due to the variation of the number of snipshots used in the redshift bins.

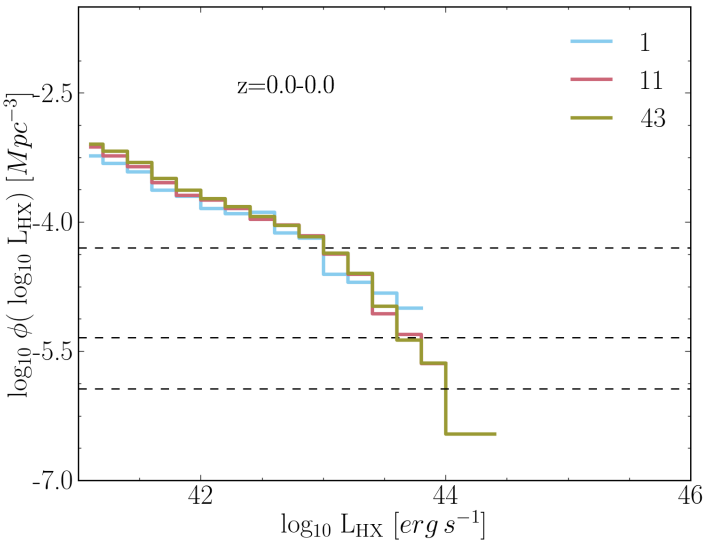

Figure 5.5: Hard X-ray luminosity function varying snipshots in the redshift range $z = 0.8 - 1.0$. Solid lines represent different numbers of snipshots. Horizontal dashed lines represent the corresponding density of 10 objects in the comoving volume weighted by the number of snipshots in this redshift range. Good agreement is found in the HXRLF using a different number of snipshots. A larger number of snipshots (better time resolution) enhances the range of densities in the hard X-ray luminosity function explored in the simulation. However, it is not sufficient to capture the AGN variability of rare luminous events.

From the Figure, we can see two important properties: the HXRLF presents a strong evolution in shape and normalization, and overall, the HXRLF is in excellent agreement with observations proving a consistent picture of the galaxy formation subgrid model used where parameters were calibrated to match the stellar mass function at $z = 0$. Specifically, we found a remarkable agreement with observations at $z < 0.5$ over the complete range of luminosities observed while the HXRLF is slightly underestimated ($\lesssim 0.7dex$) for $L_{\rm HX} > 10^{44}$erg s^{-1} at higher redshift. At $z > 2$, the predicted HXRLF is overpredicted for the faintest AGNs observed and continues to increase in even lower luminosities than those observed. However, the faintest end of the HXRLF ($L_{\rm HX} < 10^{42}$erg s^{-1}) is affected by the value of the seed mass.

The slight mismatch seen in the bright end of HXRLF in $L_{\rm HX} \gtrsim 10^{44}$erg s^{-1} could be attributed to two main reasons. Firstly, it is possible that the variability

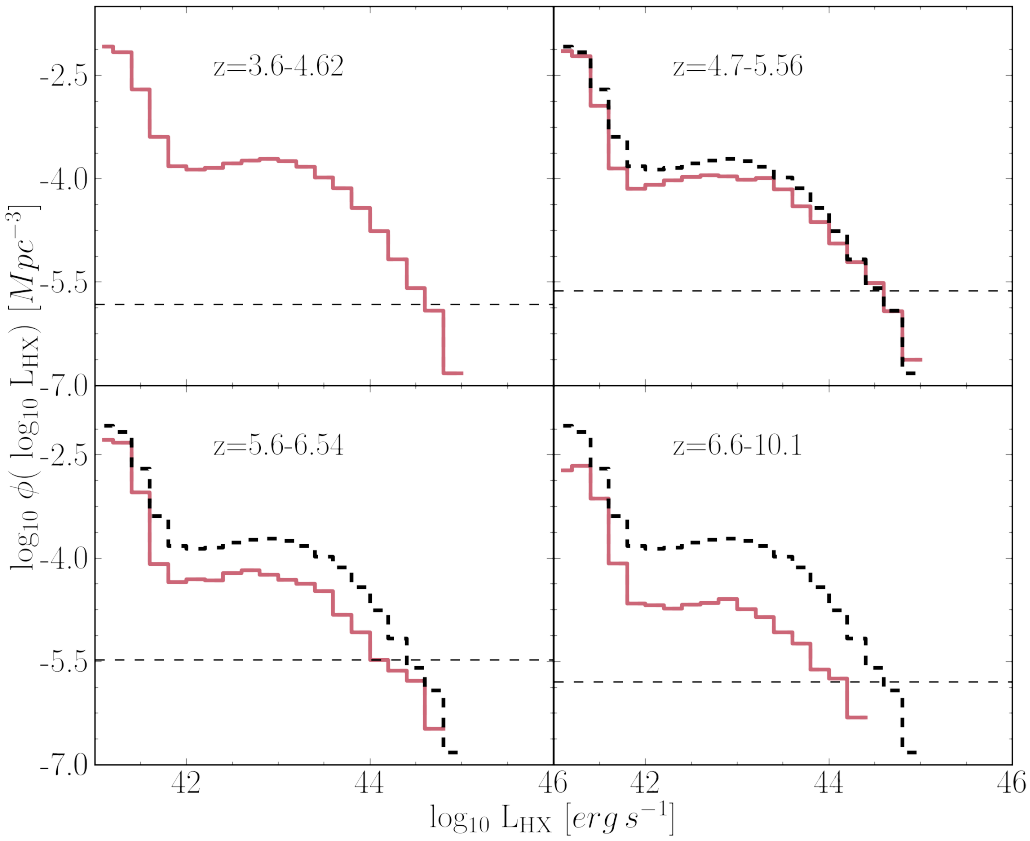

Figure 5.6: Hard X-ray luminosity function at high z. Each panel represents the HXRLF (pink solid lines) for various high-z from 3.6 to 10. Black dashed lines represent the HXRLF at $z = 3.6$. The horizontal dashed line represents the density of 10 AGNs in the comoving volume weighted by the number of snipshot used in each redshift range. Strong evolution in normalization is seen from $z = 5.6$ to $z = 10$. From redshift 3.6 to 5.5, the faint end of the HXRLF only evolves, showing higher normalization for objects with $L_{\rm HX} > 10^{44}$erg s^{-1}.

of AGNs is not completely captured in the HXRLF. Initially, it is possible to follow AGN activity at timescales of the order of the AGN lifetime (~ 10 Myr) because the timesteps in the simulation can vary between 10 Myr and 0.1 Myr. However, to determine the HXRLF, we account for 405 snipshots over time which correspond to timescales of 60-10 Myrs that makes it easy to miss the most luminous events in the simulation. Secondly, there could be an effect due to the size of the simulation, so that we would not have a representative sample of the luminous AGNs.

To further analyse this mismatch, Fig 5.4 shows the HXRLF at $z = 0.8 - 1.0$ for the simulation (100 Mpc; pink solid line) and for a simulation with half size (50 Mpc; light-blue solid line). Both simulations show good agreement between them with small discrepancies that are not large than 0.5 dex at $L_{\rm HX} > 10^{43.5}$erg s^{-1}. Both also shows the slight mismatch with observations by the same order of discrepancy suggesting that the size is not the main cause but the inability to completely capture the variability of AGNs. Fig 5.5 shows the HXRLF at $z = 0.8 - 1.0$ varying the number of snipshots to determine the HXRLF. The HXRLF is not affected by the number of snipshots used expect to enlarge the range of densities resolved in the simulation.

Finally, we will finish this section by showing the HXRLF at high redshift. Fig 5.6 shows the predicted HXRLF (pink solid lines) for various redshift ranges from $z = 3.6$ to $z = 10$. The HXRLF evolves in amplitude remaining similar in shape as can be seen by comparing the HXRLF to the one at $z = 3.6$ (black dashed line). The predicted density of the completely faintest AGNs increases as redshift increases, but as we mentioned before this is an effect of our choice of the seed mass. Something interesting is that the simulation can still capture AGNs over the whole range of moderate luminous AGNs.

5.5.3 Soft X-ray Luminosity Function

The predicted SXRLF is shown in Fig 5.7 for various redshifts. The SXRLF is shown as pink solid lines and pink dashed lines when obscuration is not applied. We show both so that the effect of obscuration is clear. The horizontal dashed line

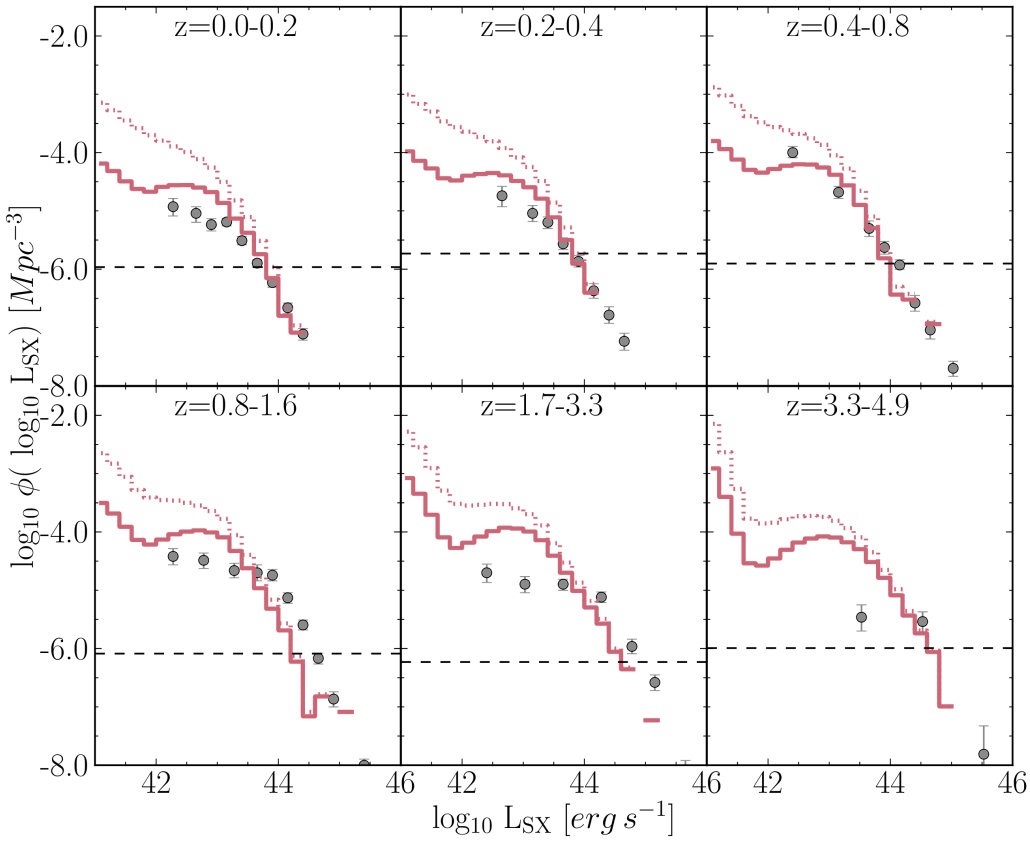

Figure 5.7: Soft Xray Luminosity Function. Each panel represents the SXLF for different redshift bins. Pink solid lines indicate the SXLF applying obscuration 5.4 and pink dotted lines show the SXLF without obscuration. The simulation is compared to the observational estimates of SXLF from Hasinger et al. (2005) shown as grey circles. For comparison, the SFXLF at $z = 0$ is included as black dashed lines in all the panels. The horizontal solid line represents the density of 10 AGNs divided by the number of snipshot used in each redshift range.

shows the corresponding density of 10 objects in the comoving volume weighted by the number of snipshots used in each redshift bin and below this line, the SXRLF is affected by the size of the simulation. The predictions are compared with the estimated SXRLF from Hasinger et al. (2005). For comparison, we include the SXRLF at $z = 0$ as black dotted lines.

From Fig 5.7, we can see that the SXRLF provides a good match with observations when obscuration is applied. In particular, the faint end of the LF is strongly attenuated by obscuration ($L_{\rm SX} < 10^{43}$erg s^{-1}), showing an offset up to 1 dex while obscuration does not affect the brightest end of the SXRLF ($L_{\rm SX} > 10^{44}$erg s^{-1}). The fraction of obscured AGNs can vary between 0.83 and 0.01 where the large value is found at $L_{\rm SX} = 10^{42}$erg s^{-1} and the lowest value at $L_{\rm SX} = 10^{46}$erg s^{-1}. For lower luminosities than $10^{42}\, erg, s^{-1}$, we assume that the obscured fraction of AGNs remains constant.

In contrast with the HXRLF, the bright end of SXRLF is in good agreement with observations even in the brightest bins. Note that this remarkable agreement of the bright end with observations is not a result of our recipe of obscuration since it is almost negligible at higher luminosities, suggesting that bolometric corrections does not provide a good description of the brightest AGNs.

At higher redshift ($z > 1.61$), the SXRLF presents a different shape from observations in the faintest end (10^{42}erg s^{-1} $< L_{\rm SX} <$ $10^{43.5}$erg s^{-1}). While the observational faintest end flattens as luminosity decreases, the predicted SXRLF presents a bump which is caused by obscuration. Note that the SXRLF without obscuration has a similar shape to the observed SXRLF, but because of the luminosity-dependency of the obscuration model, this flat shape is converted into a bump. This result from the simulation suggests that a different redshift-dependency could be required for the faintest end of the SXRLF. The rise seen in SXRLF for lower luminosities $L_{\rm SX} < 10^{42}$erg s^{-1} is probably artificial due to our choice of the seed mass.

Finally, the fact that the SXRLF is in agreement with observations is expected since we have excellent agreement with the HXRLF. This is also consistent with the

investigations done in Hasinger et al. (2005). They found that both the SXRLF and the HXRLF evolve at the same rate but differ in normalization and this difference can be attributed to obscuration. Indeed, we found that the agreement between observations and the simulation could be obtained by applying obscuration. Similar results where found by Fanidakis et al. (2012) who adopted a similar model of obscuration in semi-analytic models to study the evolution of AGN luminosity function. However, our results differ from them in the shape of faintest end at high redshift even when obscuration is not applied.

5.5.4 Bolometric luminosity functions

In this section, we investigate the evolution of the predicted bolometric luminosity to be consistent with our analysis and to explore possibly hidden trends of the complete AGN population that are not seen in the X-rays LF.

The predictions for the bolometric LF are shown in Fig 5.8. Different colours represent different redshift ranges as indicated in Fig 5.8. For clarity, we show the bolometric LF divided into two groups: solid lines that represent the bolometric LF at low redshift ($z < 1.6$) and dotted lines that represent the bolometric LF at higher redshift ($z > 1.6$). The simulated bolometric LF strongly evolves at higher redshifts up to $z = 1.6$, increasing in normalization and varying in shape over the complete range of luminosities that the simulation can resolve that is between 10^{42}erg s^{-1} $< L_{\rm Bol} <$ $10^{45.5}$erg s^{-1}. Below 10^{42}erg s^{-1}, the evolution of the bolometric LF has effects of the choice of the seed mass.

The faint end of the bolometric LF ($L_{\rm Bol} \lesssim 10^{45}$erg s^{-1}) increases as redshift decreases while the slope of the brightest end of the bolometric LF is steeper with decreasing redshift even though the normalisation of the bolometric LF is higher. The bump seen in the faintest end of the bolometric that disappears at $z = 1.6$, is caused by BHs with mass slightly above the seed mass and it is an effect due to the choice of the seed mass.

The evolution of the bolometric LF is not so strong at low redshift(solid lines, $z < 1.6$). While the shape does not change considerably, the normalization

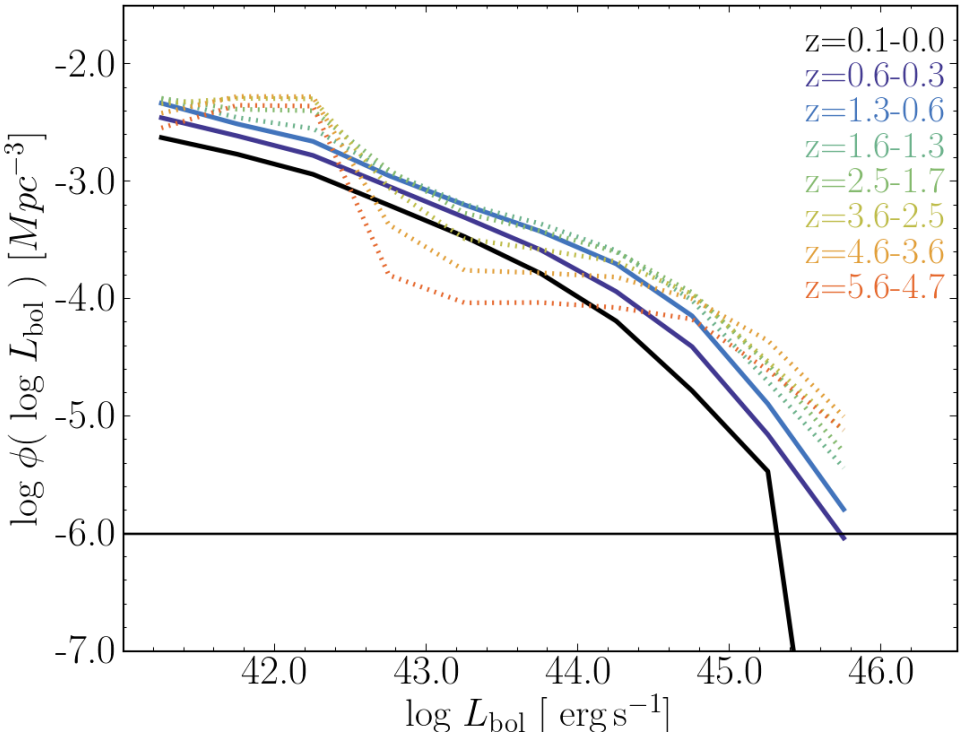

Figure 5.8: The predicted bolometric LF for the simulation L100N1540. Colours represent different redshift bins spanning from $z = 5.6$ to $z = 0$. The horizontal solid line indicates the space density of one object in the simulation. For clarity solid lines represent the bolometric LF at low redshift($z < 1.6$) and dotted lines at high redshift $z > 1.6$. The predicted bolometric LF undergoes a rapid evolution in normalization and shape up to $z = 1.6$. After that redshift, it decreases in normalization, however, the shape approximately remains similar. The brightest AGNs are brighter at higher redshift.

decreases as redshift decreases over the whole luminosity range. However, there is a slight evolution in the slope of the brightest end of the bolometric LF, indicating that the brightest AGNs are brighter at high redshift.

The evolution of the bolometric LF is consistent with the evolution of the BH mass function seen in Chapter 2 for the complete BH population and in Fig 5.1 for the contribution of active BHs (purple lines). Both the BH mass function and bolometric LF evolve rapidly up to $z = 1$. After this redshift, no considerable evolution occurs apart from the build up of the most massive BHs in the case of the BH mass function while the bolometric LF decreases on average. This is consistent with the evolution of active BHs shown in the Fig 5.1. Here, the BH mass function

is largely shaped by active BHs at higher redshift and their contribution decreases as decreasing redshift, showing simultaneously the hierarchical BH growth and the *downsizing* of AGNs. We will further explore the effect of *downsizing* in AGNs in the next section.

5.6 Evolution of the space density of AGNs

In sections 5.5.2 and 5.5.3, we have shown that the simulation can reproduce the evolution of X-ray luminosity functions from $z = 4$ to $z = 0$ reasonably well over a range of densities that the simulation can resolve well ($10^{42} - 10^{45}$erg s^{-1}) without any effect due to the simulation size or seed mass. This implies that our simulation should reproduce the observed trend *downsizing* in the density of AGNs across time (eg. Miyaji et al. 2000; Ueda et al. 2003; Hasinger et al. 2005; Ebrero et al. 2009; Yencho et al. 2009; Silverman et al. 2008; Aird et al. 2010), where *downsizing* refers to the observational result, namely that the space density of AGNs peaks at higher redshift as increasing luminosity. In order to compare our simulation with observations, we provide the predicted space density of AGNs in hard and soft X-ray bands in Fig 5.9 and Fig 5.10 respectively, as a function of $\log_{10}(z + 1)$.

Fig 5.9 provides the evolution of the space density AGNs in hard X-rays for two different AGN populations: $L_{\rm HX}$ from $10^{43-44.5}, 10^{44.5-46}$erg s^{-1}. Note that these bins are prior to and after the knee seen in the HXRLFs, so that they can show the differences between the evolution of faint and bright AGNs. These AGN populations are compared to observational estimates from Aird et al. (2010) (squares; observational fit, dashed lines) and the observational fits from Yencho et al. (2009) (dotted lines) and Silverman et al. (2008) (dotted-dashed lines) in hard X-ray bands. The observational fits reveal that the space density of of the brightest AGNs (green lines) peaks at higher redshift than the density of a faint population of AGNs (blue lines) even though they show discrepancies between them at higher redshift. At $\log_{10}(z + 1) < 0.3$, the predicted space density of

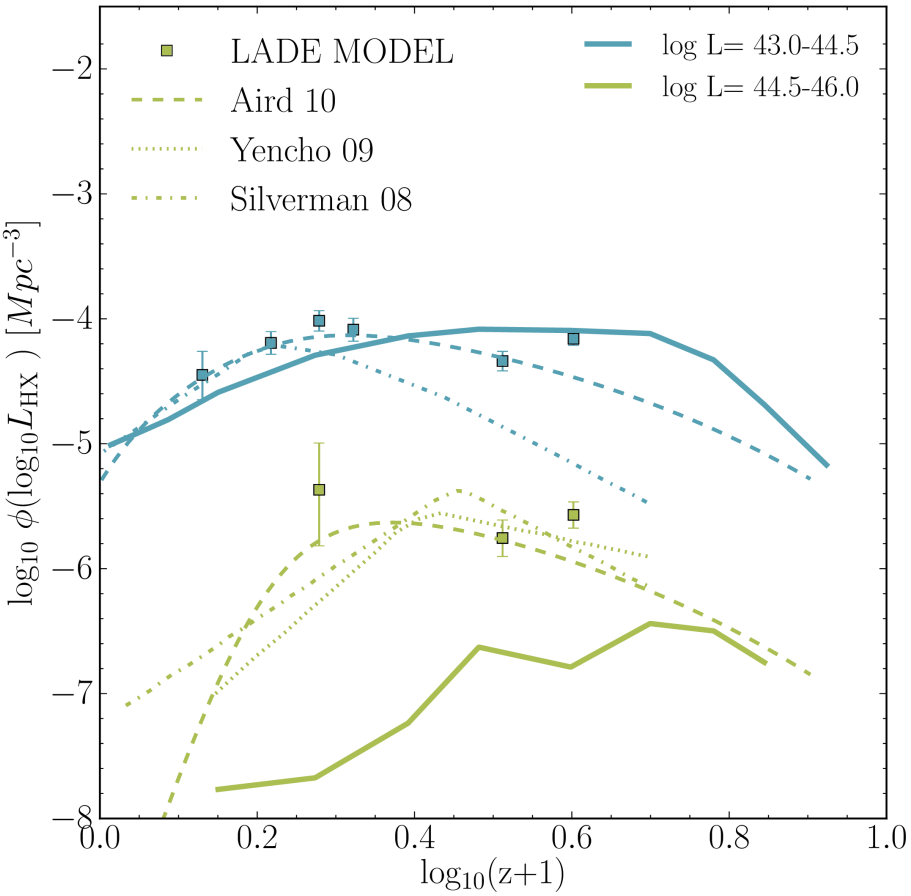

Figure 5.9: The evolution of the space density of AGNs for several $L_{\rm HX}$ ranges: $L_{\rm HX} = 10^{43.} - 10^{44.5}$erg s^{-1} (light blue, solid lines) and $L_{\rm HX} = 10^{44.5} - 10^{46}$ (green solid lines). The predicted space density of AGNs is compared to observations from Aird et al. (2010) and observational fits from Yencho et al. (2009), Silverman et al. (2008) and Aird et al. (2010) as indicated in Fig. The predicted space density of AGNs in $L_{\rm HX} = 10^{43.} - 10^{44.5}$erg s^{-1} is in good agreement with observations from Aird et al. (2010) by up to 0.5 dex and larger discrepancies are shown where the observational constraints are larger between observational fits. For the brightest AGNs, the space density is underestimated due to the number of snipshots used in the HXRLF that does not capture the full variability of the brightest AGNs. However, the downsizing effect, which refers to the shift of the peak of the AGN density toward lower redshifts as faintest AGNs are considered, is captured by the simulation.

the faintest AGNs (in $L_{\rm HX}$ -bin in $10^{43-44.5}$erg s^{-1}) converge to observations with discrepancies that are not larger than 0.2 dex. After that, the space density of AGNs tend to be overproduced in the best case by 0.2 dex, however observational fits show even larger discrepancies between different observed estimates.

In the case of the brightest AGNs (green lines), the space density peaks at higher redshift ($\log_{10}(z+1)=0.5$) and it decreases at lower redshift. We remark that the hard X-ray luminosity functions for AGNs with $L_{\rm HX}10^{44.5}$erg s^{-1} are underestimated for redshifts >0.8 and then it is not a surprise that the predicted evolution space density of the brightest AGNs is underestimated in comparison to observations. The discrepancy in the space density is larger (up to 2 dex at $\log_{10}(z+1)=0.3$) than that seen in the hard X-ray luminosity functions because we take wider $L_{\rm HX}$-bins in the evolution of the space density and then there is a combined effect due to boxsize and due to the extreme X-ray variability of AGNs that is not completely captured with our method. AGN luminosities may drop more than 10^2 in less than 10^5 years (Keel et al., 2012). One possible solution to account for the variabiality of AGNs in hard X-rays would be to weigh the hard X-ray luminosity function by a factor which includes the time that the AGN is active and the probability to observe the AGN radiating at the maximum luminosity.

Similar results are shown in Fig 5.10 for the space density of AGNs observed by applying obscuration in soft X-ray band. Here, the space density of AGNs (solid lines) for three populations of AGNs are shown: $10^{42-43}, 10^{43-44}, 10^{44-45}$erg s^{-1} and compared with data from Hasinger et al. (2005) (circles). To show the effects of obscuration, we have included the space density without obscuration as dotted lines. A similar trend of AGN *downsizing* as observed in the hard X-ray band can be seen in the evolution of space density of AGNs in the soft X-ray band. The predicted space density in the two faintest $L_{\rm SX}$ bins (dark and light blue lines) are in good agreement with observations with small discrepancies that are not larger than 0.4 dex, at low redshift ($\log_{10}(z+1)<0.4$). However, the space density of the AGNs is overpredicted at higher redshift by up to ~ 0.8 dex.

Regarding the highest luminosity bin (green lines), the shape of the space

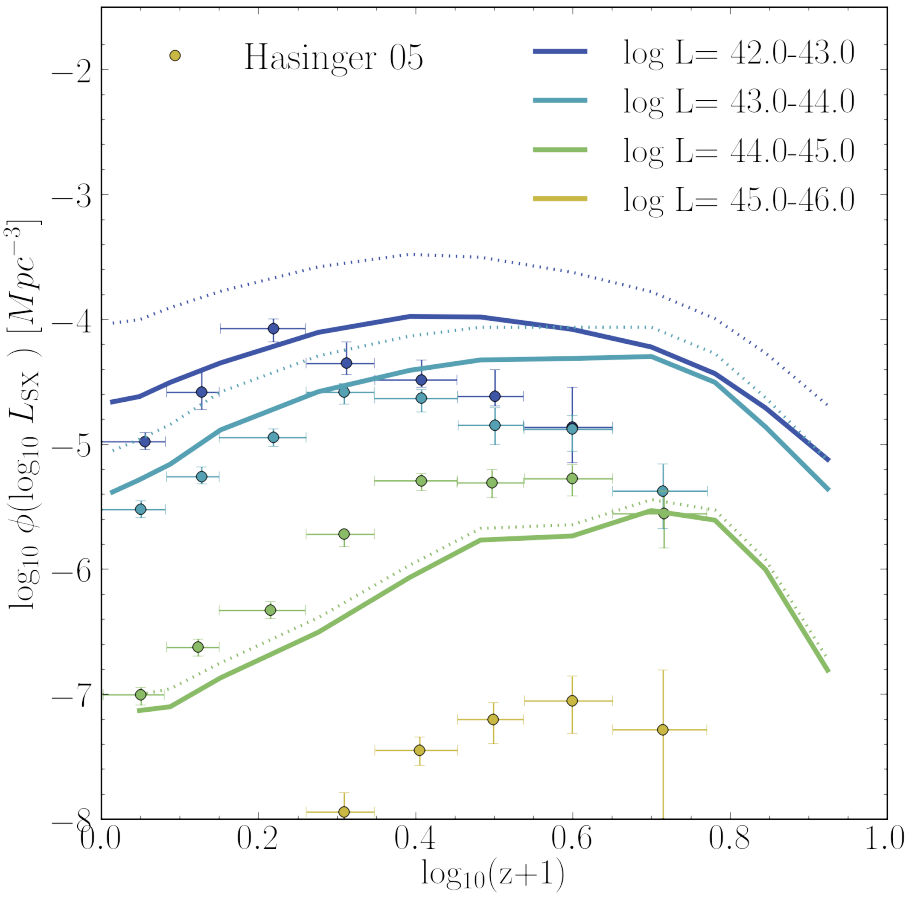

Figure 5.10: Evolution of the space density of AGNs for various $L_{\rm SX}$ ranges:$L_{\rm SX} = 10^{42} - 10^{43}$ (dark blue), $L_{\rm SX} = 10^{43} - 10^{44}$ (light blue) and $L_{\rm SX} = 10^{44} - 10^{45}$erg s^{-1} (green). Solid lines indicate the space density that accounts for obscuration and dotted lines without it. The space density of AGNs is compared to observations from Hasinger et al. (2005) (circles). The simulation is in reasonable agreement with the observed downsizing of AGNs in soft X-rays when obscuration is accounted for in the faintest AGNs while the space density of luminous AGNs is underestimated by up to 0.5 dex.

density of AGNs broadly agrees with observations. However, the space density of the most luminous AGNs is underpredicted across time by up to 0.8 dex. This discrepancy is also due to the extreme variability of the most luminous AGNs and that is not captured by the simulation.

As we have seen in the SXRLF, obscuration is important to shape the evolution of AGNs in the soft X-ray band. As fainter AGN populations are considered, the fraction of visible AGNs is reduced from < 0.8 dex for the faintest AGNs ($L_{\rm SX} = 10^{42-43}$erg s^{-1}) to < 0.1 for the brightest AGNs ($L_{\rm SX} = 10^{44-45}$). From our adopted prescription to account for obscuration we know that there is little evolution in the fraction of obscured objects. However a strong evolution of obscured AGNs seems to be required in our simulation.

To summarise our results above; the simulation reproduces the evolution of the spaced density of AGNs and the observed trend of AGN *downsizing* in both X-ray bands in a good level (0.2 dex) in the range of luminosities ($L_{\rm SX}/L_{\rm HX} < 10^{44}$erg s^{-1}) than the simulation captures the full AGN variability and observations also converge. In the case of the brightest AGNs, the shape of the evolution of AGNs broadly agrees with observations but it is underestimated by up to 0.8 dex. This is also affected by the inability to capture the variability of the most luminous AGNs that occur in the simulation.

5.7 The Soltan Argument

In this section, we track the global build-up of BH mass more directly by integrating an AGN population over luminosity and redshift as first proposed by Soltan (1982) which is given by

$$\rho_{\rm BH} = \frac{1-\epsilon}{\epsilon c^2} \int \int L_{\rm bol} \phi(L_{\rm Bol}, z) dL_{\rm Bol} \frac{dz}{dt} dt, \tag{5.6}$$

where we calculate the bolometric luminosity by adopting the bolometric correction given by the inverse of eq.5.3, ϕ is the bolometric AGN luminosity function at

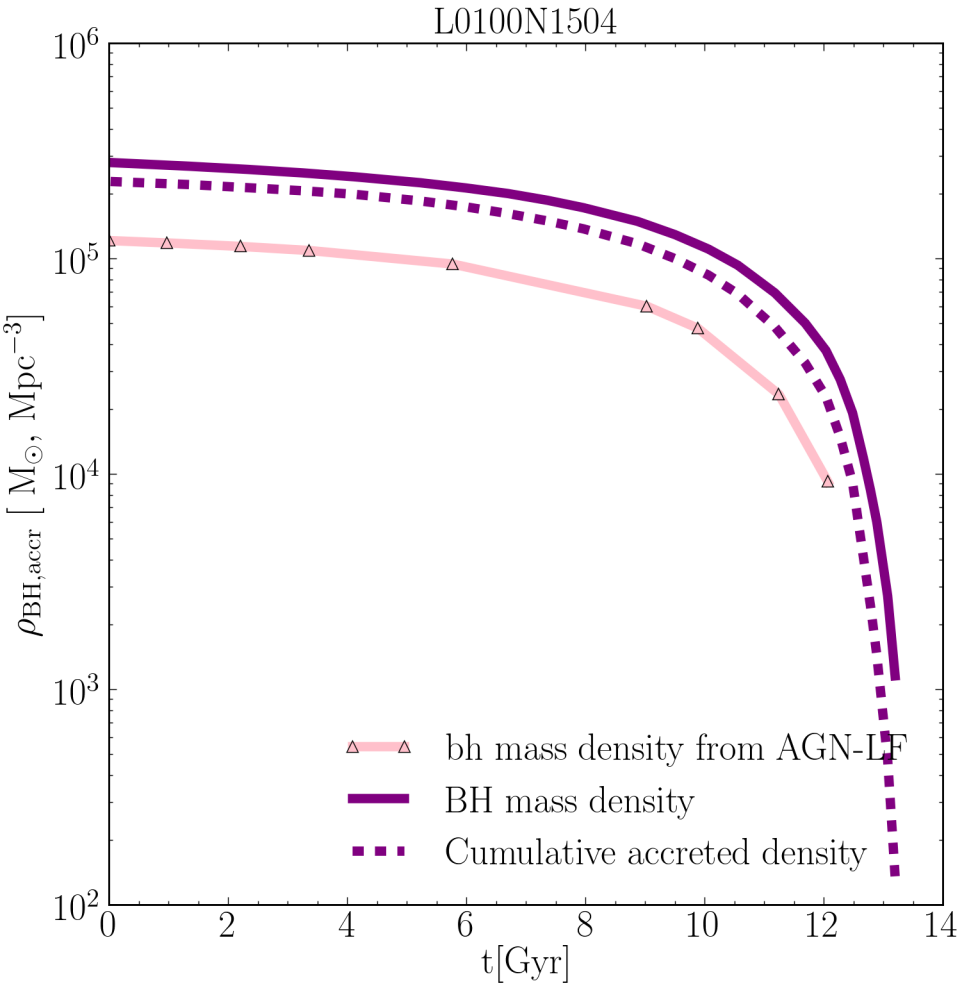

Figure 5.11: Soltan Argument: The evolution of the cumulative accreted BH mass per unit volume. Purple solid line shows the evolution of the total BH mass density; dotted line shows the evolution of cumulative accreted BH mass density (mass built up by gas accretion with the full time resolution in the simulation) and pink solid line shows the BH mass density obtained by integrating the AGN luminosity function (partial time resolution) and with an energy-to-mass conversion factor of $\epsilon = 0.1$. The discrepancy between the evolution of the cumulative accreted BH mass density and the total BH mass density is less than 20%. This result indicates that most of the mass in BHs is built up via gas accretion consistent with observations. However, the pink line is below the dotted line by 50% percent. That illustrates that the AGN luminosity function partially captured the variability of AGNs reached in the simulation.

a given redshift and luminosity and ϵ is the radiative efficiency. In the case of the simulation, the cumulative accreted BH mass that corresponds to the cumulative mass built up by gas accretion, is stored every time that BHs accrete. Using the cumulative accreted BH mass allow us to track the contribution by gas accretion to the global build-up of the BH mass in the full time resolution that the simulation can reached. This exercise also allows us to quantify the AGN activity somehow that we can not capture via the AGN luminosity functions.

Fig 5.11 shows the evolution of the global BH mass density (purple solid line) and the evolution of the cumulative accreted BH mass (purple dotted line). As expected, the discrepancy increases with time, presenting an offset of 10% at $z = 0$. This small discrepancy demonstrates that most of the build up of the local BH mass density is acquired by gas accretion across time and only a tiny fraction of the local BH mass density is given by the initial mass where BHs formed.

Fig 5.11 also includes the BH mass density by integrating the bolometric AGN luminosity functions across time (pink solid lines). The BH mass density estimated by this method is lower by 50% in comparison to the cumulative accreted BH mass. This discrepancy illustrates, as we discussed in section 5.5.2, the fact that the AGN luminosity functions can not capture the full variability of the brightest objects.

5.8 Distribution of Eddington ratio $\lambda_{\rm Edd}$

To explore the complete population of BHs which are accreting, Fig 5.12 provides the predicted logarithmic density distribution of $\lambda_{\rm Edd}$. We refer to the distribution of $\lambda_{\rm Edd}$ as $\log\,\phi(\log\lambda_{\rm Edd}) = \log {\rm d}n/{\rm dlog}\,\lambda_{\rm Edd}$. Fig 5.12 shows the distribution of log Eddington ratio, $\lambda_{\rm Edd}$, for various redshifts from $z = 0$ to $z = 6$. Coloured shaded regions represent the different regimes of accretion that we have defined previously. It is immediately apparent from the figure that the Eddington ratio distribution evolves strongly as redshift decreases. For $z \geq 2$, the normalization of the Eddington ratio distribution increases over the complete range of $\lambda_{\rm Edd}$.

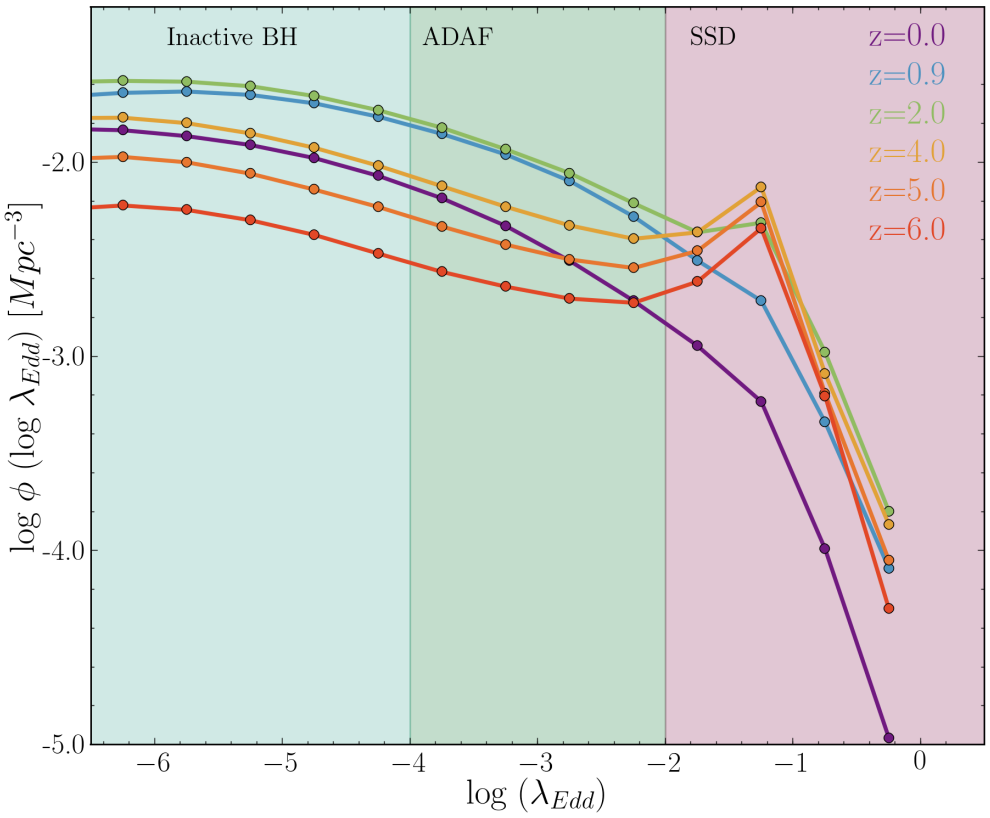

Figure 5.12: Evolution of the Eddington ratio distirbution $\lambda_{\rm Edd} = L_{\rm Bol}/L_{Edd}$ for various redshifts from $z = 0.$ to $z = 6$ (coloured lines). The coloured shaded regions represent the distinct accretion regimes: red for SSDs, green for ADAFs and cyan for inactive BHs. The normalization of the Eddington ratio distribution increases from $z = 6$ to $z = 2$, over the complete range of $\lambda_{\rm Edd}$. A peak is shown at $\log \lambda_{\rm Edd} = -1.2$, which is less prominent as redshift decreases. Toward lower redshifts a more pronounced decline is shown in BHs accreting as SSDs. This suggests that the global activity of AGNs is higher at high redshifts and specifically the brightest AGNs are brighter at higher redshifts.

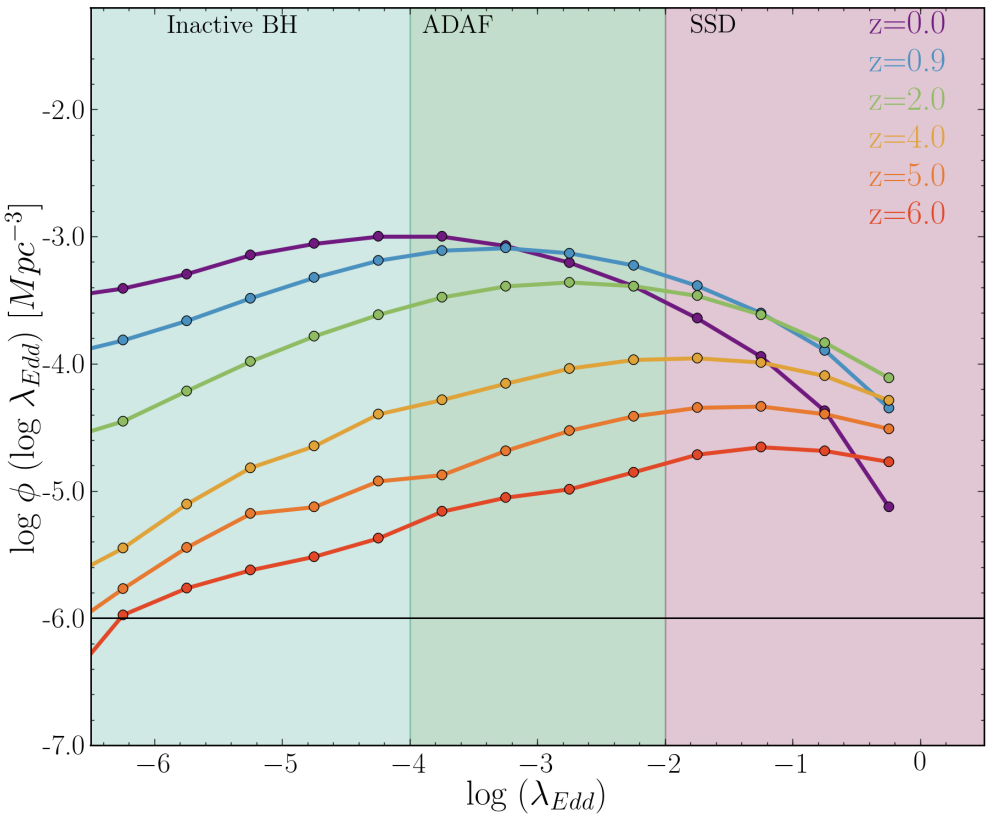

Figure 5.13: Evolution of the Eddington ratio distribution for various redshift from $z = 0.0$ to $z = 6.$. The same notation as Fig 5.12. It differs from that figure in that only BHs with $M_{\rm BH} > 10^6 {\rm M}_\odot$ are considered here. The normalization of the high-z Eddington ratio distribution is much lower and the peak at $\log \lambda_{\rm Edd} = -1.2$ seen in Fig 5.12 is not present anymore. While the evolution of the Eddington ratio distribution at lower redshift remains unchanged (the normalization decreases with increasing z and decreasing SSDs as redshift increases). Toward high redshifts, the normalization and shape are affected by the $M_{\rm BH}$-cut, presenting a power law. However, the normalization increases with increasing redshift.

The Eddington ratio distribution shows one prominent peak at $\log \lambda_{\rm Edd} \sim -1.2$. This peak becomes less prominent as redshift decreases. For $\log \lambda_{\rm Edd} \leq -2$, BHs contribute to the AGN luminosity function and the peak at $\lambda_{\rm Edd} \sim -1.2$ is mainly constituted by a population of small BHs that are accreting, however, they contribute to the faintest end of the luminosity functions ($L_{\rm HX} < 10^{42}$erg s^{-1}) which is affected by the seed mass.

Toward lower redshifts, the normalization decreases, presenting the largest decrease from $z = 0.0$ to $z = 0.9$ over the complete $\lambda_{\rm Edd}$ range by up to 0.4 dex. A more pronounced sharp decline is seen for BHs accreting at $\lambda_{\rm Edd} > 0.01$ with increasing redshift. This evolution of the Eddington ratio distribution for $\log \lambda_{\rm Edd} > -2$ illustrates the downsizing trend that we discussed in Fig 5.9: the peak of the density of the faintest AGNs takes place at $z \sim 1.0$ ($\log (z+1)$=0.3), whereas the peak of the brightest objects occurs at higher redshift.

To further investigate the effects of the BH population with mass close to the seed mass on the Eddington rate distribution, we include Fig 5.13. This figure is a version of Fig 5.12, but excluding BHs with mass $< 10^6 {\rm M}_\odot$. While the normalization of the Eddington ratio distribution is much lower ($\phi \sim 10^{-6} - 10^{-5} {\rm Mpc}^{-3}$) for $z > 2$, the trend that we have discussed previously is more or less preserved. The normalization of the Eddington ratio distribution increases up to redshift $z = 1$ over a wide range of $\lambda_{\rm Edd}$, apart from accreting BHs with $\log \lambda_{\rm Edd} > -1.2$. The density of such BHs starts to decline from $z = 2$ instead of $z = 1$ and that is more consistent with the peak of the density of the brightest AGNs than we have seen in the evolution of the AGN density in hard X-ray band (see Fig 5.9). Different trend is seen for accreting BHs with $\lambda_{\rm Edd} < -3$ (inactive and ADAFs) when only BHs with $M_{\rm BH} > 10^6 {\rm M}_\odot$ are considered. Their density continue increasing as redshift increases which suggests that BHs accreting as ADAFs or inactive are preferentially found at lower redshift.

In summary, the majority of AGNs at $z = 0$ are hardly radiating at or near Eddington limit which is qualitatively in agreement with several observational studies using type-1 quasars from SDSS survey (ie. Kelly & Shen 2013).

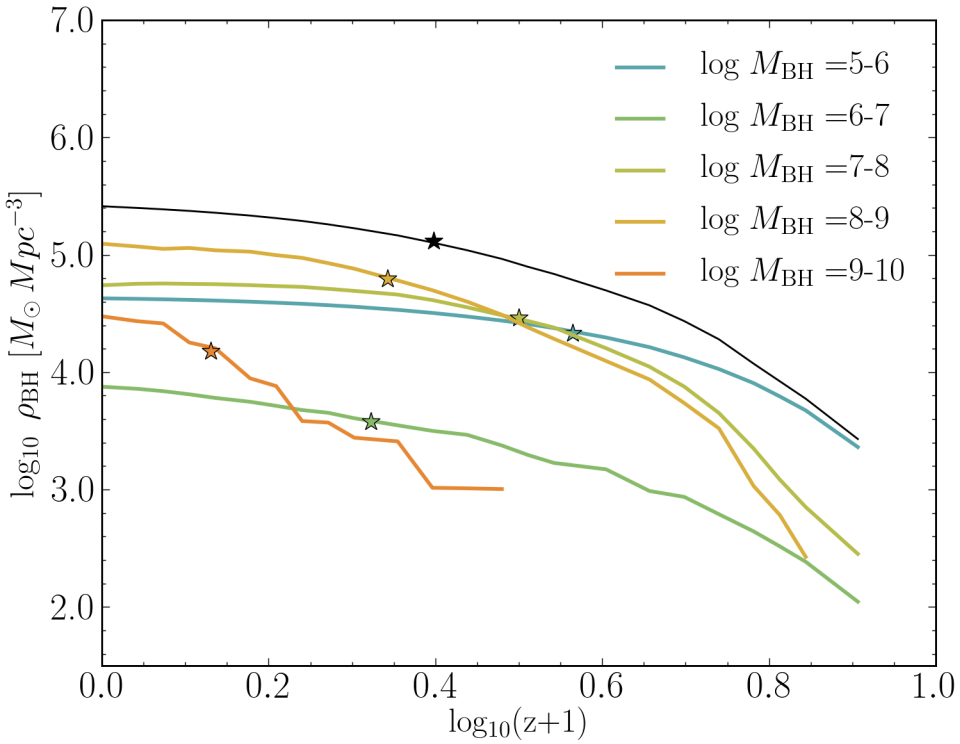

Figure 5.14: The evolution of BH mass per unit volume for different BH mass bins. Different colours represent different mass bins as indicated in the plot. The plot shows the *hierarchical* growth of the BHs where *hierarchical* growth is defined as the build-up of small BHs occurs at high redshift and then the build-up of the most massive BHs occurs later on. As an illustration, we show the pattern of the stars which represent half of the local BH mass density for a given BH mass. Half of the BH mass density of the smallest BHs is at $z > 3$ while half of the mass for the most massive BHs occurs at $z < 0.4$.

5.9 The global growth of BHs

In this section we will show the global BH growth and BH activity as a function of redshift. Fig. 5.14 shows the evolution of the global BH mass density and the contribution from different BH populations (that are divided into bin mass) across time.

At high redshift($z > 2.58$, $\log(z+1) > 0.8$), the main contribution to the total BH density is dominated by small BHs with $M_{\rm BH} = 10^5 - 10^6 {\rm M}_\odot$ (light blue line). More massive BHs are formed and their mass density increases through cosmic time. When BHs with $M_{\rm BH} = 10^5 - 10^6 {\rm M}_\odot$ have built up half of their

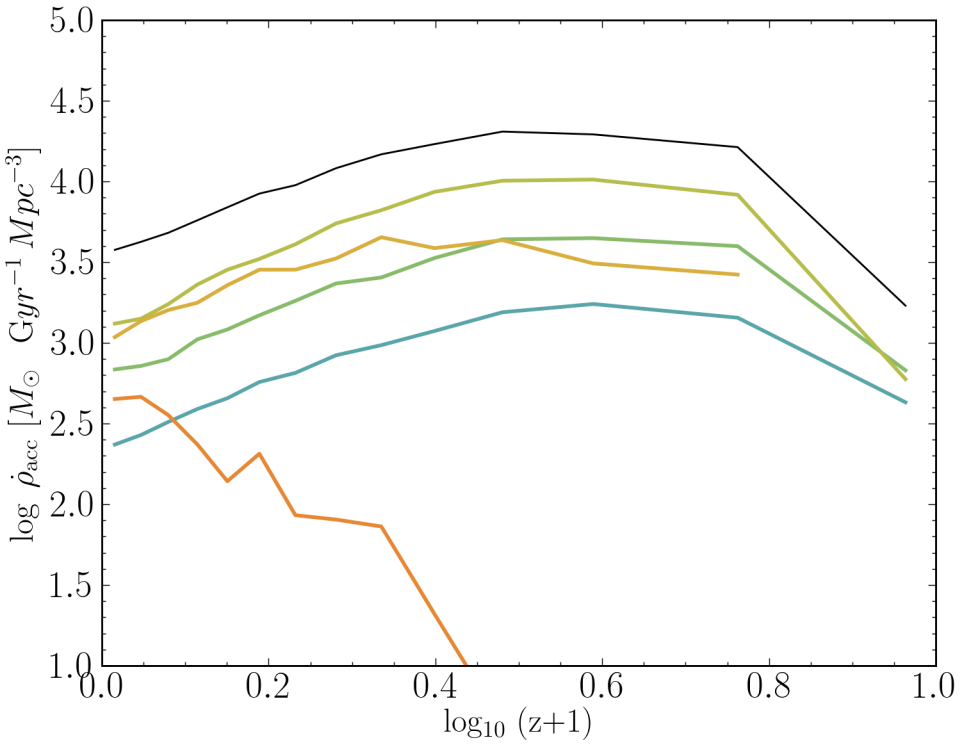

Figure 5.15: The evolution of global accretion rate per unit volume for different BH mass bins where the global mass accretion rates correspond to the average mass accretion rate in 1 Gyr. This is only with the purpose of visualising the general trends since mass accretion rates seem to be noisy. Different colours represent different mass bins as indicated in Figure 5.14. The plot shows a peak at $z = 2$ in accordance with observational studies. The most active BHs have a mass of $10^{7-8}\mathrm{M}_\odot$ while little contribution comes from the most massive BHs. This corroborates our previous results that the most massive BHs are not the most active population.

mass, more massive BHs have been formed. At $z = 3 - 2$ ($\log(z + 1) = 0.5 - 0.6$), the BH mass density in $M_{\rm BH}$ bins between $10^7 - 10^8\mathrm{M}_\odot$ (green-orange line) and $10^8 - 10^9\mathrm{M}_\odot$ (orange line) become equally significant as that from the small BHs. At $z = 2$ ($\log(z + 1) \sim 0.5$), the population of the most massive BHs (10^9-$10^{10}\mathrm{M}_\odot$) has already been assembled and their density continues to rise at lower redshifts. At $z = 1.5$ ($\log(z + 1) = 0.4$, $\sim 10^5$ Gyrs look back time), half of the present-day BH mass density (black stars) has been formed where the main contribution to the global BH mass density comes from BHs with mass 10^8-$10^9\mathrm{M}_\odot$. Toward lower redshifts, the population of the most massive BHs continues growing, building

half of their mass at $z = 1.2$ ($\log(z+1) \sim 0.35$) for $M_{\rm BH} = 10^{8-9}{\rm M}_{\odot}$ and $z \sim 0.4$ ($\log\,(z+1) \sim 0.15$) for $M_{\rm BH} = 10^{9-10}{\rm M}_{\odot}$. The results above show that the BH growth is hierarchical, by that we mean that the small BHs grow first and then most massive BHs grow later. These results suggest that even though the AGN activity present a downsizing effect, this does not contradict a hierarchical growth of BHs.

Fig. 5.15 shows the evolution of global BH accretion rate per unit volume for different BH populations (colours correspond to those in fig 5.15) which are related to the activity of AGNs. Here, the BH accretion rates per unit volume are calculated as the average accretion rates in 1 Gyr. The purpose of the plot is to visualise the general trends of the BH accretion rates as a function of redshift, since the BH accretion rates can be very noisy from consecutive snipshots. A notable feature is that BHs in the mass bins $10^5 - 10^6{\rm M}_{\odot}$ (light blue lines), $10^6 - 10^7{\rm M}_{\odot}$ (cyan line) and $10^7 - 10^8{\rm M}_{\odot}$ (light green line) have similarities in their accretion history which peaks at $z \sim 2$ ($\log(z+1) = 0.5$). The BHs with mass of $10^7 - 10^8{\rm M}_{\odot}$ are the most active BHs through time and the total BH accretion rates per unit volume peaks at $z = 2$, this is consistent with results from observational studies of the global AGN activity across time. As we expect, the most massive BHs with $M_{\rm BH} > 10^8{\rm M}_{\odot}$ (orange and red colours) have lower contribution to the total BH accretion rate.

This plot visualises the evolution that we have previously found in the evolution of the BH mass function and in the evolution of the space density of AGNs namely that BHs can grow hierarchically while AGN evolution presents a downsizing pattern. Something interesting is that the most massive BHs are not powering the most luminous AGNs and in fact they contribute little to the total mass accretion rates.

5.10 Connection between AGN activity and halo

In a previous section, we showed that the simulation presents the *downsizing* of AGNs that is consistent within the observational constraints (Hasinger et al., 2005; Hopkins et al., 2006; Aird et al., 2010). Additionally, semianalytic models are able to produce the *downsizing* trend (Fanidakis et al., 2012). In semianalytic models, AGN feedback is given by two different modes that are assumed in one way or another dependent on the properties of the halos that BHs inhabit. A difference from semi analytics, in the BH accretion model and AGN feedback used here, the BH accretion rates are only dependent on the gas properties in the vicinity of the BH. Such BH accretion rates are suppressed when the circular velocity of the gas is larger than sound speed where the gas does not fall onto the BH as rapidly as the Bondi model estimates. As a prediction of the model, BHs in small haloes ($\lesssim 10^{12}\mathrm{M}_{\odot}$) grow differently than BHs residing in more massive haloes. Moreover, in the last chapter, we show that the self-regulation growth of BHs that inhabit the most massive galaxies is preserved, being the binding energy of the halo, the fundamental property that controls the growth of BHs in the most massive haloes. In addition, we speculate that there is a transitional region where the injection of energy by AGN feedback into the haloes is sufficient to affect the properties of the falling gas and this region of transition occurs in halos with a mass similar to the Milky-way host halo mass. One way to investigate how host haloes affect the growth of BHs is by looking at the halos that are inhabited by AGNs. Here, we investigate the halo mass- hard X ray luminosity for the BHs that contribute to the HXRLF.

We show L_{HX} of AGNs as a function of the host halo mass, M_{200}, in Fig 5.16. Here, we show the predicted distribution of AGNs in the L_{HX}-M_{200} plane at various redshifts($z = 0 - 5$). The median of the distribution of AGNs in the L_{HX}-M_{200} plane is shown as purple solid lines for AGNs and the shaded region shows the 10^{th}-90^{th} percentiles of the distribution. In this plot, the resolution in time is not as good as the one that builds the HXRLF because we only account for

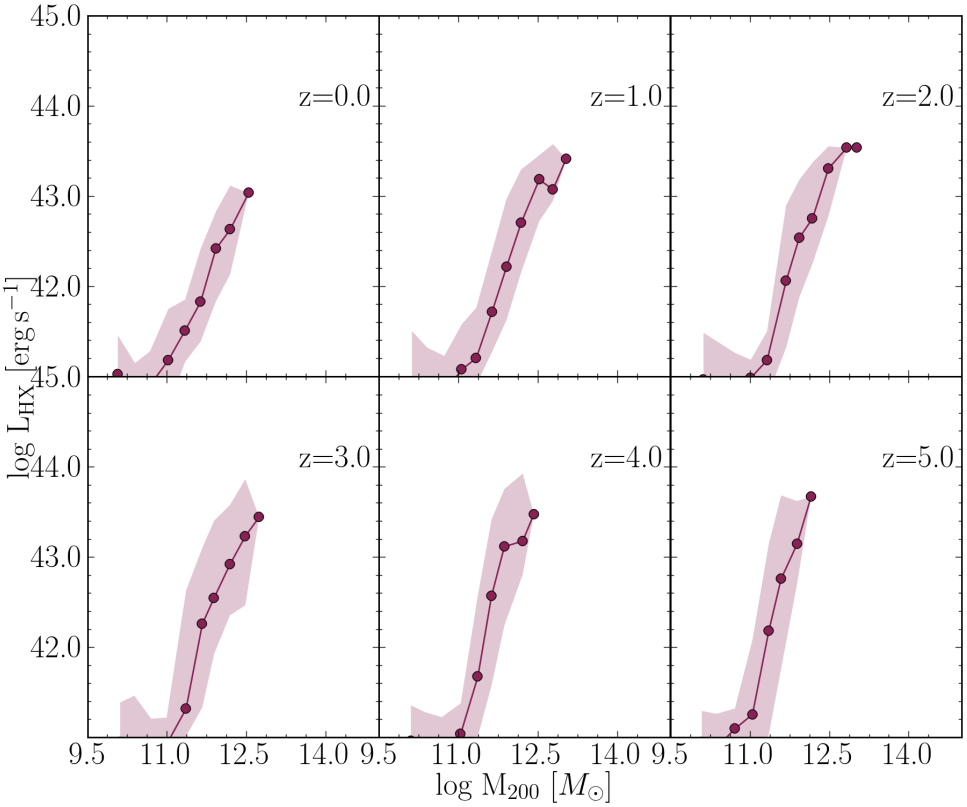

Figure 5.16: M_{200}-$L_{\rm HX}$ relation for various redshifts from $z = 0$ to $z = 5$. The purple solid lines represent the median M_{200}-$L_{\rm HX}$ relation for AGNs powered by SSDs and the shaded regions represent the 10^{th} and 90^{th} percentiles of the distribution. More luminous AGNs live in more massive haloes for halos with $M_{200} \sim 10^{12.5}{\rm M}_\odot$ at all redshifts. These AGNs are being powered by SSDs and contribute to the HXRLF. The slope of the median M_{200}-$L_{\rm HX}$ relation is steeper as redshift increases, indicating that halos for a given mass host more luminous AGNs than those halos at lower redshift.

28 snapshots across time. However, the shape of the HXRLF is not altered by the number of outputs except to reduce the poisson noise in the HXRLF and extend the luminosity range resolved in the simulation a bit further. Therefore, we expect that the M_{200}-$L_{\rm HX}$ relation presented here does not affect our results either.

From Fig. 5.16, in principle, more luminous AGNs are sitting in more massive haloes which M_{200} and $L_{\rm HX}$ varying between $10^{10} - 10^{12.5}{\rm M}_\odot$ and $10^{42} - 10^{44}$erg s^{-1}, respectively. This trend occurs at all redshifts. The slope of the $L_{\rm HX}$-M_{200} relation becomes steeper as increasing redshift. This indicates that more luminous AGNs

are living in the centre of massive haloes for a given mass toward higher redshifts. For instance, halos with $M_{200} = 10^{11.75}\mathrm{M}_{\odot}$ are hosting an AGN shining at $L_{\mathrm{HX}} \sim 10^{42}$erg s^{-1} at $z = 1$, while similar halos are hosting AGNs with $L_{\mathrm{HX}} \sim 10^{43}$erg s^{-1} at $z = 4$.

It is interesting that the most luminous AGNs ($L_{\mathrm{HX}} \sim 10^{44}$erg s^{-1} that corresponds to $L_{\mathrm{Bol}} \sim 10^{46}$erg s^{-1}) are residing in halos with $M_{200} \lesssim 10^{12.5}\mathrm{M}_{\odot}$ for all redshifts. Unfortunately, the size of the simulations does not provide a representative sample of the most luminous quasars to quantitatively estimate the typical halos of the most luminous quasars resides in. However, the prediction obtained from the plot is in agreement with recent studies of observational clustering analysis where suggest that the typical haloes mass in where luminous quasars are found lies in $M_{200} \sim 10^{12}$ and $10^{13}\mathrm{M}_{\odot}$. This is in agreement with recent observational studies that found that quasars inhabit DM haloes of constant mass $\sim 3 \times 10^{12}\mathrm{M}_{\odot}$ at $0.3 < z < 2.2$ by studying quasars in SDSS (Ross et al., 2009).

To investigate the complete population of accreting BHs over a wide range of halo masses, Fig 5.17 shows the Eddington ratio distribution for halos with $M_{200} > 10^{12.5}\mathrm{M}_{\odot}$ as green solid lines and halos below this mass as purple solid lines for various redshifts ($z = 0$ to 5). Note that the plot also accounts for only 28 snapshots which again it does not give us the same resolution in time as in the AGN luminosity functions. However, our results are not affected apart from the statistical noise.

The Eddington ratio distributions peak at different λ_{Edd} for the two groups of halos considered. While the Eddington ratio distribution of AGNs that inhabit halos with $M_{200} \leq 10^{12.5}\mathrm{M}_{\odot}$ presents higher values of λ_{Edd} and peak at $\lambda_{\mathrm{Edd}} \sim -1.2$ (which are BHs powering SSDs), AGNs residing in halos with $M_{200} > 10^{12.5}\mathrm{M}_{\odot}$ tend to have lower values of logλ_{Edd} where their Eddington ratio distribution peaks from log $\lambda_{\mathrm{Edd}} \sim -2$ at $z = 4$ to log $\lambda_{\mathrm{Edd}} \sim -4$ at $z = 0$. These values of the Eddington ratio corresponds to accreting BHs as ADAFs. This trend can be seen at all redshifts apart from those at $z = 4$ and $z = 5$. In those panels, halos with mass $M_{200} > 10^{12.5}\mathrm{M}_{\odot}$ have not been placed in the simulation yet.

Interestingly, the Eddington ratio distributions of the most massive halos seem to undergo more evolution than halos less massive while the peak of Eddington ratio distributions in the low massive halos ($< 10^{12}\mathrm{M}_{\odot}$) tend to have a similar value across time.

The results described above have some implications to the connection of the AGN activity and halo mass. The evolution of the L_{HX}-M_{200} relation along with the evolution of the M_{200}-M_{BH} relation in Fig 4.10 in Chapter 4 shows that the central BH mass in halos below $10^{12.5}\mathrm{M}_{\odot}$ have BH mass $\sim 10^{8}\mathrm{M}_{\odot}$. Such a BH mass corresponds to the critical mass where the BH growth is likely to be self-regulated via AGN feedback that shuts off star formation and quenches gas accretion onto the BH. The evolution of both L_{HX}-M_{200} and M_{200}-M_{BH} relations also imply that the M_{BH}-L_{HX} relation likely evolves with redshift. The slope in both relations becomes steeper toward high redshifts ($z > 2$), implying that halos for a given mass host more massive BHs and then more luminous AGNs for halos below $M_{200} \sim 10^{12.5}\mathrm{M}_{\odot}$. The evolution of both relations toward high redshifts also explains that the peak of the Eddington rate distribution remains approximately constant across time in such halos.

The fact that BHs powering the luminous AGNs inhabit in halos below or up to $M_{200} \sim 10^{12.5}\mathrm{M}_{\odot}$ can be explained in terms of the interplay of the evolution of BH growth and evolution of the halo. The energy injected into the ISM by those BHs is not sufficient in comparison to the binding energy of the halo in a relevant timescale, then the BHs are not able to disrupt the thermodynamic state of the gas or if they are able to disrupt the gas, the cooling time in such halos is too short for the halo to be recovered from AGN feedback. However, once BHs reach a critical mass ($10^{8}\mathrm{M}_{\odot}$) , their host halos have grown ($> 10^{12.5}\mathrm{M}_{\odot}$) sufficiently as well. Therefore, the BHs are able to change the thermodynamic state of the gas because the cooling time is long enough. It is possible that some gas is expelled out of the halo but it can be re-accreted later on.

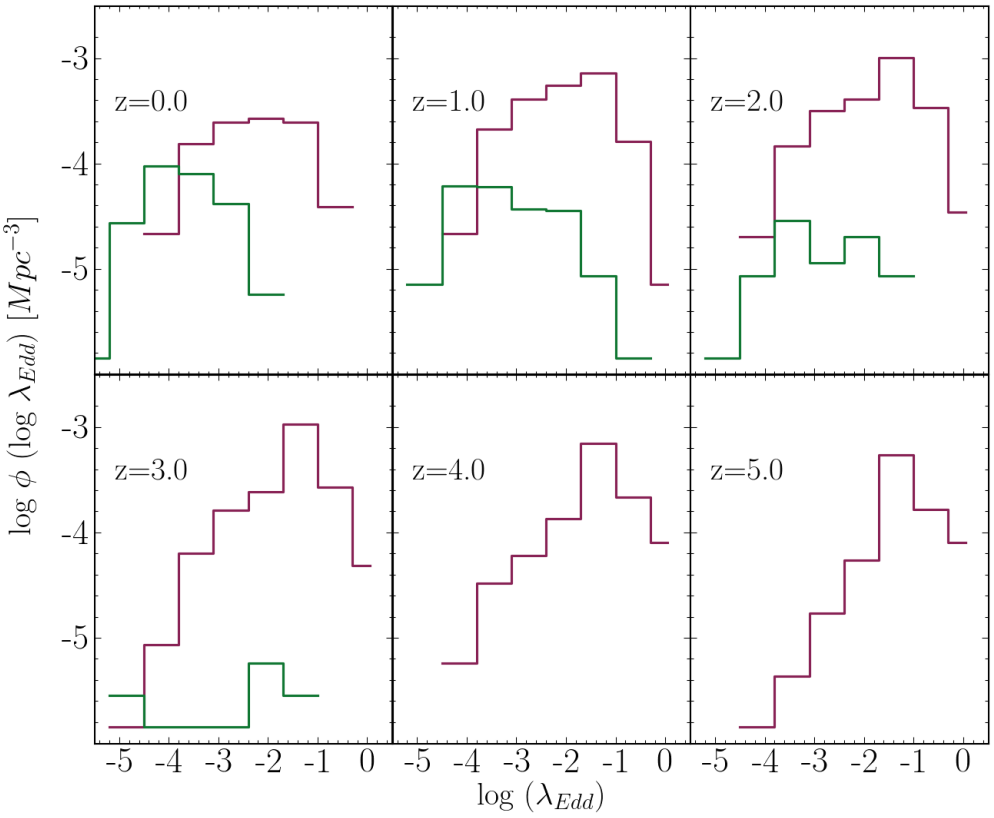

Figure 5.17: The distribution of Eddington ratio $\lambda_{\rm Edd} = L_{\rm Bol}/L_{Edd}$ for AGNs with $L_{\rm Bol} > 10^{41}$erg s^{-1} at various redshifts from $z = 0$ to $z = 6$. Green lines show the distribution of log $\lambda_{\rm Edd}$ for AGNs residing in halos with $M_{200} > 10^{12.5}{\rm M}_{\odot}$ and red lines, the distribution for AGNs in halos $M_{200} \leq 10^{12.5}$. The Eddington ratio distribution for halos $M_{200} < 10^{12.5}{\rm M}_{\odot}$ shows a peak at high values of log $\lambda_{\rm Edd}$ (~ -1.5) while the Eddington ratio distribution for halos below this mass peaks at lower log $\lambda_{\rm Edd}$ values from -4 at $z = 0$ to -2 at $z = 3$.

5.11 Summary and Conclusions

In this chapter, we have analysed mainly a hydrodynamical , fully cosmological simulation of 100 comoving Mpc region (and 50 comoving Mpc region) from $z = 127$ to $z = 0$. The simulation accounts for less than 7 billions of particles with an initial baryonic particle mass of $1 \times 10^6 \mathrm{M}_\odot$ and force resolution of 0.7 proper kpc. This simulation includes a-state-of-the-art galaxy formation subgrid models that include radiative cooling, star formation, reionization, chemical evolution, stellar evolution and mass loss, feedback from star formation and BH growth and AGN feedback which were calibrated to reproduce the observational stellar mass function at $z = 0$, and the efficiency of AGN feedback was set to reproduce the break of the stellar mass function and the normalization of the BH mass-Stellar mass relation. In the last chapter, we also analysed the BH mass function at $z = 0$ that is in excellent agreement with observations as an immediate consequence of the good agreement with the stellar mass function. In this chapter, we focused on some aspects of the AGN evolution and BH growth. In particular, we investigate the prediction of the simulation in the evolution of X-ray AGN luminosities from $z = 5$ to $z = 0$ and the observed downsizing trend in the evolution of the density of AGNs. We stress that the AGN evolution are a prediction of the simulation since it was not considered in the calibration of the subgrid parameters. We only considered one type of AGN feedback in the simulation, therefore we made the distinction between two regimes of accretion as ADAFs and Shakura-Sunyaev (thin) disc (SSD) and inactive BHs in terms of the Eddington ratio. We came to the following conclusions:

- We consider the different contributions of different accreting BH populations to the BH mass function at $z = 0$ and the evolution of BH mass function for such populations. We estimate the average duty cycle of AGNs powered by SSDs by comparing the global BH Mass function to that of SSDs. We obtain the duty cycle is ~ 0.01 overall, which is comparable to observations.

- The soft and hard X ray luminosities were calculated by considering the

bolometric luminosity from the intrinsic mass accretion rates and the bolometric corrections found by Marconi et al. (2004). In the case of soft X ray band, obscuration effects were calculated by observational constraints using the empirical law from Hasinger (2008) which is a function of luminosity with a weak dependence on redshift.

- The AGN luminosity functions were determined with a relatively good resolution time, allowing to capture the variability of intermediate luminous AGNs ($< 10^{44}$erg s^{-1}). This resolution in time was achieved by accounting for 406 outputs across time. However, the full variability of the most luminous AGNs are not captured, resulting in missing the most luminous events in the simulation.

- The resulting hard and soft X-ray luminosity functions are in excellent agreement with observations. To be more specific we find a striking agreement at $z < 1$ in hard X ray bands. In the case of soft X-ray luminosity functions, the agreement is possible when strong obscuration (~ 0.83 obscured AGN fraction) was accounted for in the faint end of the LF whereas the bright end is not significantly affected by obscuration effects. For the brightest objects ($L_{\rm HX} > 10^{44}$) , however, the hard X-ray LF is underestimated because we have not captured the complete variability of the massive objects toward high redshifts.

- As a consequence of the excellent agreement of the X-ray luminosity functions, the simulation can successfully reproduce the *downsizing* of the space density evolution of AGNs. By *downsizing*, we refer to the observational trend seen in the evolution of the space density of AGNs. The evolution of the space density of bright AGNs peak at higher redshifts and the peak shifts toward lower redshifts in the evolution of the space density of fainter AGNs. We find an excellent match for both X ray bands and for objects with X ray luminosities $< 10^{44}$erg s^{-1} at $z \lesssim 1.5$ whereas toward higher redshifts, the predicted space density shows a shallower decline as increasing red-

shift than in observations. However at high redshift there are remaining uncertainties in the exact evolution of the space density of fainter objects. This discrepancy could be attributed to the lack of a representative sample of AGNs at high redshift. Additionally, the evolution of the density of the brightest objects are underestimated. However, it shows a similar shape to that observational constraints, confirming that the full variability of the brightest AGNs can not be captured. The evolution of the space density of AGNs in soft X-ray band is in good agreement with observations where an obscured fraction is considered. This obscured fraction is calculated by observational constraints. Similarly, the evolution of the density of the most luminous AGNs ($> 10^{44}$erg s^{-1}), is underestimated but in a lower degree than that shown in the hard and soft Xray bands.

- We showed the evolution of the Eddington ratio distribution from $z = 6$ to $z = 0$. The Eddington ratio distribution evolves with redshifts. Toward high redshifts, the Eddington ratio distribution increases in normalization over a wide range of Eddington ratios up to $z = 1$. At lower redshifts, the AGNs powered by SSDs ($\log \lambda_{\rm Edd} < -2$) decline whereas BHs accreting as ADAFs and inactive BHs increase as decreasing redshift. The evolution of the Eddington ratio distribution shows *downsizing* signatures as the brightest AGNs are more abundant at higher redshifts that in the Universe today.

- We have investigated the evolution of global BH mass density and BH accretion rate density across time. We have looked at the contributions of the BHs divided into mass bins. We find that the largest contribution to the BH mass density originates from BHs between $10^8 {\rm M}_\odot$ and $10^9 {\rm M}_\odot$ while the smallest contribution comes from small BHs. In the case of the BH accretion rate density (or AGN activity), the most active BH population is BHs with $M_{\rm BH} = 10^7 - 10^8 {\rm M}_\odot$ while the smallest contribution to the global mass accretion rates density comes from the most massive BHs in the simulation. This shows that the downsizing trend of AGNs and the hierarchical growth

of BHs are in agreement with each other.

Finally, we look at the connection of AGN activity and halo mass by studying the distribution of AGNs in $L_{\rm HX}$-M_{200} plane as well the Eddington ratio distributions in halos with masses below and above $10^{12.5}\mathrm{M}_{\odot}$. We find that the AGNs contributing to the HXRLF are more likely to inhabit halos below $10^{12.5}\mathrm{M}_{\odot}$. We also find that the Eddington ratio distribution for haloes with $M_{200} < 10^{12.5}$ peaks at log $\lambda_{\rm Edd} \sim -1.5$ while the Eddington ratio distribution in halos above this M_{200}, peaks between log $\lambda_{\rm Edd} = -2$ for higher redshifts and log $\lambda_{\rm Edd} = -4$ for lower redshifts. This Bi-modality is seen at all redshifts.

The above results suggest that the host halo is related to the quenching of the accretion onto the BHs and this evolves with time . We speculate that in terms of self regulation, the quenching of accretion onto the BHs occurs at a critical BH mass scale. The host halos that host BHs with the critical BH mass scale are halos below $10^{12.5}\mathrm{M}_{\odot}$ in our model. This suggests that the host haloes play a role in the downsizing of the evolution of AGNs. However, the understanding of the underlying physical processes that produce the downsizing will be investigated in a future project.

Chapter 6 | *Conclusions*

In this thesis, we have explored the connection between BH mass and galaxies in a cosmological context. We have used cosmological simulations that are currently one of the most powerful tools for understanding the evolution of the galaxies together with observations. From cosmological initial conditions, it is possible (in principle) to follow the evolution of dark matter along with gas from first principles.

Galaxy formation subgrid models are a vital ingredient that integrates the physical processes that are relevant for galaxy formation but that operates below the scales resolved in the simulation. Such subgrid models include star formation, gas cooling, feedback from star formation, chemical evolution, reionization and BH growth and AGN feedback. By adjusting the parameters of galaxy formation subgrid models we have shown that it is possible to reproduce the fundamental observables of the galaxy population such as the galaxy stellar mass function. These subgrid models are summarised in Chapter 2.

One of the improvements carried out in this thesis includes an extension of the typical BH accretion model (the Bondi accretion model) used in cosmological simulations. Specifically, we have presented a development of the subgrid accretion model of Booth & Schaye (2009) based on Springel et al. 2005 that takes into account the angular momentum of the accreting gas using the local SPH kernel to estimate the circular speed at the Bondi radius and to define the circularisation radius of the material passing through the Bondi radius. This creates an additional timescale in the problem which characterizes the transport of material through the disc and the fraction of this material ejected out of the disc before it is accreted by the BH. We incorporate this new timescale into a revised accretion rate estimate that can be simply implemented as a subgrid model in cosmological simulations.

We compare the behaviour of cosmological simulations using both the Booth & Schaye (2009) description and the revised model that accounts for angular momentum. The cosmological simulations were run in P-Gadget 3 and include gas cooling, metal enrichment, star formation and supernova feedback that we keep fixed in both models. We show that simulations that do not account for the circulation of gas in the neighbourhood of the BH result in self-regulation of the gas supply by BH growth rather than star formation. As a result, BH masses correlate well with the parent halo over a wide range of scales, but self-regulation by the BH results in insufficient star formation to match the observed dependence of stellar mass fraction on halo mass.

In contrast, when the angular momentum is taken into account, we find that BH accretion rates are strongly suppressed in haloes less massive than $10^{12}\mathrm{M}_{\odot}$, allowing stars to form efficiently. This leads to a strong division into two regimes of galaxy formation. Below a halo mass of $\sim 10^{12}\mathrm{M}_{\odot}$, we find that the presence of the BH has little effect on forming galaxies, but above this halo mass star formation is suppressed and galaxies grow much more slowly in stellar mass. The model broadly matches the observed stellar mass fractions of haloes and reproduces the expected correlation between the stellar velocity dispersion and BH mass (McConnell & Ma, 2012). The distribution of BH accretion rates also seems compatible with that observed (Aird et al., 2012). The model thus provides a promising representation of the real Universe.

We speculate that there are two critical factors that establish the break in the galaxy mass function. The first factor is the ability of the BH to accrete the material. Accounting for the angular momentum of the material surrounding, the BH suppresses accretion from quiescent discs allowing the growth of the galaxy in galactic mass haloes to be regulated by star formation. The second factor is the response of the halo to outbursts of BH feedback and growth. This introduces a strong dependence on the ratio of cooling time to dynamical time of the halo through the ability of the halo to recover from a brief episode of energy injection from the BH. In lower mass haloes the cold gas disc surrounding

the BH quickly recovers because of the rapid supply of fresh material from the surrounding cosmic web. In high mass haloes, the recovery of the halo is slower than the timescale between AGN outbursts. As a result star formation in the most massive galaxies is strongly suppressed and the break in the stellar mass function is established.

This description of BH accretion is a critical point to further explore the evolution of BHs and their connection with the evolution of galaxies. We achieved that by using a cosmological simulation that is large enough to provide a representative BH population.

In Chapter 4, we have analysed a hydrodynamical, fully cosmological simulation of 100 comoving Mpc region from $z = 127$ to $z = 0$. The simulation accounts for less than 7 billions of particles with an initial baryonic particle mass of $1 \times 10^8 \mathrm{M}_\odot$ and force resolution of 0.7 proper kpc. This simulation includes a state-of-the-art galaxy formation subgrid models that include radiative cooling, star formation, reionization, chemical evolution, stellar evolution and mass loss, feedback from star formation, BH growth and AGN feedback. Altogether, they were calibrated to reproduce the observational galaxy stellar mass function at $z = 0$. Particularly, the BH growth and AGN feedback, that are similar in spirit to those used in chapter 3, were set to reproduce the break of the galaxy stellar mass function and the normalization of the BH mass-stellar mass relation at $z = 0$.

The agreement between the galaxy stellar mass function and observational data is as good as 0.2 dex in difference. This is the highest level of agreement with data that cosmological simulations have achieved. Similarly, we find good agreement between the BH mass function and the estimates from observational data within the observational discrepancies. This is a direct consequence of the good agreement of the galaxy stellar mass function and BH mass- stellar mass relation. Because BHs self-regulate their growth, the $M_{\rm BH}$-$M_{\rm star}$ relation at $z = 0$ is also in good agreement with data for the most massive galaxies, where $M_{\rm BH}$ is the central massive BHs. We also find reasonable agreement with observations in the other BH scaling relations $M_{\rm BH}$-M_{200} and $M_{\rm BH}$-σ_* at z=0.

We explore the evolution of the BH scaling relations even though currently there are no clear observational constraints. This is because of the selection effects in the current sample of AGNs available at high redshifts. In addition to this, the challenges that determine the BH mass and the properties of their host galaxies increases the uncertainties in observational constraints.

We find that the BH mass-stellar mass relation undergoes no significant evolution up to $z = 2$. Toward higher redshifts, the BH mass-stellar mass relation presents a steeper slope in galaxies with $M_{\rm star} = 10^{9.6-10.6}{\rm M}_{\odot}$ along with a prominent break that shifts to lower stellar masses with increasing redshift. Similarly, we find no evolution in the $M_{\rm BH}$-M_{200} relation at $z < 2$ for high mass haloes ($M_{200} > 10^{12}{\rm M}_{\odot}$) while halos below this mass are inhabited by typically less massive BHs as redshift increases. A steeper relation for massive haloes is found toward higher redshifts while a steep rise is presented in haloes between $10^{11.5-12.0}{\rm M}_{\odot}$. The evolution of high mass halos and their BHs can be explained in terms of self-regulation growth with the binding energy of the halos as the fundamental property (Booth & Schaye, 2010). In contrast, in the evolution of the low mass halos and their BHs, it is likely that self-regulation is not applied.

In Chapter 4, we also look at the connection of the properties of the falling gas in the inner part of the halo such as SFR and non-star-forming gas, as a function of halo mass. Overall, we find a large scatter in the relation for halos below $10^{11.5}{\rm M}_{\odot}$ and a small scatter for halos above $10^{12.5}{\rm M}_{\odot}$. We compare the scatter of the relation with the ratio of the cumulative accreted BH mass to halo mass that is linked to the ratio of energy injected into the ISM to binding energy of the host halo. We note that the ratio, apparently, does not have any relation with the scatter in the two groups of halos: in small haloes ($10^{11.5}{\rm M}_{\odot}$), it is due to the combined effect that BHs are too small to affect the halos in a relevant timescale along with halos are efficient to cool gas; in the massive haloes, the scatter is small because BHs self regulate their growth. We find a transitional region between halos with $10^{11.5} - 10^{12.5}{\rm M}_{\odot}$, where the scatter of the relations is likely to be related to the ratio of the cumulative accreted BH mass to halo mass. This region may frame

the transition between halos where the self-regulated BH growth takes place and halos where the self-regulated growth is not strong. This result suggests that the host halo plays an important role in determining the growth of BHs. Further investigation is required to understand the physical process taking place in such a range of halos.

Finally in Chapter 5, we explore some aspects of the evolution of AGNs and BH growth across time. In particular, we analyse the evolution of the X-rays luminosity in soft and hard X ray bands. We find that the resulting hard and soft X-ray luminosity functions are in excellent agreement with observations toward low redshifts. We find that at high redshift the difference becomes not more than 0.5 dex over the whole range of luminosities that the simulation can match ($\sim 10^{42-44}$erg s^{-1}). In the case of the soft-X rays, we confirm that an obscured fraction of AGNs is necessary to reproduce the faint end of the soft X ray luminosity function.

As a consequence of the excellent agreement of the X-ray luminosity functions, the simulation can successfully reproduce the *downsizing* of the space density evolution of AGNs in both X rays bands. By *downsizing*, we refer to the observational trend which have been seen in which the evolution of the space density of bright AGNs peaks at higher redshifts and the peak shifts toward lower redshifts in the evolution of the space density of fainter AGNs. We find an excellent match for both X ray bands and for objects with X ray luminosities $< 10^{44}$erg s^{-1} at $z \lesssim 1.5$. Toward higher redshifts, the predicted space density shows a shallower decline as increasing redshift than in some observations. However, at high redshift there are remaining uncertainties in the exact evolution of the space density of fainter objects. Additionally, the evolution of the density of the brightest objects is underestimated, but it shows a similar shape as observational constraints. This is because we are missing the most luminous events in the simulation.

We also examine the Eddington ratio distributions which are consistent with the evolution of the hard X ray luminosity functions and evolution of the space density of AGNs. Toward high redshifts, the Eddington ratio distribution in-

creases in normalization over a wide range of Eddington ratios up to $z = 1$. At lower redshifts, the AGNs powered by SSDs ($\log \lambda_{\rm Edd} < -2$) decline whereas BHs accreting as ADAFs and inactive BHs rise.

Finally, we inspect the possible connection between AGN activity and halo mass. We find that the AGNs contributing to the HXRLF are more likely to inhabit halos below $10^{12.5}\mathrm{M}_{\odot}$. We also find a large difference in the Eddington ratio distributions for BHs living in halos above $> 10^{12.5}\mathrm{M}_{\odot}$ and BHs living in halos below this mass. The eddington ratio distribution for haloes with $M_{200} < 10^{12.5}$ peaks at higher Eddington ratios, most BHs living in these haloes contribute to the AGN luminosity functions while the Eddington ratio distribution in halos above this M_{200}, peaks at lower values. This bi-modality in the Eddington ratio distribution is seen at all redshifts. This suggests that the host halo is related to the quenching of the accretion onto the BHs. We speculate that in terms of self regulation, the quenching of accretion onto the BHs occurs at a critical BH mass scale. The host halos that host BHs with such critical BH mass scale are halos below $10^{12.5}\mathrm{M}_{\odot}$ in our model. This suggest that the host haloes play a role in the downsizing of the evolution of AGNs. However, the understanding of the underlying physical processes that produce the downsizing will be investigated in a future project.

6.1 Future prospects

Several topics we have investigated in this thesis concerned the BH-galaxy connection in the cosmological context. We have created a simulated Universe where it is possible to study the linked evolution of BHs and galaxies consistently since the fundamental observables between galaxies and BHs are obtained in good agreement in comparison with observations so far. However, there are some open questions regarding the physical processes underlying the observational phenomena that need to be addressed in the future:

- Regarding the extended subgrid BH accretion model, we will investigate

the degeneracy between the assumed ISM substructure parameter, β, and the viscous parameter, $C_{\rm visc}$, in more detail and explore larger variations of $C_{\rm visc}$. Clearly, one of the most important future steps is to base the choice of these parameters on finer-scale simulations that simultaneously resolve the circularisation radius and the multiphase structure and turbulence of the interstellar medium around the BH and preserve the conditions of cosmological scales. In the foreseeable future, such a multiscale approach seems the only feasible route to capture simultaneously the microphysics of BH accretion and the large-scale distribution of galaxies and quasars.

- Regarding the theorical framework for the connection of BH-galaxies, we will investigate the physical origin of the downsizing trend that we have seen in our simulation. Since the different modes of BH growth (AGN feedback) result naturally from resolving the hydrodynamic equations and not because of any explicit mode of feedback implemented or dependency on the halos properties, the downsizing trend of AGNs is caused by an underlying physical process and it requires to be explored. In particular, to study the different processes that AGNs can be triggered. For example what the relative roles of the mergers and secular processes are.

- We want to exploit the predictive power of the simulations by studying the diverse physical processes that drives the BH scaling relations and how they vary by environment in order to determine the characterization of a representative BH population.

- In a further future, we will investigate the relation between the SFR and AGN activity in an object-by-objects basis, since both physical processes have different timescales. While AGN activity has a short timescale in comparison to SFR, there is not a clear correlation as expected from their global evolutions which present similarities.

In conclusion, this thesis demonstrates that numerical simulations are one of the most powerful resources to simultaneously study galaxy formation and AGN

evolution so far. Numerical simulations are able to provide a robust framework in which AGN evolution and galaxy formation can be consistently studied. The ability of the cosmological simulation to reproduce the fundamental observables of both galaxy and AGN populations at the level presented in this thesis, it was only achieved by semianalytics models of galaxy formation with the advantage of making fewer simplifying assumptions. This shows the large capabilities of numerical simulations have achieved and it will continue in the near future. This will enable to investigate specific questions in a consistent framework with observations than so far it has been difficult to address.

Yetli Rosas Guevara

Durham, 2014

Bibliography

Aarseth, S. J., 1963, MNRAS, 12, 223.

Abramowicz, M. A. , Chen, X. , Taam, R. E., 1995, ApJ, 452, 379.

Aird, J. , Nandra, K. , Laird, E. S. and Georgakakis, A. , Ashby, M. L. N. , Barmby, P. , Coil, A. L. , Huang, J.-S. , Koekemoer, A. M. , Steidel, C. C. and Willmer, C. N. A. 2010, MNRAS, 401, 2531.

Aird J., Coil A. L., Moustakas J., Blanton M., R.,Burles S. M., Cool R. J., Eisenstein D. J. and Smith M. S. M. *et al.*, 2012, ApJ, 746, 90.

Anglés-Alcázar D., ÃŰzel, F. and Davé R., 2013, ApJ 770, 5,[arXiv:1303.5058 [astro-ph.CO]].

Aguirre, A. , Schaye, J. , Hernquist, L. , Kay, S. , Springel, V. and Theuns, T., 2005, ApJ, 620, L13

Angulo R. E. , Lacey C. G., Baugh C. M. and Frenk C. S, 2009, MNRAS, 399, 983.

Angulo R. E., Springel V., White S. D. M., Cole S., Jenkins A., Baugh C. M. and Frenk C. S., 2012, MNRAS, 425, 2722.

Antognini, J. , Bird, J. and Martini, P., 2012, ApJ, 756, 116.

Baldry, I. K. , Driver, S. P. , Loveday, J. , Taylor, E. N. and Kelvin, L. S. and Liske, J. and Norberg, P. and Robotham, A. S. G. and Brough, S. and Hopkins, A. M. and Bamford, S. P. and Peacock, J. A. and Bland-Hawthorn, J. and Conselice,

C. J. and Croom, S. M. and Jones, D. H. and Parkinson, H. R. and Popescu, C. C. and Prescott, M. and Sharp, R. G. and Tuffs, R. J., 2012, MNRAS, 421, 621.

Ballantyne, D. R. and Shi, Y. and Rieke, G. H. and Donley, J. L. and Papovich, C. and Rigby, J. R., 2006, ApJ, 653, 1070.

Balsara, D. S., Journal of Computational Physics, 121, 357.

Bandara, K., Crampton, D., Simard, L., 2009, ApJ, 704, 1135.

Barai P., Viel M.; Murante G., Gaspari M., Borgani S., 2013, MNRAS, Advance access 20.

Barger A. J., Cowie L. L., Capak P., Alexander D. M., Bauer F. E., Brandt W. N., Garmire G. P., Hornschemeier A. E., 2003, ApJ, 584, L61.

Barger A. J., Cowie L. L., 2005, ApJ, 635, 115

Barnes, J., Hut, P. , 1986, Nature,324,446

Bell E. F., McIntosh D. H., Katz N., Weinberg M. D., 2003, ApJS, 149, 289.

Benson A. J., Bower R. G., Frenk C. S., Lacey C. G., Baugh C. M., Cole S., 2003, ApJ, 599, 38.

Benson A. J., 2010, Phys. Rep., 495, 33.

Bertone G., Hooper D., Silk J., 2005, Physics Reports, 405 , 279.

Bîrzan L., Rafferty D. A., McNamara B. R. Wise M. W. and Nulsen P. E. J., 2004, 607, 800.

Birzan L. , Rafferty D. A. , Nulsen P. E. J. ,McNamara B. R., Rottgering H. J. A., M. W. Wise and R. Mittal, MNRAS, 2012, 427, 3468

Bigiel F. , Leroy A., Walter F., Brinks E. de Blok W. J. G., Madore B. and Thornley M. D., 2008, AJ, 136, 2846.

Blumenthal G.R., Faber S.M., Primack J.R., Rees M.J., 1984, Nature 311, 517.

Bondi H., Hoyle F., 1944, MNRAS, 104, 273.

Booth C. M., Schaye J., 2009, MNRAS, 398, 53.

Booth C. M., Schaye J., 2010, MNRAS, 405, L1.

Booth C. M. & Schaye J., 2011, MNRAS, 413, 1158

Bower R. G., Benson A. J., Malbon R., Helly J. C., Frenk C. S., Baugh C. M., Cole S., Lacey C. G., 2006, MNRAS, 370, 645.

Bower R. G., McCarthy I. G., Benson A. J., 2008, MNRAS, 390, 1399.

Bower R. G., Vernon I., Goldstein M., Benson A. J., Lacey C. G., Baugh C. M., Cole S., Frenk C. S., 2010, MNRAS, 407, 2017.

Bower R. G., Benson A. J. and Crain R. J., 2012, MNRAS, 422, 2816.

Boyle, B. J. and Terlevich, R. J., 1998, MNRAS, 293, L49.

Bromley J. M., Somerville R. S., Fabian A. C., 2004, MNRAS, 350, 456.

Bryan, G. L. and Norman, M. L., 1998, ApJ, 495, 80.

Buat-Menard, V., Hameury, J.-M., Lasota, J.-P., 2001, A& A 369, 925.

Cannizzo, J.K., 2001, ApJ, 556, 847.

Cannizzo, J.K., 2001, ApJ, 561, L175.

Cannizzo, J.K., Chen, W., Livio, M., 1995, ApJ, 454, 880.

Cen, R. and Ostriker, J., 1992,ApJ, 393, 22.

Chabrier, G., 2003, PASP, 115, 763.

Cisternas, M. and Jahnke, K. and Bongiorno, A. and Inskip, K. J. and Impey, C. D. and Koekemoer, A. M. and Merloni, A. and Salvato, M. and Trump, J. R., 2011, ApJ, 741, L11.

Cole, S., Norberg, P., Baugh, C.M., Frenk, C.S., Bland-Hawthorn, J., Bridges, T., Cannon, R., Colless, M., Collins, C., Couch, W., Cross, N., Dalton, G., Propris, R.D., Driver, S.P., Efstathiou, G., Ellis, R.S., Glazebrook, K., Jackson, C., Lahav, O., Lewis, I., Lumsden, S., Maddox, S., Madgwick, D., Peacock, J.A., Peterson, B.A., Sutherland, W., Taylor, K., 2001, MNRAS, 326, 255.

Cole, S., Percival, W.J., Peacock, J.A., Norberg, P., Baugh , C.M., Frenk, C.S., Baldry, I., Bland-Hawthorn, J., Bridge s, T., Cannon, R., Colless, M., Collins, C., Couch, W., Cross, N.J.G., Dalton, G., Eke, V.R. , Propris, R.D., Driver, S.P., Efstathiou, G., Ellis, R.S., Glazebrook, K., Jackson, C., Jenkins, A., Lahav, O., Lewis, I., Lumsden, S., Maddox, S., M adgwick, D., Peterson, B.A., Sutherland, W., Taylor, K., 20 05, MNRAS, 362, 505.

Collmar W., Mem. Soc. Astron. Ital. 73, 99 (2002).

Cowie L. L., Barger A. J., Bautz M. W., Brandt W. N., Garmire G. P., 2003, ApJ, 584, L57.

Crain R. A., Theuns T., Dalla Vecchia C., Eke V. R. , Frenk S. C., Jenkins A., Kay S. T. and Peacock J. A. *et al.*, 2009, MNRAS, 399, 1773.

Creasey P., Theuns T., Bower G. R. and Lacey C. G.,2011, MNRAS, 415, 3706.

Creasey P., Theuns T. and Bower G. R., 2013, MNRAS, 429, 1922

Croton D. J., Springel V., White S. D. M., De Lucia G., Frenk S. C., Gao L., Jenkins A. and Kauffmann G. *et al.*, 2006, MNRAS, 365, 11.

Cullen, L. and Dehnen, W., 2010, MNRAS, 408, 669.

Dalla Vecchia C. and Schaye J., 2008, MNRAS, 387, 1431.

Dalla Vecchia C. and Schaye J., 2012, MNRAS, 426, 140.

DeBuhr, J., Quataert E., and Ma C. -P., 2011, MNRAS, 412, 1341, arXiv:1006.3312 [astro-ph.CO].

Decarli, R. and Falomo, R. and Treves, A. and Labita, M. and Kotilainen, J. K. and Scarpa, R., 2010, MNRAS, 402, 2453.

Degraf, C. and Di Matteo, T. and Springel, V., 2010, MNRAS, 402, 1927.

DeGraf, C. and Di Matteo, T. and Khandai, N. and Croft, R. and Lopez, J. and Springel, V., 2012, 424,1892.

Dekel A., Birnboim Y., 2006, MNRAS, 368, 2.

Di Matteo T., Springel V. and Hernquist L., 2005, Nature, 433, 604.

Di Matteo, T. and Colberg, J. and Springel, V. and Hernquist, L. and Sijacki, D., 2008, ApJ, 676, 33.

Di Matteo, T. and Khandai, N. and DeGraf, C. and Feng, Y. and Croft, R. A. C. and Lopez, J. and Springel, V., 2012, ApJ, 745, L29.

Dolag, K. and Borgani, S. and Murante, G. and Springel, V., 2009, MNRAS, 399, 497.

Dubois Y. & Teyssier R.,2008, A&A, 477, 79.

Dubois Y., Devriendt Y., Slyz A. and Teyssier R.,2010, MNRAS, 409, 985.

Dubois Y., Pichon C., Devriendt J., Silk J., Haehnelt M., Kimm T. and Slyz A., 2013, MNRAS, 428, 2885.

Durier, F. and Vecchia D. C., 2012, MNRAS, 419, 465.

Ebrero J., Carrera F. J., Page M. J., Silverman J. D., Barcons X., Ceballos M. T., Corral A., Della Ceca R., Watson M. G., 2009, A&A, 493, 55

Edge A. C. and Frayer D. T 2001, ApJ, 594, L13.

Edge, A. C., Ebeling, H., Bremer, M., et al. 2003, MNRAS, 339, 913

Eggen O. J., Lynden-Bell D. and Sandage A. R., 1962, ApJ, 136, 748.

Evrard A. E., 1988, MNRAS, 235, 911.

Fabian A. C., Annu. Rev. Astron. Astrophys., 32, 277.

Fanidakis N. and Baugh C. M. and Benson A. J. and Bower R. G. and Cole S. and Done C. and Frenk C. S. and Hickox R. C. and Lacey C. and Del P. Lagos C., 2012, MNRAS, 419, 2797.

Fanidakis N., Maccio, A. V., Baugh C. M., Lacey C. G. and Frenk C. S., 2013, [arXiv:1305.2199 [astro-ph.CO]].

G. J. Ferland, R. L. Porter, P. A. M. van Hoof, R. J. R. Williams, N. P. Abel, M. L. Lykins, Gargi Shaw, W. J. Henney, and P. C. Stancil, 2013, Rev. Mex. Soc., 49, 1.

Ferrarese L., Merritt D., 2000, ApJ, 539, L9.

Fiore F., Brusa M., Cocchia F., Baldi A., Carangelo N., Ciliegi P., Comastri A., La Franca F., Maiolino R., Matt G., Molendi S., Mignoli M., Perola G. C., Severgnini P., Vignali C., 2003, A&A, 409, 79.

Fiore F., Puccetti S., Grazian A., Menci N., Shankar F., Santini P., Piconcelli E., Koekemoer A. M., Fontana A., Boutsia K., Castellano M., Lamastra A., Malacaria C., Feruglio C., Mathur S., Miller N., Pannella M., 2012, A&A, 537, A16.

Frank, J., King, A., Raine, D., Cambridge, UK: Cambridge University Press, February 2002.

Fryxell B., Olson K., Ricker P., Timmes F. X., Zingale M., Lamb D. Q., MacNeice P., Rosner R., Truran J. W., and Tufo H., 2000, ApJS, 131, 273.

Gao, L., Yoshida, N., Abel, T., Frenk, C.S., Jenkins, A., Springel, V., 2007, MNRAS, 378, 449.

Gebhardt K., Bender R., Bower G., Dressler A., Faber S. M., Filippenko A. V., Green R., Grillmair C., Ho L. C., Kormendy J., Lauer T. R., Magorrian J., Pinkney J., Richstone D., Tremaine S., 2000, ApJ, 539, L13

Gerritsen, J. P. E. and Icke, V.: 1997, A&A, 325, 972.

Gilli, R. and Comastri, A. and Hasinger, G., 2007, A&A, 463, 79.

Goulding, A. D. and Alexander, D. M. and Lehmer, B. D. and Mullaney, J. R., 2010, MNRAS, 406, 597.

Gingold, R. A. and Monaghan J. J., 1977, MNRAS,181,375.

Granato G. L., De Zotti G., Silva L., Bressan A., Danese L., 2004, ApJ, 600, 580.

Greif, T. H. and Glover, S. C. O. and Bromm, V. and Klessen, R. S., 2010, ApJ, 716, 510.

Guo, Q., White, S., Li, C. & Boylan–Kolchin, M. 2010, MNRAS, 404, 1111

Guo, Q., White S., Boylan-Kolchin M., De Lucia .G, Kauffmann G., Lemson G., Li C. and Springel V. *et al.*, 2011, MNRAS, 413, 101.

Gultekin, K., Richstone, D. et al., 2009, ApJ, 698, 198.

Haardt, F. and Madau, P., 2001, Clusters of Galaxies and the High Redshift Universe Observed in X-rays, astro-ph/0106018.

Haas M. R., Schaye J,Booth C. M., Vecchia C. D., Springel V.,Theuns T. and Wiersma . P. C., arXiv:1211.1021

Haring N. and Rix H. W., 2004, ApJ, 604, L89.

Hasinger, G. and Miyaji, T. and Schmidt, M., 2005, A&A, 441, 417.

Hasinger, G., 2008, A&A, 490, 905.

Hirschmann M., Somerville R. S., Naab T., Burkert A., 2012, MNRAS, 426, 237

Hopkins P. F. and Hernquist L. and Cox T. J. and Di Matteo T. and Martini P. and Robertson B. and Springel V., 2005, ApJ, 630, 705.

Hopkins P. F., Hernquist L., Cox T. J., Di Matteo T., Robertson B.and Springel V., 2006 ApJ Suppl.,163,1, [astro-ph/0506398].

Hopkins P. F., Hernquist L., Cox T. J. and Keres D., 2008 ApJ Suppl., 175, 356, [arXiv:0706.1243 [astro-ph]].

Hopkins P. F., and Hernquist L., Cox T. J. , Keres D. and Wuyts S., 2009, ApJ, 691, 1424.

Hopkins, P. F., 2013, arxiv prepints:1305.006.

Huang, J.-S. and Glazebrook, K. and Cowie, L. L. and Tinney, C., 2003,584, 203.

Hubble, E.P., 1929. ApJ, 69, 103.

Jahnke, K. and Bongiorno, A. and Brusa, M. and Capak, P. and Cappelluti, N. and Cisternas, M. and Civano, F. and Colbert, J. and Comastri, A. and Elvis, M. and Hasinger, G. and Ilbert, O. and Impey, C. and Inskip, K. and Koekemoer, A. M. and Lilly, S. and Maier, C. and Merloni, A. and Riechers, D. and Salvato, M. and Schinnerer, E. and Scoville, N. Z. and Silverman, J. and Taniguchi, Y. and Trump, J. R. and Yan, L., 2009, ApJ, 706, L215.

Jenkins A., 2010, MNRAS, 403, 1859.

Jenkins A., 2013, MNRAS, 434, 2094.

Jenkins, A. and Booth, S., 2013, ArXiv e-prints, arxiv:1306.5771.

Katz, N. and Weinberg, D. H. and Hernquist, L., 1996, ApJS, 19.

Katz, N. and Weinberg, D. H. and Hernquist, L., 1996, ApJS, 19.

Kauffmann G., Haehnelt M., 2000, MNRAS, 311, 576.

Kauffmann, G. and Heckman, T. M. 2009, MNRAS, 397,135.

Keel, W., et al. 2012, AJ, 144, 66.

Kelly B. C., Shen Y., 2013, ApJ, 764, 45.

Kennicutt, Jr., R. C., 1983, ApJ, 272, 54.

Kennicutt, Jr., R. C., 1998, ARA&A, 36, 189.

Kereš D., Katz N., Fardal M., Weinberg D. H., Davé 2005, MNRAS, 353, 2.

Kereš D., Katz N., Fardal M., Davé R., Weinberg D. H., 2009, MNRAS, 395, 160.

Khandai, N. and Di Matteo, T. and Croft, R. and Wilkins, S. M. and Feng, Y. and Tucker, E. and DeGraf, C. and Liu, M.-S., 2010, [arxiv:1402.0888[astro-ph.CO]].

King, A. R., Pringle, J. E., Livio, M.,2007 MNRAS, 376, 1740.

Klypin, A. A. and Shandarin, S. F., 1983, MNRAS, 204, 891.

Koester, B. P. and McKay, T. A. and Annis, J. and Wechsler, R. H. and Evrard, A. and Bleem, L. and Becker, M. and Johnston, D. and Sheldon, E. and Nichol, R. and Miller, C. and Scranton, R. and Bahcall, N. and Barentine, J. and Brewington, H. and Brinkmann, J. and Harvanek, M. and Kleinman, S. and Krzesinski, J. and Long, D. and Nitta, A. and Schneider, D. P. and Sneddin, S. and Voges, W. and York, D., 2007, ApJ, 660, 239.

Kolodzig A., Gilfanov M., Sunyaev R., Sazonov S., Brusa M., 2013, A&A, 558, A89.

Komatsu, E, *et al.* WMAP Collaboration 2011, ApJ, 192, 18.

Kochanek, C. S. and Pahre, M. A. and Falco, E. E. and Huchra, J. P. and Mader, J. and Jarrett, T. H. and Chester, T. and Cutri, R. and Schneider, S. E., 2001, ApJ, 560, 566.

Kormendy, J. and Ho, L. C., 2013, ARA&A,51,511.

Kowalski, M., Rubin, D., Aldering, G., Agostinho, R.J., Ama don, A., Amanullah, R., Balland, C., Barbary, K., Blanc, G., Challis, P.J., Conley, A., Connolly, N.V., Covarrubias, R., Dawson, K.S., Deustua , S.E., Ellis, R., Fabbro, S., Fadeyev, V., Fan, X., Farris, B ., Folatelli, G., Frye, B.L., Garavini, G., Gates, E.L., Germany, L., Goldhaber, G. , Goldman, B., Goobar, A., Groom, D.E., Haissinski, J., Hard in,

D., Hook, I., Kent, S., Kim, A.G., Knop, R.A., Lidman, C., Linder, E.V., Mendez, J., Meyers, J., Miller, G.J., Moniez, M., ao, A.M.M., Newber g, H., Nobili, S., Nugent, P.E., Pain, R., Perdereau, O., Perlmutter, S., Phil lips, M.M., Prasad, V., Quimby, R., Regnault, N., Rich, J., R ubenstein, E.P., Ruiz-Lapuente, P., Santos, F.D., Schaefer, B.E., Schommer, R.A. , Smith, R.C., Soderberg, A.M., Spadafora, A.L., Strolger, L., Strovink, M., Suntzeff, N.B., Suzuki, N., Thomas, R.C., Walton, N.A., Wang, L., Wood-Vasey, W.M., Yun, J.L., 2008, ApJ, 686, 749.

Krumholz M. R, McKee C. F. and Klein R. I., 2005 ApJ, 618, 757, [astro-ph/0409454].

Kuo, C. Y. and Braatz, J. A. and Condon, J. J. and Impellizzeri, C. M. V. and Lo, K. Y. and Zaw, I. and Schenker, M. and Henkel, C. and Reid, M. J. and Greene, J. E., 2011, ApJ, 727,20.

La Franca, F. and Fiore, F. and Comastri, A. and Perola, G. C. and Sacchi, N. and Brusa, M. and Cocchia, F. and Feruglio, C. and Matt, G. and Vignali, C. and Carangelo, N. and Ciliegi, P. and Lamastra, A. and Maiolino, R. and Mignoli, M. and Molendi, S. and Puccetti, S., 2005, 635, 864.

Lauer, T. R., Tremaine, S., Richstone, D., & Faber, S. M. 2007, ApJ, 670, 249

Li, C. and White, S. D. M, 2009, MNRAS, 398, 2177.

Lynden-Bell D., 1969, Nature, 223, 690.

Lucy, L. B., 1977, Astronomical Journal, 82, 1013.

Ma, C. J., McNamara, B. R. and Nulsen P. E. J., 2013, ApJ, 763, 63.

Madau, P. and Ferguson, H. C. and Dickinson, M. E. and Giavalisco, M. and Steidel, C. C. and Fruchter, A., 1996, MNRAS, 283,1388.

Magorrian J., Tremaine, Richstone D. S., Bender R., Bower G., Dressler A., Faber S. M. and Gebhardt K. *et al.*, 1998, ApJ, 115, 2285.

Maiolino R., Neri R., Beelen A., et al., 2007, A&A, 472, L33

Malbon R. K., Baugh C. M., Frenk C. S. and Lacey C. G, MNRAS, 382, 1394.

Marconi, A. and Hunt, L. K., 2003, ApJ, 589,L21.

Marconi, A. and Risaliti, G. and Gilli, R. and Hunt, L. K. and Maiolino, R. and Salvati, M. 2004, MNRAS, 351, 169.

Marigo P., 2001, A&A ,370, 194.

Marri, S. and White, S. D. M., 2003, MNRAS, 345, 561.

Marulli F., Bonoli S., Branchini E., Moscardini L., Springel V., 2008, MNRAS, 385, 1846.

McCarthy I. G., Schaye J., Ponman T. J., Bower R. G., Booth C. M., Dalla Vecchia C., Crain R. A. and Springel V., 2010, MNRAS, 406, 822, [arXiv:0911.2641 [astro-ph.CO]].

McCarthy I. G., Schaye J., Bower R. G., Ponman T. J., Booth C. M., Vecchia C. D. and Springel V. *et al.* 2011, MNRAS, 412, 1965, [arXiv:1008.4799 [astro-ph.CO]].

McConnell N. J. and Ma C. P.,2012 ,[arXiv:1211.2816 [astro-ph.CO]].

McGee, S. L., 2013,MNRAS, [arxiv:1302.6237[astro-ph.CO]]

McKee, C. F. and Ostriker, J. P., 1977, ApJ, 218, 148.

McLure R. J. & Jarvis M. J. 2002, MNRAS, 337, 109.

McLure R. J., Jarvis M. J., Targett T. A., Dunlop J. S., & Best P. N. 2006, MNRAS, 368, 1395

McNamara B. R. and Nulsen P. E. J. and Wise M. W. and Rafferty D. A. and Carilli C. and Sarazin C. L. and Blanton E. L., 2005, Nature, 433, 45.

McNamara B. R. and Nulsen P. E. J., 2007, ARA&A, 45, 117.

Meier D. L., 2001, ApJ, 548, L9, [arxiv:0010231[astro-ph.CO]].

Menci N., Fiore F., Lamastra A., 2013, ArXiv e-prints

Menci N., Fiore F., Perola G. C., Cavaliere A., 2004, ApJ, 606, 58.

Merloni, A. and Bongiorno, A. and Bolzonella, M. and Brusa, M. and Civano, F. and Comastri, A. and Elvis, M. and Fiore, F. and Gilli, R. and Hao, H. and Jahnke, K. and Koekemoer, A. M. and Lusso, E. and Mainieri, V. and Mignoli, M. and Miyaji, T. and Renzini, A. and Salvato, M. and Silverman, J. and Trump, J. and Vignali, C. and Zamorani, G. and Capak, P. and Lilly, S. J. and Sanders, D. and Taniguchi, Y. and Bardelli, S. and Carollo, C. M. and Caputi, K. and Contini, T. and Coppa, G. and Cucciati, O. and de la Torre, S. and de Ravel, L. and Franzetti, P. and Garilli, B. and Hasinger, G. and Impey, C. and Iovino, A. and Iwasawa, K. and Kampczyk, P. and Kneib, J.-P. and Knobel, C. and Kovač, K. and Lamareille, F. and Le Borgne, J.-F. and Le Brun, V. and Le Fèvre, O. and Maier, C. and Pello, R. and Peng, Y. and Perez Montero, E. and Ricciardelli, E. and Scodeggio, M. and Tanaka, M. and Tasca, L. A. M. and Tresse, L. and Vergani, D. and Zucca, E. 2010, ApJ, 708,137, [arXiv:1306.4327 [astro-ph.CO]]

Miyaji T., Hasinger G., Schmidt M., 2000, A&A, 353, 25.

Monaghan, J. J. and Lattanzio, J. C., 1984, A&A, 149, 135.

Monaco P., Fontanot F., 2005, MNRAS, 359, 283

Mortlock D. J., Patel M., Warren S. J, Hewett P. C., Venemans B. P., McMahon R. G., and Simpson C. J., 2012, MNRAS, 419, 390.

Moster B. P., Somerville R. S., Maulbetsch C., v. d. Bosch F. C., Maccio' A. V., Naab T. and Oser L., 2010, ApJ, 710, 903.

Muldrew S. I., Pearce F. R. and Power C.,2013, arXiv:1306.4327 [astro-ph.CO].

Mullaney J. R.,Daddi E., Bethermin M., Elbaz D., Juneau S., Pannella M., Sargent M. T. and Alexander D. M *et al.* 2012, ApJ, 753, 2, arXiv:1204.2824 [astro-ph.CO].

Murante, G. and Monaco, P. and Giovalli, M. and Borgani, S. and Diaferio, A., 2010, MNRAS, 405, 1491.

Nandra K., Laird E. S., Steidel C. C., 2005, MNRAS, 360, L39.

Narayan, R. and Yi, I., 1994, ApJ, 428, L13.

Narlikar J.V., Padmanabhan T., 2001. Annual Review of Astronomy & Astrophysics 39, 211.

Nemmen R. S., Bower R. G., Babul A. and Storchi-Bergmann T., 2007, MNRAS ,377,1652, [astro-ph/0612354].

Newton R. D. A. and Kay S. T., 2013, MNRAS, 434, 3606.

Norman M. L. & Bryan G. L., 1999, in S. M. Miyama, K. Tomisaka, and T. Hanawa, 1999, Numerical Astrophysics, 240, 19.

Okamoto T., Gao L. and Theuns T., 2008, MNRAS, 390, 920

Oppenheimer, B. D. and Davé, R., 2008, MNRAS, 387, 577.

Padovani, P., 1997, arxiv-eprints, arXiv:astro-ph/9701074.

Peebles, P. J. E., 1980, Phys. Scr, 21, 720.

Pen, U.-L., 1998, ApJS, 115, 19.

Percival, W.J., Nichol, R.C., Eisenstein, D.J., Frieman, J .A., Fukugita, M., Loveday, J., Pope, A.C., Schneider, D.P. , Szalay, A.S., Tegmark, M., Vogeley, M.S., Weinberg, D.H., Zehavi, I., Bahcall, N.A., B rinkmann, J., Connolly, A.J., Meiksin, A., 2007a ,ApJ, 657, 645.

Perlmutter, S. and Turner, M. S. and White, M., 1999, Physical Review Letters, 83, 670.

Peterson J. R., 2003, ApJ, 590, 207.

Peterson B. M. and Ferrarese L. and Gilbert K. M. and Kaspi S. and Malkan M. A. and Maoz D. and Merritt D. and Netzer H. and Onken C. A. and Pogge R. W. and Vestergaard M. and Wandel A., 2004, ApJ, 613, 682.

Pilbratt G. L. , Riedinger J. R., Passvogel T., Crone G., Doyle D., Gageur U., Heras A. M., Jewell C., Metcalfe L., Ott S. and Schmidt M., 2010, A&A, 518, L1.

Planck Collaboration and Ade, P. A. R. and Aghanim, N. and Alves, M. I. R. and Armitage-Caplan, C. and Arnaud, M. and Ashdown, M. and Atrio-Barandela, F. and Aumont, J. and Aussel, H. and et al., 2013, arxiv e-prints, 1303.5062.

Portinari L., Chiosi C., & Bressan A. 1998, A&A, 334, 505.

Power, C. and Nayakshin, S. and King, A., 2011, MNRAS, 412, 269.

Price D. J., 2008, Journal of Computational Physics, 227, 10040.

Puchwein E. and Springel V., 2013, MNRAS, 428, 2966.

Quilis V., 2004, MNRAS, 352, 1426.

Rafferty DA, McNamara BR, Nulsen PEJ, Wise MW, 2006, ApJ, 652, 216.

Rees, M. J. and Begelman, M. C. and Blandford, R. D. and Phinney, E. S., 1982, NATURE, 295, 17.

Rees, M. J. and Ostriker, J. P., 1977, MNRAS, 179, 541.

Riess, A. G. and Nugent, P. and Filippenko, A. V. and Kirshner, R. P. and Perlmutter, S., 1998, ApJ, 504, 935.

Romano-Diaz E., Schlosman I., Trenti M. and Hoffman Y., 2010, ApJ, 736,66.

Ross, A. J. and Brunner, R. J., 2009, MNRAS, 399, 878.

Salpeter E. E., 1964, ApJ, 140, 796.

Sanders D. B. and Soifer B. T. and Elias J. H. and Madore B. F. and Matthews K. and Neugebauer G. and Scoville N. Z., 1988, ApJ, 325, 74.

Sazonov S. Y., Revnivtsev M. G., 2004, A&A, 423, 469.

Scannapieco, E. and Kawata, D. and Brook, C. B. and Schneider, R. and Ferrara, A. and Gibson, B. K., 2006, ApJ, 661, 10.

Schaye, J., 2004, ApJ , 609, 667.

Schaye J., Dalla Vechia C., 2008, MNRAS, 383, 1210.

Schaye J., Dalla Vecchia C., Booth C. M., Wiersma R. P. C., Theuns T., Haas M. R., Bertone S. and Duffy A. R.*et al.*, 2010, MNRAS, 402, 1536.

Schaye J., Crain R. A., Bower R. G., et al. 2014, ArXiv e-prints, arXiv:1407.7040.

Schmidt, M., 1959, ApJ, 129, 243.

Schreiber M. R., Hameury J. -M. and Lasota J. -P., 2004, Astron.& Astrophys, 427, 621.

Schulze, A. and Wisotzki, L., 2014, MNRAS, 438, 3422.

Seyfert, C. K. 1943, ApJ, 97, 28.

Shakura N.I ., Syunyaev R. A., 1973, AAP, 24, 337.

Shankar, F. and Salucci, P. and Granato, G. L. and De Zotti, G. and Danese, L., 2004, MNRAS, 354, 1020.

Shankar, F. and Weinberg, D. H. and Miralda-Escudé, J., 2009, ApJ, 690, 20.

Shen Y. & Kelly, B. C. 2010, ApJ, 713, 41.

Sijacki D., Springel V., Di Matteo T. and Hernquist L., 2007 MNRAS, 380, 877.

Silk J.and Rees M. J., 1998, Astron.& Astrophys, 331, L1.

Silverman J. D. and Green P. J. and Barkhouse W. A. and Kim D.-W. and Kim M. and Wilkes B. J. and Cameron R. A. and Hasinger G. and Jannuzi B. T. and Smith M. G. and Smith P. S. and Tananbaum H., 2008, ApJ, 679, 118.

Soltan A., 1982, MNRAS, 200, 115.

Somerville R. S., Hopkins P. F., Cox T. J., Robertson B. E., Hernquist L., 2008, MNRAS, 391, 481.

Springel V.,Yoshida, N., White, S. D. M., 2001, New Astron, 6,79.

Springel, V. and Hernquist, L., 2002, MNRAS, 333, 649.

Springel, V. and Hernquist, L., 2003, MNRAS, 339, 289.

Springel V., Di Matteo T. and Hernquist L., 2005, MNRAS, 361, 776.

Springel, V., 2005b, MNRAS, 364, 1105.

Steffen, A. T. and Barger, A. J. and Cowie, L. L. and Mushotzky, R. F. and Yang, Y., 2003, ApJ, 596, L23.

Stinson, G. and Seth, A. and Katz, N. and Wadsley, J. and Governato, F. and Quinn, T., 2006, MNRAS, 373, 1074.

Sutherland, R. S. and Dopita, M. A., 1993,ApJ, 88, 253.

Targett, T. A., Dunlop, J. S., & McLure, R. J. 2012, MNRAS, 420, 3621.

Tegmark, M., Silk, J., Rees, M.J., Blanchard, A., Abel, T., P alla, F., 1997, ApJ, 474, 1.

Tegmark, M., Blanton, M.R., Strauss, M.A., Hoyle, F., Schle gel, D., Scoccimarro, R., Vogeley, M.S., Weinberg, D.H., Ze havi, I., Berlind, A., Budavari, T., Connolly, A., Eisenstein, D.J., Finkbeiner, D., Frieman, J.A., Gunn, J.E., Hamilton, A.J.S., Hui, L., Ja in, B., Johnston, D., Kent, S., Lin, H., Nakajima, R., Nichol, R.C., Ostriker, J.P., Pop e, A., Scranton, R., Seljak, U., Sheth, R.K., Stebbins, A., S zalay, A.S., Szapudi, I., Verde, L., Xu, Y., Annis, J., Bahcall, N.A., Brinkmann, J., B urles, S., Castander, F.J., Csabai, I., Loveday, J., Doi, M. , Fukugita, M., Gott, J.R., Hennessy, G., Hogg, D.W., Ivezic, Z., Knapp, G.R., Lamb, D.Q ., Lee, B.C., Lupton, R.H., McKay, T.A., Kunszt, P., Munn, J. A., OâĂŹConnell, L., Peoples,

J., Pier, J.R., Richmond, M., Rockosi, C., Schn eider, D.P., Stoughton, C., Tucker, D.L., Berk, D.E.V., Yan ny, B., York, D.G., 2004, ApJ, 606, 702.

Teyssier R., 2007, Astrophysics Software Database, 33.

Torres D. F., 2004, arXiv-eprints ,arXiv:astro-ph/0308069.

Tremaine S., Gebhardt K., Bender R., Bower G., Dressler A., Faber S. M., Filippenko A. V. and Green R. *et al.*, 2002, ApJ, 574, 740.

Ueda, Y. and Akiyama, M. and Ohta, K. and Miyaji, T., 2003,ApJ, 598, 886.

Urry, C. M. and Padovani, P., 1995, PASP,107 , 803.

van de Voort F, Schaye J., Booth C. M., Haas M. R. and Dalla Vecchia C., 2011, MNRAS, 414, 2458.

Vikhlinin, A. and Kravtsov, A. V. and Burenin, R. A. and Ebeling, H. and Forman, W. R. and Hornstrup, A. and Jones, C. and Murray, S. S. and Nagai, D. and Quintana, H. and Voevodkin, A., 2009, ApJ, 692, 1060.

Vestergaard, M. & Peterson, B. M. 2006, ApJ, 641, 689

Volonteri M., Haardt F., Madau P., 2003, ApJ, 582, 559.

Vogelsberger M., Genel S., Sijacki D., Torrey P., Springel V., Hernquist L., 2013, arXiv, arXiv:1305.2913

Yencho, B. and Barger, A. J. and Trouille, L. and Winter, L. M, 2009, ApJ, 698, 380.

York, D. G. and Adelman, J. and Anderson, Jr., J. E. and Anderson, S. F. and Annis, J. and Bahcall, N. A. and Bakken, J. A. and Barkhouser, R. and Bastian, S. and Berman, E. and Boroski, W. N. and Bracker, S. and Briegel, C. and Briggs, J. W. and Brinkmann, J. and Brunner, R. and Burles, S. and Carey, L. and Carr, M. A. and Castander, F. J. and Chen, B. and Colestock, P. L. and Connolly, A. J. and Crocker, J. H. and Csabai, I. and Czarapata, P. C. and Davis, J. E. and Doi, M. and Dombeck, T. and Eisenstein, D. and Ellman, N. and Elms, B. R. and Evans,

M. L. and Fan, X. and Federwitz, G. R. and Fiscelli, L. and Friedman, S. and Frieman, J. A. and Fukugita, M. and Gillespie, B. and Gunn, J. E. and Gurbani, V. K. and de Haas, E. and Haldeman, M. and Harris, F. H. and Hayes, J. and Heckman, T. M. and Hennessy, G. S. and Hindsley, R. B. and Holm, S. and Holmgren, D. J. and Huang, C.-h. and Hull, C. and Husby, D. and Ichikawa, S.-I. and Ichikawa, T. and Ivezić, Ž. and Kent, S. and Kim, R. S. J. and Kinney, E. and Klaene, M. and Kleinman, A. N. and Kleinman, S. and Knapp, G. R. and Korienek, J. and Kron, R. G. and Kunszt, P. Z. and Lamb, D. Q. and Lee, B. and Leger, R. F. and Limmongkol, S. and Lindenmeyer, C. and Long, D. C. and Loomis, C. and Loveday, J. and Lucinio, R. and Lupton, R. H. and MacKinnon, B. and Mannery, E. J. and Mantsch, P. M. and Margon, B. and McGehee, P. and McKay, T. A. and Meiksin, A. and Merelli, A. and Monet, D. G. and Munn, J. A. and Narayanan, V. K. and Nash, T. and Neilsen, E. and Neswold, R. and Newberg, H. J. and Nichol, R. C. and Nicinski, T. and Nonino, M. and Okada, N. and Okamura, S. and Ostriker, J. P. and Owen, R. and Pauls, A. G. and Peoples, J. and Peterson, R. L. and Petravick, D. and Pier, J. R. and Pope, A. and Pordes, R. and Prosapio, A. and Rechenmacher, R. and Quinn, T. R. and Richards, G. T. and Richmond, M. W. and Rivetta, C. H. and Rockosi, C. M. and Ruthmansdorfer, K. and Sandford, D. and Schlegel, D. J. and Schneider, D. P. and Sekiguchi, M. and Sergey, G. and Shimasaku, K. and Siegmund, W. A. and Smee, S. and Smith, J. A. and Snedden, S. and Stone, R. and Stoughton, C. and Strauss, M. A. and Stubbs, C. and SubbaRao, M. and Szalay, A. S. and Szapudi, I. and Szokoly, G. P. and Thakar, A. R. and Tremonti, C. and Tucker, D. L. and Uomoto, A. and Vanden Berk, D. and Vogeley, M. S. and Waddell, P. and Wang, S.-i. and Watanabe, M. and Weinberg, D. H. and Yanny, B. and Yasuda, N. and SDSS Collaboration,2000, AJ, 120, 1579

Yu, Q. and Tremaine, S., 2002, MNRAS, 335, 965.

Wadsley, J. W., Stadel, J. and Quinn, T., 2004, New Astronomy, 9, 137.

Wang, R. and Carilli, C. L. and Neri, R. and Riechers, D. A. and Wagg, J. and

Walter, F. and Bertoldi, F. and Menten, K. M. and Omont, A. and Cox, P. and Fan, X., 2010, ApJ, 714, 699.

Werner, M. W. and Roellig, T. L. and Low, F. J. and Rieke, G. H. and Rieke, M. and Hoffmann, W. F. and Young, E. and Houck, J. R. and Brandl, B. and Fazio, G. G. and Hora, J. L. and Gehrz, R. D. and Helou, G. and Soifer, B. T. and Stauffer, J. and Keene, J. and Eisenhardt, P. and Gallagher, D. and Gautier, T. N. and Irace, W. and Lawrence, C. R. and Simmons, L. and Van Cleve, J. E. and Jura, M. and Wright, E. L. and Cruikshank, D. P., 2004, ApJS, 154, 1.

Wiersma R. P. C., Schaye J., Theuns T., Smith B. D, 2009, MNRAS, 393, 99.

Wiersma R. P. C., Schaye J., Theuns T., Dalla Vecchia C. and Tornatore L., 2009, MNRAS, 399, 574.

White, S. D. M., Rees, M. J., 1978. MNRAS, 183, 341.

White D. M.S. and Frenk S. C., 1991 ApJ, 379, 52.

Zeld́ovich Y. B, 1964, Soviet Physics Doklady, 9, 195.